# A Deterministic Method To Detect Wave Directions From Surface Elevations

## Accuracy And Sensitivity Analysis For The SWDD Method By Using Synthetic Wave Signals And The Mild-Slope Wave Model WIHA

MSc Thesis

**R. Klarenbeek**



**TU**Delft

Witteveen+Bos

# A Deterministic Method To Detect Wave Directions From Surface Elevations

Accuracy and sensitivity analyses for the SWDD method by using
synthetic wave signals and the mild-slope wave model WIHA

By

**Rick Klarenbeek**

in partial fulfilment of the requirements for the degree of

**Master of Science**
in Civil engineering

at the Delft University of Technology,
to be defended publicly on Wednesday November 14, 2018 at 14:30 PM.

| Thesis committee: | Prof. dr. ir. A.J.H.M. Reniers, | TU Delft, chairman |
| | Dr. ir. M. Zijlema, | TU Delft |
| | Dr. ir. B. Hofland, | TU Delft |
| | Dr. ir. G.Ph. van Vledder, | TU Delft |
| | Dr. ir. G. Klopman, | Witteveen+Bos |
| | Ir. L. Straatsma, | Witteveen+Bos |

An electronic version of this thesis is available at http://repository.tudelft.nl/.

**TU**Delft

Witteveen+Bos

# Preface

In this master thesis, you will read my graduation work on the understanding, analysing and validating of the new mild-slope wave model WIHA and the new deterministic directional wave-analysis method SWDD. This thesis is the final product of my master Hydraulic Engineering at the Technical University of Delft and has been carried out in cooperation with Witteveen+Bos.

During my BSc in Civil Engineering, I grew very interested in Coastal Engineering and especially in hydrodynamics, morphology and the prevention of flooding. The immense power, infinite presence, and unproductiveness in ocean waves is what triggers me the most.

At the start of my master – Hydraulic Engineering – I realized that I wanted to put my studies into practice and obtain practical experience at an engineering firm. However, I was very interested in many elective courses as well. This made me decide to fill 20 elective ECTS by various in depth courses and perform my MSc thesis project externally.

I am glad that – after my application – I was given the opportunity and trust from the TU Delft and Witteveen+Bos to start my graduation project on WIHA and SWDD. I would like to thank professor A.J.H.M Reniers and D.W. Dusseljee for their honest input during this preliminary process. Furthermore, I would like to thank Ad Reniers, Marcel Zijlema, Bas Hofland and Gerbrant van Vledder for their interest in the subject and representing TU Delft in my thesis committee. And, Gert Klopman and Leonie Straatsma on representing Witteveen+Bos in my thesis committee.

My gratitude goes out to all the committee members for their time, optimism, great ideas and feedback. I want to also show my recognition to Gert for his endless patience, assistance and inspiration during the weekly meetings we had. And of course, I would like to thank the remaining employees in the group of Hydrodynamics and Morphology at Witteveen+Bos for their input and nice coffee & lunch breaks.

In almost nine months – from February till October – I learned to solve a complex and broad engineering subject maintaining a high quality of scientific approach. Furthermore, I learned to organize, plan, manage and monitor such an extensive project from the beginning to the end including many intermediate presentations and reports.

My journey towards becoming a civil engineer was exciting and enjoyable, among others due to my friends, family and girlfriend. I would like to thank my friends in Delft for the nice times during – and in between – the lectures and assignments. And, many thanks to my friends in Amsterdam for the great non-technical and cosy hang outs. Last but not least, thanks to my family for their trust, patience and (financial) support. And, to my girlfriend for her understanding, encouragement and love.

I wish you a pleasant read.

*Rick Klarenbeek*
*Delft, October 2018*

# Abstract

This research describes a new method called SWDD (Klopman, Witteveen+Bos, 2018b), which can obtain information on wave propagation directions from the surface elevations at a set of positions. The primary intention of the method is to separate multiple incoming wave components, i.e. wave heights, phases and directions. The goal is to obtain the incoming wave conditions, that can among others be used in the design of (coastal) structures and assessment of moored ship response.

The novelty of this method is that a large number of incoming wave directions is prescribed, equally distributed around a circle. For each of these many incoming wave conditions, the wave amplitude and phase are the unknowns (while the directions are known). The main advantage is that this makes the problem linear and in that aspect easier to solve. The disadvantage is that, most often, the resulting system becomes ill-posed (having more unknowns than equations). This problem is solved by using Tikhonov regularization (Tikhonov and Arsenin, 1977) together with the L-curve method (Hansen, 1992; 2000). The main differences with other common deterministic directional wave-analysis methods are: the SWDD method is free of user-checks after each analysis, the directional resolution is higher, the computation time is faster and a wave field reconstruction after the directional wave-analysis is possible.

The applicability of the SWDD method has been tested using synthetic wave signals for (the sum of) monochromatic long-crested waves, prescribed wave patterns – containing wave-crest curvature and wave amplitude variation – and model results of a mild-slope wave model (WIHA). Multiple sensitivity analyses have been applied to check the sensitivity of the SWDD method to: various physical phenomena (e.g. diffraction and wave amplitude variation), domain variations (e.g. slopes) and input parameter variation. The study shows that the SWDD method is able to analyse irregular wave-fields using an array configuration containing a low number of gauges and a dense grid containing many gauges. Based on the findings an advisory flowchart is presented on how to determine the optimum radius of the array setup for using the SWDD method in practice, both for the analysis of data from phase-resolving numerical wave models and from measurements.

The study shows that the SWDD method is a robust and reliable method to analyse (complex) wave fields on a (near) homogeneous bathymetry. The incoming wave direction(s) and associated wave height(s) are graphically depicted in a polar plot or a directional spectrum.

**Keywords:** *Wave direction(s), deterministic directional wave-analysis, wave component splitting, harbour design wave conditions.*

# Executive summary

This research describes a new method called SWDD (Klopman, Witteveen+Bos, 2018b), which can obtain information on wave propagation directions from the surface elevations at a set of positions. The primary intent of the method is to **separate multiple incoming wave components**, i.e. wave heights, phases and directions. **The main need** and goal of the SWDD method is to obtain these incoming wave conditions, which among others can be used in the design of (coastal) structures and assessment of moored ship response in harbours. An example of such a directional analysis is presented below. The left plot shows the distribution of wave height, for waves approaching a harbour basin from the upper left (black arrow). The amplitude at a set of locations (black dots) is analysed by the SWDD method and afterwards presented in a polar plot (right plot).
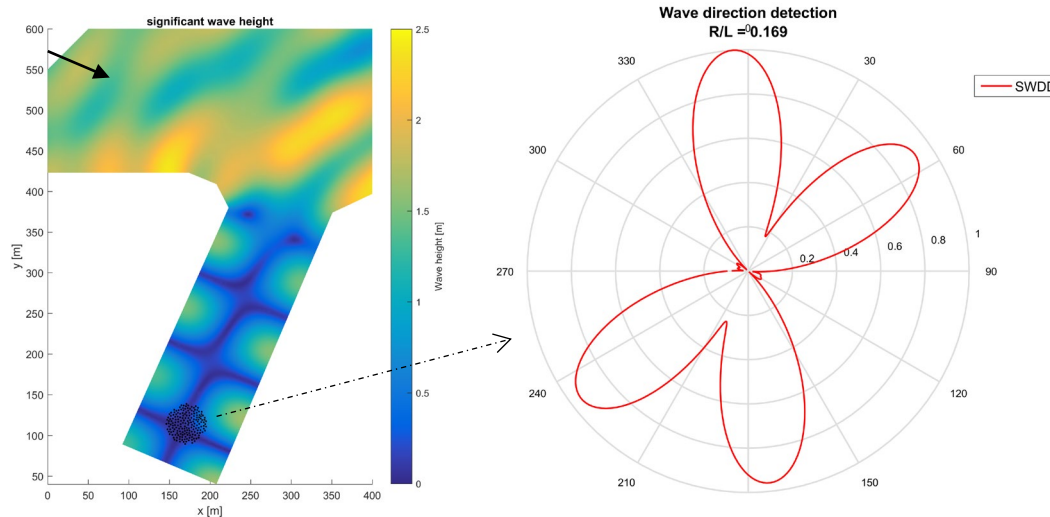


**Overall**, the study shows that the SWDD method is a robust, reliable and user friendly method to analyse (complex) wave fields on a (near) homogeneous bathymetry. The incoming wave direction(s) and associated wave height(s) are graphically depicted in a polar plot or a 2D (directional) spectrum. The results show that the most important factor for success is the array-configuration, i.e. the number of gauges and the gauge-array radius ($R/L$-value). Based on the findings from this research an **advisory flowchart** is presented to determine the optimum radius of the array setup for using the SWDD method in practice.

**The novelty** of this method is that a large number of incoming wave directions is prescribed, equally distributed around a circle. For each of these many incoming wave conditions, the wave amplitude and phase are the unknowns (while the directions are known). The main advantage is that this makes the problem linear and in that respect easier to solve. The disadvantage is that, most often, the resulting system becomes ill-posed (having more unknowns than equations). This problem is solved by using Tikhonov regularization (Tikhonov and Arsenin, 1977) together with the L-curve method (Hansen, 1992; 2000). The main differences with other deterministic directional wave-analysis methods are: the SWDD method is free of user-checks after each analysis, the directional resolution is higher, the computation time is fast and a wave field reconstruction after the directional wave-analysis is possible.

The applicability of the SWDD method has been **tested** using:
- Synthetic wave signals consisting of (the sum of) monochromatic long-crested waves considering laboratorial array setups (e.g. CERC-6 by Panicker and Borgman, 1970; Davis and Regier, 1977; Hawkes et al., 1997) and dense array setups.
- Prescribed wave patterns containing wave-crest curvature and wave amplitude variation.
- The output of a phase-resolving mild-slope wave model (WIHA) considering different cases. Containing among others: diffraction patterns and irregular bathymetries (e.g. a slope).

Since **WIHA** is a new mild-slope wave model developed by Witteveen+Bos and is used in the study of the applicability of the SWDD method, a preliminary validation had been performed for WIHA as well. The validation considers the following cases: Homma's island (Homma, 1950), the Berkhoff shoal (Berkhoff, 1972), benchmark tests of wave penetration in harbours (Van der Ven and Deltares, 2016) and the navigation channel case (Dusseljee et al., 2014). It came forward that WIHA computed the results accurate when non-linear processes are minimally present (not yet implemented) and was considered an appropriate and suitable model to use in one of the validation testcases of the SWDD method.

To evaluate **the applicability of the SWDD method**, multiple sensitivity analyses have been performed, among others to check the influence to: various physical phenomena (e.g. diffraction and wave amplitude variation), domain variations (e.g. slopes) and input parameter variations. The SWDD method assumes a spatial homogeneity (wave field and bathymetry) in the considered region (array setup). So it assumes the wave dynamics can be approximated by linear wave theory over a uniform bottom implying a constant wave number (e.g. Airy, 1845).

The study shows that the SWDD method is able to analyse **non-homogeneous wavefields**. The SWDD method is not influenced by wave amplitude variation and mainly sensitive for high effects of wave-crest curvature (e.g. circular **diffraction patterns**) close to the source (*i.e.* $L/R_c > 1.00$). More than one wavelength away from the diffraction source the results are accurate when the radius of the array setup is chosen according to the range of applicability of: $0.10 \leq R/L \leq 0.30$. Then the results contain an accuracy limit for the directional error of 2.50° and for the reconstruction error inside the array setup of 2%.

The study shows that the SWDD method can be largely influenced by a **non-homogeneous bathymetry** (i.e. slopes), because SWDD assumes a constant wave number value. When a slope is present – containing high gradients ($\Delta kd/\overline{kd} > 0.25$) and where the $kd$ value at the centre of the array configuration is relatively low (< 0.50) – the wavenumber, phase-velocity and the wave profile change as a result of shoaling and refraction effects. When such a slope is present within the array configuration, the optimal range of applicability to use for the radius depends on the $kd$-value. For $kd < 0.50$ the advised range of applicability is: $0.10 \leq R/L \leq 0.20$ and for $kd > 0.50$ an approximated range of applicability of: $0.10 \leq R/L \leq 0.30$ is advised.

A comparison study with other directional wave-analysis methods has been performed, among others using a deterministic method (**r-DPRA** by de Jong and Borsboom, 2012) and stochastic methods (**MLM and BDM**). The main differences between the SWDD method and the r-DPRA method is: user checks for each directional wave-analysis performed are not needed, the directional resolution is higher and the computation time is faster.

It is demonstrated that the SWDD method is able to produce **2D wave spectra** at the user specified output locations (both for an array containing few gauges and containing many gauges) using the mild-slope wave model WIHA. In contrast with the stochastic directional wave-analysis methods, the SWDD method is able to analyse dense array configurations and separate a **high number of wave components**. The maximum separation of the different wave components depends on the directional resolution This in turn mainly depends on the array configuration (i.e. the radius of the array configuration and the number of gauges). A directional resolution of 10° up to 5° is obtainable by using a dense array configuration containing a radius that is larger than two wavelengths.

# Contents

# Nomenclature

**Acronyms**

| | |
|---|---|
| **BDM** | Bayesian directional method |
| **CERC** | Coastal Engineering Research Centre |
| **DPRA** | Directional phase-resolving analysis |
| **DSF** | Directional spreading function |
| **FEM** | Finite element method |
| **FSD** | Fourier series decomposition |
| **GRSM** | Golfrichting spreiding meter (wave directional-spreading gauge) |
| **HARES** | Harbour resonance (mild-slope wave model by SVASEK) |
| **HAWAII** | Shallow water initiative (Joint Industry Project) |
| **HWHM** | Half-width height maximum |
| **JONSWAP** | Joint North Sea Wave Project |
| **MEM** | Maximum entropy method |
| **ML** | Main lobe |
| **MLM** | Maximum likelihood method |
| **MWL** | Mean water level |
| **NPWL** | Nodes per wavelength |
| **PHAROS** | Program for harbour oscillations (mild-slope wave model by Deltares) |
| **PHM** | Physical model |
| **r-DPRA** | Rotational directional phase-resolving analysis |
| **SL** | Spurious lobe |
| **SVD** | Singular-value-decomposition |
| **SW** | Shallow water |
| **SWAN** | Simulating waves nearshore (Delft University of Technology) |
| **SWASH** | Simulating waves till shore (Delft University of Technology) |
| **SWDD** | SVD wave direction detection (by Wittveen+Bos) |
| **SWE** | Shallow water equations |
| **TFS** | Truncated Fourier series |
| **WHM** | Wave height meter |
| **WIHA** | Waves in harbours (mild-slope wave model by Witteveen+Bos) |

**List of terms**

| | |
|---|---|
| **Wave array** | A setup of gauges (or grid nodes) positioned and configured in a particular way |
| **Dipole** | A pair of equal and oppositely wave sources |
| **Wave gauge** | An instrument, which measures the wave height (i.e. WHM) and possibly the orbital velocities (i.e. GRSM) |
| **Main lobe** | A lobe containing the largest strength in a polar radiation plot |
| **Noise** | Unwanted disturbance in the data, e.g. uncertainty in the sensor positions, uncertainty in the measured surface elevations, dispersion errors, round-off errors and low wind waves |
| **Spurious lobe** | Spurious side lobes which arise besides the main lobes due to the Gibbs phenomenon |

## Symbols

| | | |
|---|---|---|
| $\alpha$ | Functions of the horizontal position (*x,y*) dependent on mild-slope variant | [-] |
| $\alpha_m$ | Parameter depend on the type of wave signal | [-] |
| $\alpha_{ML}$ | The complex valued amplitude corresponding to the main lobe | [m] |
| $\alpha_s$ | Bottom slope | [-] |
| $\alpha_{SWDD}$ | Solution vector of the SWDD complex amplitudes | [m] |
| $\beta$ | Functions of the horizontal position (*x,y*) dependent on mild-slope variant | [-] |
| $\beta_m$ | Parameter depend on the type of wave signal | [-] |
| $\beta_{SWDD}$ | Vector with wave directions corresponding with alpha | [rad or deg] |
| $\gamma$ | Scaling factor dependent on mild-slope variant | [-] |
| $\gamma_b$ | Breaking coefficient | [-] |
| $\Gamma$ | Gamma function | [-] |
| $\nabla$ | La place operator | |
| $\varepsilon$ | Error | [-] |
| $\varepsilon_{dir}$ | The error in the direction | [-] |
| $\varepsilon_{recon,array}$ | The reconstruction error only inside the array setup | [-] |
| $\varepsilon_{recon,large}$ | The reconstruction error on a large domain *(L by L)* | [-] |
| $\zeta$ | Free-surface elevation (+MWL) | [m] |
| $\eta$ | (Complex valued) surface elevation | [m] |
| $\theta$ | Direction | [rad or deg] |
| $\theta_0$ | Offshore incoming wave direction | [rad or deg] |
| $\kappa$ | Added parameter to fulfil a condition | [-] |
| $\lambda$ | Tikhonov parameter | [-] |
| $\mu$ | Free parameter | [-] |
| $\nu$ | Free parameter | [-] |
| $\xi_0$ | Breaking parameter | [-] |
| $\rho_{lobe}$ | Ratio highest SL/ML amplitude | [-] |
| $\rho_{ML}$ | Ratio between the area of the main lobe and the total area | [-] |
| $\rho_w$ | Water density | kg/m$^3$ |
| $\sigma$ | Relative wave frequency | [Hz] |
| $\sigma_N$ | Singular value | [-] |
| $\phi$ | Velocity potential | |
| $\psi$ | Scaled surface elevation | [m] |
| $\omega$ | Angular wave frequency | [Hz] |
| $A_{recon}$ | Transfer matrix for the wave field reconstruction | |
| $a$ | (Complex valued) Wave amplitude | [m] |
| $a_s$ | Parameter dependent on type of structure (eq. reflection) | [-] |
| $a_n$ | Fourier coefficients | [-] |
| $b_s$ | Parameter dependent on type of structure (eq. reflection) | [-] |
| $b_n$ | Fourier coefficients | [-] |
| $c_\sigma$ | Propagation velocity in frequency space | [m/s] |
| $c_{g_0}$ | Offshore group velocity | [m/s] |
| $c_g$ | Group velocity | [m/s] |
| $c_p$ | Phase velocity | [m/s] |
| Corr(1,2) | The correlation value between two characteristics or parameters | [-] |
| $D$ | Time duration | [s] |
| $D(f,\theta)$ | Directional spreading function | [1/Hz/rad] |

| | | |
|---|---|---|
| $d$ | Water depth | [m] |
| $E(f)$ | One sided variance spectrum | [m$^2$/Hz] |
| $f$ | Frequency | [Hz] |
| $g$ | Gravitational acceleration | [m/s$^2$] |
| $G(f)$ | Cross-spectra | |
| $h$ | Water depth | [m] |
| $H$ | Wave height | [m] |
| $H(f,\theta)$ | Transfer function between the wave signals | |
| $h_m$ | Parameter depend on the type of wave signal | [-] |
| $H_{m0}$ | Incident wave height | [m] |
| $H_n$ | Hankel function | [-] |
| $Inh_{bath}$ | The inhomogeneity value in the bathymetry | [-] |
| $Inh_{curv}$ | the inhomogeneity value for the wave curvature | [-] |
| $J_n$ | Bessel function of the first kind | [-] |
| $k$ | Wavenumber | [m$^{-1}$] |
| $K$ | The maximum value of the decomposition | [-] |
| $K_r$ | Reflection coefficient | [-] |
| $K_R$ | Refraction coefficient | [-] |
| $K_s$ | Shoaling coefficient | [-] |
| $L$ | Wavelength | [m] |
| $L_0$ | Deep-water wavelength | [m] |
| $M$ | Number of wave directions used in the wave direction analysis | [-] |
| $n$ | Number of grid nodes per wavelength | [-] |
| $N$ | Number of measurement signals | [-] |
| $N(f,\theta)$ | Wave action density | [m$^2$s/Hz/rad] |
| $P$ | Parabola parameter | |
| $r$ | Horizontal distance from source | [m] |
| $R$ | Radius of the circular domain | [m] |
| $R_c$ | Distance of the array centre to the diffraction source | [m] |
| $S$ | Sources/sink of energy | [m$^2$/Hz/s/rad] |
| $S(f,\theta)$ | Directional wave spectrum | [m$^2$/Hz/rad] |
| $t$ | Time | [s] |
| $\Delta t$ | Sampling time step | [s] |
| $T$ | Wave period | [s] |
| $T_p$ | Peak period | [s] |
| $u$ | Current velocity | m/s |
| $v$ | Flow velocity | m/s |
| $x$ | Horizontal space coordinate | [m] |
| $X$ | Measurement signal | [-] |
| $y$ | Horizontal space coordinate | [m] |
| $Y_n$ | Bessel function of the second kind | [-] |
| $z$ | Vertical space coordinate | [m] |

# 1

# Introduction

## 1.1 Background

In coastal engineering design projects – e.g. coastal (defence) structures, harbour structures and ship mooring studies – design forces are required to be able to get to a reliable and **safe design**. The design forces can be calculated when the **design wave condition(s)** – i.e. incoming wave height(s) and wave direction(s) – near the structure or ship are known. There are various ways for the prediction of the wave design conditions, e.g. physical and numerical wave modelling that are able to consider changes in the wave propagation towards the coast due to various wave phenomena. These changes include, but are not limited to, dissipation, reflection, refraction, diffraction, shoaling, generation and nonlinear wave-wave interactions.

Physical laboratory experiments are often time consuming and expensive, which makes it nowadays interesting to use numerical wave modelling. Many models already exist, but research and development of these models and potentially new variants is always ongoing. Because of the continuing exponential growth of computer power such numerical wave models become faster and more easy to use.

In wave modelling a distinction between computation time and model accuracy has to be made. For many applications phase-averaged models, with fast computation time, satisfy both requirements. However, when physical phenomena like diffraction become of importance, which is the case for several coastal structures and harbours, these models can become inaccurate (e.g. Dusseljee et al., 2014).

For such projects, engineers often use state-of-the-art models like the phase-resolving non-hydrostatic wave model SWASH. SWASH gives accurate results, but the computational effort is large. In initial design stages and for simpler problem cases it would be beneficial to quickly assess the wave transformations, including diffraction. Where wave models based on mild-slope equations (e.g. PHAROS are HARES) are considered suitable. Witteveen+Bos developed a new mild-slope wave model as well, called **WIHA** *(Waves In Harbours).*

The numerical modelling and measurement results (e.g. single points systems like a heave-pitch-roll buoy or an array of gauges carefully positioned in the ocean or laboratory basin) only give the surface elevation (1D wave spectra) and possibly the velocities at the desired output locations, but they do not (directly) give wave directional information. However, **post-processing** methods exist which are able to analyse the measured or modelled surface elevation from a set of positions – e.g. a CERC-6 array (Panicker and Borgman, 1970; Davis and Regier, 1977; Hawkes et al., 1997) or a dense numerical grid – and present **wave directional information** to become able to calculate the wave design conditions. The most commonly used directional wave-analysis methods can be divided in two groups: 1) stochastic methods based on a random phase assumption which are able to analyse directional wave spectra for a low number of gauges and 2) deterministic methods using the measured or computed phase information which are able to analyse both directional wave spectra and monochromatic waves for respectively a low and high number of gauges.

Often used stochastic methods are: **MLM** *(Maximum Likelihood Method)* introduced by Capon et al. (1967) and extended by Capon (1969), Lacoss (1971), Davis & Regier (1977), Isobe and Kondo (1984) and Krogstad (1988), **MEM** *(Maximum Entropy Method)* (Lygre and Krogstad, 1986) and **BDM** *(Bayesian Direction Method)* (Hashimoto et al., 1987).

A well-known deterministic directional wave-analysis method is the ***r-DPRA*** method *(rotating directional phase-resolving analysis method)* (de Jong and Borsboom, 2012). Witteveen+Bos developed a new deterministic directional wave-analysis method, called **SWDD** *(Singular-value-decomposition Wave Direction Detection)* (Klopman, 2018b).

The **novelty** of the SWDD method is that a large number of incoming wave directions are prescribed, equally distributed along a circle. For each of these incoming wave conditions, the wave amplitude and phase are the unknowns (instead of the directions). The main advantage is that this makes the problem linear and easier to solve. The main differences with other common deterministic directional wave-analysis methods are: the SWDD method is free of user-checks after each analysis, the directional resolution is higher and the computation time is faster.

In contradiction to stochastic directional wave-analysis methods, deterministic methods are able to **separate multiple incoming wave components**, i.e. wave heights, phases and directions. However, a dense array setup of gauges is needed, which assumes spatial homogeneity (wave field and bathymetry) in the considered region (e.g. Goda and Suzuki, 1976; Mansard and Funke, 1980; Zelt and Skjelbreia, 1992). This means that the wave dynamics can be approximated by linear wave theory over a uniform bottom implying a constant wave number (e.g. Airy, 1845). This seems to indicate that for that for irregular wave fields and bathymetries the results might become unreliable and inaccurate. This study tries to obtain a better understanding to the possible sensitivities – e.g. to irregular wave fields and bathymetries – and optimal range of applicability of the new SWDD method with emphasis on the use for phase-resolving wave models.

## 1.2 Problem description

Many aspects of coastal engineering design require knowledge about the incoming wave(s). However, at this moment, especially for complex harbours, there often is a gap between the model set-up and computing times for accurate phase-resolving non-hydrostatical models (like SWASH and Boussinesq-type models) on the one hand, and the accuracy and applicability of the phase-averaging models (like SWAN) on the other hand. This gap is partially bridged by numerical wave models, based on the mild-slope equations. WIHA is such a model, which still has to be validated. The current existing phase-resolving models (including WIHA and SWASH), only give the surface elevations and often the velocities at the grid nodes as output. This means wave directions remain unknown at the output locations, although the incoming and reflected wave directions are important parameters for the design of coastal of engineering projects. Post-processing methods do exist to obtain directional information, however often these methods require a high technical expertise and time-consuming setup to converge to a stable solution. Even when a stable solution is obtained often the solution does not present a good (smooth) fit of the real situation and needs to be checked by the user for each analysis performed.

**In summary, at this moment there is not an optimal, reliable and easy to use method to obtain wave directional information from the results of phase-resolving wave modelling computations.**

## 1.3 Research questions and objective

The research questions exists of the main question and multiple sub questions which help to answer the main question.

*Main Question:*

*What is the range of applicability of the SWDD directional wave-analysis method, with emphasis on the use for the mild-slope wave model WIHA?*

*Sub Questions:*

<div style="border:1px solid">*Literature study*</div>

    I.    Which theories are used in the SWDD method?

    II.    Which wave processes and theories are used in the wave model WIHA?

    III.    What is the difference between the two deterministic directional wave-analysis methods SWDD and r-DPRA?

    IV.    What is the difference between a deterministic and a stochastic directional wave-analysis method?

    V.    What are relevant cases for the accuracy analyses for WIHA and SWDD?

---

*Modelling*

    VI.    What is the sensitivity of the SWDD method to long waves?

    VII.    What is the sensitivity of the SWDD method to the number of wave components and wave reflection?

    VIII.    What is the sensitivity of the SWDD method to a non-homogeneous wave field within the array setup?

    IX.    What is the sensitivity of the SWDD method to a non-homogeneous bathymetry within the array setup?

    X.    What is the sensitivity of the SWDD method to the array setup and the number of gauges used in this array setup?

---

    XI.    How do the results from the SWDD method compare with analytical data and results from other comparable directional wave-analysis methods?

    XII.    What is the computational accuracy of the mild-slope wave model WIHA?

---

The main objective of this research is to get to a better understanding of the capabilities, sensitivities and range of applicability of the SWDD method, with emphasis on the use for phase-resolving wave models (e.g. WIHA) in complex domains (e.g. approach channels and harbours).

## 1.4 Approach

This section describes the approach of this research. First, the theoretical background is treated. Second, the approach for the WIHA validation study is treated, because WIHA is not yet validated and the model results will be used as input for the SWDD analysis. Third and final, the approach for the SWDD accuracy and sensitivity analysis is treated.

### 1.4.1 Theoretical background

The first step is the understanding, summarizing and reporting of the relevant theoretical background for this research. The consecutively important wave processes, numerical wave models and directional wave-analysis methods will be treated.

### 1.4.2 WIHA validation study

The second step is to determine the accuracy of the mild-slope wave model WIHA. As the results from WIHA are going to be used as input for the accuracy and sensitivity analyses of the SWDD method, a thorough understanding of the accuracy, strengths and weaknesses of WIHA should be known. In order to be able to qualify the obtained results from the SWDD method applied to the output of WIHA.

Various relevant cases will be considered to be able to understand and compare the WIHA model results. The relevant cases that will be modelled by WIHA need additional quantitively measured information. Among others, the following input: the incoming wave conditions, bathymetry, geometry, and boundary conditions. To be able to compare the output, the wave amplitude (at specific output locations) should be known as well. Relevant cases for the accuracy analysis of the mild-slope wave model WIHA:

    I.    Dispersion, how the WIHA numerical dispersion compares to the theoretical dispersion relation (Holthuijsen, 2007, §5.4.3).

II.    Navigation channel case (Dusseljee et al., 2014)

  - Reflection, diffraction, refraction, transmission and nonlinear effects.

III.   Benchmark dataset Van der Ven (Van der Ven and Deltares, 2016)

  i.   Variant 1

  - Reflection and harbour oscillation effects.

  ii.  Variant 2

  - Reflection, diffraction and harbour oscillation effects.

  iii. Variant 3

  - Reflection, diffraction, refraction, transmission and harbour oscillation effects.

IV.    Berkhoff shoal (Berkhoff, 1972)

  - Refraction, diffraction and non-linear effects.

V.     Homma's island (Homma, 1950)

  - Refraction and diffraction effects.

The steps that will be made are: first, calibrate for the chosen WIHA cases. Second, understand the influence of the physical phenomena and if necessary link them as explanation to deviations in the results. And third, perform an accuracy analysis and discuss the output.

## 1.4.3 SWDD accuracy and sensitivity analysis

The third step contains the sensitivity and accuracy analysis for the directional wave-analysis SWDD method using synthetic and analytically prescribed wave signals, as well as results from WIHA. The SWDD method will also be compared with other directional wave-analysis methods. For these cases the input should be known quantitively.

Relevant cases to model for the sensitivity analyses of the SWDD method:

VI.    Prescribed synthetic wave signals analysed using different array setups

  i.   dense grid

  - First validation.
  - Sensitivity to the $\lambda$-parameter.
  - Sensitivity to the radius of the array setup.

  ii.  Circular array setups containing 25 gauges

  - One ring.
  - Two rings.

  iii. CERC-6 array setup (modified from CERC-5, introduced by Panicker and Borgman, 1970).

VII.   Analytically prescribed wave signals using Hankel functions

  i.   Hankel wave source

  - High wave-crest curvature effects.
  - Low wave-crest curvature effects.

  ii.  Hankel wave dipole (includes wave amplitude variation)

  - High wave-crest curvature effects.
  - Low wave-crest curvature effects.

VIII.  Output of the mild-slope wave model WIHA

  i.   100% reflective wall

  - Homogeneous reference case.
  - Diffraction effects.
  - Non-homogeneous grid effects (for each grid node).
  - Slope effects.

Relevant cases for the comparison study of the SWDD method:

IX.    Comparison study SWDD method

  i.   Side basin (r-DPRA)

  ii.  2D wave spectra (MLM and BDM)

  iii. Navigation channel

▪ Output locations GRSM1-4 (MEM).

The SWDD method will be tested for the multiple testcases using various model set-ups, which makes it possible to explain the sensitivity to the different parameters (which will be varied). The possibilities, limitations and expectations of the SWDD method should become clear after these analyses. The data analysis is shortly introduced in the next section and is further explained in chapter *3 Hypotheses and methodology.*

## 1.5 Data analysis

The results from the computations for the WIHA validation study will be analysed using a MATLAB script that will present deviation figures between the computed wave height and the measured or analytical wave height.

The results from the accuracy and sensitivity analyses of the SWDD method will also be analysed using a MATLAB script, which analyses the resulting polar plot and presents the most important characteristics. This MATLAB script will be further explained in chapter *3 Hypotheses and methodology.*

## 1.6 Thesis outline

The structure of this report, which is divided in different steps, will look like:

*Step 1:* **Literature review (chapter 2)**
- ▪ Theoretical overview of important wave processes, numerical wave models and directional wave-analysis methods.

*Step 2:* **Modelling**

*Step 2a:* Model set-up WIHA validation study cases
- ▪ Relevant cases: use boundary conditions and calibrate with various set-ups for the different cases.

*Step 2b:* Validation study WIHA **(chapter 4)**
- ▪ Accuracy analysis of the mild-slope wave model WIHA.

*Step 2c:* Model set-up SWDD accuracy and sensitivity analyses cases
- ▪ Relevant cases: model various set-ups for the different cases considering the domain and the input parameters.

*Step 2d:* Accuracy and sensitivity analysis SWDD **(chapter 5)**
- ▪ Accuracy and sensitivity analysis of the SWDD method using synthetic wave signals.
- ▪ Accuracy and sensitivity analysis using prescribed wave patterns containing high effects of wave-crest curvature and amplitude variation.
- ▪ Accuracy and sensitivity analysis using output of the mild-slope model WIHA.
- ▪ Comparison with other directional wave-analysis methods.

*Step 3:* **Discussion (chapter 6)**
- ▪ Treats the limitation and links the study results to the research questions

*Step 4:* **Conclusion (chapter 7)**
- ▪ Conclusion and recommendations.

# 2

# Theoretical background

Chapter two contains the most important findings from the literature study performed and is subdivided in three sections. The first section lists the description of ocean waves by a wave spectrum and the most important wave processes for waves approaching a coast or penetrating a harbour. The second section gives a theoretical background of WIHA and an overview of various other numerical wave models. The third and final paragraph describes the theory used in the SWDD method and presents an overview of other directional wave-analysis methods.

## 2.1 Important wave processes

When waves are propagating towards the coast, various physical phenomena occur. These phenomena influence the behaviour of the waves. The more varied the environment, the more changes will be present. The sensitivity of the SWDD method to the effects of such non-homogeneous wave fields and bathymetries will be analysed. This section treats a short summary of relevant descriptions and processes for waves approaching a coast, respectively: the wave spectrum, dispersion, shoaling, refraction, diffraction, reflection, dissipation, nonlinear wave-wave interactions and low-frequency waves. A more extensive overview, including formulas, is presented in appendix A1.

*The wave spectrum*
In the ocean wave discipline, often a variance density spectrum is used to describe the surface elevation. The variance density spectrum is based on the random-phase/amplitude model. The amplitude model presents the expected value of the amplitude as a function of frequencies where the phase is uniformly distributed and the amplitude is Rayleigh distributed. The variance density spectrum considers the amplitude spectrum into a continuous distribution of the variance over frequencies and can be seen as a description of how the energy of the waves is distributed for the frequencies (1D spectrum) and possibly directions (2D spectrum), for which graphically depicted examples are presented in appendix A1. Main contributors are Phillips (1957) and Miles (1957) which looked at random pressure fluctuation at the sea surface increasing by wind effects. Where after Pierson and Moskowitz (1964) introduced a spectrum for a fully-developed sea state Pierson-Moskowitz spectrum and Hasselmann et al. (1973) introduced the JONSWAP spectrum which considers wave growth and loss as well (Holthuijsen, 2007, §3.5).

*Dispersion*
According to linear wave theory (e.g. Airy, 1845), in waves a mutual relation exists between the wave period, wavelength and water depth. This relation is called the dispersion relation. Because of differences in wave speed for different Fourier components, frequency dispersion occurs: waves adopt to a wavelength for a certain frequency (Holthuijsen, 2007, §5.4.3).

*Shoaling*
Shoaling occurs when waves start to feel the bottom and the shore is gradually getting shallower. The less deep the water becomes, the lower the wave speed and wavelength gets. When waves propagate from deep water into decreasing water depth, the group speed will decrease - after an initial small increase - and thus the wave height will increase (e.g. Mei, 1989 §3.3.1 and Holthuijsen, 2007, §7.3.1).

*Diffraction*

Diffraction occurs whenever there is an abrupt change in wave amplitude. This is often the case near breakwaters, islands and small gaps (harbour basins). The diffraction behind these obstacles and/or gaps forces the waves to bend, spread and interfere with each other. The resulting scattered wave pattern due to this phenomenon often look circular, i.e. originating from diffraction points at breakwater tips etc. (Holthuijsen, 2007, §7.3.3).

*Refraction*

Refraction plays an important role when depth changes occur and the wave incidence is oblique. The wave propagation direction changes and the wave bends towards the shallower water region. This happens because of the phase velocity difference along a wave-crest. The wave travels faster in the deeper region, which explains the refraction towards the shallower region and often has a critical angle for which it can cross a navigation channel (Dusseljee et al., 2014) (Holthuijsen, 2007, §7.3.2).

*Reflection*

Reflection occurs when waves encounter an obstacle, for example: breakwaters, quay walls and (steep) beaches. The reflection coefficient depends on the type of structure, wave frequency and wave amplitude. The less dissipative the structure and/or the longer the period of the wave, the more reflection occurs. Shorter period waves dissipate more due to wave breaking on the structure. Wave breaking will be explained in the next subsection (Holthuijsen, 2007, §7.3.6) A famous description for wave reflection by slopes is written by Battjes (1974), where after Seelig and Ahrens (1981) introduced a new description which is revised by Zanuttigh and van der Meer (2006). All the equations can be found in appendix A1.

*Dissipation*

Considering approaching waves towards the coast, dissipation of wave energy due to bottom friction and wave breaking can be present. In shallower waters there are higher oscillatory velocities near the bottom. This results in a loss of energy due to bed friction. Short waves will be less influenced by this phenomenon.

Breaking of waves can be subdivided in steepness-induced breaking (white-capping) and depth-induced breaking (surf-breaking). Steepness-induced breaking starts to occur when the waves become too steep. This happens especially in deeper waters. In shallower waters depth-induced breaking becomes important (Holthuijsen, 2007, §8.4.5). Battjes and Janssen (1978) introduced for coastal regions a following relation between the maximum wave height and the water depth.

*Nonlinear wave-wave interactions*

Nonlinear wave-wave interactions results in the redistribution of energy over the various frequency bands of the wave spectrum. This in contrast with linear waves, where wave components can be considered as independent. This nonlinearity, in the form of interactions between wave triads (primarily in shallow water) and quadruplets (primarily in deep water), results for instance in surf beat (wave motion at relatively low frequencies with periods of $30 - 200$ s where the surf zone has a periodically vertical movement due to the grouping of the waves, Longuet-Higgins and Stewart, 1962) and changes of the spectral shape. Triads (three-wave interactions) and quadruplets (four-wave interactions) are most prominent when the wave components are in resonance (Holthuijsen, 2007, §8.4.4).

*Low-frequency waves*

Low-frequency waves are waves with large periods, and consequently have a long wavelength. Those long waves are often forced by wave groups and can result in surf beat, which can produce excitation of harbours resonances. Besides the possible negative effects of long waves approaching coasts, numerical difficulties also arise. The array setup used in the SWDD method needs to become larger for longer waves, while the SWDD method assumes a homogeneous domain. This can be contradicting demands, which may cause problems and inaccuracies.

## 2.2 Numerical wave models

In this section an overview of different numerical wave models is given. These can be subdivided in two groups: those based on phase averaging modelling and those based on phase-resolving modelling. For each of these groups, various subgroups and examples will be discussed. The information of the corresponding wave modelling group is found in the report from the HAWAI initiative which gives an overview of numerical wave models in coastal engineering (de Jong and Borsboom, 2007). At the end of this section a table is presented which contains a summarizing overview.

### 2.2.1 Phase-averaged models

Phase averaged models do not contain information on individual waves. Most often the wave field is assumed to be a random process, of which statistical quantities are modelled – using a random phase distribution over $[0;2\pi]$ (e.g. de Jong and Borsboom, 2007 and Rusu and Soares, 2013).

*Spectral wave models*

Spectral wave models are based on the conservation of wave action and make use of a directional (2D) wave energy spectrum. Spectral wave models solve the wave action balance equation (appendix A2) and are computational efficient, due to the fact that horizontal grid spacing is dominated by changes in bathymetry and coastal/harbour geometry - and not limited by the wavelength. However, as a first drawback, they often do not include bound low-frequency components and the generation of free low-frequency waves. Secondly, diffraction and reflection effects can only be brought into account approximately, because spectral wave models do not contain phase-resolving individual wave information.

This type of modelling is often used in coastal regions for the conversion of the offshore wave data to the input for the more nearshore wave modelling data, where information of the individual wave phase is often not yet interesting (Booij et al., 1996).

### 2.2.2 Phase-resolving models

Phase resolving models describe the wave propagation deterministically. The considered WIHA model belongs to this group of modelling (e.g. de Jong and Borsboom, 2007 and Rusu and Soares, 2013).

*Potential flow models*

Potential flow models computes the wave dynamics with a 3D velocity potential flow formulation:

$$\vec{V} = \nabla \phi \qquad (2.2.1)$$

Where $\vec{V}$ is the flow velocity, $\nabla = \left[\frac{\partial}{\partial x}, \frac{\partial}{\partial y}, \frac{\partial}{\partial z}\right]$ and $\phi$ is the velocity potential. The potential flow equation assumes irrotational flow. When an assumption is made for fluid incompressibility, the well-known Laplace equation is found:

$$\nabla^2 \phi = 0 \qquad (2.2.2)$$

The potential flow models are often subdivided in linear and (partly) nonlinear potential flow models. However, most of the potential flow models are linear based models. Potential flow models do not have restrictions on the bathymetry. When the potential flow model uses the complete 3D equations, the model has high computational effort, even the more in case of non-linear modelling (Holthuijsen, 2007, §5.3.4).

*Mild-slope models*

Mild-slope wave models use a 2D horizontal description of the wave transformation as pioneered by Eckart (1952), introduced by Berkhoff (1972) and was extended by among others Chamberlain (1995) and Porter (2003). To get from the 3D linear potential flow equations to the used 2D equations, the velocity potential is assumed to have a prescribed velocity profile over the water depth vertical. The WIHA model considered in this study belongs to this category. In the next subsection a description of WIHA is given.

Mild-slope wave modelling has a fast computation speed and can be used for complex geometries. However, due to the assumptions of gradual changes in the bathymetry, the classical models in this group are only applicable to mild-slopes. Another drawback is that the mild-slope equations, since they are based on linear

wave theory, do not contain nonlinear effects and wind driven wave generation. But, it is possible to expand the equations and implement several nonlinear effects (Kostense et al., 1986).

This type of modelling is often used for wave computation in nearshore modelling and areas with complex geometries (harbours and surroundings nearshore).

### The wave model WIHA

The wave model WIHA (Klopman, 2018a), which is used to compute free-surface waves, is based on the mild-slope equation (e.g. Berkhoff 1972) and Porter 2003):

$$\partial_x(\beta\partial_x\psi) + \partial_y(\beta\partial_y\psi) + \alpha\psi = 0 \tag{2.2.3}$$

With $\psi$ is the scaled surface elevation and $\alpha$ and $\beta$ are functions of the horizontal position *(x,y)*. Three model variants are implemented in the mild-slope wave model WIHA, resulting in different formulations of $\alpha$ and $\beta$, which will be elaborated in the following subsection.

The free surface-elevation can be written as:

$$\zeta(x,y,t) = \Re\{\eta(x,y)e^{-i\omega t}\} \tag{2.2.4}$$

Where $\omega$ is the angular frequency and $\eta(x,y)$ is the complex valued amplitude, which can be transformed to:

$$\psi(x,y) = \gamma(x,y)\eta(x,y) \tag{2.2.5}$$

The scaling factor $\gamma(x,y)$ depends on the mild-slope variant used, as presented in the next subsection as well.

#### *WIHA model variants*

Thee different variants are implemented in the mild-slope wave model WIHA. Respectively the Shallow Water Equations *(SWE)*, as well as the Berkhoff (1972) and Porter (2003) mild-slope equations. The SWE variant (which is derived by depth integrating of the Navier-Stokes equations with a horizontal length scale much larger than the vertical length scale) can be used for long waves. The Berkhoff variant is the 'classical' mild-slope equation, which can be used when the slope in the bathymetry is not too steep. The Porter variant is an extended mild-slope model, which is valid for steeper slopes and does show improved results for wave reflections by variation in the bottom slope. Below are, per variant (I to III) of the mild-slope model, the three corresponding coefficients ($\alpha, \beta$ and $\gamma$) given. With the water depth $h$ and the wavenumber $k$, the phase- and group speed ($c_p$ and $c_g$) can be written as:

$$c_p = \sqrt{\frac{g}{k}\tanh(kh)} \quad and \quad c_g = \frac{1}{2}c_p\left[1 + kh\frac{1-\tanh^2(kh)}{\tanh(kh)}\right] \tag{2.2.6a and b}$$

I.   The SWE variant uses:

$$\alpha = \omega^2, \quad \beta = gh = \frac{\omega^2}{k^2} \quad and \quad \gamma = 1 \tag{2.2.7}$$

II.   The Berkhoff variant uses:

$$\alpha = k^2 c_p c_g, \quad \beta = c_p c_g \quad and \quad \gamma = 1 \tag{2.2.8}$$

III.   The Porter variant uses:

$$\alpha = 1, \quad \beta = \frac{1}{k^2} \quad and \quad \gamma = k\sqrt{c_p c_g} \tag{2.2.9}$$

Note the difference in unit of the scaled surface elevation for the different variants, where the first two variant are [m] and the third variant (Porter) is [m/s]. The obtained equations with the corresponding $\alpha, \beta$ and $\gamma$ for each variant can be found in appendix A2. Standard for WIHA is to use is the Porter variant (Eq. 2.2.9).

#### *WIHA characteristics*

The WIHA model does include the effects of wave refraction, diffraction and shoaling. Like discussed in the section 'mild-slope models', this type of modelling starts from the 3D linear potential flow equations. Further, the flow is assumed to be irrotational, inviscid and the effects of bathymetry variations on the flow-velocity distribution over the fluid vertical are neglected.

WIHA uses higher-order extensions of the Sommerfeld boundary conditions (Appendix A2) for wave reflection. With these type of boundary conditions both (partial) reflective structures and incoming-wave boundaries, resulting in low spurious wave-reflections can be modelled. The reflection equation is written as:

$$K_r = \frac{i\beta k \cos\theta + \mu + \nu k^2 \sin^2\theta}{i\beta k \cos\theta - \mu - \nu k^2 \sin^2\theta} \tag{2.2.10}$$

Where $K_r$ is the reflection coefficient, $\beta$ is a parameter from one of the used mild-slope variations (Eq. 2.2.7 to 2.2.9), $\theta$ is the incoming wave angle and $\mu$ & $\nu$ are free parameters. Five different variants *(a - e)* are implemented in WIHA all aiming at zero reflection. Figure 1 displays for *a* (normal) and *b* (oblique) the 'classic' Sommerfeld condition, adopted for two values of incoming wave directions. And, respectively *c, d* and *e* second-order Sommerfeld conditions, where *c* is 0° optimized (normal), *d* is *xx°* optimized (oblique) and *e* is the minmax approximation. The used free parameters $\mu$ & $\nu$ can be found in Klopman (2018a). The minmax-variant (variant e) is default in WIHA.
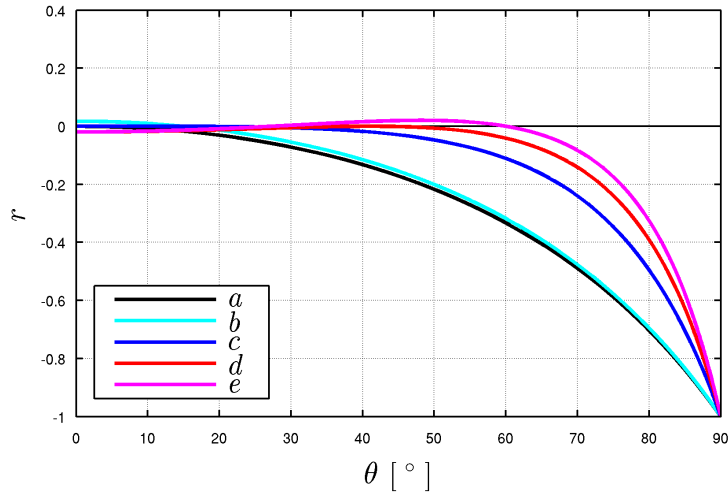


Figure 1: An overview five different variants with varied $\mu$ & $\nu$ coefficients
all aiming at zero reflection (Klopman, 2018a).

WIHA is written in MATLAB where the bathymetry is inserted with an unstructured 'xyz' matrix. For the implementation of the boundaries a polygon should be made, or for 'real life' cases can be implemented with Google Earth using a *.kml* file. WIHA uses the Finite Element Method *(FEM)* on a grid with linear triangular elements. In WIHA, the finite element discretization can be obtained by two different variants, the 'quadrature variant' (standard) and the 'analytical variant'. The 'analytical variant' uses analytic integrals of the basic functions products for the finite element discretization. While for the 'quadrature variant' Gaussian quadrature is used in the finite element discretization to reduce numerical dispersion errors, according to Thompson (2006).

The incoming-wave conditions for the simulations can be a monochromatic wave, a series of monochromatic waves with range of different frequencies and directions, a series of waves with directional spreading and for a frequency spectrum with directional spreading.

The output of WIHA computations, for each incoming wave frequency and direction, are complex-valued Fourier amplitudes, containing both the wave amplitude and wave phase.

Main differences with many other mild-slope wave models:
- WIHA uses the more recent Porter mild-slope equation.
- WIHA uses higher order boundary conditions, variant *e*, the minmax approximation.
- WIHA has improved numerical dispersion (the 'quadrature variant') which is achieved by using numerical quadrature for the required integrations over the elements.

At this moment, WIHA does not have wave breaking, bottom friction and transmission implemented yet. However, this implementation is planned for the next coming period.

*Boussinesq models*

Boussinesq models are based on the 3D nonlinear potential flow equations. However these models use a polynomial expansion (with an assumption of irrotational flow) of the horizontal velocity over depth. This reduces the equations from 3D to 2D, but gives a satisfying approximation of the full 3D equations.

Boussinesq models also compute the nonlinear wave-wave interactions, wave breaking and the description of the primary waves simultaneously with the low-frequency waves. Often, wave breaking is also included through flow assumptions and/or empirical models. However, wind-driven wave input is not included.

This type of modelling is often used in nearshore shallow areas with large differences in bathymetry, where the model area has to be relatively small, due to long computation time.

*Non-hydrostatic models*

The non-hydrostatic models make use of the 3D nonlinear flow equations, including a momentum equation in the vertical direction. Non-hydrostatic models are often computed in multi-layer mode, which means that a discretisation (instead of truncation) over the vertical is performed. The vertical is divided in multiple layers where for each layer a numerical approximation is made.

These methods are nonlinear and thus very accurate. However, they have a time-consuming set-up and computation time.

This type of modelling is often used in nearshore shallow areas when high accuracy is required and/or the bathymetry varies a lot (Casulli and Stelling, 1998).

*Navier-Stokes models*

Full free-surface Navier-Stokes models solve the Reynolds Averaged Navier-Stokes equations. This is the most accurate type of modelling, but also has the longest computation time. This type of modelling is not used for relatively larger areas where waves approach the coast and thus will not be treated further.

## 2.2.3 Overview numerical wave models

In Table 1 an overview of the different models per group, subgroup and examples is given.

Table 1: An overview of the described wave models with various examples
(retrieved from de Jong and Borsboom (2009 and 2007).

| Group | Sub Group | | Examples |
|---|---|---|---|
| **Phase- averaged** | Spectral models | | *SWAN, Mike 21 NSW, TOMAWAC* |
| | SW models forced on wave group scale | | *X-beach surfbeat, Delft3D surfbeat* |
| **Phase-resolving** | Potential flow models | Linear | *AQWA, DIFFRAC, WAMIT* |
| | | Nonlinear | |
| | | Mild-slope | **WIHA**, *PHAROS, CG Wave, Mike 21 EMS* |
| | Boussinesq models | Single-layer | *TRITON, Mike 21 BW* |
| | | Multilayer | *Coulwave, HAWASSI* |
| | Non-hydrostatic models | Single-layer | *SWASH, X-beach* |
| | | Multilayer | *SWASH* |
| | Navier-stokes models | | *OpenFOAM, IH2VOF, COMFLOW* |

The subgroups in Table 1 are presented from low too high regarding the computation time and the model accuracy.

For harbour penetration often mild-slope models can be used, because of the accurate computation of refraction and diffraction. These models are beneficial to quickly assess the wave transformations for initial design stages compared to the more sophisticated modelling type like Boussinesq or non-hydrostatic models.

## 2.3 Directional wave-analysis methods

This section treats the theoretical background of the SWDD method and different other comparable directional wave-analysis methods. At the end of this chapter an overview is given of the described directional wave-analysis methods. The first methods for wave component separation are from the 70's, all assuming homogeneous 1D wave fields and homogeneous bathymetries, where Goda and Suzuki (1976) introduced a two point method. Where after Mansard and Funke (1980) introduced a three point technique using a least square method. An update for more than three locations was presented by Zelt and Skjelbreia (1992). Frigaard and Brorsen (1995) introduced a two point methods by including observations in real-time and Baldock and Simmonds (1999) extended their method for an uneven bathymetry.

The most commonly used methods to estimate 2D wave directional information – the directional spectrum – can be divided in two different groups: stochastic and deterministic methods. Stochastic methods are based on the assumption of a random phase. While on the other hand, deterministic methods use the phase information available from the measured or computed data. In this study the data is taken from computed synthetic wave signals and model results of the mild-slope wave model WIHA. Examples of other methods to obtain (measurement) data are single-points systems (heave-pitch-roll buoy), gauge arrays, remote sensing systems and the output from other phase-resolving wave models.

According to Benoit et al. (1997), the determination of the directional spectrum uses the following classical decomposition of the wave spectrum:

$$S(f,\theta) = E(f)D(f,\theta) \quad \text{with} \quad E(f) = \int_0^{2\pi} S(f,\theta)d\theta \tag{2.3.1}$$

$S(f,\theta)$ is the directional variance spectrum with $f$ the frequency and $\theta$ the direction, $E(f)$ is the one-sided variance spectrum and $D(f,\theta)$ is the directional spreading function *(DSF)*, where two important properties should be satisfied:

$$D(f,\theta) \geq 0 \; for \; [0,2\pi] \tag{2.3.2}$$

And:

$$\int_0^{2\pi} D(f,\theta)d\theta = 1 \tag{2.3.3}$$

### 2.3.1 Stochastic methods

Stochastic directional wave-analysis methods uses the assumption of a random phase distribution over the directions. According to Benoit et al. (1997) this directional wave spectrum determination can often be subdivided in two steps:

1. Computation of the cross-spectra between each pair of wave signals. For $N$ measurement signals $(X_n \dots X_N)$, a time duration $D$ with a sampling time-step of $\Delta t$ and for each couple $(X_m; X_n)$, the cross-spectra is defined by:

$$G_{mn}(f) = \int_{-\infty}^{+\infty} R_{mn}(\Delta t)e^{i2\pi f \Delta t}d\Delta t \quad \text{with} \quad R_{mn}(\Delta t) = \lim_{D \to \infty} \frac{1}{D}\int_0^D X_m(t)X_n(t+\Delta t)dt \tag{2.3.4}$$

2. Determination of the wave spectrum by inverting the relationship between the directional spectrum and the cross-spectra:

$$G_{mn}(f) = E(f)\int_0^{2\pi} H_m(f,\theta)H_n^*(f,\theta)e^{-i\vec{k}.(\overrightarrow{x_n}-\overrightarrow{x_m})}D(f,\theta)d\theta \tag{2.3.5}$$

The symbol $^*$ stands for the conjugate operator and $H_m(f,\theta)$ is the response transfer function between the wave signals which depends on the type of wave signal (surface elevation, surface slope, velocity, acceleration, displacement and dynamic pressure). This transfer function can also be written as:

$$H_m(f,\theta) = h_m(f)\cos^{\alpha_m}\theta \sin^{\beta_m}\theta \tag{2.3.6}$$

Where $h_m$, $\alpha_m$, $\beta_m$ depend on the type of the wave signal. For example, when considering the surface elevation: $h_m = 1$, $\alpha_m = 0 \; and \; \beta_m = 0$. Then the cross spectra will become:

$$G_{mn}(f) = \int\limits_0^{2\pi} S(f,\theta)e^{-\vec{k}\vec{x}_{mn}}d\theta \tag{2.3.7}$$

For other type of wave signals the corresponding values of these parameters can be found in Benoit et al. (1997). The system of integral equations from the cross-spectra given in Eq. 2.3.5 are used for the estimation of the directional spectrum. With only a limited amount of equations given by the cross-spectra, additional assumptions are needed to produce a satisfactory solution. Three stochastic methods which are often used (and will also be used in this study) to produce an estimation of the directional spectrum are the Maximum Likelihood Method *(MLM)*, the Maximum Entropy Method *(MEM)* and the Bayesian Directional Method *(BDM)* will be treated in the next subsections. The measured data needs to be stationary in the considered time interval in all three methods discussed.

### MLM method

The MLM method introduced by Capon et al. (1967) and extended by Capon (1969), Lacoss (1971), Davis & Regier (1977), Isobe and Kondo (1984) and Krogstad (1988) assumes a linear combination between the obtained cross-spectra.

$$\widehat{D}_{MLM}(f,\theta) = \frac{1}{\widehat{E}(f)}\sum_{m,n}\alpha_{mn}G_{mn} \quad \text{with} \quad \alpha_{mn}(f,\theta) = H_m(f,\theta)H_n^*(f,\theta) \tag{2.3.8}$$

Where $\alpha_{mn}$ is a weighting cross spectra. Next a window-function $w$ is introduced.

$$\widehat{D}_{MLM}(f,\theta) = \int_0^{2\pi} D(f,\theta)w(\theta,\theta')d\theta' \quad \text{with} \quad w(\theta,\theta') = \sum_{m,n}\alpha_{mn}(f,\theta)H_m(f,\theta')H_n^*(f,\theta') \tag{2.3.9}$$

Which makes use of a minimum variance (linear) estimate for the complex amplitude. According to Isobe et al. (1984), the best estimation of the direction spectrum is found when the window function approximates the Dirac delta function, and can be written as:

$$\widehat{D}_{MLM}(f,\theta) = \frac{\kappa}{\sum_{m,n}H_m(f,\theta)G_{mn}^{-1}(f)H_n^*(f,\theta)} \tag{2.3.10}$$

Where $\kappa$ is an added parameter to fulfil the condition of Eq. 2.3.3.

For this method different variants were presented, which make use of iterations and eigenvectors. These methods can be found in the directional wave-analysis methods overview in Table 2. The MLM method often gives broader directional spectral peak results (Donelan et al., 2015).

### MEM method

The MEM method (Lygre and Krogstad, 1986) assumes resemblance with the probability density distribution for the DSF. It uses an entropy $H(\widehat{D})$ for the spreading function. This entropy function should be maximized at each frequency band for the given integral equations from the cross-spectra. The advantage of this method is that it works already quite well for short data series. However, the method is nonlinear, so will not always converge to a solution and can produce unstable solutions. Donelan et al. also stated that this method often produces too narrow spectra (Donelan et al., 2015) (Benoit, 1993).

### BDM method

The BDM method (Hashimoto et al., 1987) is a more sophisticated method to statistically estimate the directional spectrum. In contradiction to other stochastic directional analysis methods, the BDM method does not make a priori assumptions for the DSF. In the BDM method the DSF is divided in *K (k=1…K)* segments, and gives a piecewise-constant function, where the unknown directional values for each segment are determined by considering the limitations for the cross spectra correlations coefficients and a smoothness parameter. The BDM estimate (the logarithm to each discrete value of the DSF) for each segment is given by:

$$x_{k=\ln[\widehat{D}_{BDM}(\theta_k)]} \quad \text{with} \quad \theta_k = \left(k - \frac{1}{2}\right)\left(\frac{2\pi}{K}\right) \tag{2.3.11}$$

$$\widehat{D}_{BDM}(\theta) = \sum_{k=1}^K e^{x_k I_k(\theta)} \quad \text{with} \quad I_k(\theta) = \begin{cases} 1 & \text{if } (k-1)\Delta\theta \leq \theta \leq k\Delta\theta \\ 0 & \text{otherwise} \end{cases} \tag{2.3.12}$$

Where after the found estimation is smoothened corresponding to a gaussian distribution as follows:

$$\sum_{k=1}^{K}(x_{k+1}-2x_k+x_k-1)^2 \to 0 \qquad (2.3.13)$$

According to Benoit et al. (1997), the BDM method is robust and handles most of the DSF shapes (unimodal, bimodal, trimodal and a high number of cross spectra with a relatively large number of array components). This diversity is the main advantage of the directional analysis method BDM, however when singe-point systems are analysed, other stochastic methods with less computational effort (like MLM) computes comparable results.

## 2.3.2 Deterministic methods

Deterministic methods make use of the complex-valued Fourier amplitudes for each signal. For the currently existing deterministic methods a large number of frequencies, with a low number of directions per frequency, are assumed. This means that the complex-valued amplitude, which contains the phase and the amplitude of each component, can be determined out of the recorded time series. In this case there are (often) more knowns than unknowns. Smoothing of this data via for example Singular-Value-Decomposition *(SVD)* can then provide an estimate of the underlying directional spectrum. Spectral densities *S(f,θ)* and *D(f,θ)* are determined using 'classical' spectral methods. In the new SWDD method the wave directions are 'given' at a dense distribution of many angles along a circle. Which makes the SWDD method ill-posed due to the exceedance of unknowns to knowns. To still get to a satisfactory solution a different approach is used. The SWDD method will be described in the next subsection.

### SWDD method

The SWDD method (Klopman, 2018b) uses as input the complex-valued Fourier amplitudes (containing the amplitude and the phase for a certain frequency) of $N$ gauges, $\boldsymbol{x}_n = (x_n, y_n)$ with *n=1...N*. The array setup (configuration of the gauges) analysed by the SWDD method are chosen by the user (e.g. a CERC-6 setup). However, when the SWDD method is used to analyse wave model output (in this study WIHA) it becomes practical to use all grid nodes within a radius around a user specified output location. Which gives the (circular) domain with $N$ grid nodes. According to Goda and Suzuki (1976) and Mansard and Funke (1980) the radius for the array setup used is approximately $0.10L \le R \le 0.30L$ (where $L$ is the wavelength). It should be noted that these recommendations are based on a 1D case, i.e. only reflections from 180° to the incoming wave. The directional wave-analysis SWDD method uses $M$ wave directions, which are 'given' at a dense distribution of many angles along this circle *(e.g. M = 360)*. This makes the SWDD method ill-posed due to the exceedance of unknowns *(M)* to knowns *(N)*. Where other comparable deterministic directional wave-analysis methods use a low number of directions per frequency (with a large number of frequencies), which gives more knowns *(M)* than unknowns *(N)*.

The SWDD method assumes a homogeneous environment (wave field and bathymetry) in the selected region (array setup), i.e. the wave dynamics can be approximated by linear wave theory over a uniform bottom implying a constant wave number (e.g. Airy, 1845). Considering a large summation of incoming waves, the system of equations looks like:

$$\zeta(\boldsymbol{x},t) = \Re\left\{\sum_{m=1}^{M}a_m e^{i(\overrightarrow{k_m}\cdot\vec{x}-\omega t)}\right\} \qquad (2.3.14)$$

$$\eta(\boldsymbol{x}) = \sum_{m=1}^{M}a_m\,e^{i\,\overrightarrow{k_m}\cdot\vec{x}}, \qquad \overrightarrow{k_m} = \begin{pmatrix}k\cos\theta_m\\k\sin\theta_m\end{pmatrix} \quad \text{and} \quad \theta_m = \frac{m-1}{M}2\pi \qquad (2.3.15)$$

$$\boldsymbol{A}\vec{z}=\vec{b}, \quad \text{with} \quad A_{nm}=e^{i\overrightarrow{k_m}\cdot\vec{x}_n}, \quad z=[a_1,a_2,...,a_M]^T \quad \text{and} \quad b=[\eta_1,\eta_2,...,\eta_N]^T \qquad (2.3.16)$$

Where $\eta(\boldsymbol{x})$ are the known (measured or computed) complex Fourier amplitudes (for one angular frequency), $a_m$ are the unknown complex amplitudes and $\overrightarrow{k_m}\cdot\vec{x}$ is the inner product of each other.

The SWDD method determines for a large number of directions *(M)* the complex-valued amplitudes, $\vec{z}$. The amount of grid cells per wavelength is often *12-16* and the radius chosen approximately *0.10L - 0.30L*. Thus

the amount of wave sensors is mostly lower than the amount of wave directions. Which gives a resulting system of equations containing more unknowns than knowns (ill-posed). One way to find a solution is using a least square method (Legendre, 2015), which is often used in other comparable deterministic directional wave-analysis methods. The output from the phase-resolving model (in this study: WIHA) does not exactly satisfy Eq. 2.3.15. This is the case due to inhomogeneity of the region and numerical dispersion errors. Because of this an error vector ($\vec{\varepsilon}$) can be introduced where after a least square method needs to be used:

$$\vec{\varepsilon} = \boldsymbol{A}\vec{z} - \vec{b} \tag{2.3.17}$$

However, another approach (which is the default approach in SWDD) uses Tikhonov regularization (Tikhonov and Arsenin, 1977) to find a solution. Here Singular-Value-Decomposition *(SVD)* is used to decompose matrix $\boldsymbol{A}$ (Horn and Johnson, 2013):

$$\boldsymbol{A} = \boldsymbol{U}\textstyle\sum \boldsymbol{V}^* \tag{2.3.18}$$

With $\boldsymbol{U}_{NN}$ & $\boldsymbol{V}_{MM}$ are the unitary complex-valued matrices,* is the transposed conjugate and $\sum_{NM}$ is a diagonal matrix with positive real-valued singular values $\sigma_N$ on its main diagonal.

This decomposed matrix form is from now on used for the matrix $\boldsymbol{A}$. The Tikhonov method searches for the minimum (when there is no directional information Tikhonov forces the solution $z$ to 0) in:

$$\min_{\forall z}\left(\left[\left(\boldsymbol{A}\vec{z} - \vec{b}\right)^*\left(\boldsymbol{A}\vec{z} - \vec{b}\right) + \lambda^2\vec{z}^*\vec{z}\right]\right) \tag{2.3.19}$$

Where $\boldsymbol{A}$ is the decomposed matrix from Eq. 2.3.18, $^*$ is the transposed complex conjugate and $\lambda$ the Tikhonov regularization parameter. Eq. 2.3.19 can also be written as:

$$\vec{z}_{tikh} = \boldsymbol{VDU}^*\vec{b}, \qquad \text{with} \quad \boldsymbol{D}_{nn} = \frac{\sigma_n}{\sigma_n^2\lambda^2} \tag{2.3.20}$$

To determine the regularization parameter $\lambda$ the L-curve method is used, introduced by Hansen (1992). The parameter $\lambda$ is varied, which gives a trade-off between the size of a regularized solution (y-axis) and its fit to the given data (x-axis) the two terms appearing in Eq. 2.3.19 (Hansen, 2000). This trade-off between the left hand side and the right hand side of Eq. 2.3.19 can be seen in Figure 2 where the L-shape is clearly visible in an example of a used L-curve to determine the optimum $\lambda$ in the corner of a log-log plot.
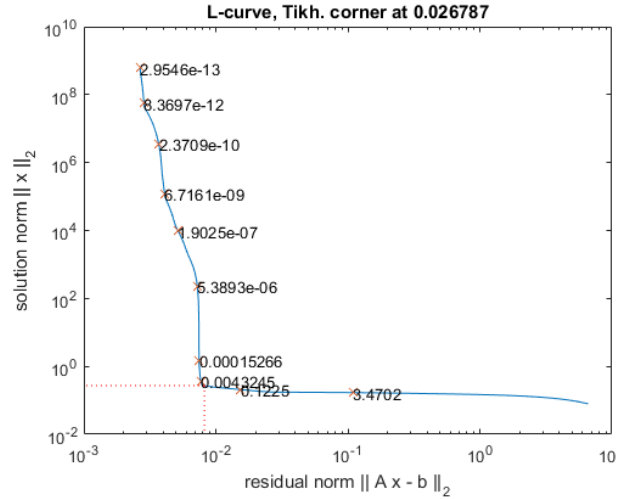


Figure 2: An example of a L-curve performed to determine the Tikhonov parameter in the SWDD method.

When $\lambda$ is chosen too small (y-axis) the solution contains too much noise. When $\lambda$ is chosen too large the solution does not give a correct fit with the given data (x-axis).

The directional wave-analysis SWDD method presents the directional distribution found in a **polar plot**, based on nautical convention. The radial axis in the polar plot is the (real-valued) wave amplitude proportion, where the highest wave is 1.00. If a main lobe is found at a certain direction, this means that the waves propagate from this direction (so **not** towards). An example of a resulted polar plot by the SWDD analysis can be seen in Figure 3.
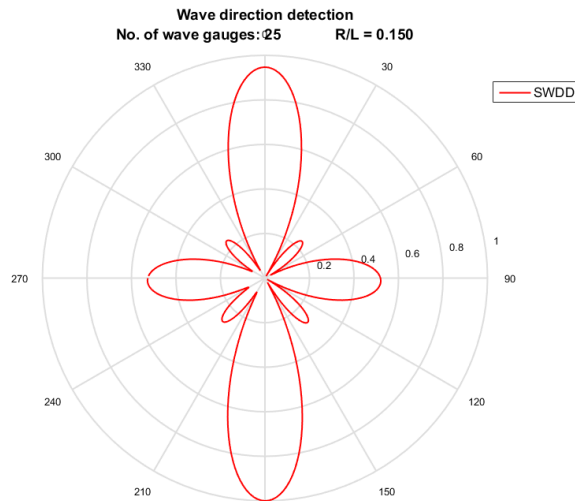
Figure 3: An example of a resulted polar plot presented by the SWDD method for four prescribed monochromatic wave signals with respectively 1.0, 0.5, 1.0, 0.5 m wave amplitude, coming from 0°, 90°, 180° and 270° analysed using a double circular array consisting of 25 gauges.

Next to the incoming wave main lobes, there are (in the case of Figure 3: 4) small spurious side lobes present. According to Klopman (2018b) these spurious side lobes are caused by the 'Gibbs phenomenon' (Hewitt and Hewitt, 1979) and behave like a sinc-function (sinc $\beta = \sin \pi\beta / \pi\beta$) where the results show large fluctuations around the main lobes, which is illustrated in Figure 4.
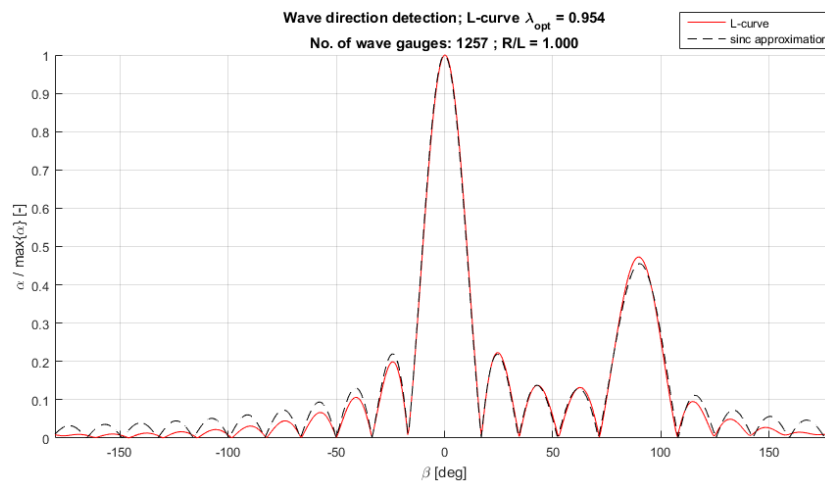


Figure 4: An example of a comparison between the results of the SWDD results and a sinc approximation.

Those spurious side lobes do not have any physical meaning for the directional wave-analysis, however the number of spurious side lobes present and the ratio between the spurious side lobes and the main lobe seem to give information on the accuracy and robustness of the results. The SWDD method has two methods implemented to reduce the presence of the spurious side lobes. The side lobes can be reduced by Lanczos filtering or Hamming filtering. These extensions are optional to use in the SWDD method and reduces the presence of the spurious side lobes. However, as a side-effect, the width of the main lobe increases (almost by a factor 2) and the analysis gets less robust due to lower directional resolution, which is especially important in case of a low number of gauges. Some examples which compare results with and without Lanczos/Hamming filtering are presented in appendix B. The presence and sensitivity of the spurious sidelobe without both filters will be studied, and is described in *5.1 Synthetic testcases accuracy and sensitivity analysis.*

*DPRA method*

The DPRA method (Janssen et al., 2001) makes use of time series of surface elevations, using Fourier sums. This method uses the MLM method (described in section *2.3.1 Stochastic methods*) to find an estimate of the directional components. Around the found estimated direction(s) approximately three (can be more) sub-directions are considered. In the case described by Janssen et al. (2001) the analysed directions are given by: $\theta_{MLM} \pm \Delta\theta$, with $\Delta\theta = 0.1\pi$ (5.73°). The wave signals obtained from the considered array setup configuration, which are mostly more than three, gives more knowns than unknowns *(N > M)*. For $A\vec{z} = \vec{b}$ it tries to find the most likely direction via a least square fit for the wave height and phase in the directions considered. The main differences between the SWDD method and the DPRA method are: the DPRA method uses a stochastic method (MLM) as a first approximation, the DPRA method is well-posed and uses a least squares fit instead of Tikhonov regularization, the DPRA method is not user parameter-free and the DPRA method is nonlinear.

*r-DPRA method*

The r-DPRA (de Jong and Borsboom, 2012) method is based on the previously described DPRA method. Instead of using a stochastic method for a first directional estimation, is r-DPRA rotating multiple ascending (e.g. 2 up to 25) directions with a fixed angle *(1/M)* around a chosen radius, see Figure 5. The highest number of considered directions is approximately equal to the number of gauges in the array setup.

r-DPRA determines the least squares fit in the considered rotated directions (180 times for two rotating directions, then 120 times for three rotating directions until the maximum number of considered directions is reached) for each frequency. For every rotated directional set the data for *M* (e.g. 360) directions is known, which gives an approximation for the distribution of the wave height and phase Where after a decision must be made, which of the considered sets represents the 'best' solution to present in a polar plot. On default this is determined by the minimum integrated energy scaled with the minimum energy value in the dataset present. Often this plot looks u-shaped, where in the beginning the relative energy is decreasing, however for higher directions considered the relative energy increases, due to noise, numerical errors and round-off errors.
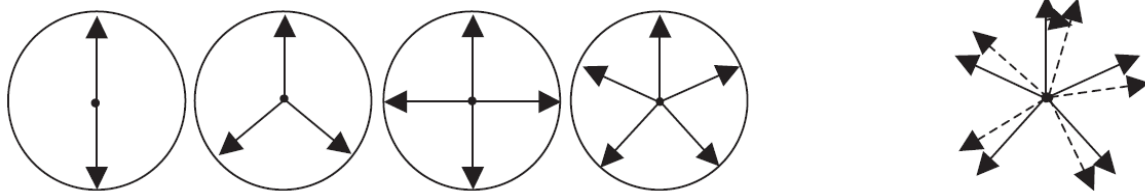


Figure 5: Left: sets of increasing number of analysis directions. Right: the rotation principle.
This figure is retrieved from de Jong and Borsboom *(de Jong and Borsboom, 2012)*.

Main advantages of the SWDD method compared to the r-DPRA method:
- The SWDD method uses Tikhonov regularization for the ill-posed problem (in contradiction to r-DPRA which uses well-posed datasets), because now all information available is used in one calculation instead of subdividing the problem and information in smaller datasets.
- Due to only one computation, SWDD outperforms r-DPRA in computational effort.
- The automatic detection of the optimum number of wave directions in the r-DPRA method, seems not to work optimally and should often be checked by the user.

## 2.3.3 Overview directional wave-analysis methods

In Table 2 an overview of different methods per group, as discussed in the previous subsections, is given.

Table 2: An overview of various available methods for the analysis of multidirectional wave spectra (Benoit et al., 1997).

| Group | Subgroup | Method | Variants |
|---|---|---|---|
| **Stochastic** | Fourier series decomposition methods | Truncated Fourier Series Decomposition | *TFS* |
| | | Weighted Fourier Series Decomposition | *WFS* |
| | Parametrical methods | Direct Fitting | *Unimodal / Bimodal* |
| | | Statistical Fitting | *Unimodal* |
| | Statistical | Maximum Likelihood Method | *MLM* |
| | | Iterative Maximum Likelihood Method | *IMLM1, IMLM2* |
| | | Eigenvector Methods | *EVM, EVM1, EVM2* |
| | | Long-Hasselman Method | *LHM* |
| | | Maximum Entropy Method | *MEM1, MEM2, EMEP* |
| | | Bayesian Directional Method | *BDM* |
| **Deterministic** | Deterministic | Direction Analysis | *SDA, DDA* |
| | | Rotational Directional Phase Resolving Analysis | *r-DPRA* |
| | | Singular-Value-Decomposition Wave Directionality Detection | ***SWDD*** |
| | Hybrid | Directional Phase Resolving Analysis | *DPRA* |

As displayed in Table 2, many directional wave-analysis techniques do exist, each with their own advantages and disadvantages. Stochastic methods are not suitable for locations where waves are not independent of each other, which is the case close to reflective structures. This means for harbours the deterministic methods are advised to be used. A more extensive comparison between the directional wave-analysis method SWDD, r-DPRA, MLM and BDM will be performed in *5.4 Comparison SWDD method to other directional wave-analysis methods.*

# 3

# Hypotheses and methodology

This chapter contains the hypotheses based on the literature study and respectively the methodology for the WIHA accuracy analyses and the SWDD sensitivity analyses. For convenience the main research question is repeated:

*What is the range of applicability of the SWDD directional wave-analysis method,*
*with emphasis on the use for the mild-slope wave model WIHA?*

## 3.1 Hypotheses

The literature study provided insight on various possible sensitivities and potential risks. The hypotheses based on the performed literature study:

- The SWDD method is a robust easy to use method to analyse incoming wave directions in homogeneous wave fields and bathymetries.
- The SWDD method is applicable to use for phase-resolving wave models.
- The SWDD method is sensitive for non-homogeneous bathymetries, so a range for the radius of the domain analysed is advised: $0.10L \leq R \leq 0.30L$.
- The SWDD method is sensitive for inhomogeneous wave fields, so a range for the radius of the domain analysed is advised: $0.10L \leq R \leq 0.30L$.
- The more gauges configured in the array setup – for a constant radius – the more robust and accurate the results become.
- The SWDD method is suitable for a high number of wave components and thus for directional wave-analyses in and near harbours.

## 3.2 Methodology WIHA validation study

As the results from the WIHA computations are going to be used as input for the accuracy and sensitivity analyses of the SWDD method, a thorough understanding of the accuracy, strengths and weaknesses of WIHA should be known. The considered cases were chosen such that various physical processes are tested. The domains are created for each case considered within the WIHA validation study. All the boundaries in the domain are assigned using line segments by their $x,y$ coordinates of the beginning and ending points and the bathymetry is implemented by an unstructured $x,y,z$ matrix. When both the bathymetry and the boundaries are created, a triangular grid can be made, often desiring a number of 12-16 grid nodes per wavelength. After the grid generation it becomes possible to set the interested output locations for which measured quantitative data is available to compare. For each segment introduced, a specific boundary condition should be assigned. Which concerns either the reflection coefficient or the incoming wave boundary characteristics. The incoming wave boundary, depending on the case concerned, computes a monochromatic wave or a JONSWAP spectrum respectively with or without directional spreading. The reflection coefficients of the reflective boundaries can

often by obtained from analytical cases, (thesis) reports or calculations from one of the described formulas in appendix A1.

When the entire setup is completed, it becomes possible to compute the significant wave height on al grid nodes. However, within the comparison study, the interest is only on the significant wave height at the chosen output locations for which either exact or measured data is available. The results are compared and presented graphically for each output locations. The comparison plots contain error bands with upward and downward deviation of 10% were after the result at each individual gauge will be discussed to analyse whether specific physical processes are computed accurate. The error at each gauge and the mean error for each case is determined to compare the WIHA computed results with results from other numerical models.

## 3.3 Methodology accuracy and sensitivity analyses SWDD

The methodology of the various accuracy and sensitivity analyses for the SWDD method is explained more extensively, because this concerns the core of the study. First the data collection process is described, where after the methodology of the analysis of the data is explained.

### 3.3.1 Data collection process SWDD accuracy and sensitivity analyses

The relevant cases for the accuracy and sensitivity analyses of the SWDD method as described in the first chapter are treated consecutively.

VI.    Prescribed synthetic wave signals analysed using various array setups
      i.    Dense grid including additional noise (only) in the complex amplitudes in the wave signals.
      ii.   Circular array setup containing 25 gauges including additional noise *(x, y, z)* in the wave signals.
      iii.  CERC-6 array setup including additional noise in the wave signals (Panicker and Borgman, 1970; Davis and Regier, 1977; Hawkes et al., 1997).

In the synthetic wave signals where additional Gaussian noise is added in the inserted data, the complex wave amplitude at the grid nodes are prescribed by:

$$\zeta(x,y) = \sum a_n e^{ik(x\cos(\theta_n)+y\sin(\theta_n)} + \varepsilon_z a_n (randn) + i\, randn)) \tag{3.3.1}$$

With $\zeta$ is the free surface elevation, $a$ is the amplitude, $n$ is the number of prescribed waves, $k$ is the wavenumber, $\theta$ is the incoming wave direction of the synthetic wave signal, $\varepsilon$ is the standard deviation of the relative error in the elevation and *randn* is a normal distributed random number with a standard deviation 1 and zero mean.

The *x,y* values of the individual gauges can also be given a Gaussian distribution, with a standard deviation of $\varepsilon_x R$ and $\varepsilon_y R$ for the circular arrays and the CERC-6 array, implemented on the grid nodes as follows:

$$x = x + \varepsilon_x Rrandn \quad \text{and} \quad y = y + \varepsilon_y Rrandn \tag{3.3.2}$$

With $\varepsilon$ is the standard deviation of the relative error in the horizontal space and $R$ is the radius of the circular array.

The SWDD method analyses the obtained complex amplitudes at the *x,y* values and the transfer matrix which is described as:

$$A_{nm} = e^{i\vec{k}.\binom{x_n\cos(\beta_m)}{y_n\sin(\beta_m)}} \tag{3.3.3}$$

With $\beta$ are the considered wave directions in the SWDD analysis (0 - $2\pi$).

This is decomposed using SVD and solved using Tikhonov as described in section *2.3.2 Deterministic methods*, $\overrightarrow{\alpha_{ML}}$ contains the complex amplitudes for each direction considered (e.g. 360) which can be plotted (e.g. polarly). Where after, the synthetic testcases in VI considers the error in the wave direction and wave amplitude as relevant characteristic for the accuracy analyses. The wave direction is known which is the corresponding *x*-value to the maximum *y*-value of the considered wave lobe and the wave amplitude output from the SWDD analysis is obtained as follows:

$$\phi_{phase} = k(x_c cos(dir_j) + y_c sin(dir_j)) \tag{3.3.4}$$

$$a_{lobe} = 0.848 \cdot abs\left(\sum \alpha_{ML} e^{i\phi_{phase}}\right) \tag{3.3.5}$$

With $\phi_{phase}$ is the phase, $k$ the wavenumber, $[x_c, y_c]$ the centre of the array setup, $dir_j$ is the corresponding direction of the lobe, $\alpha_{ML}$ are the complex amplitudes of the main lobe by the SWDD analysis and 0.848 is a correction factor for the *sinc*-behaviour.

VII.    Analytically prescribed wave signals using the Hankel function
     i.    Hankel wave source
     ii.    Hankel wave dipole

The analytical solution for a wave source or wave dipole is in terms of Hankel functions of the first kind and is defined as:

$$\eta_s = a_s H_0^{(1)}(kr) \quad \text{and} \quad \eta_D = a_D H_1^{(1)}(kr)\cos\theta \tag{3.3.6a and b}$$

Where $\eta$ is the complex-valued amplitude at *(x,y)* the output location, $a$ is the strength of the Hankel source or dipole, $H$ is the wave height, $k$ the wave number, $r$ the distance to the source $[x_s, y_s]$ or dipole $[x_D, y_D]$ and $\theta$ is the angle of the source.

The Hankel function of the first kind is formulated as:

$$H_n^{(1)}(k_0 r) = J_n(k_0 r) + i Y_n(k_0 r) \tag{3.3.7}$$

With $J_n$ the Bessel function of the first kind, $Y_n$ the Bessel function of the second kind and the Bessel differential equation is defined as (Abramowitz et al., 1965):

$$r^2 \frac{d^2\hat{\eta}_n}{dr^2} + r\frac{d\hat{\eta}_n}{dr} + (k_0^2 r^2 - n^2)\hat{\eta}_n = 0 \tag{3.3.8}$$

Eq. 3.3.6 and 3.3.7 can be rewritten for large $k_0 r$ to respectively:

$$\eta_s \sim \frac{1}{\sqrt{k_0 r}} \quad \text{and} \quad \eta_D \sim \frac{1}{\sqrt{k_0 r}}\cos\theta \tag{3.3.9a and b}$$

$$H_n^{(1)}(k_0 r) = \sqrt{\frac{2}{\pi k_0 r}}\exp i(k_0 r - n\frac{\pi}{2} - \frac{\pi}{4}) \tag{3.3.10}$$

In contradiction to testcase VI the direction error and amplitude error cannot be obtained. This is why another error definition is introduced, which will be treated in section *3.3.2 Data analysis SWDD experiments.*

VIII.    Results from the mild-slope wave model WIHA
     i.    100% reflective wall

The setup and data collection of the WIHA cases uses the same steps as described in *3.2 Methodology WIHA validation study.*

IX.    Comparison study SWDD method
     i.    r-DPRA (synthetic and side basin)
     ii.    BDM and MLM (2D wave spectra)
     iii.    MEM (Navigation channel)

The comparison between the r-DPRA method uses a written MATLAB variant based on the information in the article from de Jong and Borsboom (2012).

The 2D wave spectra are generated by the summation of all wave directional analyses performed for each wave frequency and each wave direction calculated in the WIHA computation. Each frequency band for the 2D wave spectra can be computed as follows:

$$S(f_{in}, \beta) = \sum_{\theta_{in}} \frac{w_\theta(\theta_{in})w_f(f_{in})}{\Delta\theta\Delta f}|\alpha(\beta; f_{in}, \theta_{in})|^2 \tag{3.3.11}$$

Where $f_{in}$ is the frequency of the WIHA input, $\beta$ is the number of directions used in the SWDD analysis, $w_\theta$ is the weighting factors used for the corresponding directions in the WIHA computations, $w_f$ is the weighting factors used for the corresponding frequencies in the WIHA computations, $\theta_{in}$ are the directions used in the WIHA computation, $\Delta\theta$ is the directional step used in the WIHA computation, $\Delta f$ is the frequency step used

in the WIHA computation and $\alpha(\beta; f_{in}, \theta_{in})$ are the resulted complex amplitudes from the WIHA computation per frequency and direction. $S(f_{in}, \beta)$ becomes available for each frequency, where after it becomes possible to graphically present the matrix $S(f, \beta)$ in a 2D spectrum. Which are compared to spectra obtained with the MLM and BDM methods created with an open source Matlab script called 3DwavesAUU by Jakobsen (2015). The unimodal spectral input for the BDM and MLM method are prescribed by a random phase method which uses inverse Fourier transformation to calculate the coefficient in the discrete spectrum based on Frigaard and Andersen (2010). The bimodal spectra uses superposition of regular waves. The error is defined by obtaining the HWHM *(Half Width at Half Maximum)* of the input spectrum and of the directional wave-analysed obtained spectrum subtracted from each other and presented in percentage.

## 3.3.2 Data analysis SWDD experiments

The results of the various testcases from the accuracy and sensitivity analyses of the SWDD method (the obtained data and polar plots) will be analysed by MATLAB scripts. First, it is important to be able to define an error for the specific analysis performed. Second, to determine the relevant and important characteristics which can be correlated to the accuracy and robustness.

> *Error definition*

Considering an obtained polar plot from the SWDD analysis (as displayed in Figure 3), error definitions are introduced to be able to perform an accuracy assessment. In synthetic testcases these errors are rather obvious, respectively the difference between the directional input and output and the difference between the amplitude input and output. However, when wave amplitude variation is highly present or numerical wave modelling output is used in the SWDD analysis, these error definitions become less clear. For such cases a new error definition is considered, the reconstruction error, which is described in the next section *wave field reconstruction.* The reconstruction error is the error between the exact wave field on a created dense grid in and around the array setup and the reconstructed interpolated wave field on the same grid from the SWDD model results.

> *Wave field reconstruction*

In upcoming cases where a Hankel dipole and WIHA model results are used as input in the SWDD directional wave-analysis, the 'correct' directions at the output locations are unknown. Which is the case due to the physical processes wave amplitude variations, refraction and diffraction. Which is why for these sensitivity analyses a new error definition is introduced to still be able to discuss accuracy results, obtain correlations between characteristics and the accuracy results and present conclusions. The new error which will be used is the wave field reconstruction error. The complex amplitude at each gauge within the array setup before the SWDD analysis and the complex amplitude corresponding to each considered direction ($z$ in Eq. 2.3.16) after the SWDD analysis are both known. Which makes it possible to obtain the wave field for the 'exact' (complex amplitude before the analysis) and the 'reconstructed' wave field (from the complex amplitude after the SWDD analysis) both presented on a dense grid. The reconstruction of the wave field after the SWDD analysis uses interpolation between the data available from the grid nodes in the array setup to the dense grid as follows:

$$A_{mn,recon} = e^{i\overline{k}.\left(\begin{smallmatrix}\overline{x_{dense}}\cos\left(\overline{\beta_{SWDD}}\right)\\\overline{y_{dense}}\sin\left(\overline{\beta_{SWDD}}\right)\end{smallmatrix}\right)} \tag{3.3.12}$$

$$\vec{\eta}_{recon} = A_{mn,recon}\vec{\alpha}_{SWDD} \tag{3.3.13}$$

Where $A_{mn,recon}$ is the transfer matrix, $\alpha_{SWDD}$ is the solution vector of the SWDD complex amplitudes and $\beta_{SWDD}$ is a vector containing the wave directions corresponding with alpha.

Where after the obtained complex amplitudes can be subtracted from each other, like in Figure 6.
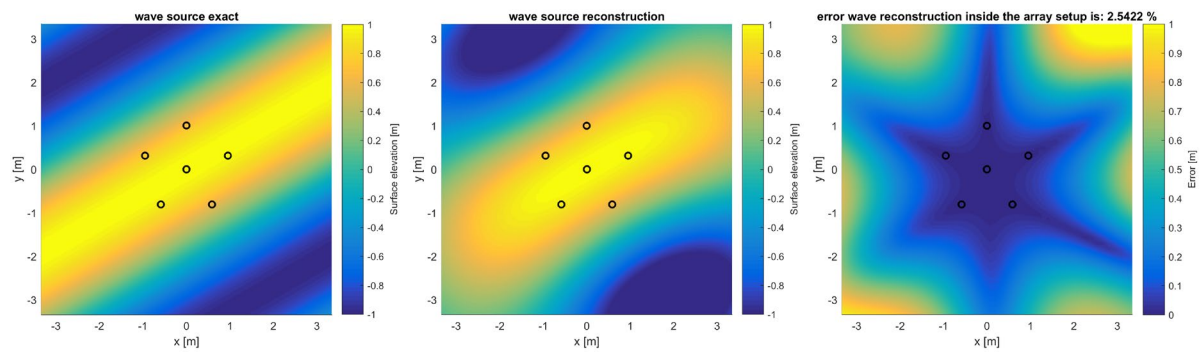
Figure 6: An example of the wave field reconstruction and the plotted error for a prescribed synthetic wave with 1.00 m wave amplitude and 150° wave direction analysed using a CERC-6 array setup.

Where after the standard deviation of the acquired error is determined. The found standard deviation is normalized with the maximum wave height to present the error in percentage. Each run reconstructs two errors, the reconstruction error on a dense grid only **inside** the array setup and the reconstruction error on a dense grid for a **large** domain of $L$ by $L$. The error only inside the array setup is a good representation of the accuracy of the specific run, however it does not represent the error due to inhomogeneity like wave-crest curvature, wave amplitude variation and bathymetry slopes well. Which are the main processes studied in the sensitivity analyses. This is why especially the last error considering a large domain is used to compare the various testcases. Both reconstruction errors are presented in the summarizing tables in the main report.

### Relevant characteristics
Not only the found error is considered important, but also relevant characteristics of the resulted polar plots are meaningful. Mainly to find correlations between the error and such characteristics for specific input in the sensitivity analyses and be able to use these characteristics in a predictive way. The following characteristics are considered relevant: the radius of the array setup, the number of gauges in the array setup, the wavelength, the $\lambda$-parameter, the number of lobes in the polar plot, the direction of the main lobe(s), the width of the main lobe(s), the ratio between the highest spurious lobe and the amplitude of the main lobe, the ratio of the area of the main lobes and the total area of the lobes, the wave field reconstruction error inside the array setup, the wavefield reconstruction error on a large domain, the mean directional error when available, the mean amplitude error when available and an inhomogeneity value either for the wave-crest curvature or the bathymetry when available. The width of the main lobe is determined using a least square fit performed by MATLAB, which is explained in the next subsection.

### Half-width maximum height
The acquired polar plots are analysed by a MATLAB script, which performs least square parabola fits on the data points of each lobe which lay higher than half of the height between the highest trough and the maximum. Figure 7 displays an example of a least square parabola fit and the determinations of specific characteristics from the lobes analysed. The black dots are the data points obtained from the SWDD analysis, where the amplitude ratio $a/a_{max}$ is plotted against the direction in degrees. An example of the half-width at maximum height ($HWHM$) determination for one of the main lobes is displayed in Figure 7.
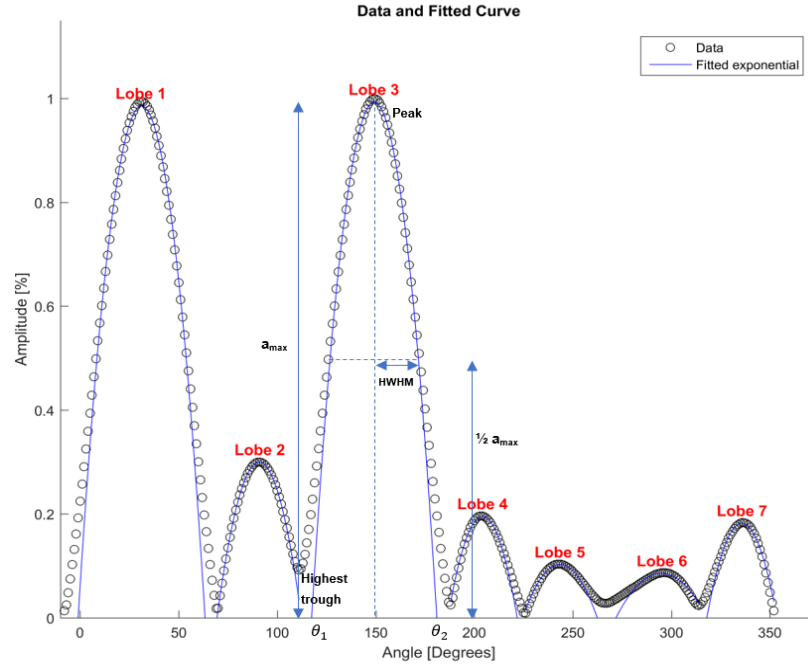
Figure 7: An example of the determination of the parabola fit and the HWHM-value.

This data fitting (on the data points which lay higher than half of the height between the highest trough and the peak) is performed on every lobe which creates multiple parabolas:

$$a(\theta) = P_1 + P_2\theta + P_3\theta^2 \qquad (3.3.14)$$

Where $a(\theta)$ is the amplitude and $\theta$ the direction in degrees.

The parabola's two zero points are found using the next equation:

$$\theta_{1,2} = \frac{-P_2 \pm \sqrt{P_2{}^2 - 4P_3P_1}}{2P_3} \qquad (3.3.15)$$

After obtaining the zero points the distance between the two zero points is known. After which it is possible to compute HWHM of each parabola (lobe) as follows:

$$HWHM = \frac{1}{4}\sqrt{2} * (\theta_2 - \theta_1) \qquad (3.3.16)$$

It is decided to present half of the width of the parabolas half maximum height as a representative value for the lobe width to compare the results of the different tests with each other in the reported tables.

When each parabola is obtained, a distinction between the main lobes and spurious side lobes is made, and the ratio of the area of the main lobes and the total area of all the lobes is calculated using integration.

### Inhomogeneity values

To be able to analyse wave-crest curvature and the inhomogeneity in the bathymetry within the array setup inhomogeneity values are introduced. First, to quantify the wave-crest curvature two inhomogeneity values are presented, with $R$ the radius of the array setup, $R_c$ the distance of the diffraction source to the array centre and $L$ the wavelength.

$$Inh_{curv} = \frac{L}{R_c} \qquad \text{and} \qquad Inh_{curv,angle} = \frac{R}{R_c} \qquad (3.3.17a \text{ and } b)$$

Second, to quantify the inhomogeneity of the bathymetry in the array setup the following value is introduced, with $k$ the wavenumber:

$$Inh_{bath} = \frac{\Delta kd}{\overline{kd}} \qquad (3.3.18)$$

# 4

# Validation study WIHA

To be able to answer the research questions and reach the objective of this research, a decision is made to use a phase-resolving wave model for one of the sensitivity analyses testcases for the SWDD method in section *5.3 SWDD method sensitivity analysis using WIHA output*. The by Witteveen+Bos inhouse developed mild-slope wave model WIHA (Klopman, 2018a) is considered the appropriate wave model to use for the input of the SWDD sensitivity analyses. Due to the easy setup, low computation time and suitability for harbour penetration. However, this mild-slope wave model WIHA still has to be validated. Which is important to obtain knowledge about the strengths, weaknesses, opportunities and threats.

The validation study for the mild-slope wave model WIHA performed is between measured wave heights by wave height meters *(WHM)* in a physical model setup and the wave heights computed on the same output locations by WIHA. This comparison analysis is performed for different cases. The first case considered in the next section treats an analysis to check the difference between the 'exact' dispersion relation and the **linear** dispersion relation used in the mild-slope wave model WIHA for various nodes per wavelength in the triangular grid. The second case considers the Navigation channel case (Dusseljee et al., 2014), the third case the Van der Ven case (Van der Ven and Deltares, 2016), the fourth case the Berkhoff shoal (Berkhoff, 1972) and the fifth and final case considers Homma's island (Homma, 1950). The accuracy limit for the WIHA results is chosen equal to 10%. This is implemented in the comparison figures by an **error band** where the upward and downward deviation is chosen equal to 10%.

## 4.1 Dispersion relation WIHA

A comparison between the phase obtained from the 'exact' dispersion relation (described in *2.1 Important wave processes* and appendix A1) and the phase obtained from WIHA computations (linear dispersion) is performed. This test case considers two different finite element discretization variants in the WIHA computations (a 'quadratic variant' (Thompson, 2006) and an 'analytical variant' both described in *2.2.2 Phase-resolving models*), where the number of grid nodes per wavelength for the triangular grid is varied with respectively 4, 6, 8, 10, 15, 20 and 30 grid nodes per wavelength per variant. This variation is performed for a rectangular flume with a length of 300 m and a width of 50 m. Figure 8 displays the realized domain.
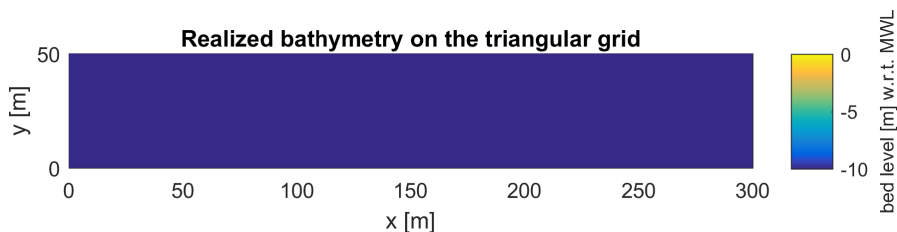


Figure 8: The realized bathymetry for the dispersion comparison case.

The incoming significant wave height, peak period and incoming direction are respectively 1.00 m, 7.00 s and 210º (Western boundary). The remaining boundaries are respectively guiding walls (North and South boundaries with a reflection coefficient of 1.00) and a fully damping beach (Eastern boundary with a reflection

coefficient of 0.00). Where all the boundaries are kept constant for all tests. Figure 9 displays the obtained triangular grid for the test containing 15 grid nodes per wavelength.
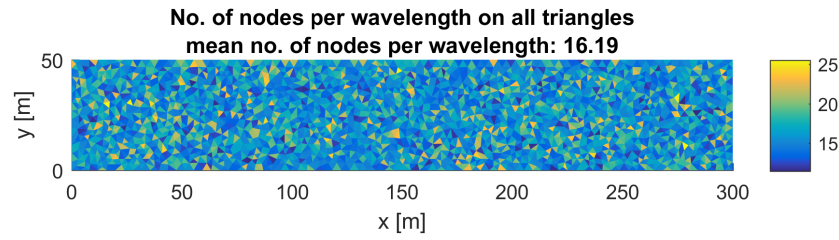


Figure 9: The realized triangular grid with a desired number of 15 nodes per wavelength.

A MATLAB script presents the obtained surface elevation from the WIHA computation and compares this to the 'theoretical' surface elevation from the 'exact' dispersion relation. The information considered relevant in the resulted plots are the wavelength and the phase, which are both determined for the interpolated WIHA surface elevation and the analytical (computed with the 'exact' dispersion relation) surface elevation. Where after the error for the wavelength and phase for each test is determined. The comparison plot for the test with 15 grid nodes per wavelength using the 'quadrature variant' for the finite element discretization is displayed in Figure 10 and the comparison plot for the test with 15 grid nodes per wavelength using the 'analytical variant' for the finite element discretization is displayed in Figure 11. The other gained plots for the number of grid node variation for both variants is reported in appendix C.
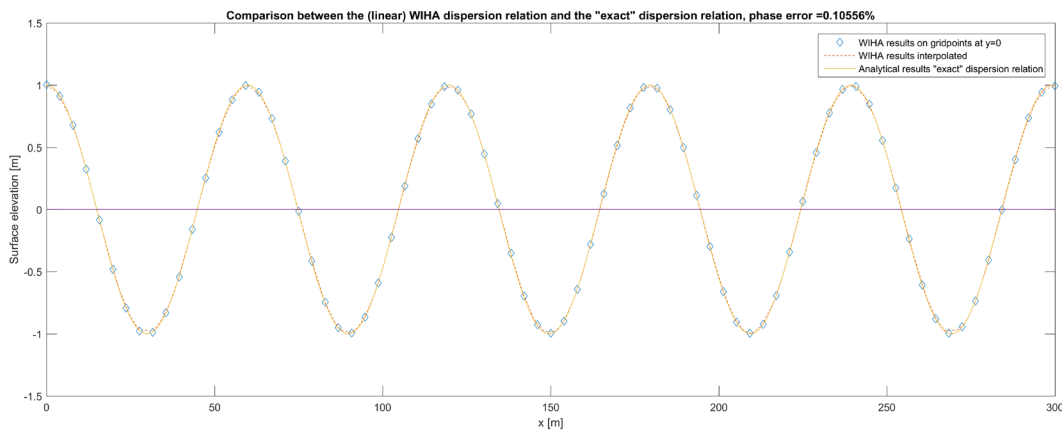


Figure 10: A comparison between the obtained surface elevation with the (linear) WIHA dispersion relation ('quadrature variant') and the 'exact' dispersion relation analysed for 15 grid nodes per wavelength
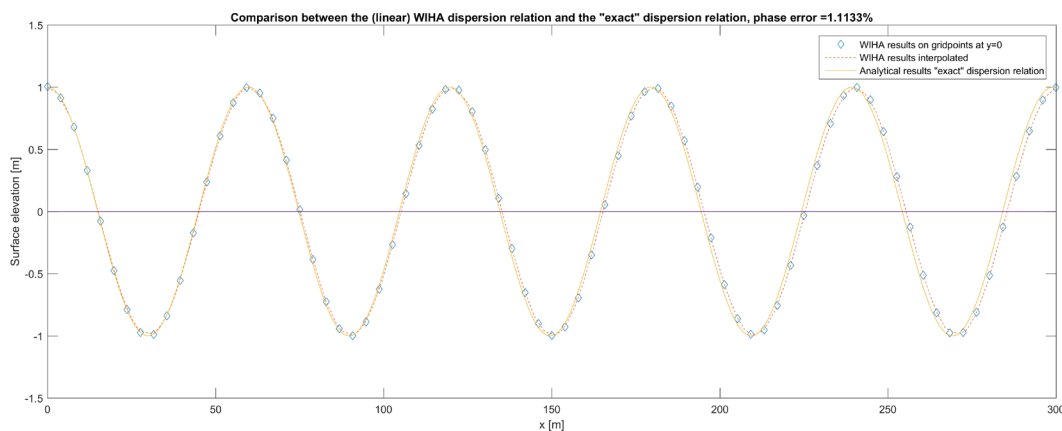


Figure 11: A comparison between the obtained surface elevation using the (linear) WIHA dispersion relation ('analytical variant') and the 'exact' dispersion relation analysed for 15 grid nodes per wavelength

In Figure 10 it becomes clear that for 15 grid nodes per wavelength, for the 'quadrature variant', the error in the phase is only 0.11%, while the mean error for the 'analytical' variant in Figure 11 is 1.11%. The errors in the phase for the other tests performed, varying the number of nodes per wavelength (No. NPWL), can be found in Table 3 below.

Table 3: Error in the phase between the WIHA interpolated results and the 'exact' results obtained from the dispersion relation (for two different types of integrating methods: 'quadrature' and 'analytical').

| No. NPWL [-] | Quadrature Error phase [%] | Analytical Error phase [%] |
|---|---|---|
| 4 | 0.92% | 7.23% |
| 6 | 0.56% | 6.45% |
| 8 | 0.37% | 3.87% |
| 10 | 0.30% | 2.50% |
| 15 | 0.11% | 1.11% |
| 20 | 0.06% | 0.63% |
| 30 | 0.03% | 0.27% |
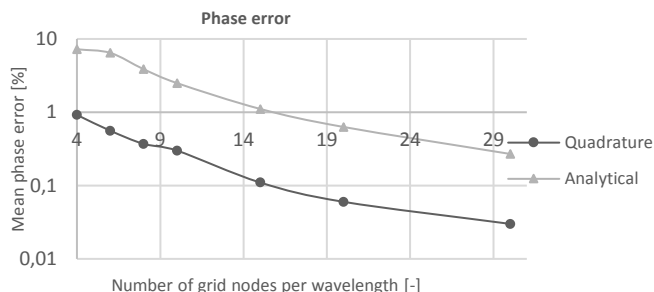
In Table 3 it becomes clear that the 'quadrature variant' for a low desired number of 4 grid nodes already performs well, where the 'analytical variant' starts to perform satisfactory from 15 desired grid nodes per wavelength. For all tests performed with different number of nodes per wavelength, the 'quadrature variant' outperforms the 'analytical variant' approximately with a factor 10, even for the higher number of grid nodes per wavelength. Also it becomes clear that (like expected) the error is decreasing quadratically.

Since, at this moment other comparable numerical wave models only have the 'analytical variant' implemented, WIHA is currently outperforming these models finite element discretization.

## 4.2 Navigation channel

The second validation study considers the navigation channel case which was performed in the Delta basin of Deltares in Delft. The tests for this case made use of a multi-directional wave generator. The physical model is Froude scaled, 1:60, based on dimensions from an existing harbour entrance. The dimension of the considered domain is 920 x 2000 m.

Two tests are performed, based on two different incoming wave spectra: a wind-sea wave spectrum (scenario C1) and a double peaked spectrum including wind and swell conditions (scenario C2). This case contains reflection, diffraction, refraction, transmission and nonlinear effects. Table 4 gives an overview of the imposed conditions at the target location GRSM1, where $H_{m0}$ is the significant wave height and $T_p$ is the peak period.

Table 4: Different setup of the two scenario's C1 and C2.

| Scenario | $H_{m0}$ [m] | $T_p$ [s] |
|---|---|---|
| C1 | 3.00 | 9.70 |
| C2 | 4.80 | 14.10 |

The created triangular grid is solved using the finite element method containing 14 nodes per wavelength. The two scenarios computed for the navigation channel case both consider an incoming wave direction from the South (180°) with a standard deviation of 20°. Thus, the South boundary is the incoming wave boundary. The remaining boundary conditions in Figure 13 are respectively wave guiding walls for the East and West boundaries ($R_f = 1.00$) and a highly dampened natural beach for the North boundary ($R_f = 0.00$). The breakwaters are modelled with a reflection coefficient of 0.53.

### Test C1

The incoming significant wave height and peak period for test C1 are respectively, $H_{m0}$ is 3.00 m and $T_p$ is 9.70 s. The wave spectrum displayed in Figure 12 is used as input on the South boundary of the domain.
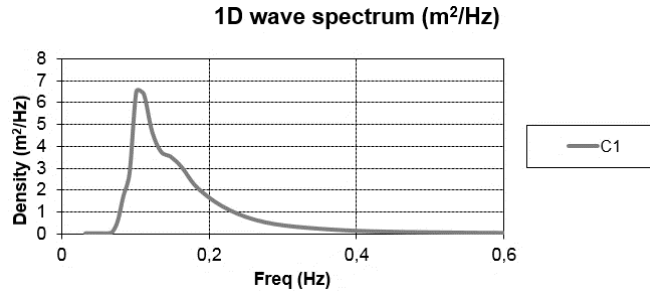
Figure 12: The 1D wave spectrum used as input for test C1 in the navigation channel.

Figure 13 displays the realized bathymetry with the considered output locations and the computed significant wave height from the wave model WIHA for test C1. The comparison between the computed wave height at the output locations and the measured values is presented in Figure 14 containing an accuracy limit of 10%.
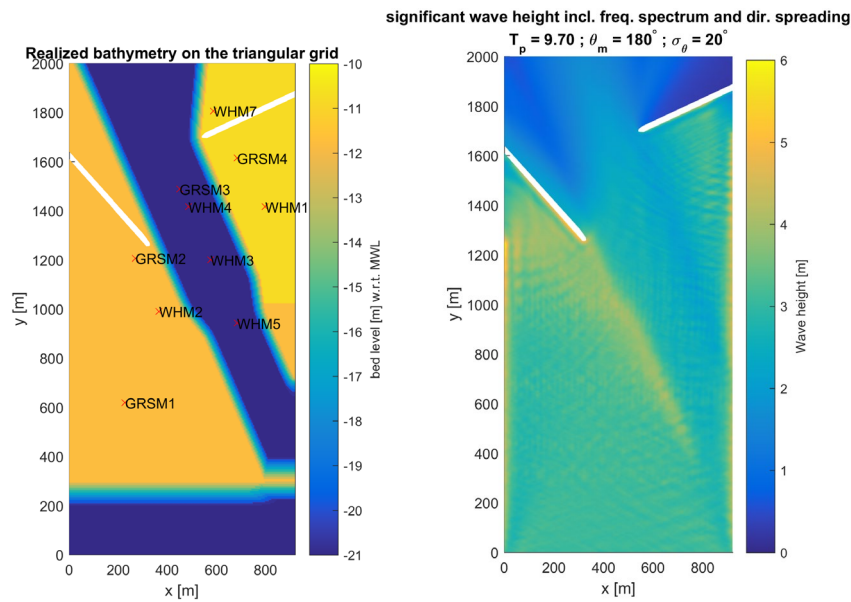


Figure 13: The realized bathymetry for the navigation channel case with the considered output locations (a) and the by WIHA computed significant wave height for test C1 (b).
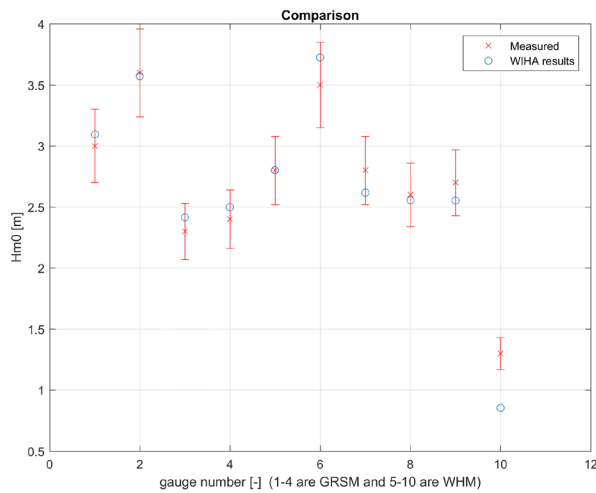


Figure 14: The comparison plot between the WIHA computed significant wave heights and the measured significant wave heights at the 10 gauges for test C1.

Figure 14 displays the significant wave heights computed by WIHA compared with the physical model *(PHM)* measured significant wave heights. WIHA computes the significant wave height with a mean error of 6% accurate. Gauge number 10 (WHM07) is computed inaccurate with an error of 35%, which can be explained due to the fact that the physical phenomenon transmission is not (yet) included in WIHA.

A comparison between the measured and computed results from the PHM, SWASH, SWAN, HARES and WIHA setup can be found in Table 5. The results of the wave models SWASH and SWAN are obtained from Dusseljee et al., 2014. And the results of the wave model HARES are obtained from Attema et al., 2018.

Table 5: The obtained results from the physical model setup and various computational wave models for scenario C1, which presents the obtained significant wave height $H_{m}0$ [m] and the (mean) error (the red colour indicates where transmission is present and WT = without transmission).

|  | PHM $H_{m0}$ [m] | SWASH $H_{m0}$ [m] | SWAN $H_{m0}$ [m] | HARES $H_{m0}$ [m] | WIHA $H_{m0}$ [m] |
|---|---|---|---|---|---|
| GRSM1 (1) | 3.03 | 2.51 (-17%) | 2.82 (-7%) | 3.04 (0%) | 3.10 (2%) |
| GRSM2 (2) | 3.63 | 3.14 (-13%) | 3.36 (-7%) | 3.67 (1%) | 3.57 (-2%) |
| GRSM3 (3) | 2.36 | 1.80 (-24%) | 2.06 (-13%) | 2.53 (7%) | 2.41 (2%) |
| GRSM4 (4) | 2.50 | 1.85 (-26%) | 1.64 (-34%) | 2.64 (6%) | 2.50 (0%) |
| WHM01 (5) | 2.81 | 2.07 (-26%) | 1.60 (-43%) | 2.88 (2%) | 2.80 (0%) |
| WHM02 (6) | 3.55 | 3.25 (-8%) | 3.30 (-7%) | 3.64 (3%) | 3.73 (5%) |
| WHM03 (7) | 2.77 | 1.93 (-30%) | 2.15 (-22%) | 2.65 (-4%) | 2.62 (-5%) |
| WHM04 (8) | 2.60 | 1.88 (-28%) | 2.11 (-19%) | 2.62 (1%) | 2.55 (-2%) |
| WHM05 (9) | 2.73 | 1.85 (-32%) | 2.10 (-23%) | 2.61 (-4%) | 2.55 (-7%) |
| WHM07 (10) | 1.30 | 0.89 (-32%) | 1.33 (+2%) | 1.22 (-6%) | 0.85 (-35%) |
| Mean error [%] |  | 24% | 18% | 3% (WT: 3%) | 6% (WT: 3%) |

In Table 5 it can be noticed that SWASH computes the significant wave height inaccurately for the complete spectrum (f < 0.33Hz) with a mean error of 24%. Which according to Dusseljee et al. (2014) can be explained due to the grid size chosen for the SWASH computation, which dampens the wave height in the first couple of grid cells. To obtain more accurate results of the computation by SWASH for scenario C1, a horizontal grid resolution of 0.50 m with 3 (or more) vertical layers are needed, which is not feasible. The computation time for the current chosen grid for SWASH is already 48 hours and 20 minutes (Eikema et al., 2018). Monteban (2016) did perform a sensitivity analysis containing a higher horizontal grid resolution of 1.50 m with two vertical layers, where only the result at the GRSM1 gauge is given, which improved by only 2% to 2.57 m.

The computed significant wave height from the SWAN computation has a mean error of 18% and especially performs inaccurate (26% mean error) in the navigation channel and East of the navigation channel. This inaccuracy can be explained due to the underestimation of channel reflection and refraction.

HARES computes the significant wave height at the output locations with a mean error of 3% accurately.

WIHA computes the significant wave height at the output locations with a mean error of 6% accurately (except at gauge number 10, which is computed inaccurate due to the lack of transmission in WIHA). WIHA (and HARES) computes gauges 1 to 9 – not considering transmission – with only a mean error of 3%.

### Test C2

The incoming significant wave height and peak period for test C2 are respectively 4.80 m and 14.10 s. The wave spectrum in Figure 15 is used as input on the South boundary of the domain.
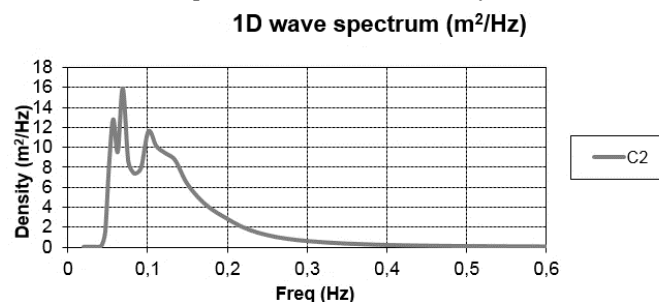


Figure 15: The 1D wave spectrum used as input for test C2 in the navigation channel case.

Figure 16 displays the realized bathymetry with the considered output locations and the computed significant wave height for test C2 by WIHA. The comparison between the computed wave height at the output locations and the measured values is presented in Figure 17 containing an accuracy limit of 10%.
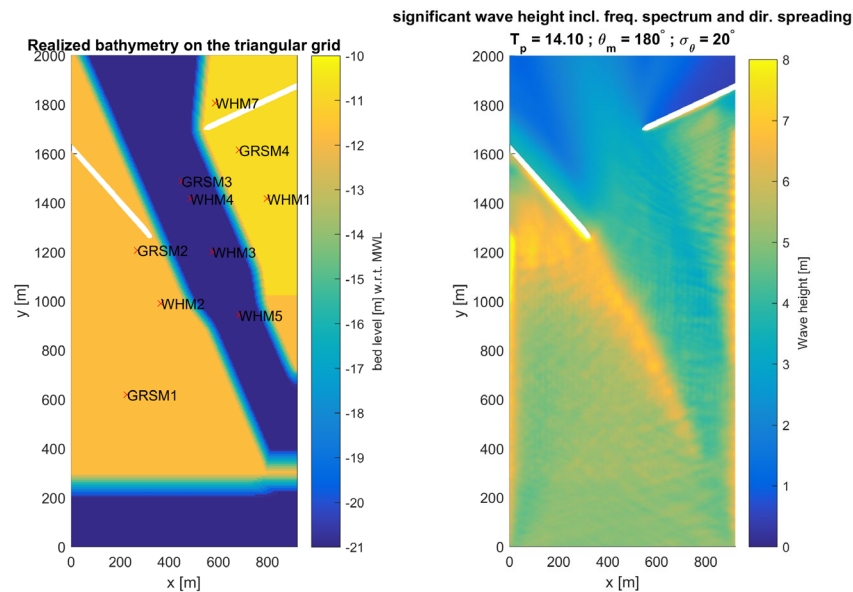


Figure 16: The realized bathymetry for the navigation channel case with the considered output locations (a) and the by WIHA computed significant wave height for test C2 (b).
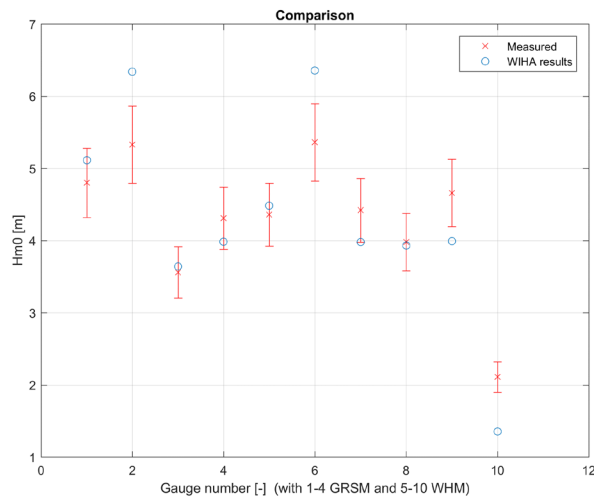


Figure 17: The comparison plot between the by WIHA computed significant wave heights and the measured significant wave heights at the 10 gauges for test C2.

The WIHA results in Figure 17 are less accurate compared to the findings from the results of scenario C1. The computed significant wave heights at gauge numbers 2 and 6 (GRSM2 and WHM02) are overestimated with approximately 18%, which can be explained due to the fact that wave breaking is not (yet) implemented in WIHA. While, at the West side of the navigation channel wave breaking is present in this scenario (at GRSM2 H/d≈0.5). The significant wave height at gauge number 7 and 9 (WHM03 and WHM05) are underestimated with approximately 12%. Which can be explained due to the fact that the higher wave frequencies in the spectrum are not modelled due to the high computational effort and especially the higher frequency waves are able to cross the navigation channel, because the lower frequency wave 'de-shoal'. Thus, less waves cross the navigation channel, which explains the underestimation of the significant wave heights at gauges 7 and 9.

And like in scenario C1, the result at gauge number 10 (WHM07) is inaccurate, due to the lack of transmission implementation in WIHA. A comparison between the measured and computed results obtained from the PHM, SWASH, SWAN, HARES and WIHA (models) is presented in Table 6.

Table 6: Results from the physical model setup and various computational wave models for scenario C2, which presents the obtained significant wave height and the (mean) error (the blue colour indicates the gauges where wave breaking is present, the red colour where transmission is present, WT = without transmission and WB = without breaking).

| | PHM $H_{m0}$ [m] | SWASH $H_{m0}$ [m] | SWAN $H_{m0}$ [m] | HARES $H_{m0}$ [m] | WIHA $H_{m0}$ [m] |
|---|---|---|---|---|---|
| **GRSM1 (1)** | 4.80 | 4.37 (-9%) | 4.64 (-3%) | 4.84 (1%) | 5.11 (6%) |
| **GRSM2 (2)** | 5.33 | 5.26 (-1%) | 5.42 (+2%) | 5.61 (5%) | 6.34 (19%) |
| **GRSM3 (3)** | 3.56 | 2.96 (-17%) | 2.93 (-18%) | 3.43 (-4%) | 3.64 (2%) |
| **GRSM4 (4)** | 4.31 | 3.82 (-11%) | 2.37 (-45%) | 3.87 (-10%) | 3.98 (-8%) |
| **WHM01 (5)** | 4.36 | 3.42 (-22%) | 2.42 (-44%) | 4.21 (-3%) | 4.48 (3%) |
| **WHM02 (6)** | 5.36 | 5.26 (-2%) | 5.44 (+2%) | 5.76 (7%) | 6.35 (18%) |
| **WHM03 (7)** | 4.42 | 3.40 (-23%) | 3.16 (-29%) | 3.81 (-14%) | 3.98 (-10%) |
| **WHM04 (8)** | 3.98 | 3.14 (-21%) | 3.07 (-23%) | 3.56 (-11%) | 3.93 (-1%) |
| **WHM05 (9)** | 4.66 | 3.47 (-25%) | 3.03 (-35%) | 3.54 (-24%) | 3.99 (-14%) |
| **WHM07 (10)** | 2.11 | 1.69 (-20%) | 2.07 (-2%) | 1.63 (-23%) | 1.35 (-36%) |
| **Mean error [%]** | | 15% | 20% | 10% (WT: 9%) (WT&WB: 10%) | 12% (WT: 9%) (WT&WB: 6%) |

Table 6 above shows that the SWASH computations are more accurate for scenario C2 than for scenario C1, due to the relatively larger grid size (compared to *L*). Still, SWASH underestimates the significant wave height in total with a mean error of 15%, especially in the navigation channel with a mean error of 22%.

SWAN computes the significant wave height inaccurately for scenario 2 with a total mean error of 20%, in particular in the navigation channel and East of the navigation channel the results are inaccurate with a mean error of 35%.

HARES computes the significant wave heights with a mean error of 10% accurately.

WIHA computes the significant wave height with a mean error of 12% accurately, which is compared to the other numerical wave models, and in mind the lack of wave breaking and transmission (until now), a decent result. The gauges (displayed in Table 6) where wave breaking or transmission is present are highlighted blue and red in Table 6. Considering the mean error of gauges 1 to 9 (without transmission) and gauges 1, 3 to 5, 7 to 9 (without transmission and breaking), the mean error is respectively 9 and 6%, which is lower than for HARES (9 and 10%).

Overall, when transmission and wave breaking are minimally present, it becomes clear that the mild-slope wave model WIHA computes the wave propagation accurately.

## 4.3 Van der Ven

The Van der Ven case was also performed in the Delta basin of Deltares in Delft and made use of a multi-directional wave generator. The total size of the basin is 40.00 x 30.00 x 0.44 m. Three different variants were tested. The first variant only considers a main basin, with dimensions of 14.53 x 8.66 m. The second variant also considers a side-basin connected at the right of the main basin (45° angle) with dimensions of 3.07 x 10.49 m. And the third variant, has a breakwater connected with a slope of 1:2, dimensions of 4.60 x 1.50 x 0.70 m and an angle of 20° with the harbour entrance. An overview of the domain and the bathymetry of the three variants is given in Appendix D. The WIHA computations uses the exact dimensions (no scaling). This paragraph treats the main findings from the three variants individually. The WIHA computed results are given in appendix D.

### Variant 1

WIHA computes the significant wave height accurately with a mean error of 3%. Where even an error within the measured wave height data might be present. This can be seen in the fact that gauge 6 to 9 have a higher significant wave height than gauge 13 to 16. As the complete domain and the placement of the wave gauges is symmetric, this error may be caused by the wooden panels used to close off the side basin.

**Variant 2**

WIHA computes the significant wave height accurately with a mean error of 5%. The largest errors are found in gauge numbers 18, 20, 21 and 22 containing a mean error of approximately 14%, however this error was known of in advance. This is the case due to the physical phenomenon sloshing and is also present in results computed with other comparable numerical wave models. The nodes and anti-nodes in the side basin are difficult to compute with a numerical wave model, which should be Fourier analysed to become more accurate.

**Variant 3**

WIHA computes the significant wave height accurately with a mean error of 6%. Again, the largest errors are found in gauge numbers 18, 20, 21 and 22 containing a mean error of approximately 17%, due to sloshing of the side basin. This variant has also been computed by Monteban (2016) with the wave models SWASH and MIKE21. The mean error found was respectively 9% and 17% for SWASH and MIKE21, this means that WIHA computes this variant more accurate.

## 4.4 Berkhoff shoal

The domain to analyse is 20 x 25 m with a decreasing depth in bathymetry (Southward) and considers an oblique monochromatic irregular wave (compared to the slope of the bathymetry). This monochromatic wave has a significant wave height of 0.0464 m, a peak period of 1.00 s and an incoming wave direction of 0° without directional spreading. The realized bathymetry is presented in appendix D. WIHA did not compute the significant wave height accurately with a mean error of 61%. This is the case due to non-linear dispersion, while the mild-slope wave model WIHA is a linear wave model. Other comparable linear mild-slope wave models experience the same limitation and present equally inaccurate results, for example the model GCwave (Demirbilek and Panchang, 1998). The obtained comparison plot is presented in appendix D.

## 4.5 Homma's island

Homma's island is a circular island where the physical phenomena refraction and diffraction are governing present. It is a linear case and thus should be computed with a high accuracy by the linear mild-slope wave model WIHA. The incoming monochromatic wave condition has a significant wave height of 1.00 m, a peak period of 35.70 s, a wavelength of 500 m and an incoming wave direction of 270°. The inner radius of the island is 500 m, the outer shelf radius is 1000 m, the semi-circle radius is 4000 m, the mean water depth outside shelf region is 20 m and the number of nodes per wavelength solved using the finite element method is 50. The realized bathymetry and computed surface elevation are displayed in Figure 18.
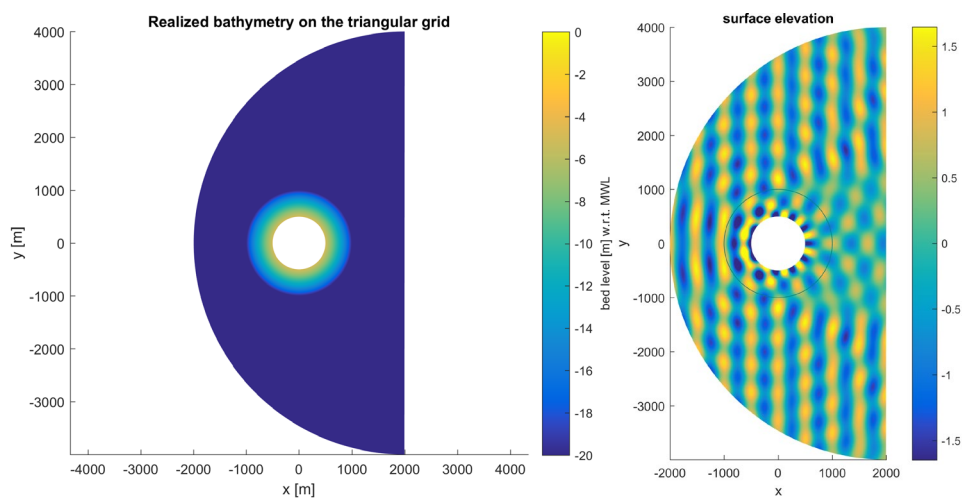


Figure 18: The realized bathymetry for Homma's island (a) and the computed surface elevation by WIHA (b).

Figure 19 displays the by WIHA computed results and the comparison with the analytical solution.
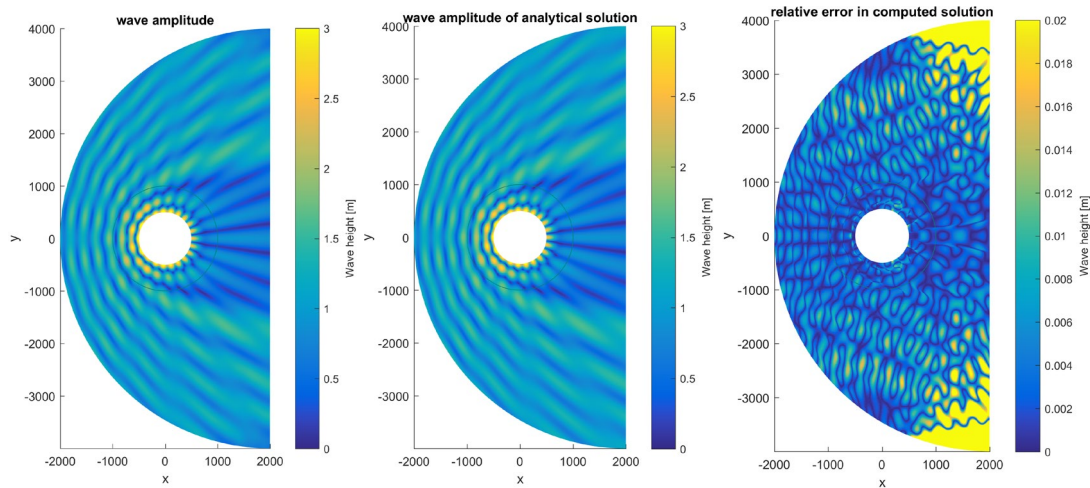
Figure 19: The wave amplitude output by WIHA (a), the analytical solution (b)
and the difference between the computed solution and the analytical solution (c).

In Figure 19 it becomes clear that WIHA indeed did compute the significant wave height accurately with only a maximum deviation of 2%.

## 4.6 Intermediate conclusion WIHA validation study

The by WIHA computed testcases in the validation study show promising results compared to the measurements obtained from wave gauges and analytical solutions. In the case where the dispersion relation has been analysed, it becomes clear that WIHA outperforms other comparable numerical models using a 'quadrature variant' for the finite element discretization, already for a low number of desired grid nodes.

In the navigation channel case – considering reflection, diffraction, refraction, transmission and nonlinear effects – the results are accurate at the gauges where wave breaking and transmission are less important, with a mean deviation of only 3% and 6%. Transmission and nonlinear effects are not yet implemented in WIHA, the remaining effects are computed accurately.

The mild-slope wave model WIHA computes the three variants of the Van der Ven case accurately with only a maximum mean deviation of 6% in the significant wave height. Again, reflection, diffraction, refraction and harbour-oscillations are computed accurately.

In the Berhkoff shoal case, where non-linear dispersion is dominantly present, the linear wave model WIHA could not compute the significant wave height accurately with a mean deviation of 61%.

And finally, the linear Homma's island case – containing refraction and diffraction effects – is computed accurately with a maximum deviation of only 2%.

Overall, when transmission and non-linear processes like bottom friction, wave breaking, non-linear dispersion are minimally present, it becomes clear that the mild-slope wave model WIHA is very accurate and often outperform comparable models due to improved numerical dispersion characteristics and higher-order Sommerfeld boundary conditions. These non-linear processes and transmission are scheduled to be implemented in a future version of WIHA, but until this implementation these shortcoming can be a threat to use WIHA in complex projects. However, to use WIHA for relatively easy and artificial controlled environments in the sensitivity analyses of the SWDD method where transmission and non-linear processes are not present, WIHA is accurate and considered suitable.

# 5

# SWDD experiments

This chapter contains the performed research experiments to get a better understanding on the applicability of the SWDD method and how the SWDD method compares to other directional wave-analysis methods. First, synthetic testcases are treated containing prescribed wave signals to be analysed by the SWDD method as a first validation and to test various accuracy and sensitivity analyses among others to: the $\lambda$-parameter, radius of the array setup and various array configurations. Second, sensitivity analyses for the SWDD method are performed on wave fields – containing high effects of amplitude variation and wave-crest curvature – created by a wave source and wave dipole. Third, sensitivity analyses for the SWDD method are performed using model results from WIHA computations to test irregular wave fields and bathymetries. Fourth and last, a comparison study is performed between the SWDD method and other deterministic *(r-DPRA by de Jong and Borsboom, 2012)* and stochastic *(BDM and MLM)* directional wave-analysis methods.

## 5.1 Synthetic testcases accuracy and sensitivity analysis

Synthetic testcases are used to perform a first validation of the SWDD method, sensitivity analysis to the $\lambda$-parameter and to the radius of the array configuration. Where after various array setups (e.g. CERC-6) are tested and compared. An accuracy limit of 2.50° and 0.10 m is chosen.

### 5.1.1 Testcase A: first validation SWDD directional wave-analysis

As a first validation testcase, the SWDD method has been applied to two relatively complex synthetic cases. In these cases the prescribed input (direction and amplitude) is known and thus can be checked whether SWDD is able to reproduce the correct wave direction and amplitude. The first case (A1) considers three wave components with respectively 1.0, 2.0 and 3.0 m wave amplitudes and 0, 120 and 180 degree incidence (based on nautical convention clockwise from the North). The second case (A2) also considers three prescribed wave components with respectively 1.0, 0.6 and 1.0 m wave amplitudes and 0, 135 and 300 degree incidence. The SWDD analysis for these two cases is performed on a dense grid without additional noise. Figure 20 displays the results of the SWDD analysis for the two considered cases.

*All polar plots in this report present the angles in degrees (in nautical convention) and the radial axis in (real-valued) wave amplitude proportion, where the highest wave amplitude is 1.00. If a main lobe is found at a certain direction, this means that the waves propagate from this direction (so **not** towards). Next to the main lobes (the incoming waves), there are small spurious lobes present. The spurious side-lobes appear frequently in the SWDD analysis and have no physical meaning. Some of their characteristics will be mentioned in overviewing tables for the corresponding testcases in this report. Among others: the ratio of the highest spurious lobe divided by the main lobe amplitude and the area of the main lobes divided by the area of the side lobes. A short introduction to the spurious lobes and an implementation to supress them using Lanczos or Hamming filtering was described in section 2.3.2.*
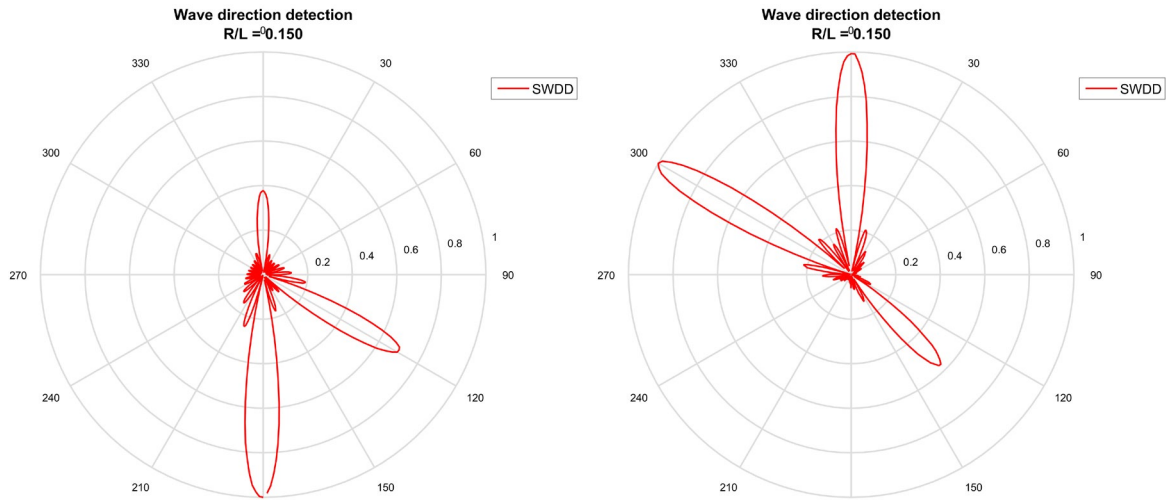
Figure 20: First validation of SWDD for two synthetic testcases: A1 (a) and A2 (b), where for A1 three monochromatic waves of respectively 1.0, 2.0 and 3.0 m wave amplitude, coming from 0°, 120° and 180° and for A2 three monochromatic waves of respectively 1.0, 0.6 and 1.0 m wave amplitude, coming from 0°, 135° and 300° are prescribed.

The output of the SWDD directional wave-analysis for cases A1 and A2 show promising results. Considering the proposed accuracy limits these results are accurate. The mean error in the direction found by SWDD for respectively case A1 and A2 is only 0.47° and 0.51°. The mean error in the wave amplitude for respectively case A1 and A2 is 0.02 m and 0.09 m. For such complex cases, with wave amplitude variation and irregular wave directions close to each other, the output is satisfying. Especially, considering the type of practical cases where the SWDD method is designed for, confidence in the potential of the method is gained. The r-DPRA method did analyse the same cases with a mean error in amplitude of approximately 0.20 m and maximum error in direction of 5.00° (de Jong and Borsboom, 2012). Cases considering many wave components (6 - 8) in the SWDD analysis are tested as well, the accurate detected polar plots are presented in appendix E.

## 5.1.2 Sensitivity to the $\lambda$-parameter and the radius for the SWDD method

This section treats respectively the sensitivity of the SWDD method to the $\lambda$-parameter and the sensitivity to the radius of the array setup. In both cases additional noise is implemented in the complex valued amplitude by a random change containing a standard deviation of 10e-8.

*Sensitivity of the SWDD method to the $\lambda$-parameter*

The sensitivity of varying the $\lambda$-parameter in the SWDD analysis is displayed in Figure 21. It comes forward that a lower $\lambda$-value presents smaller main lobes, however for a low $\lambda$-value as a side effect more spurious sidelobes are present. Considering higher $\lambda$-values the width of the main lobes gets wider and the spurious side lobes are less present.
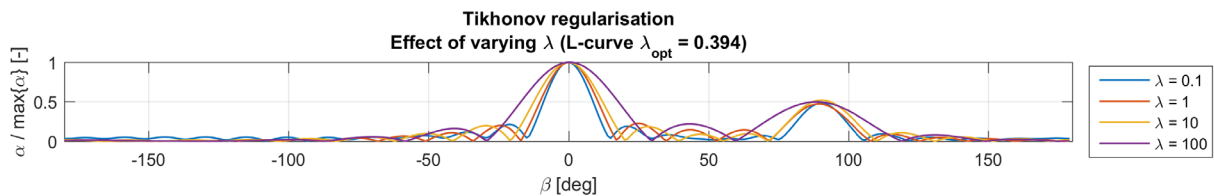


Figure 21: The sensitivity of the results to the $\lambda$-parameter.

An optimum between the width of the main lobe and the presence of the spurious side lobes can be obtained, which in the SWDD method is acquired using the the L-curve method. For example, the optimum $\lambda$-value in Figure 21 determined using the L-curve method is 0.394.

*Sensitivity of the SWDD method to the radius of the array-setup*

A sensitivity analysis is performed to check the influence of the radius of the array setup in the SWDD analysis. The accuracy of the obtained results are analysed for the directional error and the amplitude error. The wave signals considering four prescribed waves with a wave number of 1, incoming wave amplitudes of respectively 1.0, 0.5, 1.0 and 0.5 m and incoming wave directions of respectively 0, 90, 180 and 270 degree incidence. It is decided to make use of a constant spatial grid, which means that the number gauges are increasing with increasing radius, because this is more realistic. Table 7 presents the obtained characteristics from the results of the SWDD analysis for varying the radius parameter (and thus $R/L$, with $L$ is 1.0 m), where $R$ is the radius of the array, $L$ is the wavelength, $N$ is the number of gauges (numerical grid nodes) and $ML$ is the main lobe.

Table 7: Obtained characteristics from the SWDD analysis performed for the influence to the radius with additional noise of 10e-8 in the complex amplitudes.

| $\frac{R}{L}$ | $\lambda$ | N | Comp. time [s] | No. of lobes | Width ML [°] | Mean directional error [°] | Mean amplitude error [m] | Directional resolution [°] |
|---|---|---|---|---|---|---|---|---|
| **0.075** | 6.05e-07 | 57 | 0.66 | 8 | 20.40 | 2.60 | 0.03 | 35.00 |
| **0.15** | 5.62e-07 | 221 | 0.10 | 16 | 10.56 | 0.19 | 0.01 | 27.00 |
| **0.25** | 7.65e-07 | 593 | 0.35 | 16 | 11.10 | 0.21 | 0.01 | 23.00 |
| **0.50** | 7.12e-07 | 2417 | 0.58 | 24 | 7.63 | 0.04 | 0 | 17.00 |
| **2.00** | 5.01e-07 | 38797 | 7.73 | 56 | 3.53 | 0.01 | 0 | 9.00 |
| **5.00** | 4.75e-07 | 242379 | 46.14 | 105 | 1.87 | 0.02 | 0 | 6.00 |
| **10** | 2.45e-07 | 969629 | 286.61 | 168 | 1.13 | 0 | 0.01 | 3.50 |

In Table 7 it becomes clear that for a larger radius the number of spurious side lobes gets higher and the width of the main lobes gets smaller. The directional resolution improves for higher $R/L$-values, where for 'often' used radius values for the array approximately a directional resolution of 25.00° up to 15.00° is reached and for larger dense array setups even a directional resolution up to 3.50° becomes possible. Also an analysis is performed where the number of gauges are kept constant to 221, which gives similar results as found in Table 7. For a more clear overview the mean errors in percentage are plotted in Figure 22.
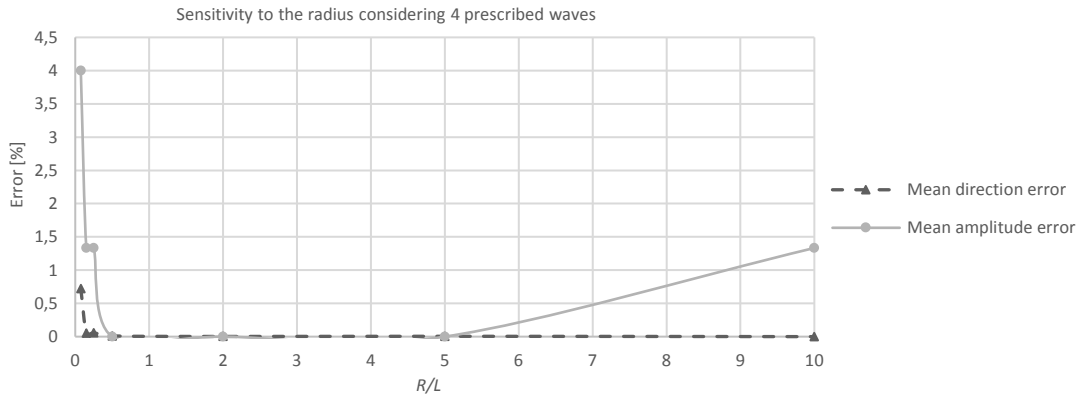


Figure 22: Mean errors from the sensitivity analysis to the radius for respectively the direction and the amplitude.

For the mean directional error it becomes clear that larger $R/L$-values gives smaller errors. However for the amplitude error, decreasing in the beginning of the plot, the error increases when $R/L > 5.00$. Which can be explained due to the large matrices present for large domains (using a dense grid) analysed (when $R/L$ is 10, $N$ is 969629). Considering both curves in Figure 22 an optimum can be found for homogeneous synthetic testcases of: $0.15 \leq R/L \leq 10.00$, based on an accuracy limit of 2%. In the next sections, noise is added in the position of the gauges as well *(thus: x, y, z)* in the tests for various array configurations.

### 5.1.3 Testcases B and C: accuracy analysis SWDD using circular arrays

The first accuracy analysis for the SWDD method uses circular array setups. All results obtained from the wave directional analyses by the SWDD method for the different circular array setups are summarized in section 5.1.5 Table 8. Additional noise is implemented in the position of the gauges *(x,y)* and the complex valued amplitudes *(z)*. An accuracy limit of 2.50° for the direction and 0.10 m for the amplitude is proposed.

*Array setup variation*

The next coming sections consider various circular array setups (using a limited amount of gauges up to only 25). First, prescribed wave signals are analysed by the SWDD method using a circular array setup. Two different circular setups are considered, with respectively 25 gauges placed in **one** ring and 25 gauges placed in **two** rings, displayed in Figure 23a and b. Second, various prescribed wave signals are analysed by the SWDD method using a CERC-6 array setup (Davis and Regier, 1977), displayed in Figure 23c.
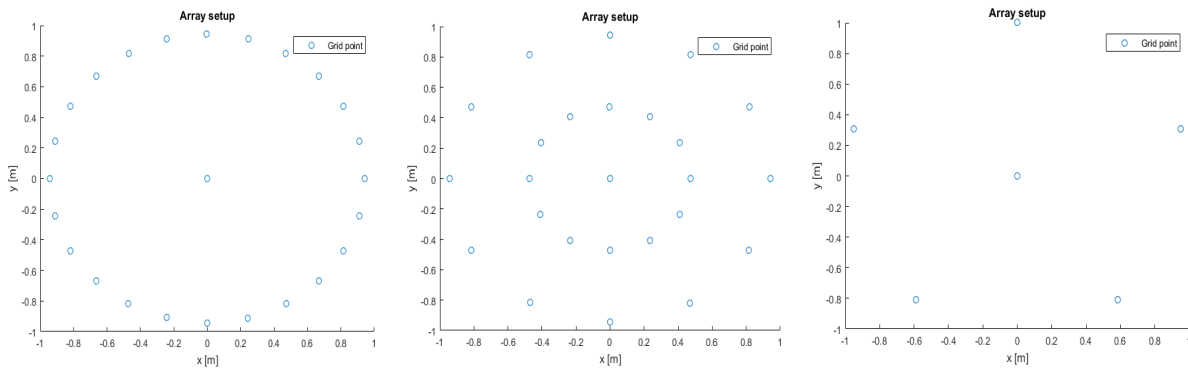


Figure 23: Three different array configurations using respectively 25 gauges in one ring (a), 25 gauges in two rings (b) and 6 gauges in the CERC-6 configuration (c).

*Two monochromatic waves under a right angle*

For the first testcase using a circular array setup (testcase B), two incoming monochromatic plane waves with respectively 1.00 and 0.50 m wave amplitudes and 0 and 90 degree incidence are prescribed. Figure 24 displays the resulted polar plots from the SWDD analyses for both circular arrays (case B1: 1-ring array and case B2: 2-rings array).
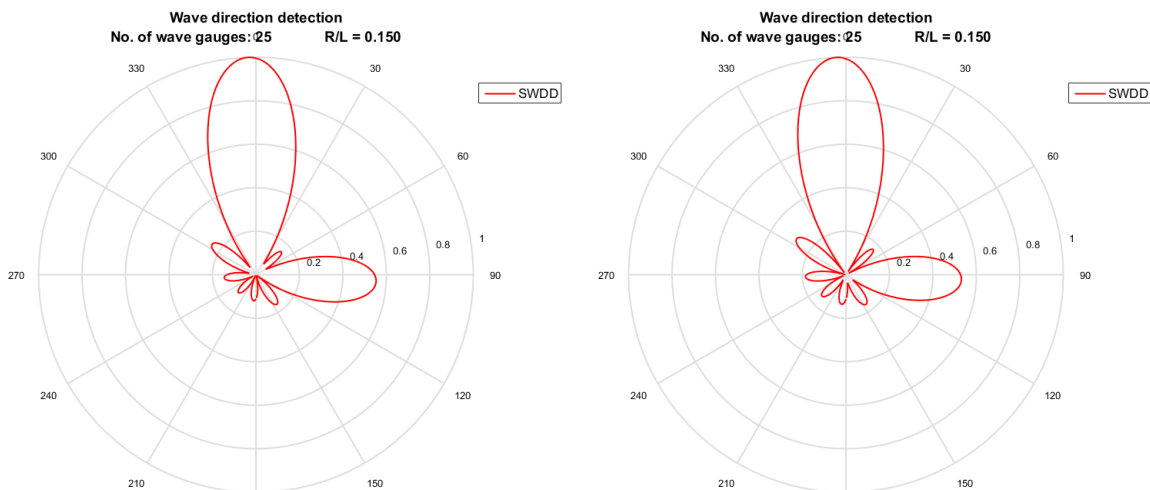


Figure 24: The polar plots obtained by SWDD for analysing two prescribed monochromatic incoming waves of respectively 1.00 m wave amplitude coming from the North (0° nautical convention) and 0.50 m wave amplitude coming from the East (90°). The left figure (a) presents the results for a 1-ring array (case B1) and the right figure (b) presents the results for a 2-rings array (case B2), both for 25 gauges.

The results of testcase B, displayed in Figure 24 for both array setups, show that indeed both incoming waves are detected accurately by the SWDD method. Considering the proposed accuracy limits it becomes clear that the wave direction is presented accurately in the polar plots with a mean error of respectively 2.20° for a 1-ring array and 1.48° for a 2-rings array setup. The mean error in the wave amplitude is respectively 0.10 m for a 1-ring array and 0.07 m for a 2-rings array setup.

### Four monochromatic waves

For the second testcase using a circular array (testcase C), four plane waves computed in MATLAB with respectively 1.00, 0.50, 1.00 and 0.50 m wave amplitude and 0, 90, 180 and 270 degree incidence are prescribed. Figure 25 displays the resulted polar plot from the SWDD analyses for testcase C.
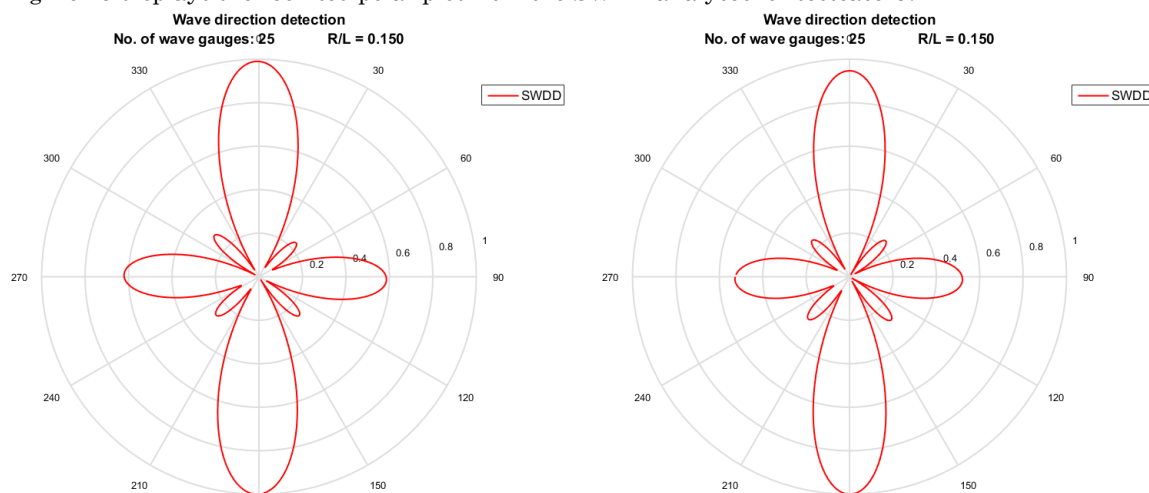


Figure 25: The polar plots obtained by SWDD for analysing four prescribed monochromatic incoming waves of respectively 1.00, 0.50, 1.00, 0.50 m wave amplitude, coming from 0°, 90°, 180° and 270°. The left figure (a) presents the results for a 1-ring array (case C1) and the right figure (b) presents the results for a 2-rings array (case C2), both for 25 gauges.

The results of testcase C, displayed in Figure 25 for both circular array setups, show that the incoming waves are detected accurately by the SWDD method. Considering the proposed accuracy limits it becomes clear that the wave direction is presented accurately with a mean error of respectively 1.03° for a 1-ring array setup and 1.23° for a 2-rings array setup. The mean error of the wave amplitude presented in the polar plots in Figure 25 for respectively the 1-ring circular array and the 2-rings circular array contain a mean error of 0.03 m and 0.05 m. The results will be further discussed in section *5.1.5 Intermediate findings synthetic testcases.*

## 5.1.4 Testcase D: accuracy analysis SWDD using the CERC-6 array setup

The next analytical testcase (testcase D) considers a CERC-6 array setup (Figure 23c). The 'stable' results obtained from the analyses by SWDD for the CERC-6 array setup are summarized in section 5.2.5 Table 8. The prescribed input of testcases B and C, where respectively two and four monochromatic waves are analysed using circular array setups, are also analysed using the CERC-6 array setup. However, for the input of testcases B and C, the SWDD method is **unable** to detect and present the wave direction accurately using the CERC-6 array setup. The resulted polar plots for the SWDD analyses for two and four prescribed wave signals using a CERC-6 array setup are presented in appendix F. It seems that for a limited number of gauges in the array setup (only 6) a maximum number of wave components can be detected. Which is why, as a first instance, relatively easy waves signals are prescribed and analysed in four cases using the CERC-6 array setup. The first case (D1) considers one incoming monochromatic wave with 1.0 m wave amplitude and 150 degree wave incidence. The second case (D2) prescribes two incoming monochromatic waves with respectively 1.0 and 1.0 m wave amplitudes and 0 and 180 degree wave incidence. The third case (D3) considers two incoming monochromatic waves with respectively 1.0 and 0.5 m wave amplitudes and 0 and 180 degree wave incidence. The fourth case (D4) prescribes two incoming monochromatic waves with respectively 1.0 and 1.0 m wave

amplitudes and 30 and 150 degree wave incidence. Figure 26 and Figure 27 displays the resulted polar plots from the SWDD analysis, for cases D1 - D4 using a CERC-6 array setup.
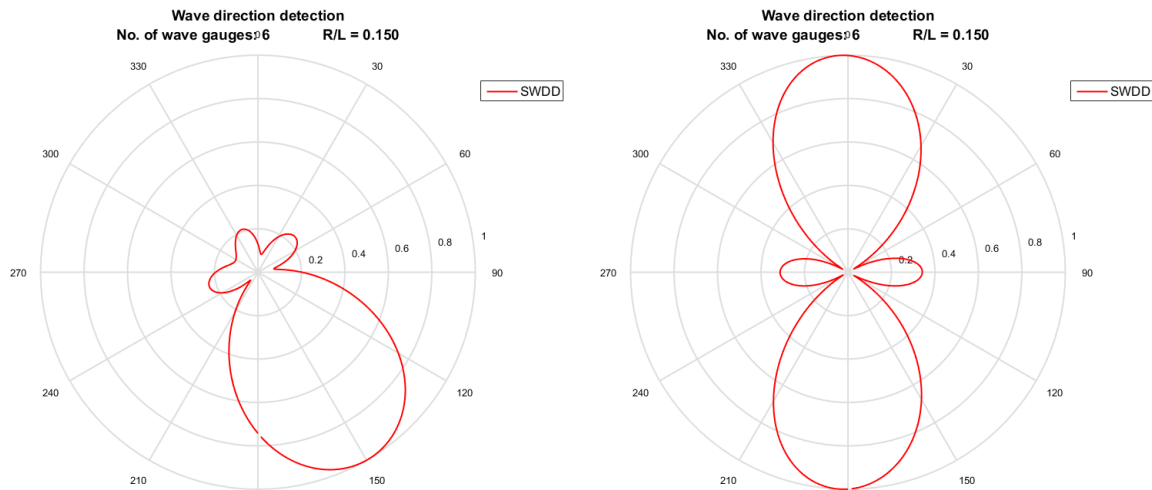


Figure 26: The polar plots from the SWDD method for cases D1 and D2, where one prescribed monochromatic wave with 1.0 m wave amplitude with 150° incidence (a) and two prescribed monochromatic waves both 1.0 m wave amplitude with respectively 0° and 180° incidence (b) are presented.
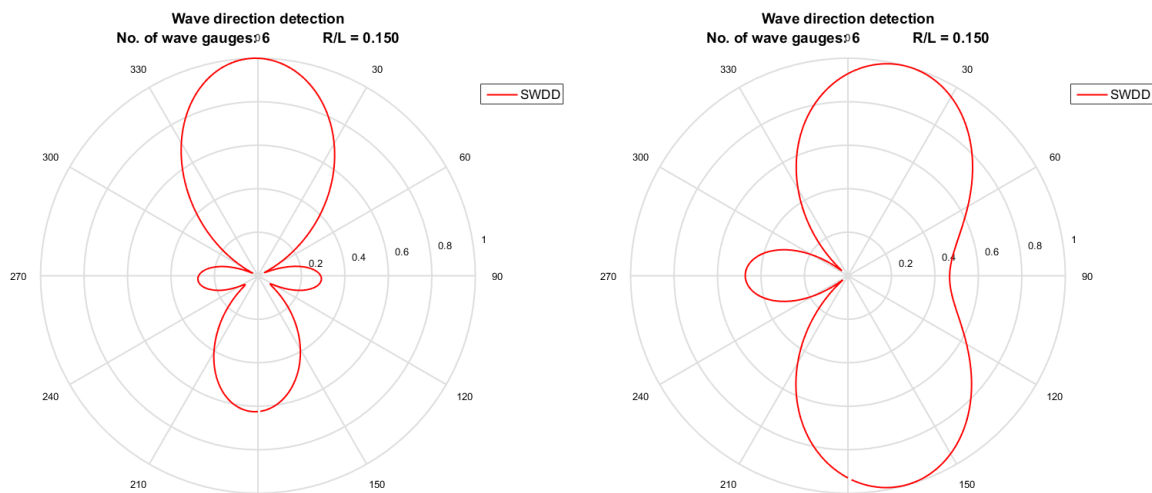


Figure 27: The polar plots from the SWDD method for cases D3 and D4, where respectively two prescribed monochromatic waves with 1.0 and 0.5m wave amplitude with 0° and 180° incidence (a) and two prescribed monochromatic waves both 1.0 m wave amplitude with respectively 30° and 150° incidence (b) are presented.

Testcase D using the CERC-6 array show meaningful results for one incoming wave and two incoming waves when they are mirrored (180° difference), with only an error in the wave direction of respectively 0.85°, 1.67° and 1.10° and an amplitude error of respectively 0.04 m, 0.02 m and 0.02 m in case D1, D2 and D3. When the two waves are under an angle, or more than two wave components are present, the results become unreliable. Case D4 has a directional error of 12.65° and an amplitude error of 0.38 m. Considering the proposed accuracy limits it becomes clear that case D1 - D3 are modelled accurately and case D4 is inaccurate.

It can also be noticed in Figure 26 and Figure 27 that the lobes found in the polar plots become wider using the CERC-6 array setup then for the previous 25-gauge array results in Figure 24 and Figure 25. Which can be explained due to the limited information of only 6 gauges. While the biggest advantage of the SWDD method is that it can be used with wave data from many grid nodes (for example 360). Which is the intention of Witteveen+Bos to use the SWDD method as a post-processing method on the grid data produced by a numerical wave model, where many grid nodes are available.

## 5.1.5 Intermediate findings synthetic testcases

The results of testcases B, C and D are summarized in Table 8, where $R$ is the radius of the array, $L$ is the wavelength, $\lambda$ is the used Tikhonov parameter, $N$ is the number of gauges in the array setup, $ML$ is the main lobe, $SL$ is the spurious lobe, $\rho_{lobe}$ is the ratio of the highest spurious lobe and the main lobe amplitude, $\rho_{ML}$ is the ratio of the main lobe area by the spurious lobe area, *dir* are the obtained directions and $\varepsilon_{recon}$ is the reconstruction error, which was described in section *3.3 Methodology accuracy and sensitivity analyses SWDD* and a short recapitulation is presented below.

*A new error description was introduced in section 3.3 Methodology accuracy and sensitivity analyses SWDD, the wave field reconstruction error. The complex amplitude at each gauge in the array setup is known before the SWDD analysis and the complex amplitude corresponding to each direction is known after the directional wave-analysis by SWDD. Which makes it possible to obtain the wave field for both the 'exact' wavefield and the 'reconstructed' wave field (from the complex amplitudes after the SWDD analysis) which are presented on a dense grid. This can be subtracted from each other, where after the standard deviation of the error is determined. The standard deviation is divided by the maximum surface elevation and multiplied by 100% to normalize it in percentage with the surface elevation. Two errors are considered: the reconstruction error on a dense grid only inside the array setup and a reconstruction error on a dense grid on a (large) domain of one wavelength, which both are presented in the tables in the main report.*

Table 8: The SWDD results for the different testcases – B, C and D – where the most important characteristics of the presented polar plots are summarized for the analysed prescribed wave signals.

| Test | Case | $\frac{R}{L}$ | $\lambda$ | N | No. of lobes | Width ML [°] | $\rho_{lobe}$ $\left(\frac{a_{maxSL}}{a_{ML}}\right)$ | $\rho_{ML}$ $\left(\frac{A_{ML}}{A_{total}}\right)$ | Error dir. [°] | Error Ampl. [m] | Error $\varepsilon_{recon, inside}$ [%] |
|---|---|---|---|---|---|---|---|---|---|---|---|
| Circular array | B1: 2 waves 1-ring array | 0.15 | 0.04 | 25 | 8 | 20.51 | 0.29 | 0.70 | 2.20 | 0.10 | 0.16 |
| | B2: 2 waves 2-rings array | 0.15 | 0.03 | 25 | 8 | 20.29 | 0.25 | 0.72 | 1.48 | 0.07 | 0.17 |
| | C1: 4 waves 1-ring array | 0.15 | 0.03 | 25 | 8 | 18.32 | 0.34 | 0.83 | 1.03 | 0.03 | 0.15 |
| | C2: 4 waves 2-rings array | 0.15 | 0.03 | 25 | 8 | 18.52 | 0.50 | 0.86 | 1.23 | 0.05 | 0.16 |
| CERC-6 | D1: 1 wave | 0.15 | 0.04 | 6 | 4 | 41.73 | 0.26 | 0.69 | 0.85 | 0.04 | 2.12 |
| | D2: 2 waves mirrored 1 m | 0.15 | 0.04 | 6 | 4 | 36.73 | 0.37 | 0.85 | 1.67 | 0.02 | 0.61 |
| | D3: 2 waves 1 m and 0.5 m | 0.15 | 0.05 | 6 | 4 | 36.88 | 0.31 | 0.84 | 1.10 | 0.02 | 1.22 |
| | D4: 2 waves oblique | 0.15 | 0.04 | 6 | 3 | 43.73 | 0.50 | 0.88 | 12.65 | 0.38 | 2.91 |

In Table 8 and the previous treated subsections it becomes clear that the SWDD method works well for relatively complex wave fields, even where additional noise and uncertainty in the sensor positions are included. It becomes clear that for practical (approximately for N < 5000) homogeneous cases, when more wave gauges are used in the array setup, the SWDD method becomes more accurate and more robust. The CERC-6 array setup, using only 6 gauges, is limited for the SWDD method to analyse more than two mirrored incoming wave directions. These errors can among others be explained due to the added noise ($x,y,z$ standard deviation) and the limited array configuration for the high number of prescribed wave signals. An array setup where wave gauges are placed in multiple rings give small accuracy increasement. Next to the advantage in accuracy, it becomes clear that the double circular array is more robust.

For the next section *5.2 SWDD method sensitivity analysis using a wave source and dipole*, where a wave source and wave dipole are used in the sensitivity analyses, the second circular array setup (25 gauges in two rings) is chosen, because of the accuracy. And in section *5.3 SWDD method sensitivity analysis using WIHA output*, more realistic and complex cases are computed using WIHA where after the output will be analysed by the SWDD method and all grid nodes within a circle are used.

## 5.2 SWDD method sensitivity analysis using a wave source and dipole

More extensive sensitivity analyses of the SWDD method are considered using a wave source and wave dipole created with the Hankel function solutions. The prescribed wave source and wave dipole are used to compute circular wave patterns. The results at specified output locations (the array setup) are used as input for the SWDD directional wave-analysis in the stated sensitivity analyses.

Two different cases by the Hankel function are examined. The first testcase (E) considers only a wave *source* function at the location $(x_s, y_s)$. Which among others, studies the influence of curved wave patterns on the accuracy of the SWDD results. Close to the source, wave-crest curvature is dominantly present. Many wavelengths away from the source, the wave-crest curvature gets less and ultimately becomes negligible.

The second testcase (F) considers a wave *dipole* at $(x_D y_D)$, which is created with a multiplicity mode of 1. This testcase (F) studies the sensitivity of the SWDD method to a variation of the amplitude gradient within the array setup to analyse. Next to the amplitude variation along the wave-crest, the dipole also has wave-crest curvature present close to the source. Figure 28 displays the by the wave *source* and wave *dipole* created wave fields. Both testcases, analyses and compares an output location nearby (2 wavelengths away with an inhomogeneity value of: $Inh_{curv} = L/R_c = 0.50$) and far away (80 wavelengths away). All tests using the Hankel function (*source* and *dipole*) consider a Hankel unit strength of 1.0, a wave period of 10.0 s and water depth of 10.0 m.
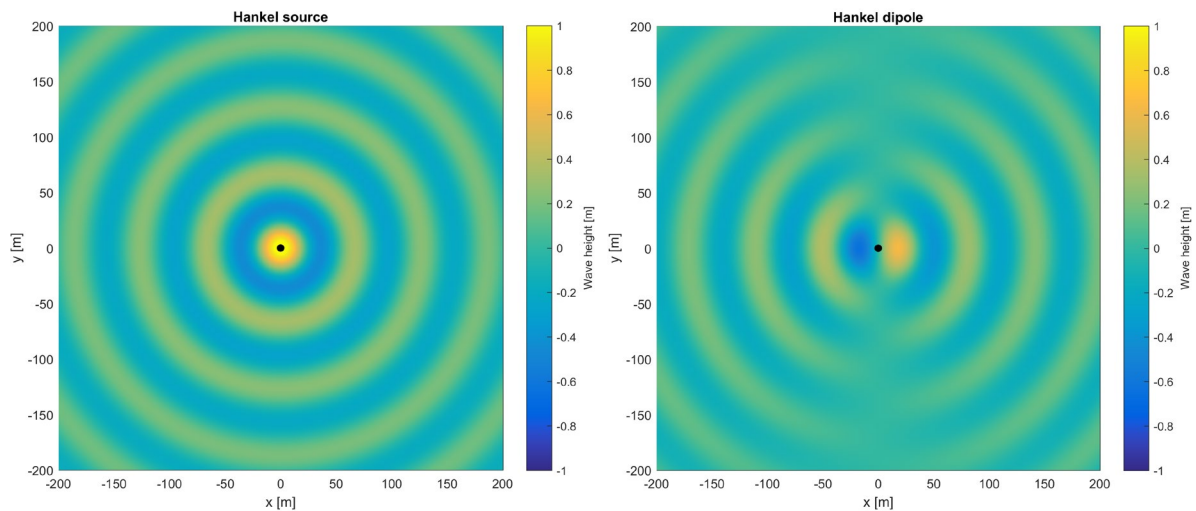


Figure 28: The resulted wave field of the Hankel source (a) and the Hankel dipole (b) respectively.

## 5.2.1 Test characteristics wave source and dipole solutions

The sensitivity analyses for the SWDD method using the Hankel function solutions consider various cases, all considering the same tests: T101 - T106. Every test examines different runs where five parameters of interest are either being varied or kept constant. The relevant parameters are respectively the wave period *(T)*, the number of gauges in the array *(N)*, the radius of the array configuration *(R)*, the radius divided by the wavelength *(R/L)* and the number of wave directions in the directional wave-analysis *(M)*.

The main characteristics of the six tests are listed below:

- ▪ T101: considers wave period variation (and thus variation of *L)*, all other parameters are kept constant.
- ▪ T102: considers four different array setups (for the same input as run R01 from T101), respectively 25 gauges placed in 2-rings, 25 gauges placed in 1-ring, a CERC-6 array setup and a 'reference' array setup using 361 gauges placed in 4-rings, like presented in Figure 23 in the previous section.
- ▪ T103: considers wave period variation, where (in contradiction to T101) the parameter $R/L$ is kept constant.
- ▪ T104: considers variation in the number of wave directions in the SWDD analysis.
- ▪ T105: considers variation in the radius of the array setup (thus variation in $R/L$).
- ▪ T106: considers variation in the number of gauges in the array and the radius of the array setup.

An overview of all parameter variation used in tests T101 - T106, summarized in tables, can be found in appendix G and the resulted polar plots for each run obtained by the SWDD analysis in appendix H.

## 5.2.2 Testcase E: wave source (wave-crest curvature) experiments

The sensitivity analyses for the SWDD method using the Hankel *source* function performs test T101 - T106 respectively nearby the source (case E1: $2L$ away, where the wave-crest curvature is still highly present $Inh_{curv} = L/R_c = 0.50$) and far away from the source (case E2: $80L$ away, where the wave-crest curvature is negligibly present). Figure 29 displays the resulted wave field for both cases E1 nearby and E2 far away from the source including the centre point of the array setup for the specific case, where all the array setups for each testcase can be found in appendix I. The 'standard' array exists of 25 gauges in 2-rings.
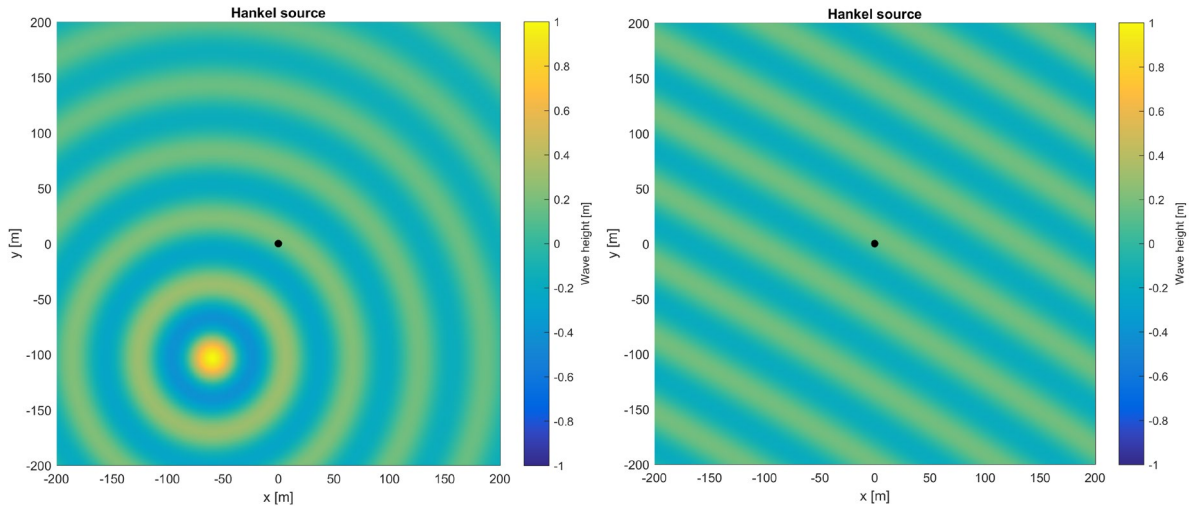


Figure 29: The wavefield computed with the Hankel function (wave source). The left figure (a) is nearby the source (2 wavelengths away) and the right figure (b) is far away from the source (80 wavelengths away).

Table 9 below presents the most important characteristics of the obtained polar plots from the SWDD method analysis for case E1 where the Hankel *source* function is used for the output location located $2L$ away under an angle of 210 degrees, where $R$ is the radius of the array setup, $L$ is the wavelength, $\lambda$ is the used Tikhonov parameter, $N$ is the number of gauges in the array setup, $ML$ is the main lobe, $SL$ is the spurious lobe, $\rho_{lobe}$ is the ratio of the highest spurious lobe and the main lobe amplitude, $\rho_{ML}$ is the ratio of the main lobe area by

the spurious lobe area, $\varepsilon_{dir}$ is the mean directional error and $\varepsilon_{recon}$ is the reconstruction error both considering the reconstruction error on a dense grid only inside the array setup and the reconstruction error reconstructed on a relatively large domain *(L* by *L)*. The findings for case E1 from Table 9 and for case E2 from Table 10 are presented in the next section. All the obtained polar plots are presented in appendix H.

Table 9: The SWDD results for the different tests of case E1 where the most important characteristics of the presented polar plots are summarized quantitively for the Hankel source nearby (2*L*) with a wave direction of 210° and a wave curvature of 0.50 (wavelength divided by distance to the source). The 'standard' array exists of 25 gauges in 2-rings.

| Test | Run | Description | $\frac{R}{L}$ | $\lambda$ | N | No. of lobes | Width ML [°] | $\rho_{lobe}$ $\left(\frac{a_{maxSL}}{a_{ML}}\right)$ | Inh. curv. ang. $R/R_C$ | Error $\varepsilon_{dir.}$ [°] | Error $\varepsilon_{recon,}$ inside [%] | Error $\varepsilon_{recon,}$ large [%] |
|---|---|---|---|---|---|---|---|---|---|---|---|---|
| **T101.E1** *varied T* | R01.1 | T = 7 s | 0.15 (8.97/60) | 8.67e-6 | 25 | 12 | 16.83 | 0.39 | 0.075 | 0 | 2.35e-4 | 0.79 |
| | R02.1 | T = 14 s | 0.067 (8.97/134) | 3.87e-8 | 25 | 12 | 16.82 | 0.39 | 0.034 | 0 | 5.92e-7 | 0.79 |
| | R03.1 | T = 28 s | 0.033 (8.97/272) | 16.93 | 25 | 1 | 360.00 | 1.00 | 0.017 | n.a. | 12.34 | 78.12 |
| | R04.1 | T = 56 s | 0.016 (8.97/561) | 9.81 | 25 | 1 | 360.00 | 1.00 | 0.008 | n.a. | 6.47 | 88.46 |
| | R05.1 | T = 4 s | 0.364 (8.97/25) | 1.28e-12 | 25 | 24 | 10.17 | n.a. | 0.182 | 0 | 7.75e-6 | 1.02e-4 |
| **T102.E1** *Diff. array setup* | R06.1 | 1-ring | 0.15 (8.97/60) | 1.33e-9 | 25 | 19 | 12.31 | n.a. | 0.075 | 0 | 2.14e-9 | 2.10e-3 |
| | R07.1 | CERC-6 | 0.15 (8.97/60) | 5.80e-4 | 6 | 4 | 42.97 | 0.26 | 0.075 | 0.25 | 1.84 | 41.34 |
| | R20.1 | dense 4-rings | 0.15 (8.97/60) | 3.63e-12 | 361 | 22 | 10.69 | n.a. | 0.075 | 0 | 6.06e-12 | 8.12e-5 |
| **T103.E1** *varied T, but R/L constant* | R08.1 | T = 14 s | 0.15 (20.09/134) | 8.67e-6 | 25 | 12 | 16.83 | 0.39 | 0.075 | 0 | 2.35e-4 | 0.79 |
| | R09.1 | T = 28 s | 0.15 (41.24/275) | 8.67e-6 | 25 | 12 | 16.83 | 0.39 | 0.075 | 0 | 2.35e-4 | 0.79 |
| | R10.1 | T = 56 s | 0.15 (83.02/553) | 8.67e-6 | 25 | 12 | 16.83 | 0.39 | 0.075 | 0 | 2.35e-4 | 0.79 |
| | R11.1 | T = 4 s | 0.15 (3.70/25) | 8.67e-6 | 25 | 12 | 16.83 | 0.39 | 0.075 | 0 | 2.35e-4 | 0.79 |
| **T104.E1** *varied M* | R12.1 | M = 90 | 0.15 (8.97/60) | 4.33e-6 | 25 | 12 | 16.83 | 0.39 | 0.075 | 0 | 2.35e-4 | 0.79 |
| | R13.1 | M = 30 | 0.15 (8.97/60) | 2.50e-6 | 25 | 12 | 16.83 | 0.39 | 0.075 | 0 | 2.35e-4 | 0.79 |
| | R14.1 | M = 10 | 0.15 (8.97/60) | 3.77e-2 | 25 | 3 | n.a. | n.a. | 0.075 | n.a. | 0.16 | 15.15 |
| | R15.1 | M = 5 | 0.15 (8.97/60) | 8.36e-1 | 25 | 1 | n.a. | n.a. | 0.075 | n.a. | 6.29 | 48.13 |
| **T105.E1** *varied R* | R16.1 | R = 2·R1 | 0.30 (17.95 /60) | 3.34e-13 | 25 | 24 | 10.15 | n.a. | 0.15 | 0 | 2.47e-6 | 9.56e-5 |
| | R17.1 | R = 4·R1 | 0.60 (35.89/60) | 2.55e-9 | 25 | 24 | 10.26 | n.a. | 0.30 | 0 | 9.00e-5 | 9.00e-5 |
| | R18.1 | R = ½ R1 | 0.075 (4.49/60) | 7.50e-8 | 25 | 12 | 16.81 | 0.39 | 0.038 | 0 | 4.07e-6 | 0.78 |
| | R19.1 | R = ¼ R1 | 0.038 (2.24/60) | 18.86 | 25 | 1 | 360.00 | 1.00 | 0.019 | n.a. | 12.22 | 86.83 |
| **T106.E1** *varied N and R* | R21.1 | N = 13 | 0.15 (8.97/60) | 1.03e-9 | 13 | 12 | 16.84 | 0.39 | 0.075 | 0 | 2.42e-4 | 0.82 |
| | R22.1 | N = 25 | 0.25 (14.96/60) | 2.75e-4 | 25 | 12 | 16.87 | 0.39 | 0.125 | 0 | 9.40e-3 | 0.82 |
| | R23.1 | N = 13 | 0.25 (14.96/60) | 2.81e-7 | 13 | 12 | 16.89 | 0.39 | 0.125 | 0 | 9.80e-3 | 0.85 |
| | R24.1 | N = 25 | 0.05 (3/60) | 5.26e-9 | 25 | 12 | 16.82 | 0.39 | 0.025 | 0 | 3.22e-8 | 0.79 |
| | R25.1 | N = 13 | 0.05 (3/60) | 8.21e-4 | 13 | 6 | 16.87 | 0.24 | 0.025 | 0 | 0.83 | 62.02 |

Table 10 presents the most important characteristics of the obtained polar plots from the SWDD analysis for case E2 where the Hankel source function is used with the output location 80*L* away under an angle of 210 degrees. The 'standard' array exists of 25 gauges in 2-rings.

Table 10: The SWDD results for different tests of case E2 where the most important characteristics of the presented polar plots are summarized quantitively for the Hankel source far away (80 wavelengths) with a wave direction of 210°.

| Test | Run | Description | $\frac{R}{L}$ | $\lambda$ | N | No. of lobes | Width ML [°] | $\rho_{lobe}$ $\left(\frac{a_{maxSL}}{a_{ML}}\right)$ | $\rho_{ML}$ $\left(\frac{A_{ML}}{A_{total}}\right)$ | Error $\varepsilon_{dir.}$ [°] | Error $\varepsilon_{recon,}$ inside [%] | Error $\varepsilon_{recon,}$ large [%] |
|---|---|---|---|---|---|---|---|---|---|---|---|---|
| **T101.E2** *varied T* | R01.2 | T = 7 s | 0.15 (8.97/60) | 3.16e-13 | 25 | 24 | 8.54 | 0.22 | 0.52 | 0 | 1.26e-6 | 1.60e-3 |
| | R02.2 | T = 14 s | 0.067 (8.97/134) | 3.51e-13 | 25 | 20 | 10.35 | 0.22 | 0.55 | 0 | 8.84e-10 | 2.00e-3 |
| | R03.2 | T = 28 s | 0.033 (8.97/272) | 4.60e-13 | 25 | 20 | 12.62 | 0.28 | 0.57 | 0.25 | 3.08e-10 | 8.96e-2 |
| | R04.2 | T = 56 s | 0.016 (8.97/561) | 3.41e-12 | 25 | 12 | 16.35 | 0.22 | 0.58 | 0.07 | 2.49e-11 | 0.51 |
| | R05.2 | T = 4 s | 0.364 (8.97/25) | 2.51e-12 | 25 | 24 | 8.53 | 0.22 | 0.52 | 0 | 8.33e-6 | 5.45e-5 |
| **T102.E2** *Diff. array setup* | R06.2 | 1-ring | 0.15 (8.97/60) | 2.88e-13 | 25 | 24 | 8.52 | 0.22 | 0.52 | 0.01 | 4.70e-12 | 3.57e-5 |
| | R07.2 | CERC-6 | 0.15 (8.97/60) | 2.80e-2 | 6 | 4 | 41.90 | 0.26 | 0.70 | 0.80 | 1.80 | 29.61 |
| | R20.2 | dense 4-rings | 0.15 (8.97/60) | 3.63e-12 | 361 | 29 | 8.38 | 0.22 | 0.60 | 0.08 | 4.49e-12 | 2.92e-5 |
| **T103.E2** *varied T, but R/L constant* | R08.2 | T = 14 s | 0.15 (20.09/134) | 3.40e-13 | 25 | 24 | 8.51 | 0.22 | 0.51 | 0 | 3.82e-7 | 4.73e-4 |
| | R09.2 | T = 28 s | 0.15 (41.24/275) | 3.40e-13 | 25 | 24 | 8.51 | 0.22 | 0.51 | 0 | 3.82e-7 | 4.73e-4 |
| | R10.2 | T = 56 s | 0.15 (83.02/553) | 3.16e-13 | 25 | 24 | 8.51 | 0.22 | 0.51 | 0 | 7.89e-8 | 1.09e-4 |
| | R11.2 | T = 4 s | 0.15 (3.70/25) | 3.16e-13 | 25 | 24 | 8.51 | 0.22 | 0.51 | 0 | 4.01e-7 | 4.99e-4 |
| **T105.E2** *varied R* | R16.2 | R = 2·R1 | 0.30 (17.95 /60) | 1.08e-12 | 25 | 24 | 8.52 | 0.22 | 0.52 | 0 | 4.41e-6 | 7.53e-5 |
| | R17.2 | R = 4·R1 | 0.60 (35.89/60) | 2.59e-13 | 25 | 32 | 7.47 | 0.16 | 0.44 | 0.03 | 4.00e-3 | 4.00e-3 |
| | R18.2 | R = ½ R1 | 0.075 (4.49/60) | 4.44e-13 | 25 | 24 | 9.89 | 0.22 | 0.62 | 0.16 | 4.31e-9 | 1.60e-3 |
| | R19.2 | R = ¼ R1 | 0.038 (2.24/60) | 5.38e-13 | 25 | 16 | 12.41 | 0.23 | 0.56 | 0.26 | 8.22e-11 | 2.99e-2 |
| **T106.E2** *varied N and R* | R21.2 | N = 13 | 0.15 (8.97/60) | 2.56e-12 | 13 | 16 | 13.16 | 0.22 | 0.49 | 0 | 1.59e-5 | 0.53 |
| | R22.2 | N = 25 | 0.25 (14.96/60) | 1.23e-12 | 25 | 24 | 8.52 | 0.22 | 0.52 | 0 | 7.48e-7 | 4.92e-5 |
| | R23.2 | N = 13 | 0.25 (14.96/60) | 2.81e-7 | 13 | 6 | 28.99 | 0.22 | 0.68 | 0 | 1.32 | 11.56 |
| | R24.2 | N = 25 | 0.05 (3/60) | 3.55e-13 | 25 | 18 | 10.55 | 0.26 | 0.43 | 0.44 | 1.02e-10 | 2.42e-2 |
| | R25.2 | N = 13 | 0.05 (3/60) | 4.16e-11 | 13 | 12 | 16.42 | 0.22 | 0.57 | 0 | 2.18e-8 | 0.52 |

An extra test (T107.E1) is introduced where the distance from the array centre to the wave source ($L/R_c$) is not kept constant, but is lowered step-by-step (from $2.00L$ up to $0.25L$ for a constant wavelength and array radius). Figure 30 displays the results of T107.E1 for the inhomogeneity values: $L/R_c$.
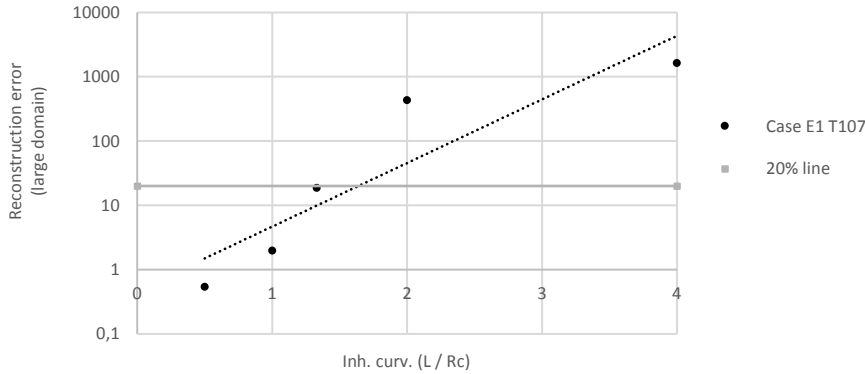


Figure 30: Displays the reconstruction error on the large domain for the inhomogeneity value *(L/Rc)*
for case E1 T107 where the distance to the source is lowered step-by-step from $2L$ to $0.25L$.

### Intermediate findings for a wave source

The intermediate findings are based on the results from cases E1 ($2L$ away containing high wave-crest curvature) and E2 ($80L$ away negligibly wave-crest curvature) found in Table 9 and Table 10, the polar plots presented in appendix H and Figure 30. The findings from tests T101 - T107 are consecutively treated for both cases E1 and E2 with emphasis on the difference between the two cases to be able to explain the effect of the physical processes wave-crest curvature. A first indication for the accuracy limit of the directional error, reconstruction error inside the array and the reconstruction error on a large domain are respectively 2.50°, 2% and 20%. Where after a section is dedicated which treats the most important findings from the influence of wave-crest curvature on four highlighted characteristics: the Tikhonov parameter $\lambda$, the number of lobes, the width of the main lobe and the ratio between the highest spurious side lobe and the main lobe. And finally, potential correlations between the characteristics and the found reconstruction errors for specific tests and cases are treated in the section: *Correlation characteristics and the reconstruction error in testcase E.*

*First observations testcase E*

Considering both reconstruction errors and the proposed accuracy limits in case E2 (minimal wave-crest curvature) all runs – R01 up R25 – are accurately. When wave-crest curvature effects are present (in case E1), it becomes clear that especially the low $R/L$ values are negatively influenced, because for these runs not enough difference in the phase is present due to the small array setup.

The reconstruction error in the large domain for the CERC-6 array setup is relatively high, due to the low number of gauges used.

It also strikes out that for T101 - T106 in case E1, when the angular inhomogeneity value ($R/R_c$) of wave-crest curvature in the array setup gets higher, the errors get lower (due to increasing radius of the array setup for a constant distance from the wave source to the array centre of $L/R_c = 0.50$). Where it can be concluded that according to this trend, the SWDD method has no problems with analysing wave-crest curvature effects, especially for larger radius values when more wave information is present for an array setup where the distance from the wave source to the array centre of $L/R_c = 0.50$. It seems like this inhomogeneity value ($R/R_c$) does not represent the error well. Which is why test T107.E1 is introduced, where the radius *(R)* is kept constant and the distance from the wave source to the centre of the array setup ($R_c$) is varied. In this test it becomes clear that a higher inhomogeneity value (higher $L/R_c$, thus closer to the source) the error increases. The latter inhomogeneity value – $L/R_c$ – is considered suitable and representative, where the SWDD method is able to analyse results when the array centre is at least $0.75L$ away from the wave source.

*Testcase E test T101*

In test T101 in both cases E1 and E2, where the wavelength is varied – and thus the parameter $R/L$ is varied: 0.016 - 0.364 – it becomes clear that for higher values of $R/L$ the results get more accurate on a regular bathymetry, considering both reconstruction errors. In case E1, where wave-crest curvature is present, the following range of applicability is found: $R/L > 0.033$.

The difference between the results of case E1 and E2 can be explained due to the presence of wave-crest curvature, the reconstruction errors becomes larger when wave-crest curvature is present, especially considering lower $R/L$ values ( $< 0.033$).

*Testcase E test T102*

Test T102.E1 and T102.E2 show that the CERC-6 array setup results are less accurate compared to the results of the other considered array setups, containing a reconstruction error of respectively 1.84% and 1.80% inside the array setup, a reconstruction error on the large domain *(L by L)* of 41.34% and 29.61% and a directional error of 0.25° and 0.80°. Considering the proposed accuracy limitations, it becomes clear that the reconstruction error inside the array setup and the found direction are both accurate. However, the error in the reconstruction on the large domain becomes inaccurate, which can be explained due to the low number of gauges present. If only interested in the main direction for monochromatic waves the CERC-6 is considered suitable. However, high directional resolutions are not possible. The errors found for the circular arrays and the dense array are all negligible.

*Testcase E test T103*

In test T103, for both cases E1 and E2, it becomes clear that the wavelength has no influence on the accuracy of the results of the SWDD method when the $R/L$ value of the array setup is kept constant at 0.15 for a constant bathymetry and number of gauges.

*Testcase E test T104*

In test T104 it becomes clear that when $M \leq 90$, the results of the SWDD method become unreliable due to the low resolution used, both with and without wave-crest curvature present. The difference in computation time between $M = 90$ and $M = 360$ is negligible, which is why the last is advised.

*Testcase E test T105*

In test T105.E1, where wave-crest curvature is present and the radius of the array setup has been varied up to *2.40L*, the following range of applicability is found: *$0.075 \leq R/L \leq 1.50$.* The lower limit is present due to the fact that not enough variation in the phase is present for the SWDD method to analyse. And the higher limit is present due to the relatively low number of wave gauges for such large radius values. When a dense array setup is considered this upper limitation is expected to extend to a higher value.

*Testcase E test T106*

In test T106 it becomes clear that when using a higher number of gauges within the array configuration, the reconstruction error gets lower. And like in the previous findings in T101, the higher $R/L$ and less wave-crest curvature present, the more accurate the SWDD results become (the radius is tested up to 2.40$L$).

*Overall effect of wave-crest curvature in testcase E*

Wave-crest curvature has a negative influence on the accuracy of the results, especially considering small $R/L$ ($\leq 0.075$) values for the array setup. When wave-crest curvature is present, the $\lambda$-parameter found in case E1 is on average 10e6 times larger, the number of lobes is on average 1.70 times lower and the width is on average 1.80 times wider.

*Correlation characteristics and the reconstruction error in testcase E*

Several parameters and characteristics show correlated behaviour between the reconstruction error on the large domain (and each other). Three considered most important correlated parameters **(per test considered)** between the reconstruction error on the large domain are displayed in Table 11 below.

Table 11: Correlations per test between characteristics and the reconstruction error for cases E1 and E2.
The symbol – stands for: constant and n.a. stands for: not available.

| Test | $\lambda$ | | No. of lobes | | Width ML [°] | |
|---|---|---|---|---|---|---|
| | Corr($\lambda$, $\varepsilon_{recon,large}$) case E1 | Corr($\lambda$, $\varepsilon_{recon,large}$) case E2 | Corr(No. of lobes,$\varepsilon_{recon,large}$) case E1 | Corr(No. of lobes,$\varepsilon_{recon,large}$) case E2 | Corr(Width ML,$\varepsilon_{recon,large}$) case E1 | Corr(Width ML,$\varepsilon_{recon,large}$) case E2 |
| T101 | 0.92 | 0.73 | -0.86 | -0.94 | 1.00 | 0.93 |
| T102 | 1.00 | 1.00 | -0.99 | -0.98 | 1.00 | 1.00 |
| T103 | – | – | – | – | – | – |
| T104 | 0.97 | 0.96 | -0.87 | -0.87 | n.a. | n.a. |
| T105 | 1.00 | -0.20 | -0.87 | -0.75 | 1.00 | 0.85 |
| T106 | 0.94 | 1.00 | -1.00 | -0.79 | 1.00 | 0.95 |
| Mean Corr. | 0.83 | | -0.87 | | 0.97 | |

The **mean** correlation (based on all the correlations per test for one specific case) between the reconstruction error on the large domain and respectively the λ-parameter is 0.83, the number of lobes is -0.87 and the main lobe width is 0.97. However, the number of lobes are related to the width of the main lobe (Corr. of -0.80), which is why the correlation between the width of the main lobe and the reconstruction error on the large domain is given more attention in the remaining of the report.

A (correlation) plot between the main lobe width and the reconstruction error on the large domain for the cases E1 and E2 (not per test considered) is displayed in Figure 31. The found correlation between the main lobe width and reconstruction error on the large domain in case E1 is 0.86 and in case E2 is 0.97.

In the results, it becomes clear that the λ-parameter shows a correlation between the reconstruction error on the large domain. Which makes sense, because when the λ-parameter becomes larger than 1, the 'minimization part' in the Tikhonov regularization does not represent a good 'fit', which is clearly visible in the results as well. Remaining correlation plots between several characteristics are treated in appendix J.
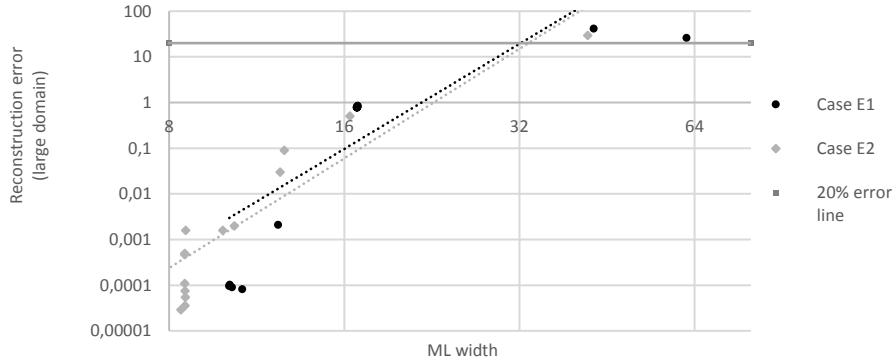


Figure 31: Correlation plots between the reconstruction error on the large domain
and the width of the main lobe respectively for case E1 and case E2.

## 5.2.3 Testcase F: wave dipole (wave amplitude variation) experiments

Testcase F considers among others – like testcase E – the sensitivity analyses of the SWDD method using the Hankel *dipole* function for test T101 - T106 respectively near the dipole source (case F1: $2L$ away, where the wave-crest curvature is still highly present) and far away from the dipole source (case F2: $80L$ away, where the wave-crest curvature is minimally present, in contradiction to E2 not under an angle from the source). Both cases contain a high presence of wave amplitude variation. Figure 32 displays the resulted wave field for both the analyses nearby and far away from the *dipole* source including the centre point of the array setup for the specific case, where all the array setups for each testcase can be found in appendix I. The 'standard' array exists of 25 gauges in 2-rings.
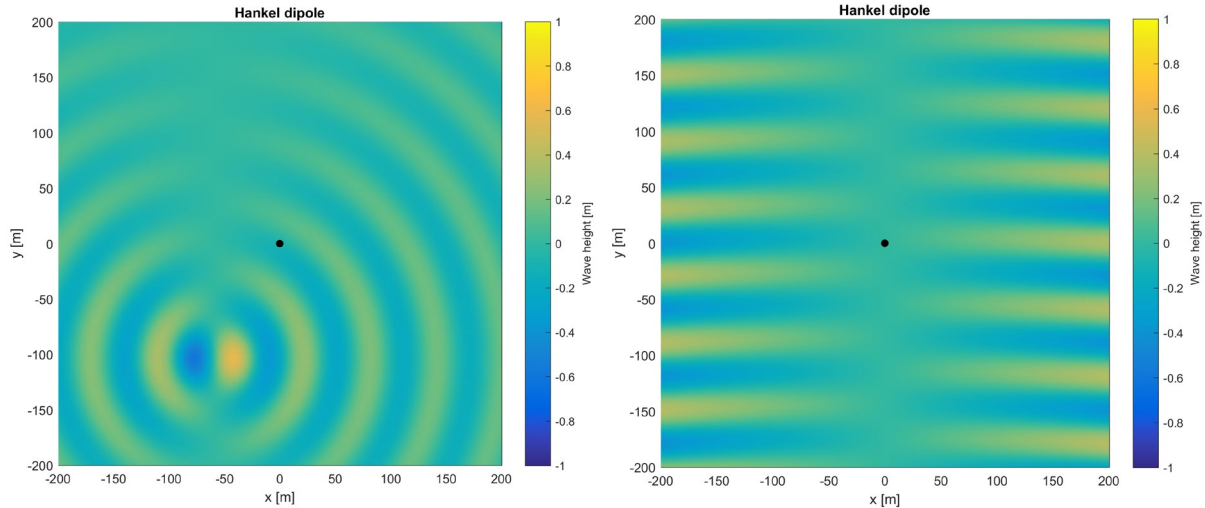
Figure 32: The analysed wavefield computed with the Hankel function (dipole). The left figure (a) is nearby the source (case F1: $2L$ away) and the right figure (b) is far away from the source (case F2: $80L$ away).

The most important characteristics of the obtained polar plots and findings per test from the SWDD analysis for case F1 ($2L$ away containing high wave-crest curvature and wave amplitude variation) and case F2 ($80L$ away containing wave amplitude variation) are presented in appendix K. All the obtained polar plots are presented in appendix H.

### Intermediate findings wave dipole

It becomes clear that wave amplitude variation has negligible influence on the accuracy of the SWDD results and that the main findings from testcase E concerning wave-crest curvature also applies to testcase F. That is why only the main findings are treated in the main report and the remaining findings are presented in appendix K.

Considering both reconstruction errors in case F2, all runs R01 up R19 are accurate, where it seems that wave amplitude variations has no effect on the results of the SWDD method. When wave-crest curvature effects are present (in case F1), it becomes clear that especially the low $R/L$ values are negatively influenced, thus just like in testcase E is the inhomogeneity value $R/R_c$ not representative.

*Overall effect of wave-crest curvature and amplitude variation in testcase F*

When wave-crest curvature is present, the $\lambda$-parameter is on average 10e6 larger, the number of lobes is on average 1.56 times lower and the width is on average 2.20 times wider.

Wave amplitude variation almost has no influence on the results of the SWDD analysis, considering the difference between the cases F1 and E1 and between the cases F2 and E2.

*Correlation characteristics and the reconstruction error in testcase F*

Several parameters and characteristics show correlated behaviour between the reconstruction error on the large domain. Three considered most important correlated parameters **(per test considered)** between the reconstruction error on the large domain are displayed in Table 12.

Table 12: Correlations per test between characteristics and the reconstruction for cases F1 and F2.

| Test | $\lambda$ | | No. of lobes | | Width ML [°] | |
|------|-----------|---|-------------|---|--------------|---|
| | $Corr(\lambda, \varepsilon_{recon,large})$ case F1 | $Corr(\lambda, \varepsilon_{recon,large})$ case F2 | $Corr(No.\ of\ lobes, \varepsilon_{recon,large})$ case F1 | $Corr(No.\ of\ lobes, \varepsilon_{recon,large})$ case F2 | $Corr(Width\ ML, \varepsilon_{recon,large})$ case F1 | $Corr(Width\ ML, \varepsilon_{recon,large})$ case F2 |
| **T101** | 0.94 | 0.48 | -0.89 | -1.00 | 1.00 | 1.00 |
| **T102** | 1.00 | 1.00 | -0.95 | -0.97 | 0.95 | 1.00 |
| **T103** | - | - | - | - | - | - |
| **T105** | 1.00 | 1.00 | -0.88 | -0.72 | 1.00 | 0.92 |
| **Mean Corr.** | 0.90 | | -0.90 | | 0.98 | |

The **mean** correlation (based on all the correlations per test for one specific case) between the reconstruction error on the large domain and respectively the λ-parameter is 0.90, the number of lobes is -0.90 and the main lobe width is 0.98. However, the number of lobes are related to the width of the main lobe (Corr. of -0.85). A (correlation) plot of the main lobe width and the reconstruction error on the large domain for the complete cases F1 and F2 (not per test considered) is displayed in Figure 33. Where the found correlation between the main lobe width and reconstruction error on the large domain in case F1 is 0.88 and in case F2 is 0.94. Remaining correlation plots between several characteristics are treated in appendix J.
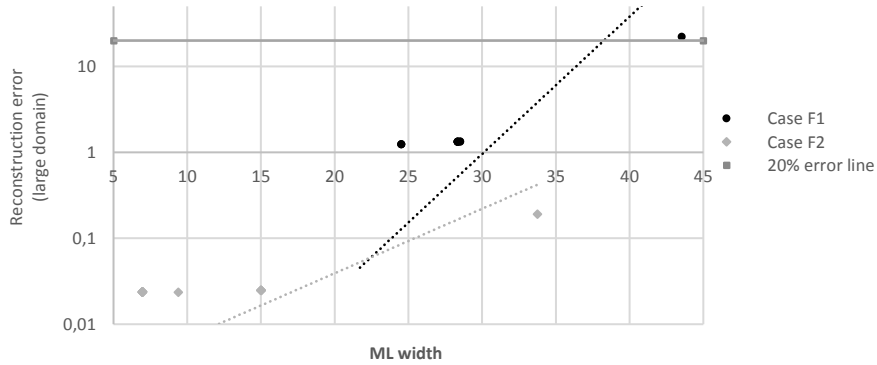


Figure 33: Correlation plots between the reconstruction error on the large domain
and the width of the main lobe respectively for case F1 and case F2.

## 5.2.4 Conclusions sensitivity analyses of the SWDD method using a wave source and dipole

The SWDD method is able to detect the main incoming wave components in prescribed wave patterns containing high wave-crest curvature and wave amplitude variation effects. Wave amplitude variations does not have an influence on the results of the SWDD analysis. Wave-crest curvature does have a negative influence on the results of the SWDD analysis, especially when the inhomogeneity value $L/R_c > 1.33$. Implying that the centre of the array configuration should be placed further than $0.75L$ from the wave source. When the inhomogeneity value $R/R_c$ of wave-crest curvature in the array setup gets higher, the errors get lower, meaning that only the first inhomogeneity value is representative. Considering a regular bathymetry and an array setup containing 25 gauges, a range of applicability is found for the radius of the array configuration when wave-crest curvature is present – using accuracy limits of 2.50°, 2% and 20% – of: *$0.075 \leq R/L \leq 1.50$.* The upper limit can be extended by using more gauges in the array configuration.

Next to the radius of the array setup, the number of gauges does have a large influence on the accuracy of the SWDD method as well. Considering realistic values *$(N \leq 10000)$*, a regular bathymetry and a constant radius of the array setup: the more gauges in the domain analysed, the more accurate the results become. Which is one of the reasons why the CERC-6 is outperformed by the other array configurations used.

Finally, correlations between several characteristics and the reconstruction error on the large domain are observed. Considering the correlations per test individually, the following mean correlations are found: between the λ-parameter and the reconstruction error on the large domain of 0.87, between the number of lobes and the reconstruction error on the large domain of -0.89 and between the width and the reconstruction error on the large domain of 0.98. A relation between the number of lobes and the width of the main lobe of -0.77 came forward, which is why more attention is given to the correlation between the main lobe width and the reconstruction error on the large domain. The correlation between the main lobe width and the reconstruction error on the large domain per case considered is 0.91.

## 5.3 SWDD method sensitivity analysis using WIHA output

The sensitivity analysis for the SWDD method has also been performed using the output from the mild-slope wave model WIHA. All tests consider five parameters of interest for the sensitivity analysis. Which, dependent on the corresponding test, are varied or kept constant. The considered parameters are respectively the wave period *(T)*, number of grid nodes within the circular domain *(N)*, radius of the circular domain *(R)*, radius divided by the wavelength ($R/L$) and number of wave directions used in the directional wave-analysis *(M)*. Multiple tests have been performed. An overview of all parameters used in the testcases T101 - T105 can be found in appendix G. For the first test (T101) the wave period (and thus the wavelength) has been varied. All other parameters are kept constant. The parameter $R/L$ is respectively equal to 0.15, 0.065, 0.031, 0.015 and 0.391. In the second test (T102) the reflection coefficient of the reflective wall has been varied. For the third test (T103) the period (and thus the wavelength) has been varied, but the radius of the circular domain is determined to get a constant $R/L$ of 0.15 for the cases R08 - R11 (which also changes the number of grid nodes). The fourth test (T104) the number of wave direction used for the analysis has been varied. And for the last test (T105) the radius (thus the number of grid nodes and $R/L$) has been varied. The parameter $R/L$ is respectively equal to 0.15, 0.300, 0.600, 0.074 and 0.037.

Various testcases with different geometries and boundaries are computed using the mild-slope wave model WIHA. The testcases consist of a 100% reflective wall where the incoming monochromatic wave has a 30 degree wave incidence with the wall. This testcase is subdivided in four cases: case G1 where diffraction is minimally present (reference case), case G2 where diffraction is dominantly present, case G3 where a non-homogeneous domain has been created (the bathymetry of each grid node is randomly created with a standard deviation of ±0.25 m) and case G4 where the last 100 m of the domain a 1:10 slope has been added.

For all cases considered in this report the North is in the top of the figures. All resulted polar plots are presented in appendix L and all used array setups can be found in in appendix M where all the reconstrued wave fields of the SWDD analyses from case G1 are presented. The found correlations are summarized in a separate section: *Correlated characteristics in testcase G*. An accuracy limit of 2% for the reconstruction error within the array setup and 20% for the reconstruction error on the large domain is considered.

### 5.3.1 Testcase G: 100% reflective wall

#### Case G1: reference case

The first case is computed as reference case, where physical processes are minimally present. The bathymetry is constant at -13.00 m. A triangular grid is solved using the finite element method with 14 nodes per wavelength. The South boundary is the incoming wave boundary where the incoming monochromatic wave has a wave height of 1.00 m and wave direction of 150° (based on nautical convention, which means that the wave has an oblique incidence of 30 degrees on the 100% reflective wall), the North boundary is a 100% reflective wall, the East boundary is a guiding wall with a reflection coefficient of 1.00 and the West boundary is a natural beach with a reflection coefficient of 0.00. The computed domain can be seen in Figure 34.
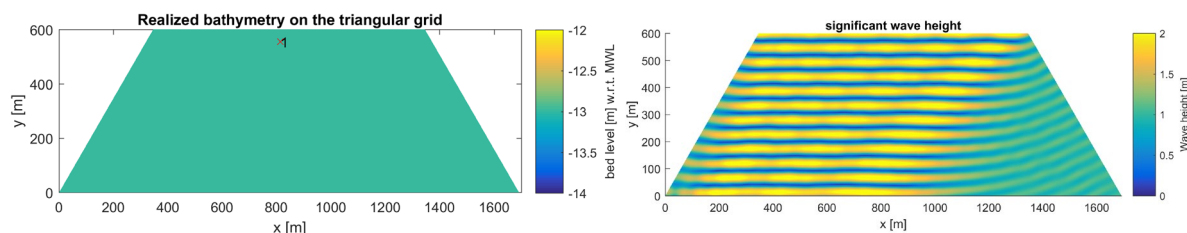


Figure 34: The left figure (a) presents the realized bathymetry and the centre point of the dense array setup in case G1, the right figure (b) presents the significant wave height output of WIHA for case G1 for run R01.

Table 13 below presents the most important characteristics of the obtained polar plots from the SWDD method for case G1 where diffraction is minimally present at the array setup and WIHA output is used as input in the SWDD analysis, where $R$ is the radius of the array, $L$ is the wavelength, $\lambda$ is the used Tikhonov parameter, $N$

is the number of gauges in the array setup, $ML$ is the main lobe, $SL$ is the spurious lobe, $\rho_{lobe}$ is the ratio of the highest spurious lobe and the main lobe amplitude, $\rho_{lobe}$ is the ratio of the main lobe areas by the spurious lobe area, $Dir$ is the obtained direction and $\varepsilon_{recon}$ is the reconstruction error both considering the reconstruction error on a dense grid only inside the array setup and the reconstruction error reconstructed on a relatively large domain *(L by L)*.

Table 13: The SWDD wave directional results for the different tests where the most important characteristics of the presented polar plots are summarized quantitatively.

| Test | Run | Description | $\frac{R}{L}$ | $\lambda$ | N | No. of lobes | Width ML [°] | $\rho_{lobe}$ $\left(\frac{a_{maxSL}}{a_{ML}}\right)$ | $\rho_{ML}$ $\left(\frac{A_{ML}}{A_{total}}\right)$ | Dir [°] | Error $\varepsilon_{recon,}$ $_{inside}$ [%] | Error $\varepsilon_{recon,}$ $_{large}$ [%] |
|---|---|---|---|---|---|---|---|---|---|---|---|---|
| **T101.G1** *varied T* | R01 | T = 7 s | 0.15 (9.75/65) | 3.47e-2 | 230 | 7 | 22.62 | 0.30 | 0.79 | 30.89/149.11 | 0.05 | 3.69 |
| | R02 | T = 14 s | 0.067 (9.75/151) | 1.97e-3 | 230 | 6 | 23.32 | 0.30 | 0.80 | 27.27/153.83 | 0.01 | 5.31 |
| | R03 | T = 28 s | 0.033 (9.75/313) | 1.48e-3 | 230 | 6 | 27.78 | 0.39 | 0.73 | 29.32/151.20 | 0.00 | 10.65 |
| | R04 | T = 56 s | 0.016 (9.75/631) | 2.22e-4 | 230 | 5 | 29.12 | 0.28 | 0.81 | 31.04/151.22 | 0.00 | 9.71 |
| | R05 | T = 4 s | 0.364 (9.75/25) | 1.32e-1 | 230 | 12 | 15.31 | 0.22 | 0.75 | 30.26/150.23 | 0.46 | 0.60 |
| **T102.G1** *varied $R_f$* | R06 | $R_f$ = 0.7 | 0.15 (9.75/65) | 3.36e-2 | 230 | 7 | 22.62 | 0.27 | 0.78 | 31.39/149.62 | 0.04 | 3.21 |
| | R07 | $R_f$ = 0.4 | 0.15 (9.75/65) | 3.25e-2 | 230 | 7 | 22.95 | 0.24 | 0.78 | 32.70/149.62 | 0.04 | 2.93 |
| **T103.G1** *varied T, but R/L constant* | R08 | T = 14 s | 0.15 (22.65/151) | 4.43e-3 | 1250 | 9 | 18.09 | 0.35 | 0.74 | 31.42/148.48 | 0.01 | 0.59 |
| | R09 | T = 28 s | 0.15 46.95/313) | 1.34e-3 | 5314 | 11 | 16.14 | 0.29 | 0.74 | 31.23/149.73 | 0.00 | 0.39 |
| | R10 | T = 56 s | 0.15 (94.65/631) | 5.48e-4 | 17383 | 9 | 16.61 | 0.25 | 0.74 | 30.96/150.49 | 0.00 | 0.29 |
| | R11 | T = 4 s | 0.15 (3.75/25) | 4.96e-2 | 35 | 7 | 23.83 | 0.40 | 0.80 | 34.82/145.82 | 0.31 | 5.15 |
| **T105.G1** *varied R* | R16 | R = 2·R1 | 0.30 (19.50/65) | 3.44e-2 | 916 | 12 | 15.32 | 0.22 | 0.76 | 29.74/150.26 | 0.07 | 0.33 |
| | R17 | R = 4·R1 | 0.60 (39/65) | 1.94e-2 | 3691 | 19 | 10.22 | 0.25 | 0.66 | 29.83/149.48 | 0.08 | 0.07 |
| | R18 | R = ½ R1 | 0.075 (4.88/65) | 2.14e-2 | 58 | 6 | 26.92 | 0.31 | 0.79 | 31.27/149.21 | 0.04 | 9.45 |
| | R19 | R = ¼ R1 | 0.038 (2.44/65) | 3.80e-3 | 17 | 5 | 30.73 | 0.23 | 0.82 | 30.42/151.59 | 0.05 | 13.52 |

## Intermediate findings case G1

Overall, the SWDD method is able to detect the wave directional components in all runs R01.G1 - R19.G1 accurately – considering the proposed accuracy limits – with a maximum reconstruction error of 0.46% inside the array setup.

In test **T101.G1**, where the wavelength is varied (and thus the parameter $R/L$ is varied: 0.016 - 0.364), it becomes clear that for higher values of $R/L$ the results get more accurate for a regular bathymetry and number of gauges considering the reconstruction error on the large domain.

Test **T102.G1** shows that the SWDD method has no problems with analysing reflecting wave components containing lower amplitudes, respectively 70% and 40% (for a wave incidence of 30°).

In test **T103.G1** it becomes clear that, in contradiction to test T103 in testcases E and F, the reconstruction errors are influenced when the $R/L$ value is kept constant for varying wavelengths. Which is the case due to the constant grid used in the WIHA computations (containing 14 NPWL considering the shortest wave tested of 25.0 m), where for larger radius values of the array setup, more grid nodes are present and the reconstruction errors gets lower.

Test **T105.G1** shows that a larger radius (containing more grid nodes) for a constant wavelength, gives more accurate results considering the reconstruction error on the large domain. When the radius is varied, the following range of applicability is found: $R/L \geq 0.038$ ($R/L$ is tested between 0.029 and 2.40).

## Case G2: diffraction

The second case has a rectangular domain with dimensions of 3000 x 600 m. The bathymetry is constant at -13.00 m. A triangular grid is solved using the finite element method with 14 nodes per wavelength. The South boundary is the incoming wave boundary where the incoming monochromatic wave has a wave height of 1.00 m and wave direction of 150°. The North boundary exists among others of a 100% reflective quay wall of three wavelengths long in the centre *(1500-1.50L ≤ x ≤ 1500+1.50L)*. All the remaining boundaries (left and right from the reflective wall, East and West) exist of incoming wave (open) boundaries as well. The computed domain can be seen in Figure 35. And just like in case E1, an additional test (T107.G1) has been performed to check the sensitivity of the SWDD method to the distant of the location of the centre of the array setup to the

diffraction source (because in T101.G1 - T105.G1 the value $L/R_c$ is constant). In this test $R_c$ varies from $2L$ to $0.15L$. The obtained results are presented in Figure 36 and appendix O.
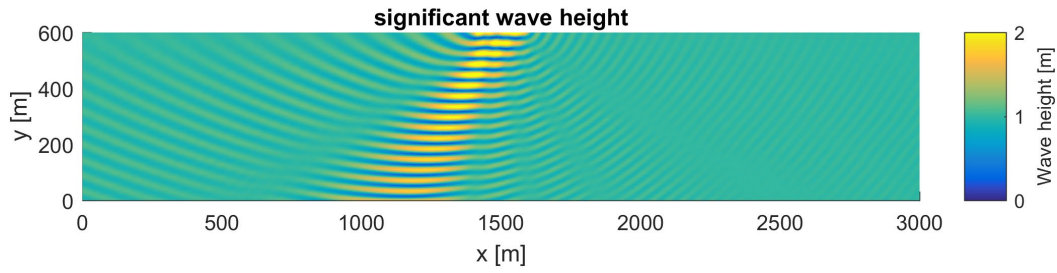


Figure 35: Presents the significant wave height output of WIHA for case G2 run R01
computed on a regular bathymetry of -13.00 m where the centre of the dense array setup lays on: [1406,555].

Table 14 presents the most important characteristics from the obtained polar plots of the SWDD analysis for case G2 where wave diffraction is present and WIHA model results are used as input in the SWDD analysis.

Table 14: The SWDD results for the different tests for case G2 where the most important characteristics of the presented polar plots are summarized quantitatively, with a wave curvature of 0.66 ($L/R_c$).

| Test | Run | Description | $\frac{R}{L}$ | $\lambda$ | N | No. of lobes | Width ML [°] | $\rho_{lobe}$ $\left(\frac{a_{maxSL}}{a_{ML}}\right)$ | Inh. curv. ang. $R/R_c$ | Dir [°] | Error $\varepsilon_{recon, inside}$ [%] | Error $\varepsilon_{recon, large}$ [%] |
|---|---|---|---|---|---|---|---|---|---|---|---|---|
| **T101.G2** *varied T* | R01 | T = 7 s | 0.15 (9.75/65) | 3.40e-2 | 235 | 7 | 23.15 | 0.27 | 0.100 | 33.40/149.11 | 0.05 | 3.24 |
| | R02 | T = 14 s | 0.067 (9.75/151) | 1.88e-3 | 236 | 6 | 22.37 | 0.33 | 0.045 | 27.36/150.89 | 0.01 | 5.95 |
| | R03 | T = 28 s | 0.033 (9.75/313) | 1.58e-3 | 235 | 6 | 27.97 | 0.39 | 0.022 | 27.80/150.21 | 0.00 | 11.18 |
| | R04 | T = 56 s | 0.016 (9.75/631) | 2.22e-4 | 232 | 6 | 26.56 | 0.41 | 0.010 | 26.30/152.83 | 0.00 | 11.36 |
| | R05 | T = 4 s | 0.364 (9.75/25) | 1.41e-1 | 232 | 11 | 16.37 | 0.24 | 0.243 | 30.73/150.82 | 0.47 | 0.61 |
| **T102.G2** *varied $R_f$* | R06 | $R_f$ = 0.7 | 0.15 (9.75/65) | 3.33e-2 | 235 | 7 | 23.06 | 0.26 | 0.100 | 33.90/149.11 | 0.04 | 2.79 |
| | R07 | $R_f$ = 0.4 | 0.15 (9.75/65) | 3.27e-2 | 235 | 7 | 23.16 | 0.23 | 0.100 | 34.18/149.88 | 0.04 | 2.54 |
| **T103.G2** *varied T, but R/L constant* | R08 | T = 14 s | 0.15 (22.65/151) | 3.84e-3 | 1263 | 9 | 17.43 | 0.43 | 0.100 | 32.46/149.01 | 0.01 | 0.49 |
| | R09 | T = 28 s | 0.15 46.95/313) | 1.28e-3 | 5365 | 11 | 15.75 | 0.28 | 0.100 | 30.22/149.74 | 0.00 | 0.35 |
| | R10 | T = 56 s | 0.15 (94.65/631) | 2.37e-4 | 17336 | 12 | 14.41 | 0.34 | 0.100 | 31.26/149.27 | 0.00 | 0.11 |
| | R11 | T = 4 s | 0.15 (3.75/25) | 1.07e-1 | 34 | 6 | 26.14 | 0.31 | 0.100 | 31.44/148.33 | 0.35 | 8.96 |
| **T105.G2** *varied R* | R16 | R = 2·R1 | 0.30 (19.50/65) | 3.31e-2 | 921 | 12 | 15.38 | 0.22 | 0.200 | 31.27/150.24 | 0.07 | 0.34 |
| | R17 | R = 4·R1 | 0.60 (39/65) | 2.47e-2 | 3728 | 15 | 11.01 | 0.23 | 0.400 | 30.79/149.83 | 0.08 | 0.81 |
| | R18 | R = ½ R1 | 0.075 (4.88/65) | 1.94e-2 | 60 | 5 | 29.57 | 0.28 | 0.050 | 33.86/151.80 | 0.05 | 10.81 |
| | R19 | R = ¼ R1 | 0.038 (2.44/65) | 1.77e-2 | 15 | 4 | 39.13 | 0.28 | 0.025 | 33.41/157.40 | 0.05 | 27.93 |

Figure 36 below displays the results of T107.G2, where $R_c$ is varied from $2L$ to $0.15L$ and the other parameters are kept constant.
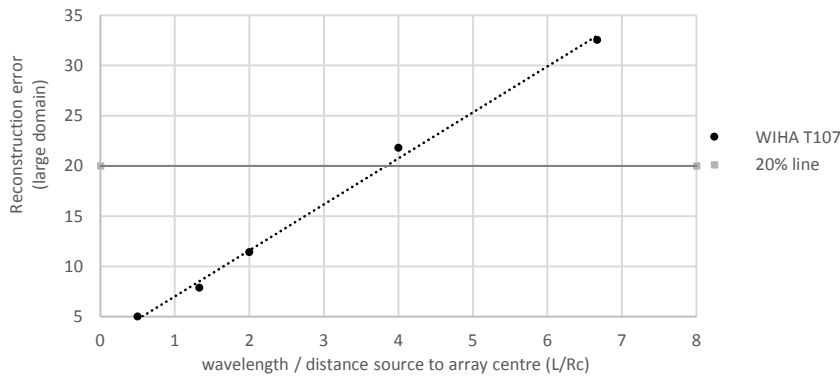


Figure 36: Displays the results of T107.G2, where the distant of the array centre is lowered step-by-step. The reconstruction error is plotted against the inhomogeneity value representing the diffraction: $L/R_c$.

### Intermediate findings case G2

Overall, the SWDD method is able to detect the wave directional components in all runs R01.G2 - R19.G2 accurately – considering the proposed accuracy limits – with a maximum reconstruction error of 0.47% inside the array setup. When the reconstruction error on the large domain is considered, R19 is inaccurate. When the inhomogeneity value of wave-crest curvature in the array setup gets higher, the errors get lower (due to increasing radius of the array setup for higher inhomogeneity values). However it can also be concluded that according to this trend, the SWDD method has no problems with analysing wave-crest curvature effects, especially for larger radius values when more wave information is present.

In test **T101.G2**, where the wavelength is varied (and thus the parameter $R/L$ is varied: 0.016 - 0.364), it becomes clear that for higher values of $R/L$ the results get more accurate for a regular bathymetry considering the reconstruction error on the large domain.

Test **T102.G2** shows that the SWDD method has no problems with analysing reflecting wave components with lower amplitudes, respectively 70% and 40% (for a wave incidence of 30°).

In test **T103.G2**, where the wavelength and the radius are varied ($R/L$ is kept constant at 0.15), it becomes clear that the reconstruction errors are influenced. Which is the case due to the fact that more grid nodes are present in the array setup for larger radius values, which gives lower reconstruction errors.

Test **T105.G2** shows that a larger radius (containing more grid nodes) for a constant wavelength, gives more accurate results considering the reconstruction error on the large domain. The following range of applicability is found: $R/L \geq 0.075$ ($R/L$ is tested between 0.038 and 2.40).

Test **T107.G2** (appendix O) shows that the SWDD results becomes accurate when the inhomogeneity value $L/R_c < 3.75$. Which means that the centre of the array configuration needs to be $0.30L$ away.

The **difference** between case G2 and G1 is due to the presence of diffraction in case G2, where it becomes clear that wave-crest curvature has a small influence on the results of the SWDD analysis. The reconstruction error on the large domain is on average 1.37 times higher when wave-crest curvature is present, especially considering low values of $R/L$. The $\lambda$-parameter, number of lobes and main lobe widths almost show no difference between case G2 and case G1.

### Case G3: non-homogeneous grid

The third case is computed with a non-homogeneous grid, where on every grid node a random number is added or subtracted in the bathymetry ($z = -13.00\ m$) with a standard deviation of 0.25 m. A triangular grid is solved using the finite element method with 14 nodes per wavelength. The South boundary is the incoming wave boundary where the incoming monochromatic wave has a wave height of 1.00 m and wave direction of 150°, the North boundary is the 100% reflective wall, which is a quay wall with a reflection coefficient of 1.00, the East boundary is a guiding wall with a reflection coefficient of 1.00 and the West boundary is a natural beach with a reflection coefficient of 0.00. The computed domain can be seen in Figure 37.
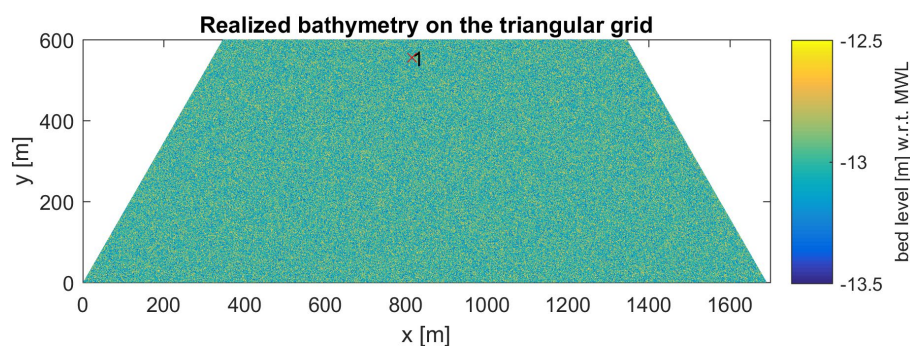


Figure 37: The realized bathymetry and the centre point of the dense array setup in case G3.

Table 15 presents the most important characteristics of the obtained polar plots from the SWDD analysis for case G3 where non-homogeneous grid nodes are implemented and WIHA output is used as input in SWDD.

Table 15: The SWDD results for the different tests for case G3 where the most important characteristics of the presented polar plots are summarized quantitatively.

| Test | Run | Descr-iption | $\dfrac{R}{L}$ | $\lambda$ | N | No. of lobes | Width ML [°] | $\rho_{lobe}$ $\left(\dfrac{a_{maxSL}}{a_{ML}}\right)$ | $\rho_{ML}$ $\left(\dfrac{A_{ML}}{A_{total}}\right)$ | Inh. bath. array $\Delta kd/\overline{kd}$ | Error $\varepsilon_{recon,\ inside}$ [%] | Error $\varepsilon_{recon,\ large}$ [%] |
|---|---|---|---|---|---|---|---|---|---|---|---|---|
| **T101.G3** *varied T* | R01 | T = 7 s | 0.15 (9.75/65) | 1.86e-1 | 230 | 7 | 25.17 | 0.34 | 0.87 | 0.05 | 0.13 | 5.84 |
|  | R02 | T = 14 s | 0.067 (9.75/151) | 4.85e-2 | 230 | 4 | 36.92 | 0.25 | 0.88 | 0.04 | 0.02 | 12.73 |
|  | R03 | T = 28 s | 0.033 (9.75/313) | 8.15 -3 | 230 | 5 | 29.58 | 0.33 | 0.71 | 0.04 | 0.09 | 16.94 |
|  | R04 | T = 56 s | 0.016 (9.75/631) | 1.29e-2 | 230 | 2 | 53.70 | - | 1.00 | 0.04 | 0.01 | 29.09 |
|  | R05 | T = 4 s | 0.364 (9.75/25) | 1.42 -1 | 230 | 12 | 15.32 | 0.22 | 0.77 | 0.07 | 0.47 | 0.62 |
| **T102.G3** *varied $R_f$* | R06 | $R_f$ = 0.7 | 0.15 (9.75/65) | 1.76e-1 | 230 | 7 | 25.04 | 0.31 | 0.79 | 0.05 | 0.11 | 5.03 |
|  | R07 | $R_f$ = 0.4 | 0.15 (9.75/65) | 1.59e-1 | 230 | 6 | 25.55 | 0.26 | 0.80 | 0.05 | 0.10 | 4.53 |
| **T103.G3** *varied T, but* R/L *constant* | R08 | T = 14 s | 0.15 (22.65/151) | 7.07e-2 | 1258 | 7 | 20.42 | 0.23 | 0.86 | 0.05 | 0.03 | 3.11 |
|  | R09 | T = 28 s | 0.15 46.95/313) | 2.72e-2 | 5345 | 9 | 19.39 | 0.28 | 0.68 | 0.05 | 0.02 | 2.33 |
|  | R10 | T = 56 s | 0.15 (94.65/631) | 3.02e-2 | 17343 | 8 | 19.80 | 0.35 | 0.70 | 0.06 | 0.01 | 2.58 |
|  | R11 | T = 4 s | 0.15 (3.75/25) | 6.36e-2 | 37 | 6 | 26.59 | 0.28 | 0.77 | 0.04 | 0.32 | 9.12 |
| **T105.G3** *varied R* | R16 | R = 2·R1 | 0.30 (19.50/65) | 2.37e-1 | 934 | 10 | 18.34 | 0.24 | 0.82 | 0.06 | 0.15 | 1.18 |
|  | R17 | R = 4·R1 | 0.60 (39/65) | 1.46e-1 | 3710 | 17 | 11.24 | 0.24 | 0.66 | 0.07 | 0.14 | 0.14 |
|  | R18 | R = ½ R1 | 0.075 (4.88/65) | 6.98e-2 | 62 | 5 | 30.25 | 0.26 | 0.84 | 0.04 | 0.13 | 13.08 |
|  | R19 | R = ¼ R1 | 0.038 (2.44/65) | 4.41e-2 | 14 | 3 | 45.39 | 0.32 | 0.91 | 0.03 | 0.14 | 32.05 |

### Intermediate findings case G3

In case G3 the inhomogeneity in the bathymetry ($\Delta kd/\overline{kd}$) within the array setup varies between 0.03 and 0.07. The SWDD method is able to detect the wave directional components in all runs R01.G3 - R19.G3 accurately with a maximum reconstruction error of 0.47% inside the array setup considering the proposed accuracy limits. When the reconstruction error on the large domain is considered, R04 and R19 are inaccurate. In test **T101.G3**, where the wavelength is varied (and thus the parameter $R/L$ is varied: 0.016 - 0.364), it becomes clear that for higher values of $R/L$ the results get more accurate for a regular bathymetry considering the reconstruction error on the large domain.

In test **T103.G3**, where the wavelength and the radius are varied ($R/L$ is kept constant at 0.15), it becomes clear that the reconstruction errors get lower when more gauges are present.

Test **T105.G3** shows that a larger radius (containing more grid nodes) for a constant wavelength, gives more accurate results considering the reconstruction error on the large domain. The value $R/L$ is tested between 0.038 and 2.40, where the following range of applicability comes forward: $R/L \geq 0.075$.

The **difference** in the results of case G3 and G1 is due to the presence of inhomogeneity in the bathymetry in case G3, where it becomes clear that the implemented inhomogeneity has a negative influence on the results of the SWDD analysis. The reconstruction error is on average 1.61 times larger inside the array setup (however still negligible). The reconstruction error on the large domain is on average 2.13 times higher when the inhomogeneity in the bathymetry is present, especially considering low values of $R/L$. The $\lambda$-parameter is on average 10e1 larger, the average number of lobes is 1.19 times lower and the main lobe width is on average 1.19 times wider all when inhomogeneity in the bathymetry is present (case G3).

### Case G4: slope

In the fourth and last case a slope has been added in the last 100 m (*y-axis*) of the domain. The first 500 m (*y-axis*) the bathymetry is kept constant at -13.00 m. A triangular grid is solved using the finite element method with 14 nodes per wavelength. The South boundary is the incoming wave boundary where the incoming monochromatic wave has a wave height of 1.00 m and wave direction of 150°, the North boundary is the 100% reflective wall, which is a quay wall with a reflection coefficient of 1.00, the East boundary is a guiding wall with a reflection coefficient of 1.00 and the West boundary is a natural beach with a reflection coefficient of 0.00. Figure 38 displays the realized domain for case G4. An inhomogeneity value is introduced for the representation of the inhomogeneity of the slope by: $\Delta kd/\overline{kd}$.
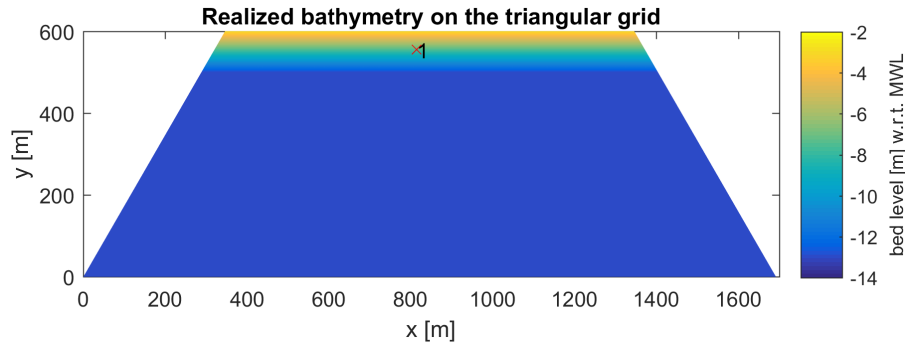
Figure 38: The realized bathymetry and the centre point of the dense array setup in case G4.

Table 16 presents the most important characteristics of the obtained polar plots from the SWDD method for case G4 where a slope is introduced and WIHA model results are used as input in the SWDD analysis.

Table 16: The SWDD results for the different tests for case G4 where the most important characteristics of the presented polar plots are summarized quantitatively. The shallow water region is reached for T ≥ 28 s.

| Test | Run | Descr-iption | $\frac{R}{L}$ | $\lambda$ | N | No. of lobes | Width ML [°] | $\rho_{lobe}$ $\left(\frac{a_{maxSL}}{a_{ML}}\right)$ | $\rho_{ML}$ $\left(\frac{A_{ML}}{A_{total}}\right)$ | Inh. bath. array $\Delta kd/\overline{kd}$ | Error $\varepsilon_{recon,\,inside}$ [%] | Error $\varepsilon_{recon,\,large}$ [%] |
|---|---|---|---|---|---|---|---|---|---|---|---|---|
| **T101.G4** *varied T* | R01 | T = 7 s | 0.18 (9.75/55) | 3.81e -1 | 230 | 6 | 25.66 | 0.40 | 0.74 | 0.16 | 0.65 | 12.83 |
| | R02 | T = 14 s | 0.08 (9.75/121) | 1.26e-1 | 230 | 5 | 28.82 | 0.49 | 0.70 | 0.14 | 0.26 | 32.59 |
| | R03 | T = 28 s | 0.04 (9.75/246) | 1.74e-1 | 230 | 4 | 41.96 | 0.24 | 0.89 | 0.13 | 0.37 | 32.91 |
| | R04 | T = 56 s | 0.02 (9.75/495) | 6.46e-2 | 230 | 2 | 53.82 | - | 1.00 | 0.13 | 0.05 | 29.60 |
| | R05 | T = 4 s | 0.41 (9.75/24) | 5.30e-1 | 230 | 10 | 17.32 | 0.31 | 0.76 | 0.22 | 0.90 | 1.48 |
| **T102.G4** *varied R_f* | R06 | $R_f$ = 0.7 | 0.18 (9.75/55) | 3.80e-1 | 230 | 6 | 26.35 | 0.34 | 0.77 | 0.16 | 0.56 | 9.83 |
| | R07 | $R_f$ = 0.4 | 0.18 (9.75/55) | 4.25e-1 | 230 | 6 | 27.60 | 0.26 | 0.78 | 0.16 | 0.50 | 8.78 |
| **T103.G4** *varied T, but* R/L *constant* | R08 | T = 14 s | 0.19 (22.99/121) | 2.19 | 786 | 5 | 27.51 | 0.24 | 0.88 | 0.32 | 2.73 | 29.87 |
| | R09 | T = 28 s | 0.19 (46.74/246) | 8.51 | 3310 | 5 | 36.07 | 0.38 | 0.77 | 0.66 | 6.81 | 26.78 |
| | R10 | T = 56 s | 0.18 (94.65/495) | 13.58 | 11671 | 4 | 32.77 | 0.52 | 0.90 | 0.68 | 5.56 | 34.09 |
| | R11 | T = 4 s | 0.15 (3.60/24) | 3.36e-2 | 33 | 7 | 23.20 | 0.33 | 0.71 | 0.03 | 0.38 | 6.00 |
| **T105.G4** *varied R* **for** **T = 28 s** | R16 | R = 2·R1 | 0.29 (71.34/246) | 30.21 | 11560 | 5 | 31.57 | 0.39 | 0.74 | 0.67 | 9.36 | 22.30 |
| | R17 | R = 4·R1 | 0.54 (132.84/246) | 54.71 | 37061 | 6 | 24.39 | 0.34 | 0.93 | 0.61 | 9.91 | 9.91 |
| | R18 | R = ½ R1 | 0.08 (19.68/246) | 1.15 | 820 | 4 | 51.01 | 0.21 | 0.92 | 0.25 | 1.43 | 31.98 |
| | R19 | R = ¼ R1 | 0.04 (9.84/246) | 0.15 | 208 | 4 | 50.84 | 0.22 | 0.91 | 0.12 | 0.37 | 33.38 |

### Intermediate findings case G4

**Overall**, it becomes clear that a slope has a large influence on the accuracy of the SWDD method, especially when the shallow water region is reached *(kd < 0.30)* and the inhomogeneity value of the slope $\Delta kd/\overline{kd} > 0.25$. Because, the SWDD method assumes a constant wave number value, i.e. linear waves over a uniform bottom. In case G4, the waves start to feel the bottom for waves containing a period of 14 s or higher and reach the shallow water zone for waves with a period of 28 s or higher, determined at the centre of the array setup. Considering the reconstruction error only inside the array, R08, R09, R10, R16 and R17 are inaccurate. The inhomogeneity value for the bathymetry within the array ($\Delta kd/\overline{kd}$) and both reconstruction errors are not showing unilateral behaviour, which is the case due to many effects, among others: shoaling, refraction and varying of the *kd*-value.

In test **T101.G4**, where the wavelength is varied (and thus the parameter $R/L$ is varied: 0.016 - 0.364), the lower wavelengths are not influenced by the slope, which is why the results did become more accurate for lower periods considering the reconstruction error on the large domain.

In test **T103.G4**, where the wavelength and the radius are varied ($R/L$ is kept constant at 0.15), it becomes clear that the runs for which the slope is 'felt' (R08 - R10) did become inaccurate. The larger the radius, the larger the inhomogeneity ($\Delta kd/\overline{kd}$), the higher the reconstruction errors (only R10 did not follow this trend, which is explained due to the fact that half of the array is on the regular bathymetry).

Test **T105.G4** seems to indicate that the SWDD method has problems with analysing data obtained from gauges laying on a slope in the shallow water region. According to the reconstruction errors R16 - R19 are analysed inaccurately, which means in this test no range of applicability can be assigned. Both reconstruction errors show different trends. According to the reconstruction error on the large domain the results get more accurate for higher radius values. While, for the reconstruction error inside the array setup the results get more accurate for lower radius values. Just like the SWDD method, the reconstruction error assumes a constant wave number, which may be the reason for the different trends. The main lobe width is also not considered the representative value, because due to the slope lots of refraction and shoaling effects are present, increasing the lobe widths. Considering the $\lambda$-parameter it seems the case that lower $R/L$ values are more trustworthy: $0.10 \leq R/L \leq 0.20$.

The **difference** between case G4 and G1 is due to the presence of inhomogeneity in the bathymetry (slope) in case G4, where it becomes clear that the implemented slope has a negative influence on the results of the SWDD analysis. The reconstruction error on the large domain is on average 5.10 times higher when the slope is present, especially considering low values of $R/L$. The $\lambda$-parameter is on average 10e2.5 larger, the average number of lobes is 1.38 times lower and the main lobe width is on average 1.37 times wider all when the slope is present.

### Overall correlated characteristics in testcase G

Several parameters and characteristics show correlated behaviour between the reconstruction error on the large domain. The correlations **(per test considered)** between the main lobe width and the reconstruction error on the large domain are displayed in Table 17. Where the **mean** correlation (based on all the correlations per test for one specific case) between the reconstruction error on the large domain and the main lobe width is 0.92.

Table 17: Correlations per test between characteristics and the reconstruction for cases G1 - G4.

| Test | Width ML [°] | | | |
|---|---|---|---|---|
| | $Corr(Width\ ML, \varepsilon_{recon,large})$ case G1 | $Corr(Width\ ML, \varepsilon_{recon,large})$ case G2 | $Corr(Width\ ML, \varepsilon_{recon,large})$ case G3 | $Corr(Width\ ML, \varepsilon_{recon,large})$ case G4 |
| **T101** | 0.96 | 0.92 | 0.82 | 0.74 |
| **T103** | 0.98 | 0.98 | 0.99 | 0.78 |
| **T105** | 0.97 | 0.95 | 0.98 | 0.96 |
| **Mean Corr.** | 0.92 | | | |

A (correlation) plot of the main lobe width and the reconstruction error on the large domain for the complete cases G1 - G4 (not per test considered) is displayed in Figure 39.
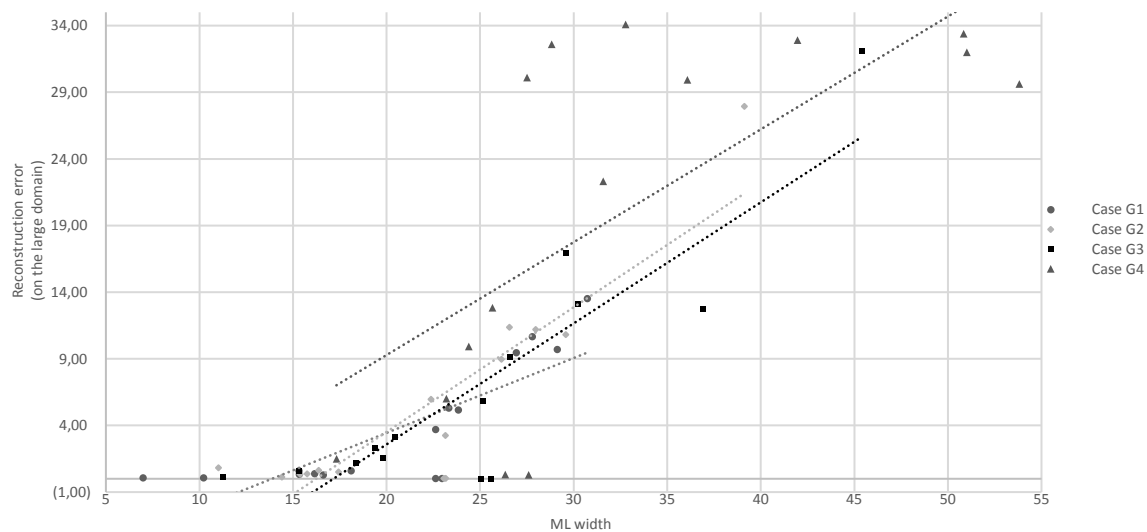


Figure 39: Correlation plots between the reconstruction error on the large domain
and the width of the main lobe for cases G1 - G4.

The found correlation between the main lobe width and reconstruction error on the large domain in case G1 is 0.85, case G2 is 0.89, case G3 is 0.88 and case G4 is 0.70.It also comes forward that the inhomogeneity of the bathymetry and the reconstruction error inside the array setup has a correlation of 0.95, where the plot is presented in appendix J. Remaining correlation plots between several characteristics are treated in appendix J as well.

## 5.3.2 Conclusions sensitivity analysis SWDD method using WIHA output

The SWDD method is able to detect incoming and reflective wave components – both considering an angle of 30° – using the output of the mild-slope wave model WIHA. If both diffraction effects and a slope are **not** present (approximately: $\Delta kd/\overline{kd} < 0.25$), all the results are computed accurately by the SWDD method considering the chosen accuracy limits of 2% for the reconstruction error inside the array setup and 20% for the reconstruction error on the large domain. And, the more grid nodes in the array configuration and larger the radius of the dense array setup ($R/L$ has been tested up to 2.40), the more accurate the results become.

When either diffraction (for $L/R_c < 0.66$) or a 'bumpy' bathymetry is present (no slope) the results of SWDD are minimally influenced mainly for smaller values of $R/L$ ($\leq 0.038$). In the test where the value $L/R_c$ has been varied, it came forward that the results get inaccurate for array configurations where the centre was placed < $0.30L$ to the diffraction source containing high effects of diffraction.

When a slope is present – containing high gradients ($\Delta kd/\overline{kd} > 0.25$) and the $kd$ value at the centre of the array configuration is relatively low (< 0.50) – the wavenumber, phase-velocity and the wave profile changes as a result of shoaling and refraction effects. Therefore, lower values for the radius of the array configuration are advised: $0.10 \leq R/L \leq 0.20$. The SWDD analysis uses the most 'relevant' information in the Tikhonov regularization, it seems when adding a part of regular bathymetry, the results get more accurate.

## 5.4 Comparison of the SWDD method to other directional wave-analysis methods

This section contains a comparison study with the SWDD method and other directional wave-analysis methods. First, the deterministic method, r-DPRA (de Jong and Borsboom, 2012) is considered. Second, often used stochastic methods, respectively BDM *(Bayesian directional method)* and MLM *(Maximum Likelihood Method)* are compared. And finally, an intermediate conclusion is presented which covers the findings of the comparison study. A short comparison between the SWDD method and the MEM *(Maximum Entropy Method)* method is presented in appendix N, where multiple spectra are obtained from four GRSM output locations in the earlier treated navigation channel case in section 4.2.

### 5.4.1 Comparison with the r-DPRA method

The comparison with the deterministic r-DPRA method uses a written MATLAB **variant** (thus not an exact copy of the original model) based on the article about r-DPRA from de Jong and Borsboom (2012) and consists of two parts, respectively the first part where synthetic wave signals are prescribed and the second part where a side basin containing many reflecting components is computed by WIHA and the model results are used to perform a directional wave-analysis by SWDD. An accuracy limit of 2.50° for the direction and 0.10 m for the wave amplitude is used in the comparison tests below.

#### Comparison between SWDD and r-DPRA using synthetic wave signals

The first comparison test between SWDD and r-DPRA considers a dense array setup containing 70 gauges and a radius of *0.15L* (30 nodes per wavelength). Four plane waves computed in MATLAB with respectively 1.00, 0.50, 1.00 and 0.50 m wave amplitude and 0, 90, 180 and 270 degree incidence containing a standard deviation of the additional noise (only) in the complex amplitudes of 1.00e-4 are prescribed. Figure 40 displays the resulted polar plots from the SWDD analysis and the r-DPRA analysis for the first comparison test.
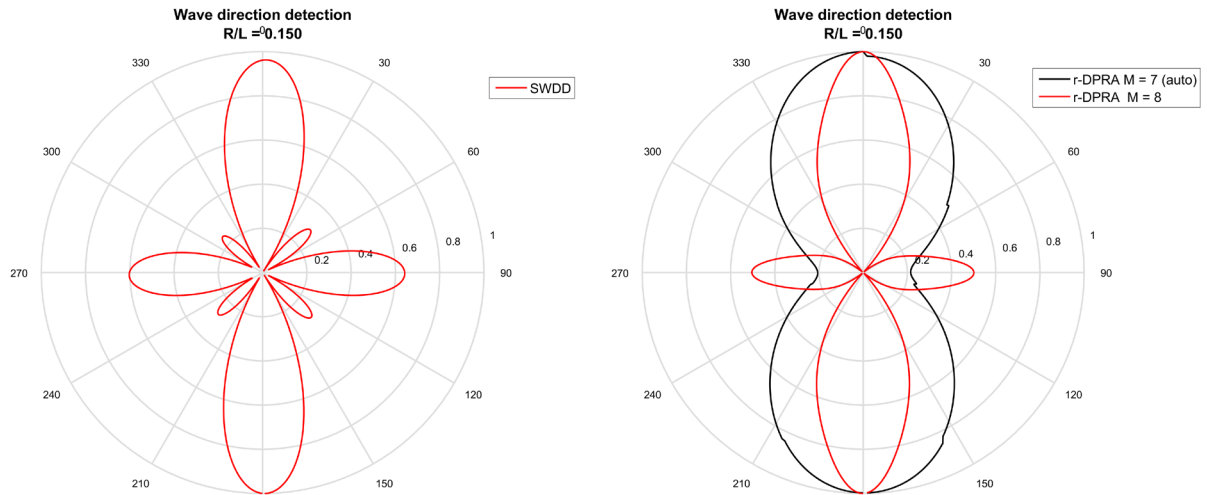
Figure 40: The polar plots obtained for the first comparison test between SWDD and r-DPRA where four monochromatic waves of respectively 1.00, 0.50, 1.00, 0.50 m wave amplitude, coming from 0°, 90°, 180° and 270° including noise in the complex amplitudes with a standard deviation of 1.00e-4 are prescribed. The left figure (a) presents the results by the SWDD method and the right figure (b) presents the results by the r-DPRA method.

The results from the first comparison test between SWDD and r-DPRA show that both methods are able to detect the prescribed wave signals accurately considering the proposed accuracy limits. However, the automatic detection method implemented in r-DPRA is not able to detect the different directional components, due to the low resolution. The SWDD method contains a mean direction error of 1.00° and a mean amplitude error of 0.025 m. The r-DPRA method contains a mean direction error of 0.25° and a mean amplitude error 0.005 m, for the number of directions **chosen by the user** (M = 8). The results by r-DPRA contain 17% wider main lobes, which is one of the reasons why for the solution using 8 directions no spurious side lobes are found.

The second comparison test between SWDD and r-DPRA considers the same dense array and prescribed waves. However, in this comparison test the standard deviation of the additional noise in the complex amplitude is lower: 1.00e-8. Figure 41 displays the resulted polar plot from the SWDD analyses for the second comparison test.
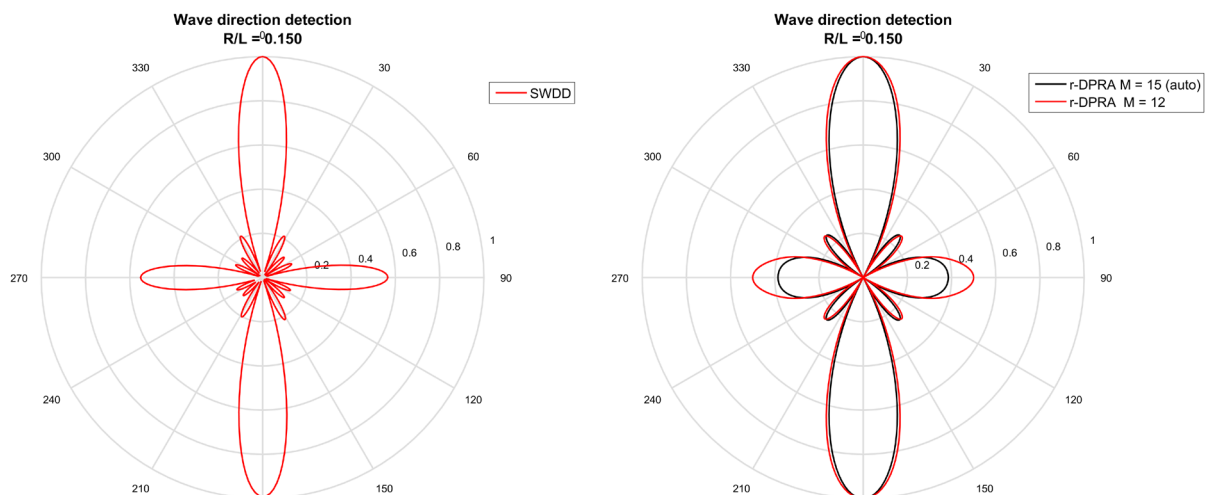


Figure 41: The polar plots obtained for the second comparison test between SWDD and r-DPRA where four monochromatic waves of respectively 1.00, 0.50, 1.00, 0.50 m wave amplitude, coming from 0°, 90°, 180° and 270° including noise in the complex amplitudes with a standard deviation of 1.00e-8 are prescribed. The left figure (a) presents the results by the SWDD method and the right figure (b) presents the results by the r-DPRA method.

The results from the second comparison test between SWDD and r-DPRA show that both methods are able to detect the prescribed directions accurately considering the proposed accuracy limits. The SWDD method contains a mean direction error of 0.50° and a mean amplitude error of 0.008 m. The r-DPRA method contains respectively a mean direction error of 0.30° and 0.80° and a mean amplitude error of 0.151 m and 0.005 m for the number of directions $M = 15$ (automatic number of directions) and $M = 12$ (number of directions chosen by the user). The results by r-DPRA contain 61% wider main lobes, which gives a lower resolution and explains the lower number of spurious side lobes.

### Side basin

The next comparison test between SWDD and r-DPRA considers a side basin where an oblique monochromatic wave enters a basin consisting of 100% reflective quay walls. The incoming wave incidence is 285° which creates a complex wave field containing many wave components. The incoming wave height and wave period are respectively 1.50 m and 15 s. Figure 42 displays the geometry, the bathymetry, the centre of the array setup (with a radius of $0.17L$ containing 181 gauges) and the by WIHA computed significant wave height.
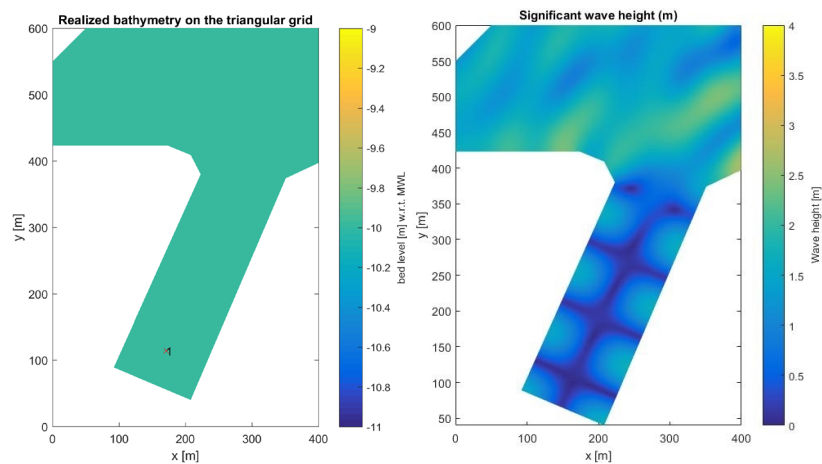


Figure 42: The bathymetry including the centre of the dense array setup containing 181 gauges (a) and the computed significant wave height by WIHA for the side basin case (b).

Figure 43 below displays the obtained polar plots for the side basin comparison test using respectively the SWDD method and the r-DPRA method.
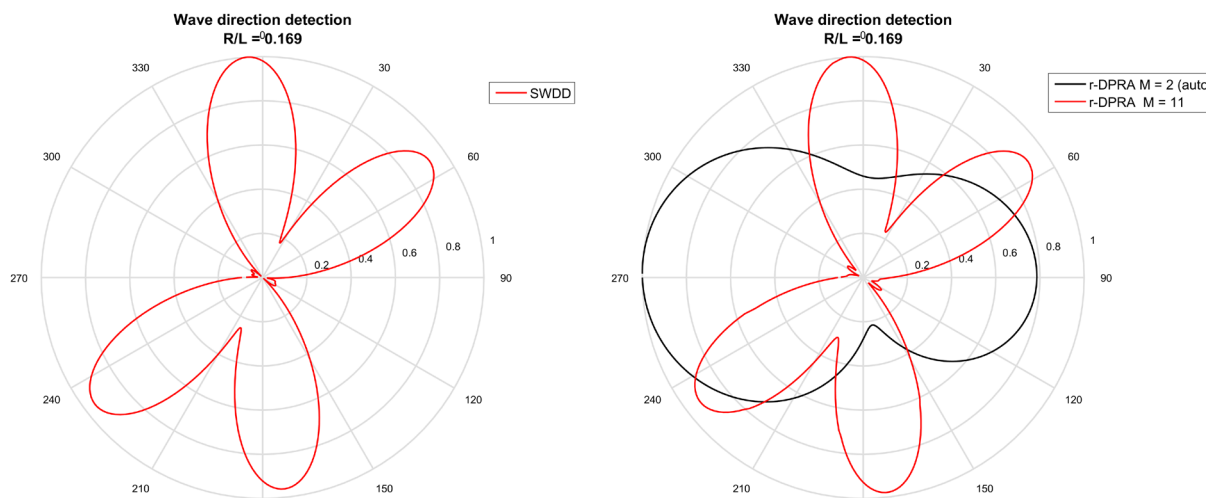


Figure 43: The polar plots obtained by respectively the SWDD method and the r-DPRA method for the side basin case.

The results from the second comparison test between SWDD and r-DPRA show that both methods are able to detect the complex wave components in the basin, where the SWDD method contains a reconstruction error of 0.43% inside the array setup and a reconstruction error of 0.77% on the large domain. In the r-DPRA method it is not possible to reconstruct the wavefield and determine a reconstruction error. Again, the automatic optimal number of analysis directions presents inaccurate results. The by the user chosen optimum number of wave directions show similar results to the SWDD method. However, it seem to contain a minimum difference of lower resolution whereas the main lobe width is on average 5% wider. Next to this, the calculation time for the SWDD analysis takes only 0.40 s, while for the r-DPRA method it takes 55 s.

### Intermediate findings comparison study between SWDD and r-DPRA

The main found differences between SWDD and r-DPRA are:
- r-DPRA has an uncertainty in the decision which resulted set (number of directions) is optimal, where it seems like the automated detection of optimal number of directions by the relative energy present is not always the 'best' solution to use.
- r-DPRA often uses a lower number of directions in the analysis, which results in wider main lobes and thus a lower directional resolution.
- The computational effort of the r-DPRA method is on average 100 - 200 times higher, e.g. to determine one dataset of Fourier complex amplitudes containing 230 gauges takes my MATLAB implementation of the r-DPRA method 80 s, While SWDD is able to compute this in 0.40 s.
- After a directional wave-analysis by r-DPRA, reconstruction of the wave field is not possible.

## 5.4.2 Comparison with the BDM and MLM methods

This section treats a comparison between the deterministic directional wave-analysis SWDD method and two stochastic methods, respectively BDM and MLM. For both stochastic methods, 2D spectra – unimodal and bimodal – are prescribed using time series created with an open source MATLAB script 3Dwaves_AUU (Jakobsen, 2015). BDM and MLM analyses the data from the gauges in the array setup, using the same script 3Dwaves_AUU, where after a 2D wave spectrum and polar rose plot are presented. In contradiction to the stochastic directional wave-analysis methods, the spectral input for the SWDD method is obtained by the mild-slope wave model WIHA. Considering the unimodal spectrum, two different array setups are used in the wave directional analyses, respectively a dense array setup and a CERC-6 array configuration (Figure 23c). Where after for the bimodal wave spectrum, the best considered array setup for each method from the unimodal wave spectral analyses is used. Each spectrum (the input as well) is analysed by obtaining the half-width at half maximum (HWHM, section 3.3.2 Figure 7) value from the concerning directional spectrum. The HWHM value is presented in percentage. An accuracy limit of 10% for the HWHM value is considered.

The incoming wave height is 1.00 m, the peak period 10 s, the main direction 270°, the standard deviation of the direction is 20° (s = 16 for the cos2s spreading) and the water depth is 10 m. Consecutively the spectral analyses by the SWDD method, BDM method, MLM method and the overall findings are treated.

### Spectral analysis by SWDD

The input wave spectra for the SWDD method are generated using the mild-slope wave model WIHA. Figure 44a displays the input of the frequency spectrum and Figure 44b displays the unimodal directional spectrum containing a HWHM value of 23.50°.
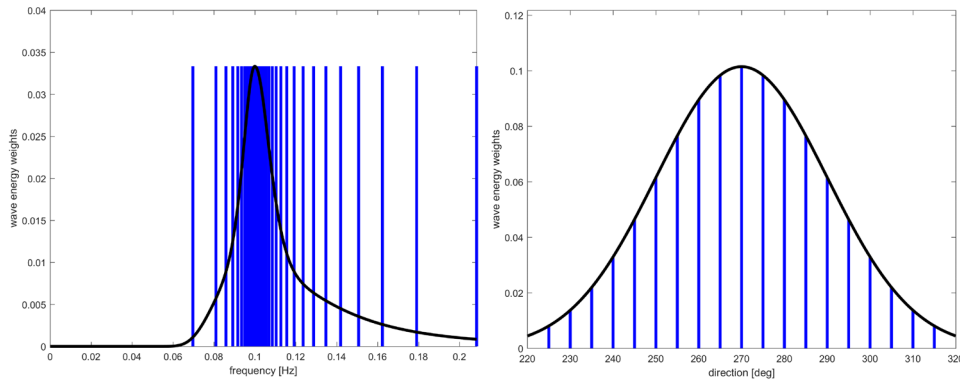
Figure 44: Respectively the frequency spectrum (a) and the direction spectrum (b) input, where the blue lines are the considered frequency's and directions (equal weight factors for the frequency and equally distribution of the direction).

The constructed wave spectrum by the SWDD analysis, using a dense grid with a radius of $0.50L_p$, is displayed in Figure 45 below.
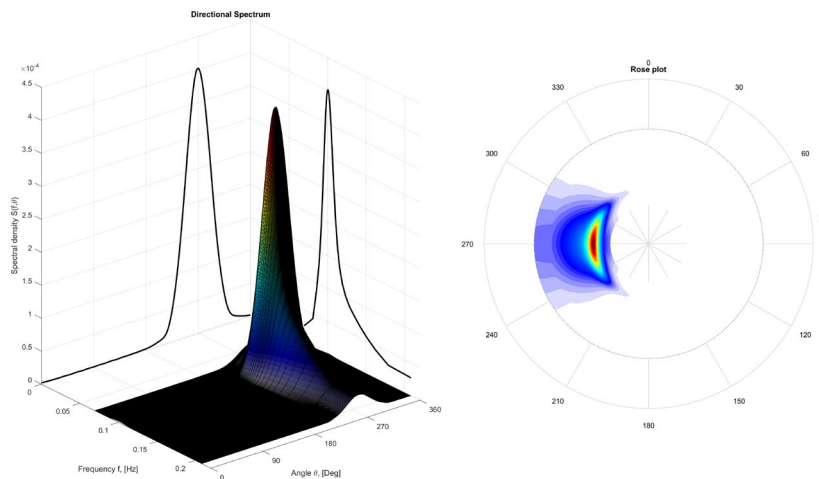


Figure 45: The obtained unimodal 2D wave spectrum (a) and polar rose plot (b) by the SWDD method using a dense array setup with $R = 0.50L_p$.

Considering the proposed accuracy limit, the obtained 2D wave spectrum using a dense grid with a radius of $0.50L_p$ is accurate containing a HWHM value of 25° and thus an error of 4.26%. In the tail of the frequency spectrum, the direction seems to be minimally overestimated. A possible cause can be that the radius of the array setup is too large for the higher frequency waves, because when an array setup containing a radius of $0.15L_p$ is used this effect is not present. However, for such array setups *(< R/$L_p$)* the HWHM value is overestimated (35%). Thus, it seems like an optimum can be determined, which is considered out of the scope of this study, but might be implemented in the recommendations.

The same spectral analysis using a CERC-6 array is computed less accurate by the SWDD method with an error of 65.96% in the HWHM value. The resulted plot can be found in appendix N.

The bimodal spectrum is analysed accurately by the SWDD method – using a dense array setup – containing an error of 9.79% in the HWHM value, displayed in Figure 46 below. The same overestimation of the direction for higher frequencies is present as for the unimodal spectrum, which presumably can be solved by using an optimum $R/L_p$ value.
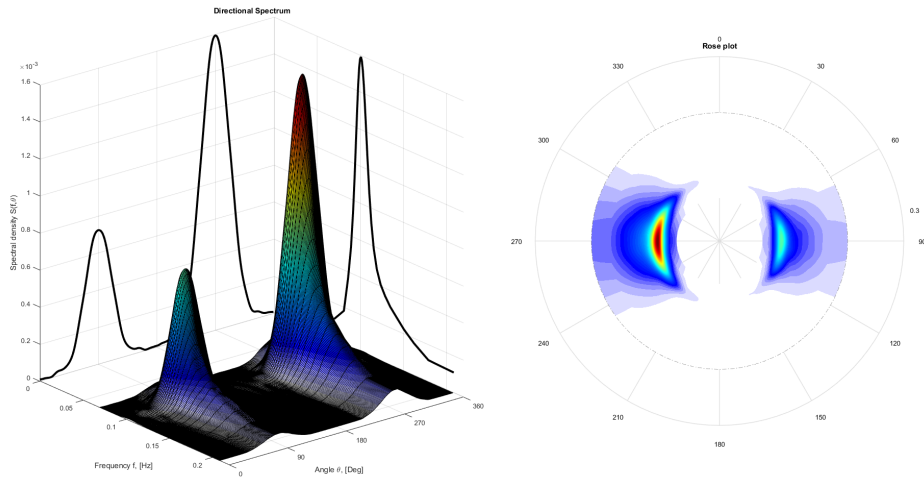
Figure 46: The obtained bimodal 2D wave spectrum (a) and polar rose plot (b)
by the SWDD method using a dense array setup with $R = 0.50L_p$.

#### Spectral analysis by BDM

The unimodal and bimodal wave spectra obtained by using the BDM directional wave-analysis method are presented in appendix N. Considering the proposed accuracy limit, the results show that using a CERC-6 array setup, both the unimodal and bimodal spectra are accurate containing an error of respectively 4.39% and 7.69%. However, the unimodal results contain non smooth peaks in the spectra. And the BDM method is not able to use a dense array setup to get to accurate results.

#### Spectral analysis by MLM

The unimodal and bimodal wave spectra obtained by using the MLM directional wave-analysis method are presented in appendix N as well. The results show that using a CERC-6 array setup, the unimodal spectrum is accurate containing an error of 3.47%. The bimodal spectrum is computed less accurate containing an error of 15.55%. Like BDM, the MLM method is not able to use the dense array setup to get to accurate results.

#### Intermediate findings comparison SWDD and MLM and BDM

All the obtained results of the spectral comparison analysis are summarized in Table 18.

Table 18: Summarizing the obtained error in the unimodal and bimodal spectral analyses with the SWDD, BDM and MLM method using various array setups. The symbol X stands for an unstable and inaccurate solution.

| Test | SWDD | | | BDM | | | MLM | | |
|---|---|---|---|---|---|---|---|---|---|
| | Unimodal | | Bimodal | Unimodal | | Bimodal | Unimodal | | Bimodal |
| | *Dense array* | *CERC-6 array* | *Dense array* | *Dense array* | *CERC-6 array* | *CERC-6 array* | *Dense array* | *CERC-6 array* | *CERC-6 array* |
| **Input** | 23.50 | 23.50 | 23.50 | 23.80 | 23.80 | 23.80 | 23.80 | 23.80 | 23.80 |
| **Output** | 25.00 | 39.00 | 25.80 | X | 22.80 | 22.10 | X | 23.00 | 27.50 |
| **Error [°]** | 1.50 | 15.50 | 2.30 | X | 1.00 | 1.70 | X | 0.80 | 3.70 |
| **Error [%]** | 4.26 | 65.96 | 9.79 | X | 4.39 | 7.69 | X | 3.47 | 15.55 |

It becomes clear that the SWDD method is designed for separation of monochromatic wave components considering both laboratorial and numerical array setups. When spectral input is considered, only the dense array configurations computes accurate results, while for the CERC-6 array setup the directional spectrum is overestimated by almost 66%.

In contradiction, the BDM and MLM methods are unable to analyse and separate multiple monochromatic waves and analyse results from a dense array setup. However, they produce accurate results for the CERC-6 array (i.e. laboratorial array configurations).

### 5.4.3 Overall conclusions SWDD comparison study

The SWDD method has among others been compared to the r-DPRA method (de Jong and Borsboom, 2012), where it becomes clear that the SWDD is a more easy to use and robust method, because it has a lower computation time, user checks are not needed and afterwards an error can be reconstructed if desired. Next to this, the SWDD method often contains less wide main lobes and thus a higher directional resolution.

The SWDD method has also been compared to the stochastic directional wave-analysis methods MLM and BDM. It becomes clear that stochastic methods are only able to analyse laboratorial array configurations (e.g. CERC-6) and are unable to analyse dense array setups. This is one of the reasons why the stochastic methods are unable to separate multiple monochromatic wave components from a considered wave field.

Contradictory, the SWDD method is mainly designed for the analysis of dense array configurations and to present the separated waves graphically in a polar plot. Spectral analyses are possible both for dense array configurations and laboratorial array configurations, however for the latter it seems like the directional spectrum is overestimated.

## 5.5 Conclusions SWDD experiments

The SWDD method successfully analysed multiple complex synthetic wave signals – containing wave amplitude variation and irregular wave directions close to each other – both with and without additional noise in the position of the gauges and in the complex amplitude. The results of the synthetic wave signals show that a lower $\lambda$-value presents smaller main lobes containing more spurious sidelobes (noise) and for higher $\lambda$-values the width of the main lobes gets wider and the spurious side lobes are less present (however, may present a poor fit). The results also show that using a larger radius (and higher number of gauges) the directional resolution and error both get lower. For radius values of the dense array configuration from $5L$ up to $10L$ a directional resolution of $3.50°$ becomes possible. When analysing measurement data the distinction capability is much lower, because of the limited amount of gauges (e.g. CERC-6), only a directional resolution of $40°$ up to $30°$ can be reached.

The results obtained by testing synthetic wave patterns (containing high wave-crest curvature and wave amplitude variation) and output from the mild-slope wave model WIHA (containing diffraction effects and irregular bathymetries) show that the SWDD method is sensitive for wave-crests containing high effects of curvature and irregular bathymetries (e.g. slopes). The first effect mainly has a large influence close to the source (*i. e.* $L/R_c > 1.00$) and the second effect has a large influence for steep slopes. The SWDD method assumes a constant wave number value, i.e. linear waves over a uniform bottom. When a slope is present – containing high gradients ($\Delta kd/\overline{kd} > 0.25$) and where the $kd$ value at the centre of the array configuration is relatively low ($< 0.50$) – the wavenumber, phase-velocity and the wave profile change and having shoaling and refraction effects. When non-homogenous effects are present a range of applicability for the radius of the array setup is advised: $0.10 \leq R/L \leq 0.30$. Within this range there is an accuracy limit for the directional error of $2.50°$ and for the reconstruction error inside the array setup of $2\%$.

In contrast to stochastic directional wave-analysis methods, the SWDD method is able to analyse dense array configurations and separate a high number of wave components. Next to this, it has been demonstrated that the SWDD method is able to produce 2D wave spectra at the output locations of the mild-slope wave model WIHA (both for an array containing few gauges and dense grids containing many gauges). However, using an array configuration containing few gauges (e.g. CERC-6), the directional spectrum is overestimated by $60\%$. The results from the comparison study between the SWDD method and the r-DPRA method (de Jong and Borsboom, 2012) show that the SWDD is a more easy to use and robust method, because it has a lower computation time, user checks are not needed and afterwards an error can be reconstructed if desired. Next to this, the SWDD method often contains less wide main lobes and thus a higher directional resolution.

# 6

# Discussion

The discussion links the study results to the research questions and interprets and describes the validity of the results obtained in Chapter 5. The first section treats the limitations, possible causes and consequences. The second section treats the link between the obtained results and the research questions. And the third section treats possible realistic scenarios for which the SWDD method might be used.

## 6.1 Validity of the results and possible limitations

Each performed sensitivity analysis from chapter 5 is treated to discuss the reliability of the results.

*Sensitivity analysis using synthetic testcases*
In the sensitivity analyses performed using synthetics testcases, the input and output were both known, which means that the obtained data and performed data analysis had a high reliability. A possible limitation might be argued:

- ▪ It can be questioned if the circular array setups used, containing 25 gauges, were the most relevant to test. While, in physical modelling often 5 - 15 gauges are used and in numerical modelling all the grid nodes within the dense circular array setup are used. However, as one of the first validations, this array setup gave a nice representation of the possibilities and weaknesses of the SWDD method.

*Sensitivity analysis using a wave source and wave dipole*
Overall, the validity of the results are considered valid. Possible limitations are described below:

- ▪ If the reconstruction error inside the array setup was below the chosen limit (< 2%), it did not necessarily mean the results were accurate. Where the complex amplitude output at the gauges were almost the same after the SWDD analysis, it still could be the case that from such data not enough information was available for the directional wave-analysis. Mainly for small $R/L$ values, because for such array setups the SWDD method modelled the incoming wave as a straight plane wave where not enough 'difference' in the phase was present to detect the wave accurately (which often came forward in the $\lambda$-parameter as well). To increase the reliability of the results the reconstruction error on the large domain was considered in each test performed as well.
- ▪ The reconstruction error on the large domain was reconstructed for each test on a domain of $L$ *by* $L$. Where it might be argued that a domain of one wavelength can be unfair to compare small array setup results of only a couple percent of the large domain to an array setup which covers almost the complete domain. However, it became clear that the large reconstruction error on a domain of $L$ *by* $L$ had a high correlation with various characteristics. Next to this, like described in the previous bullet, a low reconstruction error inside the array setup did not necessarily mean that the results were accurate. Where for some tests performed (especially $< R/L$ value) the reconstruction error inside the array setup was low, the obtained polar plot did not show a detected wave and the reconstruction error on the large domain indeed became high. Altogether, conclusions should not be made based only on the reconstruction error inside the array or only on the reconstruction error on the large domain, but both were considered to increase the reliability of the results.
- ▪ Both reconstruction errors were normalized with the maximum wave height. First, the standard deviation was determined of the complex numbers from each gauge in the considered domain, which

contained the amplitude and the phase. Where after the standard deviation was divided by the maximum surface-elevation and multiplied with 100%. Thus, the normalization did only consider the amplitude and not the phase. While, in the standard deviation the error in the phase was present as well. It can be argued that the standard deviation (non-normalized) would be a more relevant error, however than it would become harder to compare the different cases, because the amplitude did vary a lot between the Hankel wave source and dipole cases.

- In the testcase which made use of the Hankel function, the amplitude reduces further away from the source. In the cases considered, wave directional analyses were performed nearby the source ($2L$) and far away from the source ($80L$). Which means the amplitude at both array setups differed quite a lot, respectively 0.22 m and 0.05 m. In the optimal scenario both amplitudes did contain the same height. However, the SWDD method analyses the data proportional, thus most likely this would not make any difference.

- In the wave source cases, where wave-crest curvature effects were highly present ($2L$ from the source), larger $R/L$ values started to show many 'peaky' main lobes in the polar plots. This can be explained by the curvature of the wave crests, especially for larger radius values (where the SWDD method models the curvature as high directional spreading of many straight plane waves).
  It was difficult to indicate the number of lobes and width of the main lobes for such polar plots. In the results presented in this report, the 'peaky' effects were all considered as main lobes and the fitted parabolas were only performed on the peaks of such results. Which corresponds to the found expectations and correlations. It can be argued that the user does not want to obtain such results, however in first instance this was left open, because within this research the range of applicability was desired and such considerations could be added afterwards if desired. In the presented flowchart, the user interest has been taken into account.

- As a first indication, the following limits were chosen for the determination of the accuracy of respectively the error in the direction of 2.50°, the reconstruction error inside the array setup of 2% and the reconstruction error on the large domain of 20%. This was based on the obtained results and the main intended usage for the SWDD method on numerical modelling results. However, this value depends on the users interest as well, which of course can be adjusted depending on the users wishes.

*Sensitivity analysis using WIHA output*

The validity of the results obtained in the cases G1 - G3 are considered valid. In case G4 some limitations and uncertainties came forward. Further research considering a slope is advised, which is treated in the next chapter. Possible limitations are listed below:

- All the mentioned possible limitations, validity findings, possible causes and consequences discussed in the previous section, applies to this section as well.

- In the WIHA cases, the grid was kept constant for each run performed, based on 14 NPWL for the lowest wave period present in the analysis (4 s). It might be argued that the number of NPWL should be chosen constant for each run, however the current implementation is more realistic and more often used in practice.

- In case G4, where a 100 m steep slope (1:10) was considered, some runs did use larger array setups (containing information from a regular flat bathymetry as well), which lowers the reliability of the comparison between the tests mutually.

- The reconstruction errors in case G4 may be less reliable as well, due to: low $kd$ values inside the array setup (even up to shallow-water), high $\Delta kd/\overline{kd}$ within the array setup (wavenumber, phase-velocity and the wave profile changes because of the slope) having shoaling and refraction effects as a result. While, the SWDD method (and the reconstruction error) assumes a constant wave number value, i.e. linear waves over a uniform bottom. Next to this, the steeper the slope, the more reflection might be present. In sum, it looks like the optimal error is not yet found.
  However, from the data obtained it seems like the error inside the array setup gives the 'best' error indication of the parameters available (smaller area of reconstruction and high correlation between

the inhomogeneity value of the bathymetry). Which concludes an advise to use a radius within a range of applicability between: $0.10 < R/L < 0.30$, where the array setups were entirely on the slope and the described problems were relatively in a less extent present.

*Comparison of the SWDD method to other directional wave-analysis methods*

The preliminary comparison study gives an interesting first indication between the various methods. However, due to time limitations the comparison study between the stochastic directional wave-analysis method is only introductory. Possible limitations are:

- The comparison study between the SWDD method and the r-DPRA method made use of an own written MATLAB script based on de Jong and Borsboom (2012) of the r-DPRA method. So, not the official variant of this method has been used, which might contain small differences.
- The input for the spectral analyses performed by the SWDD method to reconstruct the 2D wave spectra were different from the input for the stochastic methods (BDM and MLM). Where the stochastic methods made use of time series, which uses Fourier coefficients, instead of complex amplitudes computed for each frequency and wave direction by SWDD. However, the expectation is that this difference is negligible.
- The overall reliability of the results could be improved by introducing more error values, e.g. the HWHM *(Half Width Half Maximum)* of the frequency spectrum and the minima and maximum for both the directional and frequency spectrum.

## 6.2 Link results to the research questions

The purpose of this study was to determine the range of applicability of the SWDD directional wave analysis method, with emphasis on the use for phase-resolving wave models (e.g. WIHA). To be able to present a clear overview and get to the final conclusions, the link between the results and the research questions are treated below. Finally, an overviewing advisory flowchart is presented to determine the optimum range for the radius of the array setup in a directional wave-analysis by the SWDD method using either numerical modelling input or measurement data input.

*What is the sensitivity of the SWDD method to the number of wave components and wave reflection?*

The SWDD method has been tested to analyse multiple reflective wave components, which all showed accurate results. For the tests performed with up to 4 wave components and 40% reflective amplitude height, SWDD shows no negative influences of reflection on its performance. The main finding in the study is that the maximum separation of the different wave components depends on the directional resolution which in turn depends on the array configuration. When analysing numerical modelling output of a dense grid on a regular bathymetry a directional resolution of 15.00° up to 10.00° considering a radius of 0.50 - 2.00$L$ is obtained. Using a radius of 2.00 - 10.00$L$ a directional resolution of 10.00° up to 5.00° is obtained. An example considering high oblique wave incidence on a reflective structure is treated in the next section (6.3).

When analysing measurement data, the distinction capability is much lower, because of the limited amount of gauges (< 20) only a directional resolution of approximately 40° up to 30° can be reached.

*What is the sensitivity of the SWDD method to long waves?*

The SWDD method has been tested to analyse the applicability on long waves both theoretical and WIHA results (up to 630 m where $R/L$ became 0.016). In itself the SWDD method had no problems with analysing such waves, however SWDD became sensitive when the bathymetry was irregular or only a limited amount of gauges were available (i.e. in physical model setups). In such cases the analysis of relatively long waves can become challenging, because other sensitivities may arise. Among others, the sensitivity to the bathymetry and to the array setup may become stronger. Thus, the limitation of the $R/L$-value depends on other sensitivities which were tested as well and are treated in the next sections.

*What is the sensitivity to a non-homogenous wave field within the array setup?*

The SWDD method has been tested extensively for non-homogeneous wave field effects: wave-crest curvature (e.g. diffraction patterns) and wave amplitude variation. It became clear that SWDD is able to analyse wave

fields where such effects are present. In the tests performed, wave amplitude variation had no influence on the results. And wave-crest curvature mainly had a large influence close to the diffraction source ($L/R_c > 1$) and for low $R/L$ values ($R/L < 0.075$). Considering higher $R/L$ values, the error remained small, even when a wide range of significant wave directions appeared in the results. Which is why the inhomogeneity value for wave-crest curvature inside the array setup ($R/R_c$) is not considered appropriate and the inhomogeneity value $L/R_c$ is considered relevant. A minimal distance of one wavelength away from the diffraction source is advised. Next to this, a range of applicability for the radius of the array setup is advised of: $0.10 \leq R/L \leq 0.30$. Which, depending on many aspects and effects (e.g. the type of input, users interest, angle of incidence, and the bathymetry) can be more specified following the steps in the flowchart in Figure 48.

*What is the sensitivity of the SWDD method to a non-homogeneous bathymetry in the array setup?*

The SWDD method has been tested for domains containing inhomogeneous bathymetries. Domains containing a 'bumpy' bathymetry and a 1:10 slope of 100 meter were considered. It became clear that such effects has a large influence in the accuracy of the SWDD method, because SWDD assumes a constant wave number value, i.e. linear waves over a uniform bottom. When a slope is present containing high gradients ($\Delta kd/\overline{kd} > 0.25$) and where the $kd$ value at the array centre is relatively low ($< 0.50$) the wavenumber, phase-velocity and the wave profile changes having shoaling and refraction effects as a result.

The SWDD method did not show much influence in the results for the 'bumpy' bathymetry case, due to the fact that the inhomogeneity value $\Delta kd/\overline{kd}$ remained relatively low (0.03 - 0.07) in the tests performed. However, in the case where a slope was implemented and when the wave started to feel the bottom (especially when the shallow water region is reached: $kd < 0.30$), a large negative influence became visible. Because, on the one hand the more information about the wave field *(> R)* available, the better. On the other hand, the SWDD method assumes a constant wavenumber $k$, thus when a slope is present, the lower the radius *(< R)* of the array setup, the smaller the $\Delta kd/\overline{kd}$ value gets. This contradiction makes it hard to present an optimum range of applicability for the radius of the array setup to use when a slope is present, also because a lot of other factors depend on the optimum dense array setup, among others: the type of wave field (monochromatic or spectral), the angle of wave incidence (because of refraction, which lowers the resolution) and the presence of high wave-crest curvature ($L/R_c > 1$).

However, to keep $\Delta kd/\overline{kd}$ relatively low ($< 0.25$) it is advised to use a small radius value: *$0.10 \leq R/L \leq 0.30$*. Next to this, the sensitivity to the slope might be reduced by adding a part of regular bathymetry. Which depending on many aspects and effects (e.g. the type of input, users interest, angle of incidence, and the type of wave field), can be more specified following the steps in the flowchart in Figure 48.

*What is the sensitivity of the SWDD method to the array setup and the number of gauges used?*

The SWDD method has been tested extensively for various array setups, where it became clear that the accuracy of the results was highly influenced. Considering a constant radius of the array setup, the higher the number of gauges, the more accurate the results have become and higher the directional resolution gets. Where for larger radius values than *2L*, the directional resolution became higher than 10°. The radius however is less straight forward and depends on many different aspects and effects, among others: the purpose (i.e. physical modelling or numerical modelling), inhomogeneity in the wave field (e.g. wave-crest curvature and wave amplitude variation), inhomogeneity in the bathymetry, the wave field type (i.e. monochromatic or spectral), the wavelength, the reflection coefficient, angle of incidence and the users interest.

Especially considering numerical modelling (dense) array setups, the optimal range of applicability for the radius is quite wide, because a large radius and a high number of gauges is possible.

For physical modelling often only a limited amount of gauges are available (i.e. 5 -15), which is why relatively a low value for the radius of the arrays setup is advised containing a range of applicability of: $0.10 \leq R/L \leq 0.30$. Considering accuracy limits of 2.50° for the direction and 2% for the reconstruction error inside the array setup. Both for numerical modelling and physical modelling an advisory flowchart to determine the optimum radius of the array setup is presented in Figure 48.

*Overall applicability of the SWDD method*

Due to all the discussed sensitivities not one overall range of applicability could be pointed out, but dependent on multiple aspects, effects and users interest a complete advisory flow chart is presented in Figure 48 below. When not all information is available it is advised to choose the lower range of the considered ranges and if monochromatic waves need to be analysed and inhomogeneity in the bathymetry or wave field is present the main trend shows that a radius can be approximated by: $0.10L$ - $0.30L$, unless a high directional resolution is needed. When not all information is available and a spectrum is analysed an approximation of the radius of $0.20L$ - $0.40L$ is advised.
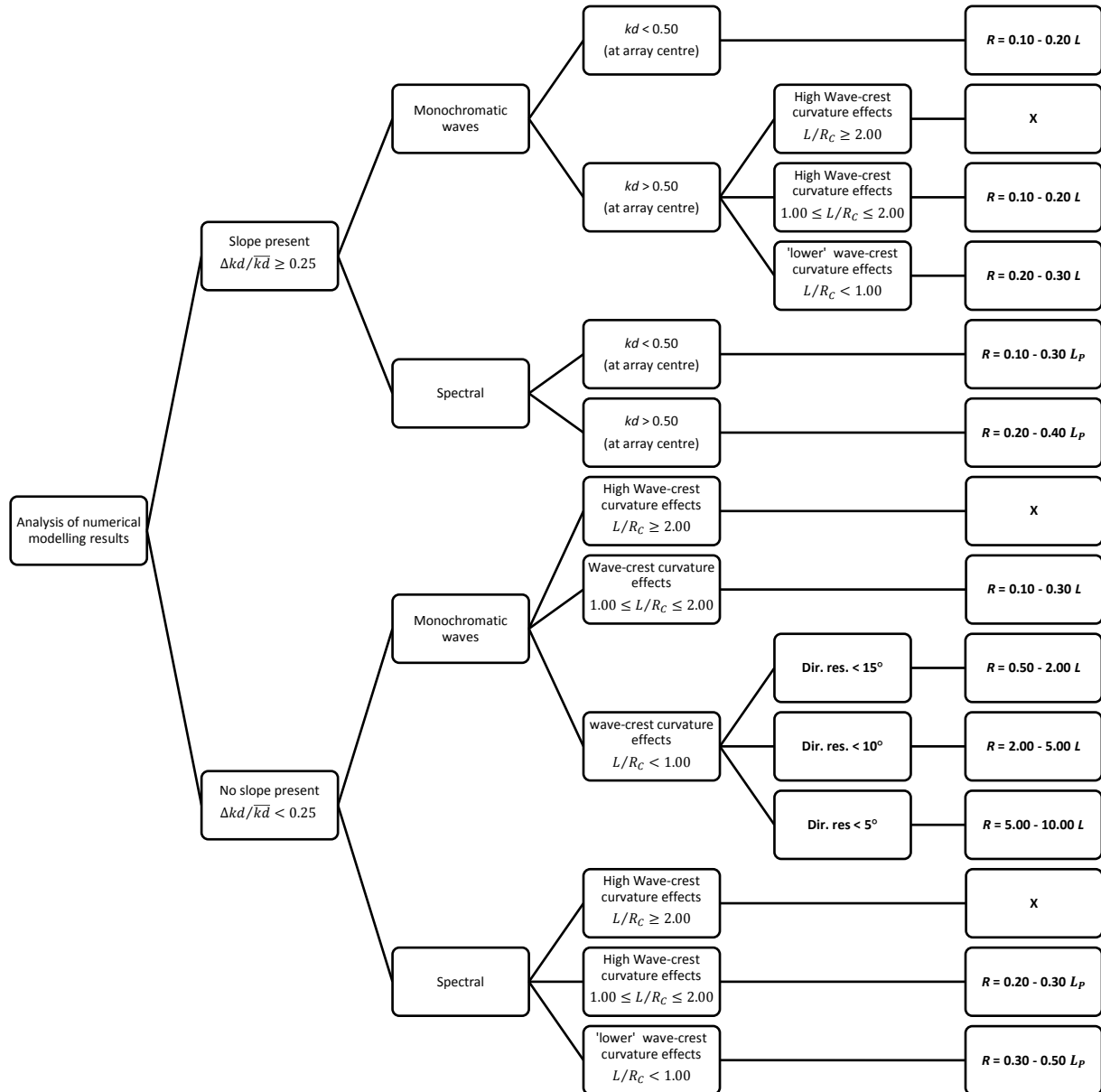


Figure 47: A recommending flowchart to determine the optimum range for the radius of the array setup
in a directional wave-analysis by the SWDD method using numerical modelling input.
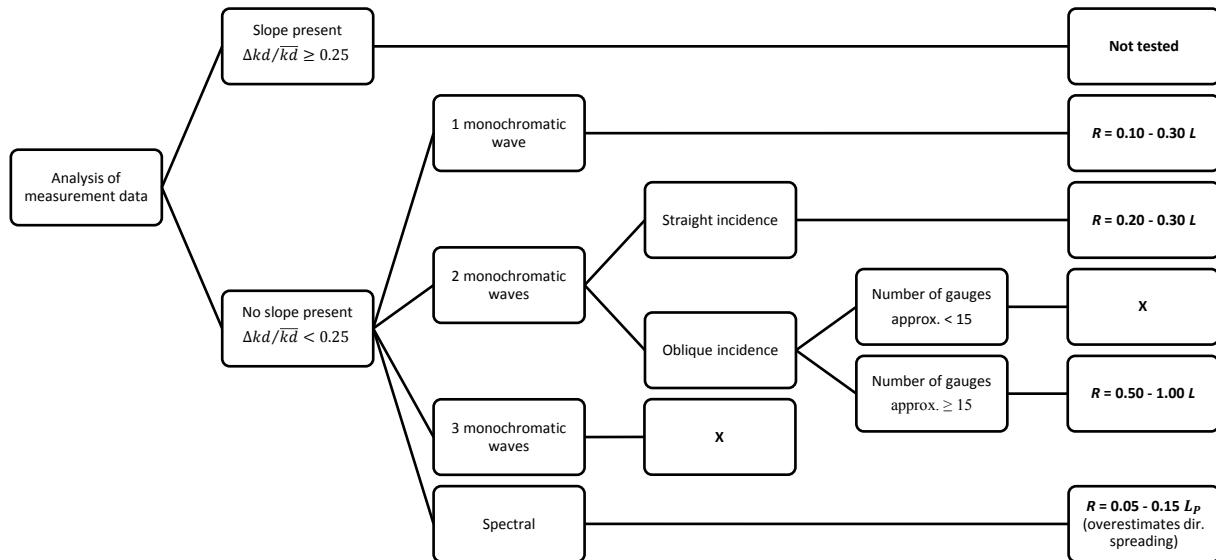
Figure 48: A recommending flowchart to determine the optimum range for the radius of the array setup
in a directional wave-analysis by the SWDD method using measurement data input.

For measurement array configurations the radius is based on circular arrays (mostly containing < 15 gauges),
where the position of each gauge influence the results as well, however to determine the most optimum
measurement array configuration is outside of the scope of this study.

*Correlations between several characteristics and the error*
Multiple characteristics and parameters were tested for correlated behaviour between the reconstruction
errors and each other. Among others, the $R/L$ value, the $\lambda$-parameter, the number of gauges, the number of
lobes, the width of the main lobe, the ratio of the highest spurious lobe and the main lobe and the
reconstruction errors. Several correlations came forward, however some of them were also mutually related,
among others: the number of lobes and the main lobe width by -0.77. The most important correlation found is
between the width of the main lobe(s) and the reconstruction error on the large domain of respectively: 0.94
averaged per test, 0.88 averaged per case and 0.80 for one large dataset. Which means that the width of the
main lobe(s) gives a good first impression of the reliability of the results.
And, as a first indication a correlation between the inhomogeneity value of the wave curvature ($L/R_c$) and the
reconstruction error on the large domain is found of 0.98 and between the inhomogeneity value of the
bathymetry ($\Delta kd/\overline{kd}$) and reconstruction error inside the array setup is found of 0.95.

*How do the results from the SWDD method compare with analytical data and results from other comparable*
*directional wave-analysis methods?*
A comparison study between SWDD and other directional wave-analysis methods has been performed as well.
Which did consider another deterministic wave analysis method: the r-DPRA method (de Jong and Borsboom,
2012) and multiple stochastic directional wave-analysis methods: BDM, MLM and MEM.
It became clear that SWDD is a more ease to use and robust method compared to r-DPRA. Mainly because, it
has a higher directional resolution, lower computation time, user checks are not needed and afterwards an
error can be reconstructed if desired.
Compared to the stochastic directional wave-analysis methods (e.g. MLM and BDM), it became clear that the
SWDD method is designed for other purposes than the stochastic methods. In the first instance, the SWDD
method is designed to detect and separate multiple (reflective) wave components, both considering the wave
direction and wave amplitude. The stochastic methods only are able to give an indication of the complete 2D
wave spectrum for a low number of gauges and unable to separate monochromatic waves. The SWDD method
is also able to perform a spectral analysis both using an array containing few gauges and containing many
gauges as well. However, the directional spectrum is overestimated by 60%.

So, the SWDD method is a widely applicable method both for monochromatic and spectral wave fields. However, the SWDD method performs better when a high number of gauges is present. Thus, especially considering numerical modelling the SWDD methods potential is used.

*Computational accuracy of the mild-slope wave model WIHA*
when transmission and non-linear processes like bottom friction, wave breaking and non-linear dispersion are minimal present, it became clear that the mild-slope wave model WIHA is accurate and often outperforms other comparable wave models. This is due to improved numerical dispersion characteristics and higher-order Sommerfeld boundary conditions. These non-linear processes and transmission are scheduled to be implemented in a future version of WIHA. However, to use WIHA for cases where wave-breaking and non-linear processes are not present, WIHA is accurate and considered suitable.

# 6.3 Possible usage of the SWDD method

This section treats some examples for which the SWDD method might be used. First an example is treated containing highly oblique reflective wave incidence. Second, the applicability for harbour design is treated. Third, the applicability of the SWDD method to use for other wave model results is treated.

*Harbour design*
For the tests performed until now the SWDD method seems highly applicable to use in harbours, even for complex geometries. The SWDD method can certainly handle diffraction when the centre of the array configuration is at least one wavelength away from the diffraction source. The SWDD method handles cross patterns, standing waves and spectra as well. For example in the navigation channel case (section 4.2) spectral input with high curved wave effects is present. The radius is advised to be approximately $0.20L$ according to the flowchart in Figure 47. The resulted 2D wave spectra at four output locations are presented in appendix N. The main limitation at this moment is the homogeneity of the bathymetry. However, when only mild-slopes ($\Delta kd/\overline{kd} < 0.25$) are present SWDD can be used to separate wave components and present wave directional information at requested output locations.

*Use SWDD on results from other phase-resolving wave models*
This study showed the applicability of the SWDD method using synthetics wave signals and model results from the mild-slope wave model WIHA. However the SWDD method can also be used on model results obtained from other wave models (e.g. SWASH or Boussinesq models) which use different (nonlinear) equations to solve the wave dynamics. The expectation is that for random waves the non-linear phase-speed effects in such models are small, so the linear dispersion used in SWDD can also be used for random irregular waves. However, for regular waves (e.g. in the Berkhoff shoal case) differences are expected between linear and nonlinear models due to nonlinear dispersion. So, the results of nonlinear models should become more accurate than WIHA. It is expected that SWDD is able to analyse such output as well, but this has to be tested in further research.

*Highly oblique wave incidence on a reflective structure*
Considering a reflective structure, the more parallel the incoming wave to the structure, the more difficult it becomes to separate the wave components by the SWDD method. Which is the case due to the high directional resolution needed for such cases, which mainly depends on the array configuration. When such cases are computed numerically – and inhomogeneity in the wave field and bathymetry are minimally present – this can be analysed accurately by the SWDD method. For example when the wave incidence is only 80° (almost parallel to the structure) and thus the reflective wave is -80° this can be solved using a dense array setup radius of one wavelength according to the flowchart in Figure 47. The resulted polar plot is presented in appendix O Figure 111.

When a measurement array configuration is used, such cases are quite difficult and limited. It is important to design the array configuration well in advance, because the optimum array varies per case, depending on: the angle of incidence, wave height, reflection parameter and wavelength. The determination of the optimal configuration is out of the scope of this study.

# 7

# Conclusions and recommendations

This chapter describes the conclusions obtained from this research. Also recommendations for further possible research are given.

## 7.1 Conclusions

It is demonstrated that the directional wave-analysis method called SWDD is a robust, reliable and user friendly post-processing method to analyse incoming wave components, i.e. wave heights, phases and directions, in complex wave fields considering (near) homogeneous (regular) bathymetries. **The applicability of the SWDD method is successfully validated** using synthetic wave signals – both for plane waves and circular wave patterns containing wave-crest curvature and wave amplitude variation – and finally using the output of a mild-slope wave model (WIHA).

Before analysing output of the new mild-slope wave model **WIHA** with the SWDD method, a validation study has been performed. It shows that WIHA computes accurate results, when transmission and non-linear processes like bottom friction, wave breaking and non-linear dispersion are minimally present. A maximum mean error of 6% is present in the cases considered. These non-linear processes and transmission are scheduled to be implemented in a future version of WIHA. However, to use WIHA for cases where wave-breaking and non-linear processes are small, WIHA is outperforming other comparable wave models. This is due to improved numerical dispersion characteristics and higher-order Sommerfeld boundary conditions. The SWDD method is applicable to use on the output of the mild-slope wave model WIHA and possibly other time-domain models (e.g. SWASH).

The study showed that the SWDD method is sensitive for wave-crests containing high effects of curvature (e.g. circular **diffraction** patterns) and **irregular bathymetries** (e.g. slopes). Where the first effect mainly has a large influence close to the source (*i.e.* $L/R_c > 1.00$). The second effect has a large influence for steep slopes, because the SWDD method assumes a constant wave number value, i.e. linear waves over a uniform bottom. When a slope is present – containing high gradients ($\Delta kd/\overline{kd} > 0.25$) and where the $kd$ value at the centre of the array configuration is relatively low ($< 0.50$) – the wavenumber, phase-velocity and the wave profile change and having lots of shoaling and refraction effects. When non-homogenous effects are present a range of applicability for the radius of the array setup is advised: $0.10 \leq R/L \leq 0.30$. Within this range there is an accuracy limit for the directional error of 2.50° and for the reconstruction error inside the array setup of 2%.

In contrast to stochastic directional wave-analysis methods, the SWDD method is able to analyse dense array configurations and separate a **high number of wave components**, e.g. in and near harbours. The maximum separation of the different wave components depends on the directional resolution. This in turn depends on the array configuration (i.e. the radius of the array configuration and the number of gauges). A directional resolution of 10° up to 5° is obtainable by using a dense array configuration containing a radius that is larger than two wavelengths. When analysing measurement data the distinction capability is much lower, because

of the limited amount of gauges (e.g. CERC-6 by Panicker and Borgman, 1970; Davis and Regier, 1977; Hawkes et al., 1997), only a directional resolution of 40° up to 30° can be reached.

Next to this, it has been demonstrated that the SWDD method is able to produce **2D wave spectra** at the output locations of the mild-slope wave model WIHA (both for an array containing few gauges and dense grids containing many gauges). The SWDD method has a higher suitability for spectral directional analysis in numerical modelling as compared to **other deterministic directional wave-analysis methods** (e.g. r-DPRA by de Jong and Borsboom, 2012), because: user checks for each directional wave-analysis performed are not needed, the directional resolution is higher and the computation time is fast.

Altogether, the applicability of the SWDD method depends mainly on the spatial location and the configuration (i.e. the radius and the number of gauges) of the array setup. The **optimal radius of the array** configuration depends on many aspects and effects. Therefore, an advisory flowchart for the determination of the optimum range for the radius value of the array configuration has been presented.

# 7.2 Recommendations

Based on the performed analyses a number of recommendations for further research and improvements in the SWDD method are suggested. First, recommendations are presented for possible future research. Second, recommendations are presented to improve the SWDD method, mainly focussed on the user experience and reliability of the results.

*Further research*
- When using the output from a wave model with non-linear effects (e.g. SWASH), it is advised to test relatively easy cases from section 5.3 and compare this with the SWDD results where WIHA output was used. For 3D models like SWASH, also use the velocities as additional input to the SWDD method.
- It is advised to test the SWDD method more extensively for array setups located on a slope. The SWDD method can be improved by performing a refraction analysis within the array setup: from the centre of the array setup, each directional component (i.e. 360 in total) should be calculated to the amount of refraction and shoaling. This can be compared with the SWDD model results. Also perform a sensitivity analysis by using a constant radius of the array configuration and then vary the angle of the slope from flat to steep.
- Perform a study on the relation between the $\sigma$-value (singular value in the SVD) to: the $\lambda$-parameter (Tikhonov parameter), main lobe width and the array configuration. Both $\sigma$ and $\lambda$ are both important parameters in the regularization of the ill-posed directional problem and seem to have a large influence on the main- and side-lobe characteristics.
- Perform a study to find the optimum laboratorial array configuration to use in the SWDD analysis to get to a higher directional resolution.
- Perform a study on the possibilities of the implementation of several non-linear effects in the mild-slope wave model WIHA according to Kostense et al., (1986).

*Recommendations for improving the wave directional SWDD method*
- Implement additional features in the resulting polar plot by the SWDD method:
  - Arrows, displaying the wave directional propagation, inside the main lobes.
  - Display the direction value(s).
  - Display the wave amplitude value(s).
  - Display the reconstruction error value.
- Implement the SWDD method in the WIHA GUI and WIHA QGIS.
  This makes it possible to select an output location in the considered (visualized) domain, where after the radius value can be set and the polar plot (or 2D spectrum) is presented.
- Implement automatic variation of the $\lambda$-parameter based on the main lobe width and the reconstruction error for wave fields where wave-crest curvature effects are highly present.

This in order to have the polar plot not show a wide range of significant wave directions, but only presents the main wave direction (if desired by the user).

- Implement a variant of the SWDD method for a (linear) sloped bottom with parallel depth contours, where the wave number can vary. For example by inserting two values for the wave number and the water depth, one at the lower part of the linear slope and one at the higher part of the linear slope. Changes of the phase component along wave rays by refraction can be computed by integration, according to Baldock and Simmonds (1999) and Wang et al. (2008). This variant would mainly be designed for relatively easy linear slopes.

- Introduce a spectral variant of the SWDD method to improve the possible overestimation of the directional spectral width (mainly for measurement array configuration). Instead of using the direct results of the SWDD analysis for each frequency (relatively wide main lobes), now first perform a lobe statistical analysis. Thereafter the summation of the monochromatic waves can be used, using a constant $R/L$ value for each frequency analysis (instead of a constant $R$ value).

# Appendices

# A  Theoretical background

## A1 Important wave processes

### The wave spectrum

In the ocean wave discipline, often a variance density spectrum is used to describe the surface elevation. The variance density spectrum is based on the random-phase/amplitude model. The amplitude model presents the expected value of the amplitude as a function of frequencies where the phase is uniformly distributed and the amplitude is Rayleigh distributed.

The variance density spectrum is often used instead of the amplitude spectrum, which is valid when the surface elevation can be seen as a stationary, Gaussian process. The variance density spectrum has two main advantageous compared to the amplitude spectrum: the sum of the variance of the wave components is the variance of the sum of the wave components and the energy of the waves is proportional to the variance. Which is the reason why in this study this type of spectrum, a variance density spectrum, is used.

The variance density spectrum considers the amplitude spectrum into a continuous distribution of the variance over frequencies and can be seen as a description of how the energy of the waves is distributed for the frequencies (1D spectrum) and possibly directions (2D spectrum). Integration over all frequencies (and directions for a 2D spectrum) is proportional to the energy held by the wave field. The variance density spectrum is given by:

$$E(f) = \lim_{\Delta f \to 0} \frac{1}{\Delta f} E\left\{\frac{1}{2}\underline{a}_i^2\right\} \tag{A.1.1}$$

Where the underscore implies random variables, with $E\{\underline{a}_i\}$ is the expected amplitude, $E\left\{\frac{1}{2}\underline{a}_i^2\right\}$ is the variance, and $\Delta f$ is the frequency band.

Figure 49 displays an example of a JONSWAP spectrum (Hasselmann et al., 1973), where the variance density is plotted against the frequency and also presents common sources, sinks and redistribution processes of the 1D wave spectrum for shallow water domains.
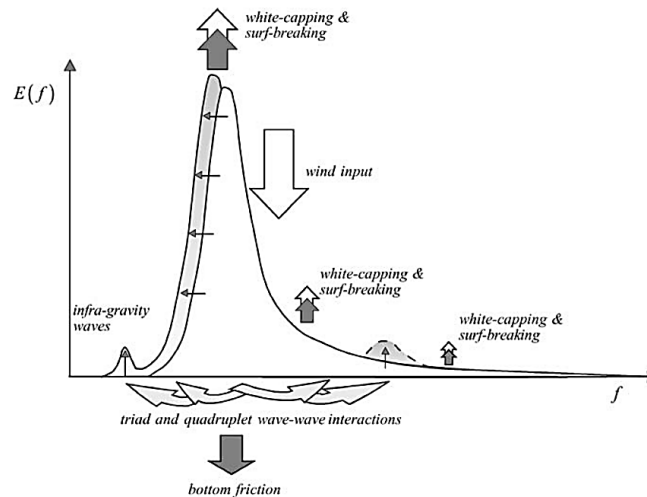


Figure 49: A 1D  JONSWAP wave spectrum which also visualizes common sources, sinks and redistribution of the spectrum in shallow water (Holthuijsen, 2007, §8.4.5).

Figure 50 displays an example of a 2D (directional) wave spectrum obtained with the Maximum Likelihood Method *(MLM)*, where the spectral density is plotted against the frequency and direction.
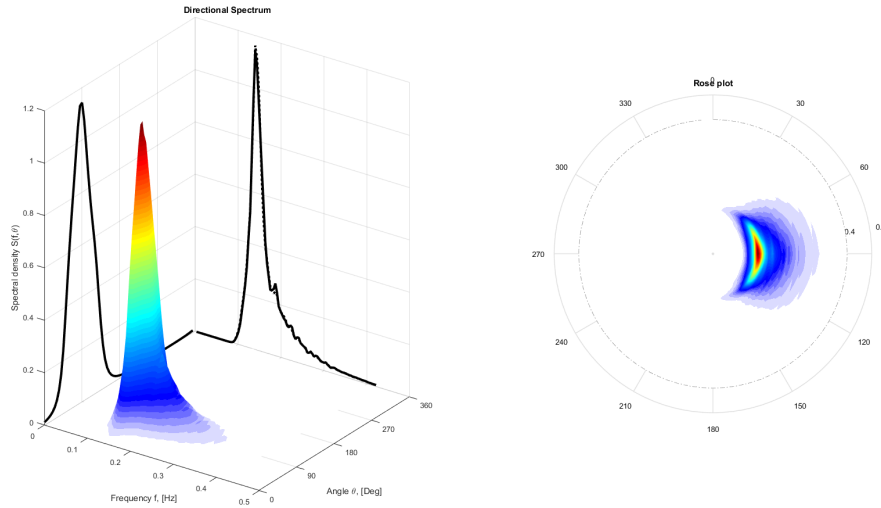
Figure 50: A 2D (directional) wave spectrum where the energy is plotted against the frequency and the direction (a) and a radial plotted density rose (b).

### Dispersion

According to linear wave theory (Airy, 1845), in waves a mutual relation exists between the wave period, wavelength and water depth. This relation is called the dispersion relation. Because of differences in wave speed for different Fourier components, frequency dispersion occurs: waves adopt to a wavelength for a certain frequency. When $k$ is the wavenumber, $h$ the water depth and $\omega$ is the radial frequency, the frequency dispersion relation is described as (Holthuijsen, 2007, §5.4.3):

$$\omega = \sqrt{gk \tanh(kh)} \qquad (A.1.2)$$

### Shoaling

Shoaling occurs when waves start to feel the bottom and the shore is gradually getting shallower. The less deep the water becomes, the lower the wave speed and wavelength gets. Considering the conservation of the wave-energy flux between two rays, there is a constant energy flux ($Ec_g$) for a stationary situation. With $c_g$ the ($c_{g_0}$: offshore) wave group velocity, the well-known shoaling coefficient can be written as:

$$K_s = \sqrt{\frac{c_{g_0}(x)}{c_g(x)}} \qquad (A.1.3)$$

When waves propagate from deep water into decreasing water depth, the group speed will decrease - after an initial small increase - and thus the wave height will increase (e.g. Mei, 1989 §3.3.1 and Holthuijsen, 2007, §7.3.1).

### Diffraction

Diffraction occurs whenever there is an abrupt change in wave amplitude. This is often the case near breakwaters, islands and small gaps (harbour basins). The diffraction behind these obstacles and/or gaps forces the waves to bend, spread and interfere with each other. The resulting scattered wave pattern due to this phenomenon often look circular, i.e. originating from diffraction points at breakwater tips etc. Longer waves show more diffraction. In harbours, diffraction is often of importance (Dusseljee et al., 2014)(Holthuijsen, 2007, §7.3.3).

### Refraction

Refraction plays an important role when depth changes occur and the wave incidence is oblique. The wave propagation direction changes and the wave bends towards the shallower water region. This happens because of the phase velocity difference along a wave-crest. The wave travels faster in the deeper region, which explains the refraction towards the shallower region. Based on the conservation of wave-energy flux between two rays, the refraction coefficients can be written as:

$$K_R = \sqrt{\left|\frac{\cos(\theta_0(x))}{\cos(\theta(x))}\right|} \qquad (A.1.4)$$

Where $\theta_0$ is the offshore incoming wave angle. For example, when a wave propagates with oblique incidence towards a coast, the wave refracts towards the coast (the angle of incidence gets smaller). Near harbours, this phenomenon is often of relevance, also close to and in the approach channel, if present (Dusseljee et al., 2014)(Holthuijsen, 2007, §7.3.2).

*Reflection*

Reflection occurs when waves encounter an obstacle, for example: breakwaters, quay walls and (steep) beaches. The reflection coefficient depends on the type of structure, wave frequency and wave amplitude. The less dissipative the structure and/or the longer the period of the wave, the more reflection occurs. Shorter period waves dissipate more due to wave breaking on the structure. Wave breaking will be explained in the next subsection (Holthuijsen, 2007, §7.3.6).

A famous description for wave reflection by slopes is written by Battjes (1974):

$$\xi_0 = \frac{\tan \alpha_s}{\sqrt{\frac{H_{m0}}{L_0}}} \quad and \quad K_r \approx 0.1\xi^2 \qquad (A.1.5)$$

Where $\xi_0$ is the breaking parameter, $\alpha_s$ is the bottom slope, $H_{m0}$ the incident wave height, $L_0$ the deep-water wavelength and $K_r$ the reflection coefficient.

Seelig and Ahrens (1981) revised the equation for the reflection coefficient to:

$$K_r = \frac{a_s\xi_0^2}{\xi_0^2 + b_s} \qquad (A.1.6)$$

Where $a_s$ and $b_s$ depend on the type of structure and material used.

Zanuttigh and van der Meer (2006) found a calibrated reflection coefficient, valid for a wide range of conditions, of the form:

$$K_r = \tanh(a_s\xi_0^{b_s}) \qquad (A.1.7)$$

With $a_s$ and $b_s$ calibrated coefficients which depend on the type of structure (material used).

In harbours, reflection plays an important role, since it contributes to harbour resonances. And therefore, among others, for the design of the mooring locations of the vessels and the design of the quays/revetments in the harbour.

*Dissipation*

Considering approaching waves towards the coast, dissipation of wave energy due to bottom friction and wave breaking can be present. In shallower waters there are higher oscillatory velocities near the bottom. This results in a loss of energy due to bed friction. Short waves will be less influenced by this phenomenon.

Breaking of waves can be subdivided in steepness-induced breaking (white-capping) and depth-induced breaking (surf-breaking). Steepness-induced breaking starts to occur when the waves become too steep. This happens especially in deeper waters. In shallower waters depth-induced breaking becomes important.

Battjes and Janssen (1978) introduced for coastal regions the following relation between the maximum wave height and the water depth:

$$H_{max} \approx \gamma_b h \qquad (A.1.8)$$

Where $h$ is the water depth and $\gamma_b$ is the breaking coefficient, which lies approximately between 0.5 and 0.8 (Holthuijsen, 2007, §8.4.5).

*Nonlinear wave-wave interactions*

Nonlinear wave-wave interactions results in the redistribution of energy over the various frequency bands of the wave spectrum. This in contrast with linear waves, where wave components can be considered as independent. This nonlinearity, in the form of interactions between wave triads (primarily in shallow water) and quadruplets (primarily in deep water), results for instance in surf beat (wave motion at relatively low frequencies with periods of $30 - 200$ s where the surf zone has a periodically vertical movement due to the grouping of the waves, Longuet-Higgins and Stewart, 1962) and changes of the spectral shape. Triads (three-

wave interactions) and quadruplets (four-wave interactions) are most prominent when the wave components are in resonance (Holthuijsen, 2007, §8.4.4).

   *Low-frequency waves*

Low-frequency waves are waves with large periods, and consequently have a long wavelength. Those long waves are often forced by wave groups and can result in surf beat, which can produce excitation of harbours resonances. Besides the possible negative effects of long waves approaching coasts, numerical difficulties also arise. The array setup used in the SWDD method needs to become larger for longer waves, while the SWDD method assumes a homogeneous domain. This can be contradicting demands, which may cause problems and inaccuracies.

## A2 Additional formulas

This section displays (additions to) relevant equations treated in the literature overview.

- ▪ The used energy balance in SWAN is defined as (Booij et al., 1996):

$$\frac{\partial N}{\partial t} + \nabla_{2D}\left((c_g + \vec{u})N\right) + \frac{\partial}{\partial \sigma}(c_\sigma N) + \frac{\partial}{\partial \theta}(c_\theta N) = \frac{S}{\sigma} \tag{A.2.1}$$

With $N$ is the wave action density ($N = \frac{E}{\sigma}$), $t$ is the time, $\nabla_{2D} = \left(\frac{\partial}{\partial x}, \frac{\partial}{\partial y}\right)$, $c_g$ is the group velocity, $u$ is the current velocity, $c_\sigma$ is the velocity in the frequency space, $c_\theta$ is the velocity in the directional space, $\sigma$ the relative wave frequency (satisfying the dispersion relation: $\sigma = \sqrt{gk\,tanh(kh)}$ ) and $S$ the sources/sinks of energy.

- ▪ SWE (from Appendix E in Holthuijsen, 2007)

$$\nabla_{2D} \cdot gh\nabla_{2D}\eta + \omega^2\eta = 0 \tag{A.2.2}$$

With $\nabla_{2D} = \left(\frac{\partial}{\partial x}, \frac{\partial}{\partial y}\right)$, h is the water depth, $\eta$ is the free surface elevation and $\omega$ is the angular frequency. The SWE variant used in WIHA is formulated as:

$$\partial_x(gh\partial_x\eta) + \partial_y(gh\partial_y\eta) + \omega^2\eta = 0 \tag{A.2.3}$$

- ▪ Berkhoff equation (1972):

$$\nabla \cdot u_0\nabla\eta + k^2u_0\eta = 0 \tag{A.2.4}$$

With $\nabla = \left(\frac{\partial}{\partial x}, \frac{\partial}{\partial y}\right)$, $u_0 = \frac{\{2kh+\sinh(2kh)\}}{4k\cosh^2(kh)}$, $\eta$ is the spatial component of the free surface elevation, $k$ is the wave number and $h$ the water depth. The Berkhoff variant used in WIHA is:

$$\partial_x(c_pc_g\partial_x\eta) + \partial_y(c_pc_g\partial_y\eta) + k^2c_pc_g\eta = 0 \tag{A.2.5}$$

- ▪ Porter equation (2003):

$$\nabla \cdot k^{-2}\nabla\eta + \eta = 0 \tag{A.2.6}$$

With $\nabla = \left(\frac{\partial}{\partial x}, \frac{\partial}{\partial y}\right)$, $k$ is the wave number, $\eta$ is the free surface elevation and $h$ the water depth. The Porter variant used in WIHA is formulated as:

$$\partial_x\frac{1}{k^2}\partial_x\psi + \partial_y\frac{1}{k^2}\partial_y\psi + \psi \tag{A.2.7}$$

With $\psi = k\sqrt{c_pc_g}\eta$

- ▪ Sommerfeld equation as defined in WIHA (1896):

$$\beta\partial_\eta\psi - \mu\psi + \partial_s\nu\partial_s\psi = \beta\partial_\eta\psi_{inc} - \mu\psi_{inc} + \partial_s\nu\partial_s\psi_{inc} \tag{A.2.8}$$

With $\beta$ is a parameter depending on the SWE or mild-slope variant used in WIHA, $\partial_\eta$ and $\partial_s$ are the normal and tangential derivative operator at the domain boundary, $\psi_{inc}$ is the incoming wave field and $\mu$ and $\nu$ are free parameters for the reflection coefficient (when $\nu = 0$ the classical Sommerfeld Eq. arises).

# B  Spurious lobe reduction using a Lanczos or Hamming filter

*Two waves dense grid*

Considering two incoming prescribed synthetic waves without noise on a dense grid, the Lanczos filter to reduce the spurious side lobes show promising and accurate results, however the main lobes are on average 57% wider. Figure 51 displays the obtained polar plots. The same test is also analysed using the Hamming filter, which performs accurate as well, where the main lobes are on average 86% wider.
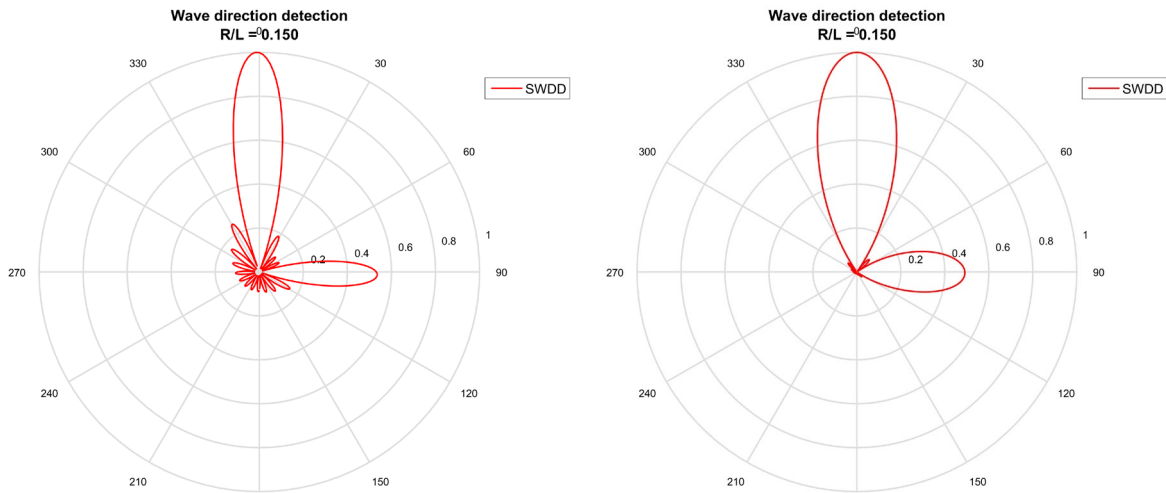


Figure 51: Two prescribed waves with 1.0 and 0.5 m wave amplitude and 0° and 90° incoming wave direction without noise respectively without Lanczos filtering (a) and Lanczos filtering included (b) where R/L is 0.15 on a dense grid.

*Four waves dense grid*

Considering four incoming prescribed synthetic waves without noise on a dense grid, the Lanczos filter to reduce the spurious side lobes shows promising and accurate results, however the main lobes are on average 97% wider. Figure 52 displays the obtained polar plots. The same test is also analysed using the Hamming filter, which performs accurate as well, where the main lobes are on average 120% wider.
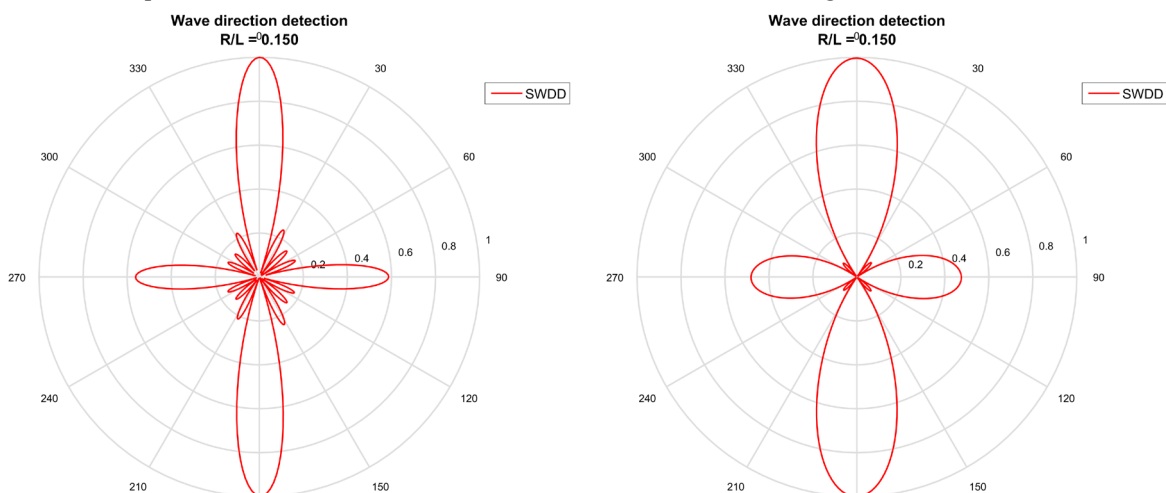


Figure 52: Four prescribed waves 1.0, 0.5, 1.0 and 0.5 m wave amplitude and 0°, 90°, 180° and 270° incoming wave direction without noise respectively without Lanczos filtering (a) and Lanczos filtering included (b) with R/L is 0.15.

*Small array setups including additional noise*

Considering two incoming prescribed synthetic waves including additional noise on a two rings circular array containing 25 gauges, the Lanczos filter to reduce the spurious side lobes shows inaccurate results, due to the large width of the main lobes less distinctiveness is possible. Figure 53 displays the obtained polar plots. The same test is also analysed using the Hamming filter, which also performs inaccurate.
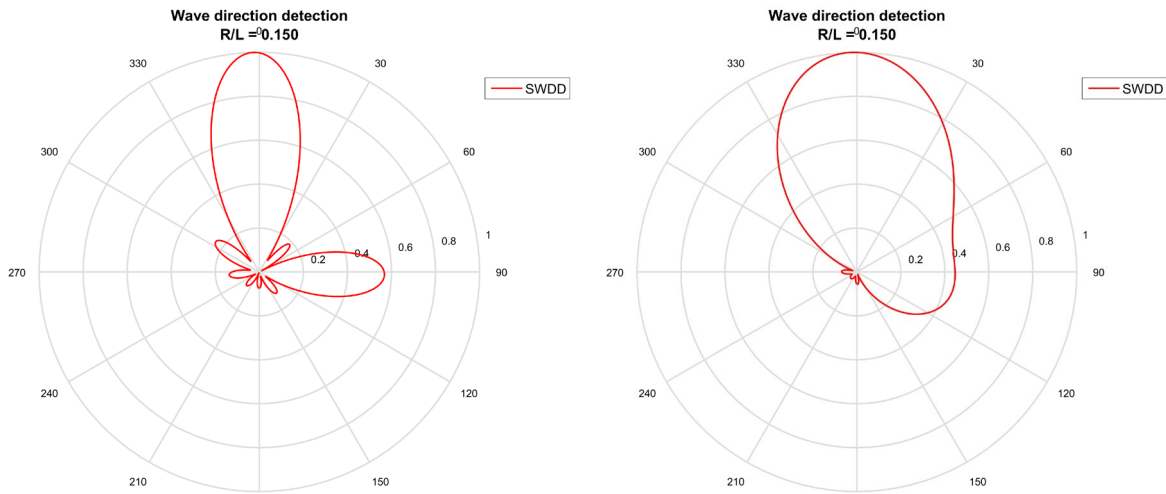


Figure 53: Two prescribed waves with 1.0 and 0.5 m wave amplitude and 0° and 90° incoming wave direction including additional noise respectively without Lanczos filtering (a) and including Lanczos filtering (b) where R/L is 0.15 using a double circular array containing 25 gauges.

It comes forward that the Lanczos filtering and Hamming filtering are accurate when a dense grid is considered, however as a side effect do the main lobes become almost two times wider.

When additional noise is included and/or only few gauges (CERC-6 array setup) are considered in the array setup, the main lobes have already a large width for the 'normal' SWDD analysis, which is one of the reasons why for such array setups the Lanczos/Hamming filtering becomes inaccurate and is not advised.

The Lanczos and Hamming filtering is a nice additional option in the SWDD analysis which can be used for the analysis of numerical wave model output.

# C  Results WIHA dispersion case
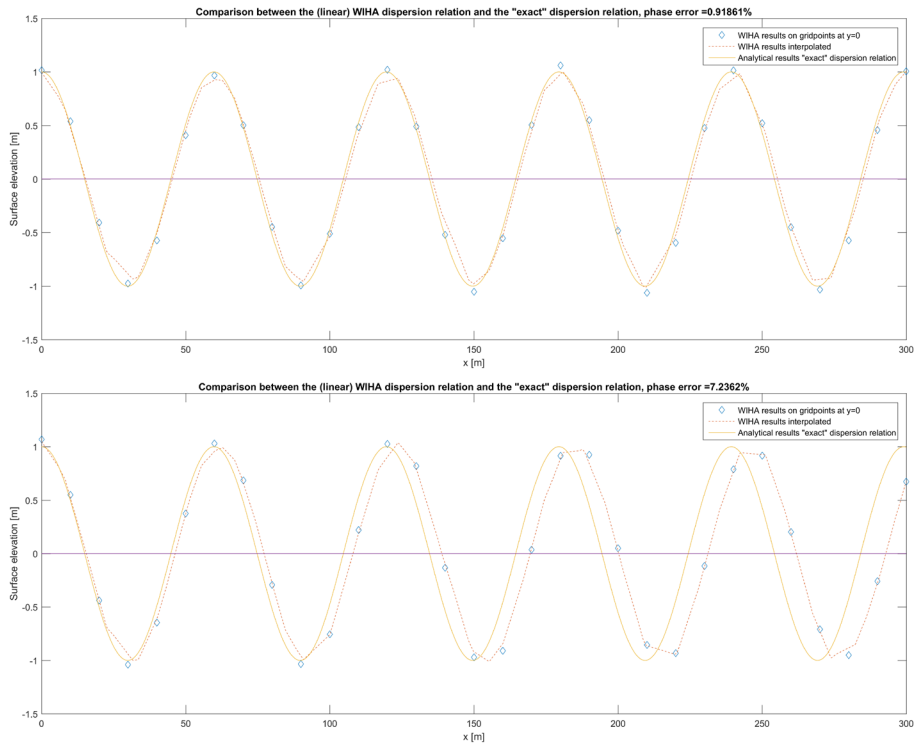


Figure 54: Obtained surface elevation plot for respectively the 'quadrature' variant at the top
and the 'analytical' variant at the bottom both using 4 nodes per wavelength.
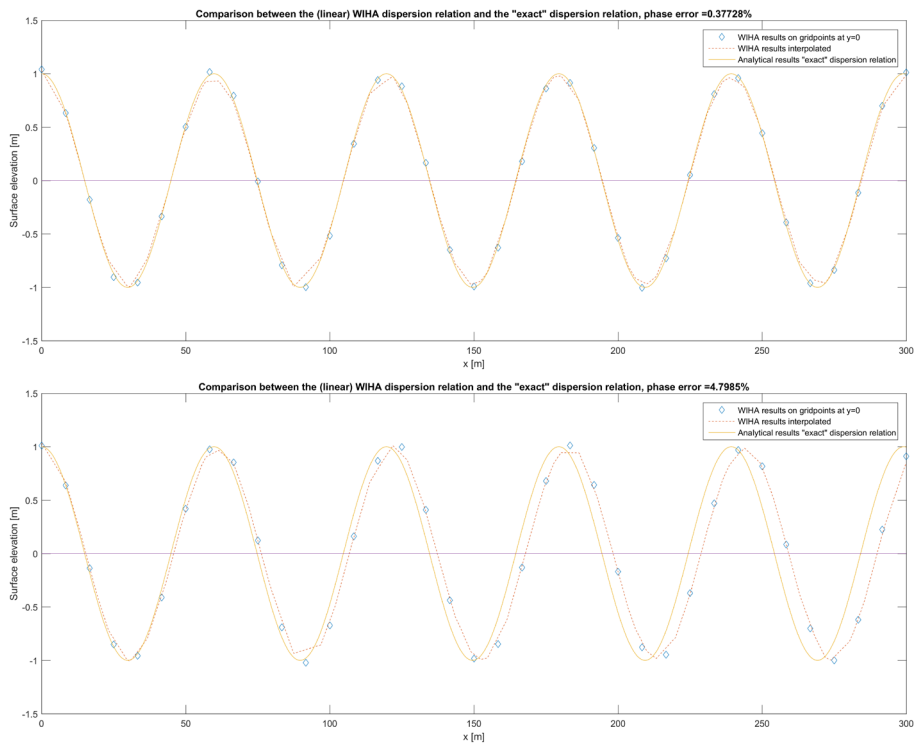


Figure 55: Obtained surface elevation plot for respectively the 'quadrature' variant at the top
and the 'analytical' variant at the bottom both using 7 nodes per wavelength.
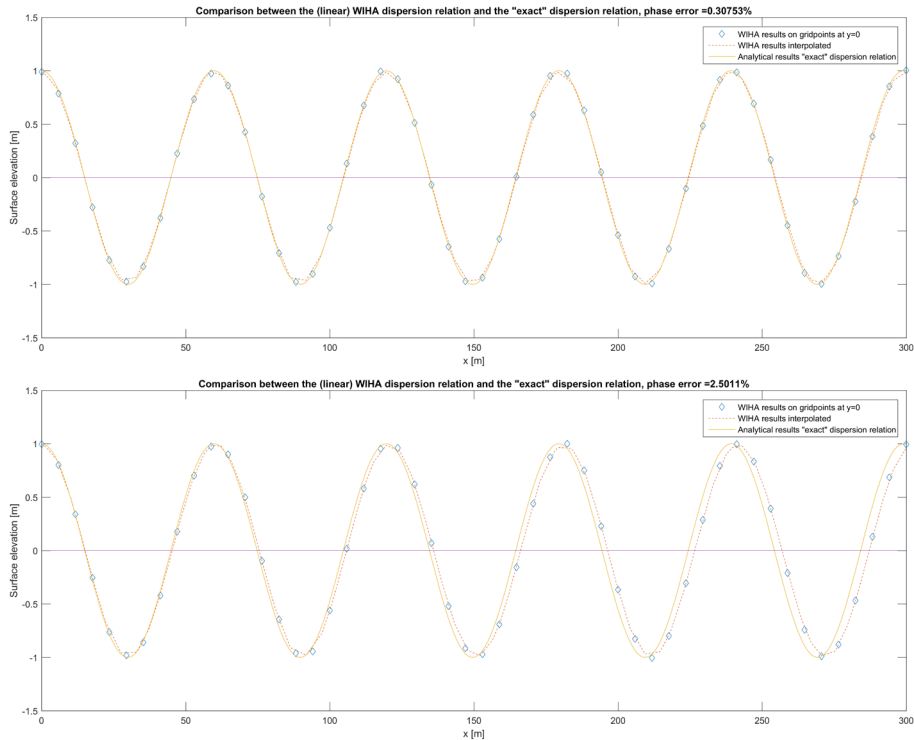
Figure 56: Obtained surface elevation plot for respectively the 'quadrature' variant at the top and the 'analytical' variant at the bottom both using 10 nodes per wavelength.
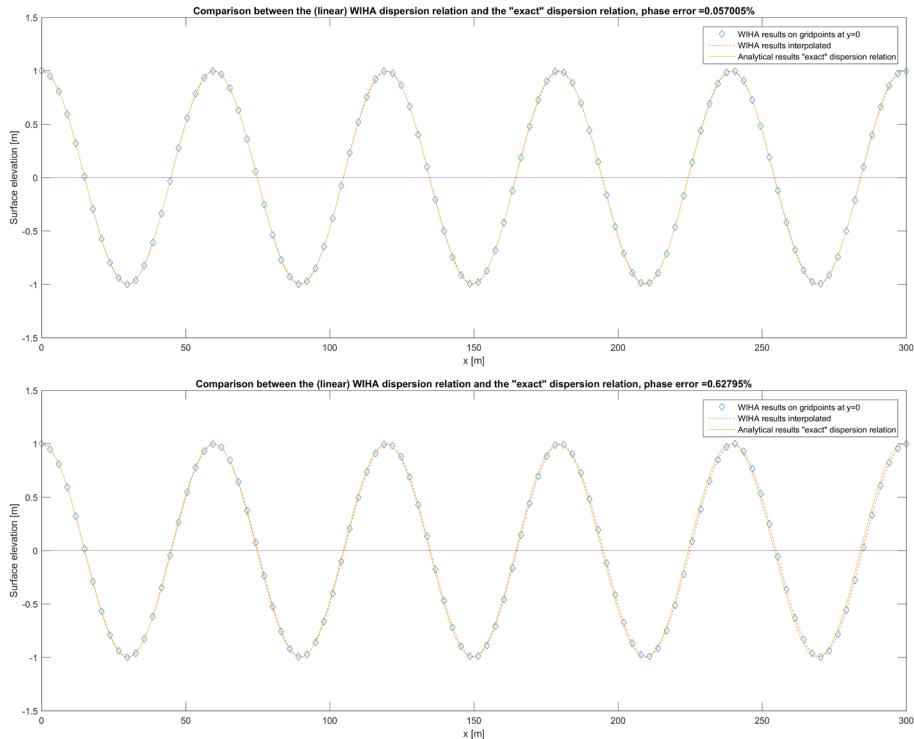


Figure 57: Obtained surface elevation plot for respectively the 'quadrature' variant at the top and the 'analytical' variant at the bottom both using 20 nodes per wavelength.

# D  WIHA accuracy analysis

## D.1 Van der Ven

### Variant 1

Figure 58 displays the geometry, bathymetry, output locations and computed significant wave height. A triangular grid is solved using the finite element method and has 14 nodes per wavelength. The South boundary is the incoming wave boundary where a JONSWAP spectrum with $H_{m0}$ = 0.032 m, $T_p$ = 1.49 s and $\gamma$ = 3.3 is considered. The incoming wave direction is 180 degrees without directional spreading.

The East and West boundaries (for x = 0.66 m and x = 39.33 m) are rubble slopes with a reflection coefficient of 0.20. The North boundaries (at y = 17 m left and right of the main basin and y = 30 m) also exist of a rubble slope with a reflection coefficient of 0.20. The six boundaries in and in front of the harbour exists of 90% reflective quay walls. Figure 59 displays the comparison between the by WIHA computed significant wave height and the measured wave height for each gauge. The obtained results are summarized in Table 19.
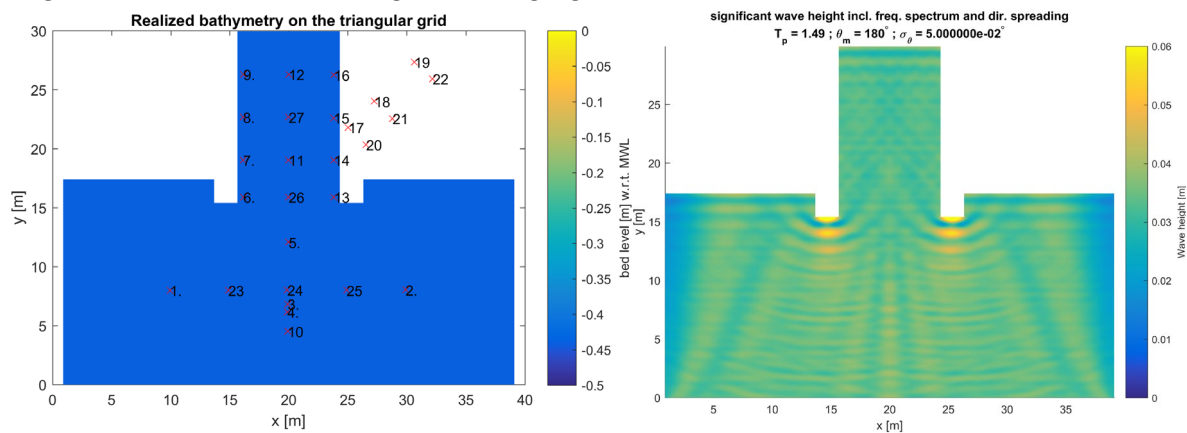


Figure 58: The realized bathymetry and considered output locations for Van der Ven case variant 1 (a) and the WIHA computed significant wave height for test T014 (b).
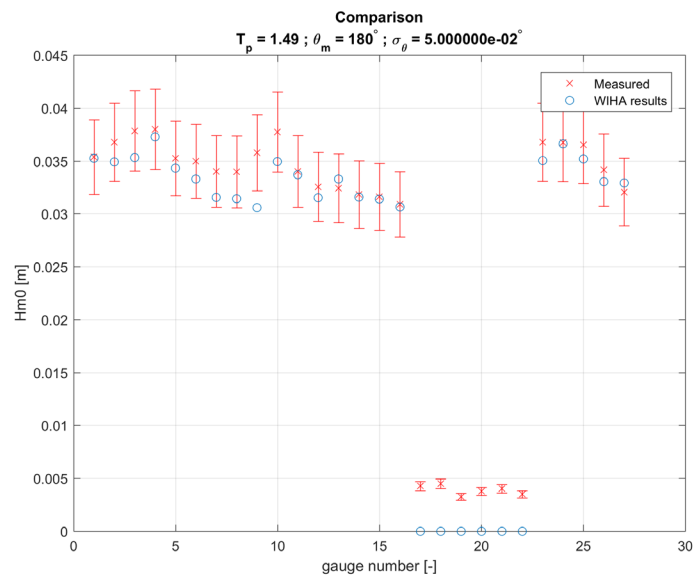


Figure 59: The comparison plot between the by WIHA computed significant wave heights and the measured significant wave heights at the 27 gauges for test T014.

### Variant 2

For the second variant a side basin is included, which among others causes diffraction. In Figure 60 the geometry, bathymetry, output locations and computed significant wave heights are displayed. The South boundary is the incoming wave boundary where a JONSWAP spectrum with $H_{m0}$ = 0.106 m, $T_p$ = 1.49 s and $\gamma$ = 3.3 is considered. The incoming wave direction is 180 degrees without directional spreading.

The side basin exists of 90% reflective quay walls. The remaining boundaries have the same reflection coefficients as for variant 1. Figure 61 displays the comparison between the WIHA computed significant wave height and the measured significant wave height for each specific gauge number. The obtained results are summarized in Table 19.
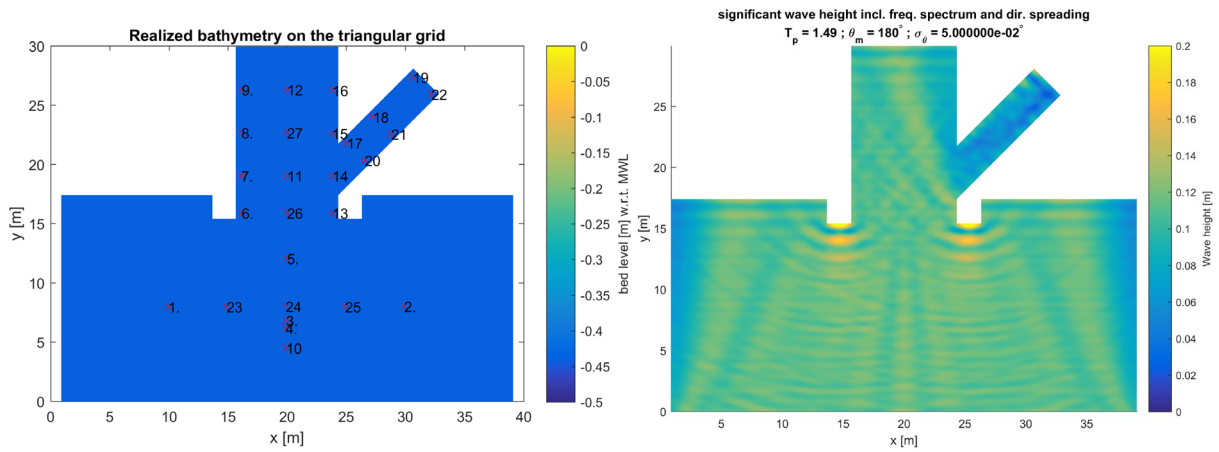


Figure 60: The realized bathymetry for the Van der Ven case variant 2 (a) and the by WIHA computed significant wave height for test T035 (b).
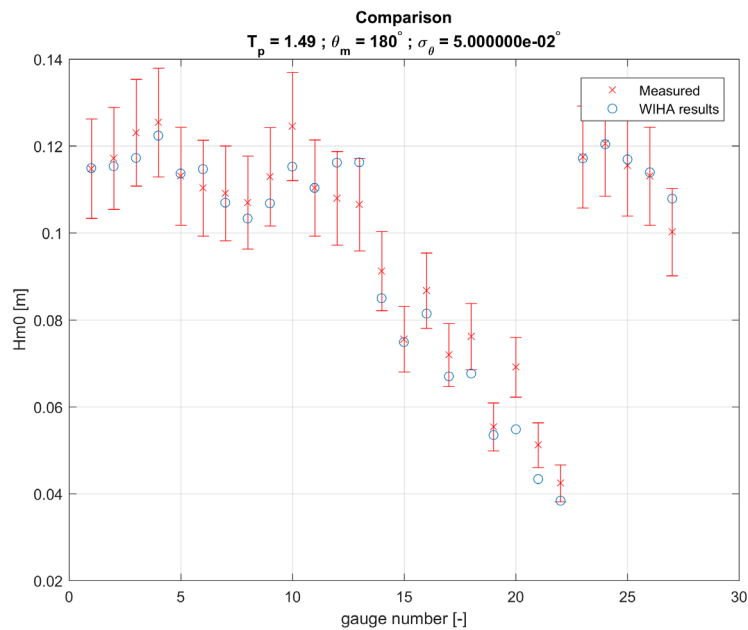


Figure 61: The comparison plot between the by WIHA computed significant wave heights and the measured significant wave heights at the 27 gauges for test T035.

**Variant 3**

In the third variant a breakwater is included, which among others causes refraction. Figure 62 displays the geometry, bathymetry, output locations and computed significant wave height. A triangular grid is solved using the finite element method which has 14 nodes per wavelength. The South boundary is the incoming wave boundary where a JONSWAP spectrum with $H_{m0} = 0.106$ m, $T_p = 1.49$ s and $\gamma = 3.3$ is considered. The incoming wave direction is 180 degrees without directional spreading.

The breakwater has a reflection coefficient of 0.30 and the reaming boundaries have the same reflection coefficients as for variant 1 and 2. Figure 63 presents the comparison between the by WIHA computed significant wave height and the measured significant wave height for each specific gauge. The obtained results are summarized in Table 19.
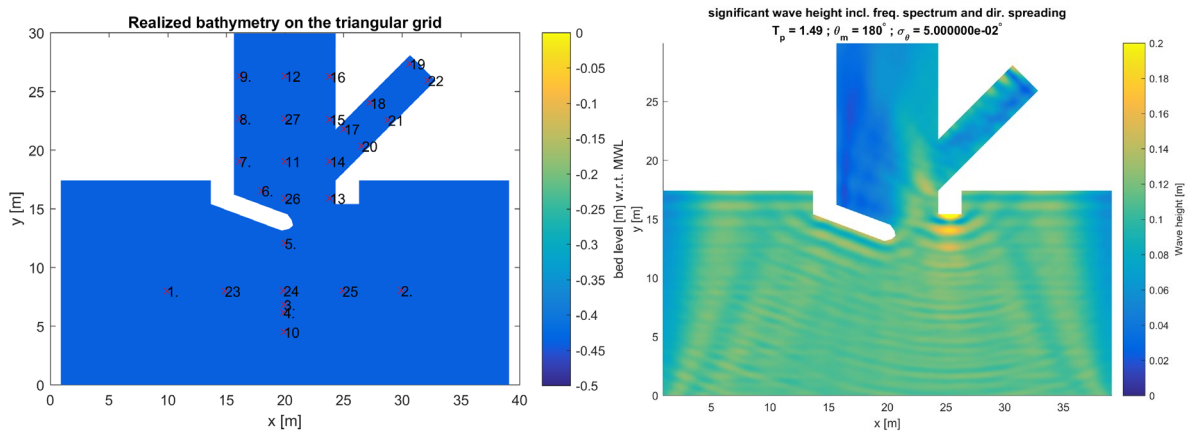


Figure 62: The realized bathymetry for the Van der Ven case variant 3 (a)
and the by WIHA computed significant wave height for test T079 (b).
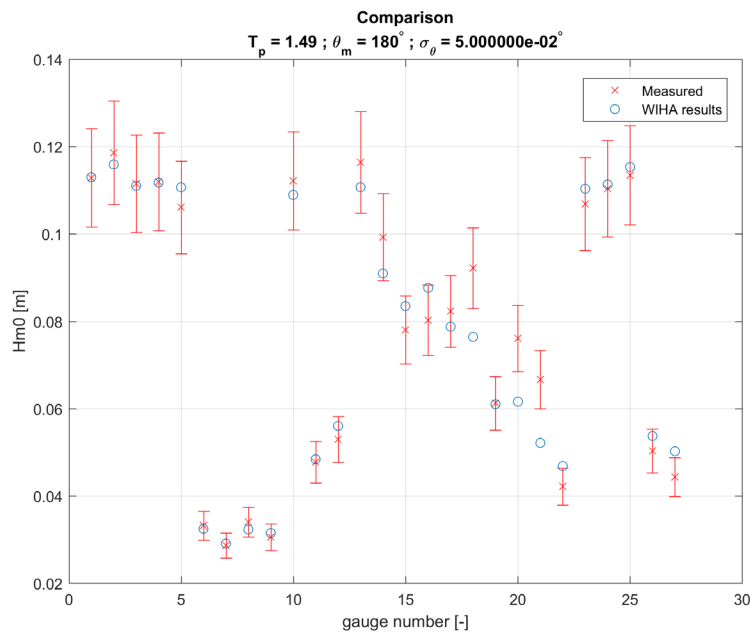


Figure 63: The comparison plot between the by WIHA computed significant wave heights
and the measured significant wave heights at the 27 gauges for test T079.

Table 19: The results from the physical model and the WIHA computations for the three variants, which presents the significant wave height ($H_m0$) and the (mean) error.

| Gauge No. | Van der Ven variant 1 | | | Van der Ven variant 2 | | | Van der Ven variant 3 | | |
|---|---|---|---|---|---|---|---|---|---|
| | PHM $H_{m0}$ [cm] | WIHA $H_{m0}$ [cm] | Error [%] | PHM $H_{m0}$ [cm] | WIHA $H_{m0}$ [cm] | Error [%] | PHM $H_{m0}$ [cm] | WIHA $H_{m0}$ [cm] | Error [%] |
| 1 | 3.54 | 3.52 | 0 | 11.48 | 11.49 | 0 | 11.29 | 11.30 | 1 |
| 2 | 3.68 | 3.49 | -5 | 11.72 | 11.54 | -2 | 11.86 | 11.59 | -2 |
| 3 | 3.78 | 3.53 | -7 | 12.31 | 11.72 | -5 | 11.15 | 11.10 | 0 |
| 4 | 3.80 | 3.73 | -2 | 12.54 | 12.24 | -2 | 11.19 | 11.17 | 0 |
| 5 | 3.53 | 3.43 | -3 | 11.31 | 11.36 | 1 | 10.61 | 11.06 | 4 |
| 6 | 3.50 | 3.33 | -5 | 11.03 | 11.47 | 4 | 3.32 | 3.25 | -2 |
| 7 | 3.40 | 3.16 | -7 | 10.91 | 10.69 | -2 | 2.87 | 2.91 | 1 |
| 8 | 3.40 | 3.14 | -8 | 10.70 | 10.33 | -3 | 3.40 | 3.24 | -5 |
| 9 | 3.58 | 3.06 | -15 | 11.29 | 10.68 | -5 | 3.06 | 3.15 | 3 |
| 10 | 3.77 | 3.49 | -7 | 12.45 | 11.52 | -7 | 11.22 | 10.89 | -3 |
| 11 | 3.40 | 3.37 | -1 | 11.03 | 11.04 | 0 | 4.77 | 4.84 | 1 |
| 12 | 3.26 | 3.15 | -3 | 10.80 | 11.61 | 8 | 5.30 | 5.60 | 6 |
| 13 | 3.24 | 3.33 | 3 | 10.66 | 11.62 | 9 | 11.64 | 11.07 | -5 |
| 14 | 3.18 | 3.16 | -1 | 9.12 | 8.50 | -7 | 9.93 | 9.09 | -8 |
| 15 | 3.16 | 3.14 | -1 | 7.55 | 7.49 | -1 | 7.80 | 8.35 | 7 |
| 16 | 3.09 | 3.07 | -1 | 8.67 | 8.14 | -6 | 8.03 | 8.76 | 9 |
| 17 | 0.00 | 0.00 | 0 | 7.19 | 6.70 | -7 | 8.23 | 7.88 | -4 |
| 18 | 0.00 | 0.00 | 0 | 7.62 | 6.77 | -11 | 9.22 | 7.65 | -17 |
| 19 | 0.00 | 0.00 | 0 | 5.54 | 5.35 | -3 | 6.12 | 6.10 | 0 |
| 20 | 0.00 | 0.00 | 0 | 6.91 | 5.48 | -21 | 7.61 | 6.16 | -19 |
| 21 | 0.00 | 0.00 | 0 | 5.12 | 4.33 | -15 | 6.67 | 5.22 | -22 |
| 22 | 0.00 | 0.00 | 0 | 4.24 | 3.83 | -10 | 4.22 | 4.68 | 11 |
| 23 | 3.68 | 3.50 | -5 | 11.75 | 11.71 | 0 | 10.69 | 11.03 | 3 |
| 24 | 3.67 | 3.66 | 0 | 12.06 | 12.04 | 0 | 11.04 | 11.13 | 1 |
| 25 | 3.65 | 3.52 | -4 | 11.55 | 11.69 | 1 | 11.34 | 11.53 | 2 |
| 26 | 3.41 | 3.31 | -3 | 11.31 | 11.39 | 1 | 5.03 | 5.37 | 7 |
| 27 | 3.21 | 3.29 | 3 | 10.02 | 10.78 | 8 | 4.43 | 5.02 | 13 |
| Mean error | | | 3.9% | | | 5.2% | | | 5.8% |

# D.2 Berkhoff shoal

Figure 64 displays the geometry, bathymetry, output locations and computed significant wave height. A triangular grid is solved using the finite element method which has 14 nodes per wavelength. The North boundary is the incoming wave boundary which considers a monochromatic wave with a significant wave height of 0.0464 m, a peak period of 1 s and an incoming wave direction of 0° without directional spreading. The East and West boundary are guiding walls with a reflection coefficient of 1.00. And the South boundary is a natural beach with a reflection coefficient of 0.00. Figure 65 presents the comparison between the by WIHA computed significant wave height and the measured wave height for each specific gauge number in section 5 (the horizontal line: gauge number 1 - 28).
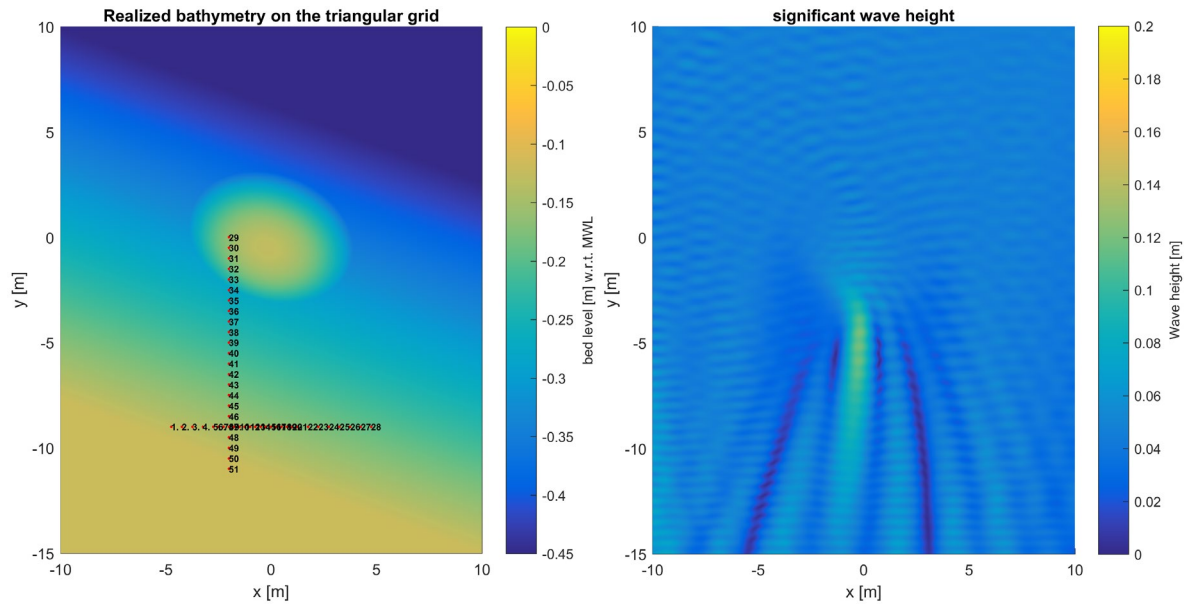


Figure 64: The realized bathymetry for the Berkhoff shoal including the output locations (a) and the by WIHA computed significant wave height for the Berkhoff shoal (b).
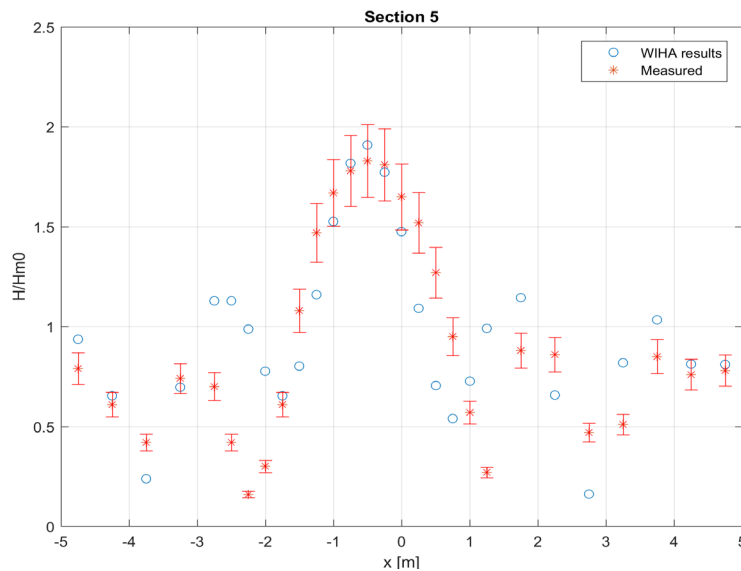


Figure 65: The comparison plot between the WIHA computed significant wave heights and the measured significant wave heights at the 28 gauges for the Berkhoff shoal.

# E  First validation SWDD directional wave-analysis
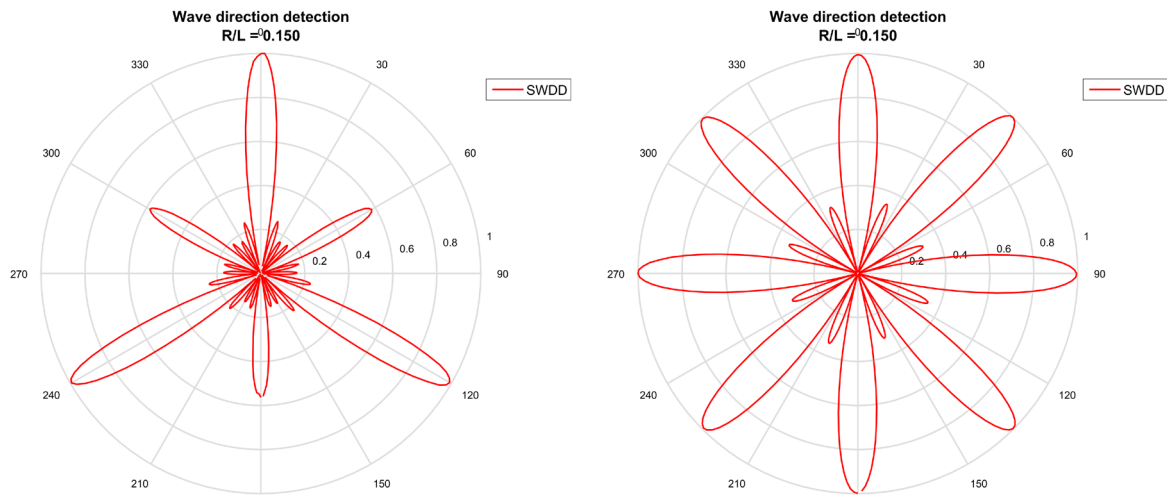


Figure 66: Two examples of the SWDD analysis results for six and eight prescribed wave components. The left figure (a) considers respectively 1.0, 0.5, 1.0, 0.5, 1.0 and 0.5 m wave amplitude and 0°, 60°, 120°, 180°, 240°, and 300° incoming wave direction. Where the right figure (b) considers respectively 1.0, 1.0, 1.0, 1.0, 1.0, 1.0, 1.0 and 1.0 m wave amplitude and 0°, 45°, 90°, 135°, 180°, 225°, 270°, and 315° incoming wave direction.

# F  Polar plots synthetic cases
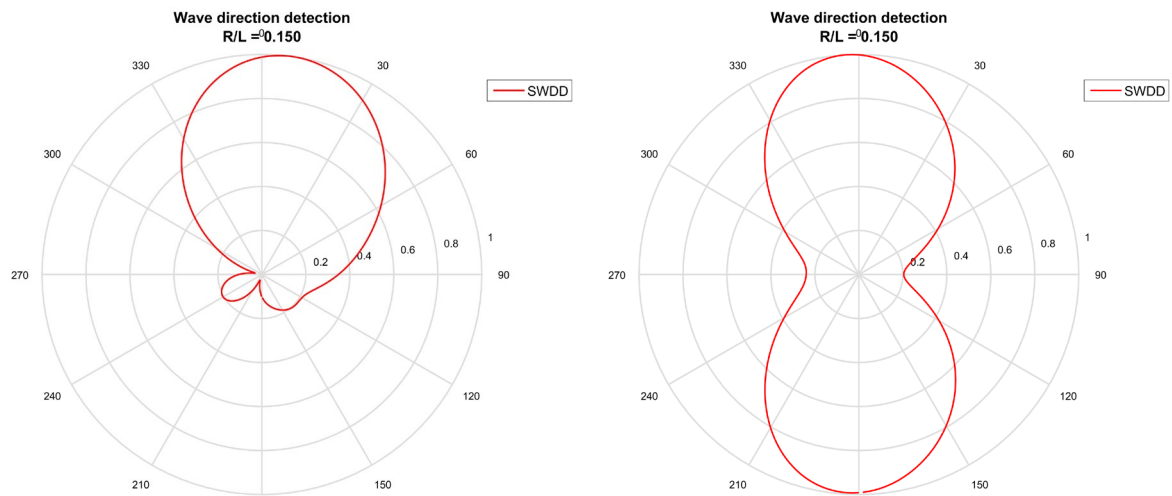


Figure 67: The results from the SWDD analysis using a CERC-6 array setup fort the two prescribed monochromatic incoming waves of respectively 1.0 m wave amplitude coming from the North (0°) and 0.5 m wave amplitude coming from the East (90°) (a) and for two prescribed monochromatic incoming waves of respectively 1.0 m wave amplitude coming from the North (0°) and 1.0 m wave amplitude coming from the East (180°) (b).

# G  Test description SWDD sensitivity analysis

The input variation in the various testcases performed for the wave source, wave dipole and WIHA output sensitivity analyses for the SWDD method are summarized in Table 20 to Table 26. The parameters which are kept constant are left empty in the tables. With $T$ is the wave period, $N$ is the number of gauges in the array setup, $R$ is the radius of the array setup, $R/L$ is the radius divided by the wavelength, $M$ is the number of wave directions used in the directional wave-analysis and $R_f$ is the reflection coefficient of the quay wall used in the considered domain.

In test T101 is the wave period (and thus the wavelength) varied. All other parameters are kept constant and left empty in Table 20.

Table 20: The input variation of the different runs with variation of specific parameters for test T101

| T101 | | | | | |
| --- | --- | --- | --- | --- | --- |
| | R01 | R02 | R03 | R04 | R05 |
| T [s] | 7 | 14 | 28 | 56 | 4 |
| N | 25 | | | | |
| R  [m] | 8.97 | | | | |
| R/L | 0.15 | 0.067 | 0.033 | 0.016 | 0.364 |
| M | 360 | | | | |

Table 21 below displays the input variation for test T102.1 where the array setup is being varied in the wave source and wave dipole testcases.

Table 21: The input variation of the different runs with variation of specific parameters for test T102.1

| T102.1 | | | | |
| --- | --- | --- | --- | --- |
| | R01 | R06 | R07 | R20 |
| T [s] | 7 | | | |
| N | 25 | 25 (1-ring) | 6 (CERC-6) | 361 (4-rings dense) |
| R  [m] | 8.97 | | | |
| R/L | 0.15 | | | |
| M | 360 | | | |

Table 22 below displays the input variation for test T102.1 where the reflection coefficient is being varied for the testcases using WIHA output as input for the SWDD method.

Table 22: The input variation of the different runs with variation of specific parameters for test T102.2

| T102.2 | | | |
| --- | --- | --- | --- |
| | R01 | R06 | R07 |
| T [s] | 7 | | |
| N | 25 | | |
| R  [m] | 8.97 | | |
| R/L | 0.15 | | |
| M | 360 | | |
| $R_f$ | 1.0 | 0.70 | 0.40 |

Table 23 below displays the input variation for test T103 where the period (and thus the wavelength) is varied, but now the radius of the circular domain is determined to get a constant $R/L$ of 0.15.

Table 23: The input variation of the different runs with variation of specific parameters for test T103

| T103 | | | | | |
|---|---|---|---|---|---|
|  | R01 | R08 | R09 | R10 | R11 |
| **T [s]** | 7 | 14 | 28 | 56 | 4 |
| **N** | 25 | | | | |
| **R [m]** | 8.97 | 20.09 | 41.24 | 83.02 | 3.70 |
| **R/L** | 0.15 | | | | |
| **M** | 360 | | | | |

Table 24 below displays the input variation for test T104 where the number of wave direction used for the analysis is varied.

Table 24: The input variation of the different runs with variation of specific parameters for test T104

| T104 | | | | | |
|---|---|---|---|---|---|
|  | R01 | R12 | R13 | R14 | R15 |
| **T [s]** | 7 | | | | |
| **N** | 25 | | | | |
| **R [m]** | 8.97 | | | | |
| **R/L** | 0.15 | | | | |
| **M** | 360 | 90 | 30 | 10 | 5 |

Table 25 below displays the input variation for test T105 where the radius (thus the number of grid nodes and $R/L$) is varied.

Table 25: The input variation of the different runs with variation of specific parameters for test T105

| T105 | | | | | |
|---|---|---|---|---|---|
|  | R01 | R16 | R17 | R18 | R19 |
| **T [s]** | 7 | | | | |
| **N** | 25 | | | | |
| **R [m]** | 8.97 | 17.945 | 35.89 | 4.49 | 2.24 |
| **R/L** | 0.15 | 0.30 | 0.60 | 0.075 | 0.038 |
| **M** | 360 | | | | |

Table 26 below displays the input variation for test T106 where the number of grid nodes and $R/L$ is varied.

Table 26: The input variation of the different runs with variation of specific parameters for test T106

| T106 | | | | | |
|---|---|---|---|---|---|
|  | R01 | R21 | R22 | R23 | R24 | R25 |
| **T [s]** | 7 | | | | | |
| **N** | 25 | 13 | 25 | 13 | 25 | 13 |
| **R [m]** | 8.97 | 8.97 | 14.96 | 14.96 | 3 | 3 |
| **R/L** | 0.15 | 0.15 | 0.25 | 0.25 | 0.05 | 0.05 |
| **M** | 360 | | | | | |

# H  Polar plots wave source and dipole

### T101
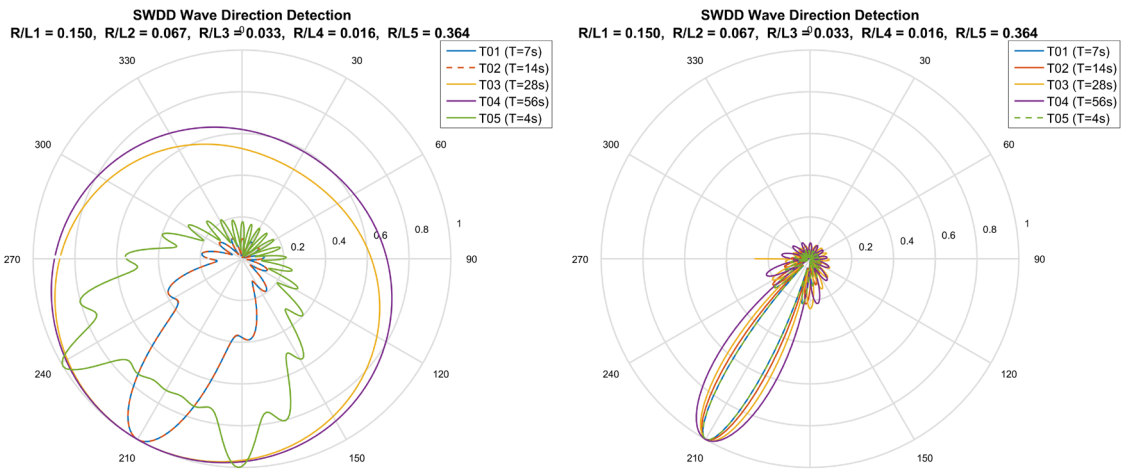


Figure 68: Wave source for respectively testcase E1 2 wavelengths (a) and testcase E2 80 wavelengths away (b).
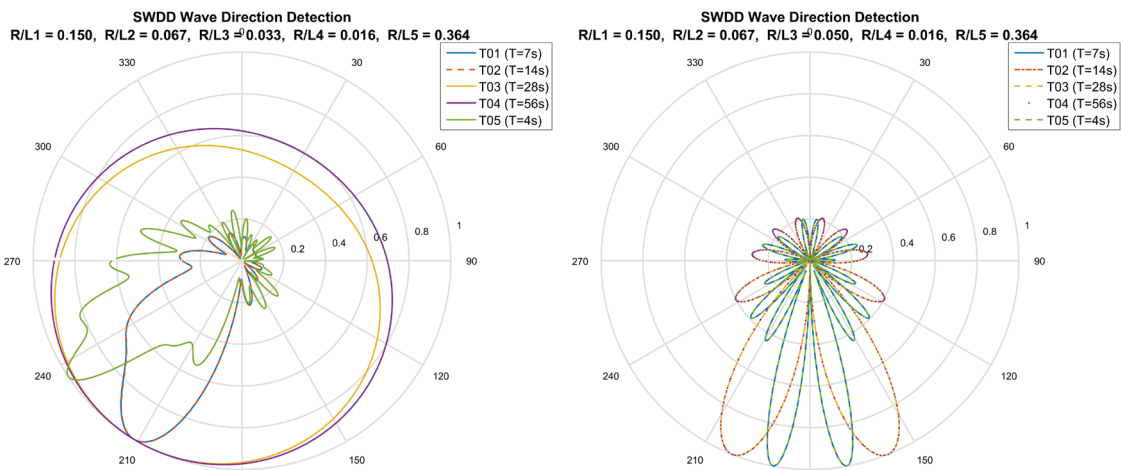


Figure 69: Wave dipole for respectively testcase F1 2 wavelengths (a) and testcase F2 80 wavelengths away, no angle (b)

**T102**
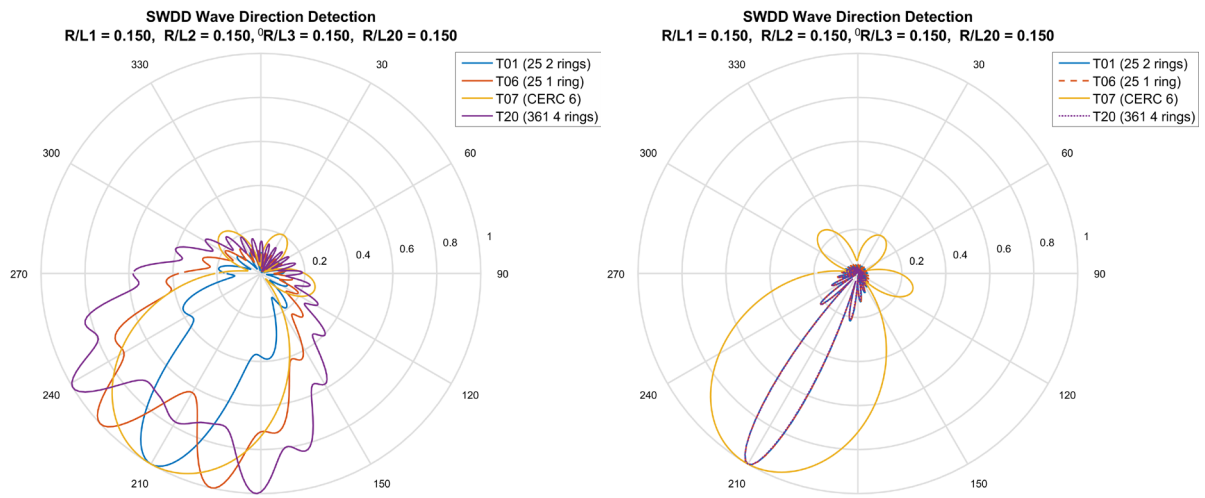


Figure 70: Wave source for respectively testcase E1 2 wavelengths (a) and testcase E2 80 wavelengths away (b).
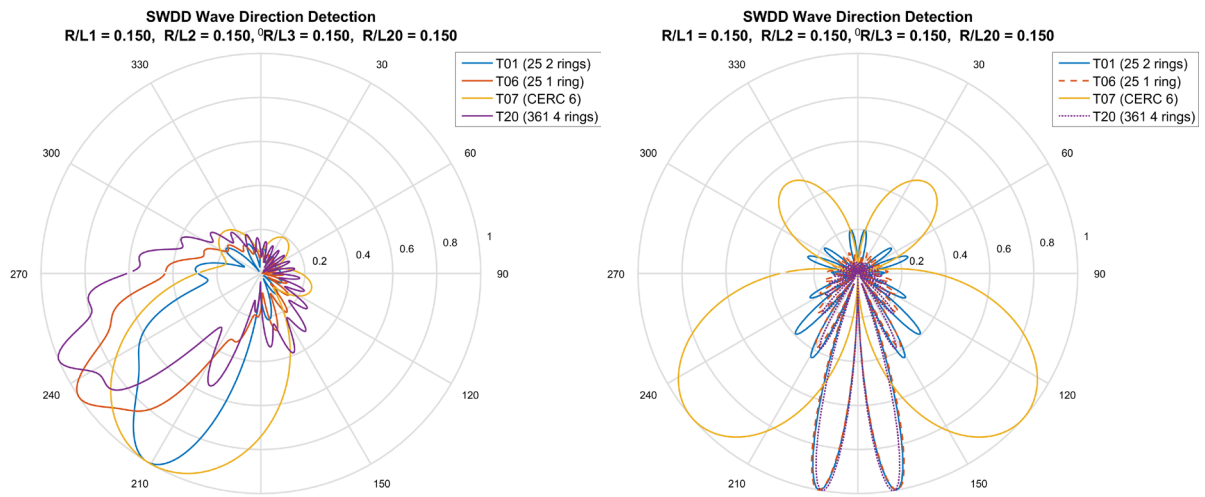


Figure 71: Wave dipole for respectively testcase F1 2 wavelengths (a) and testcase F2 80 wavelengths away (b).

**T103**
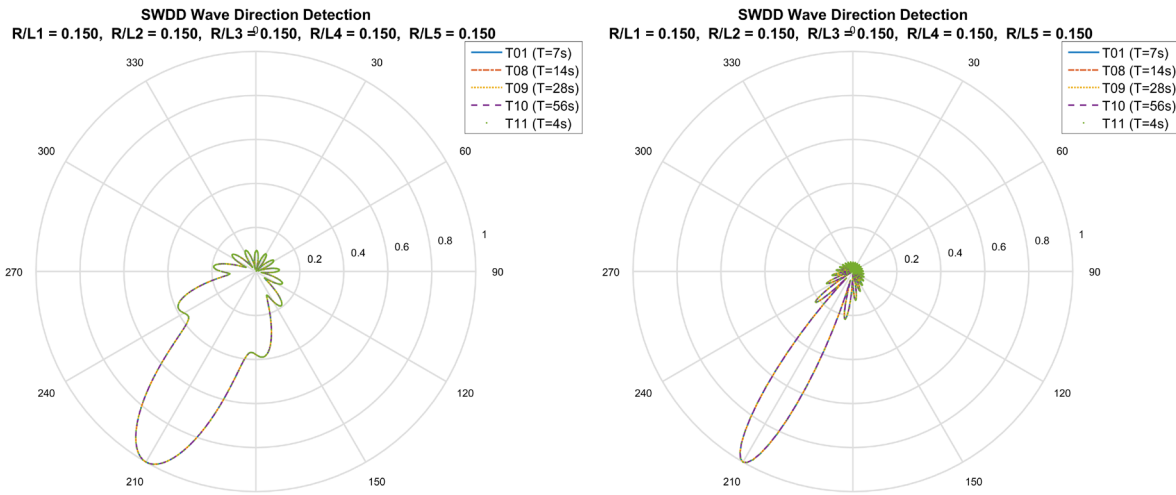


Figure 72: Wave source for respectively testcase E1 2 wavelengths (a) and testcase E2 80 wavelengths away (b).
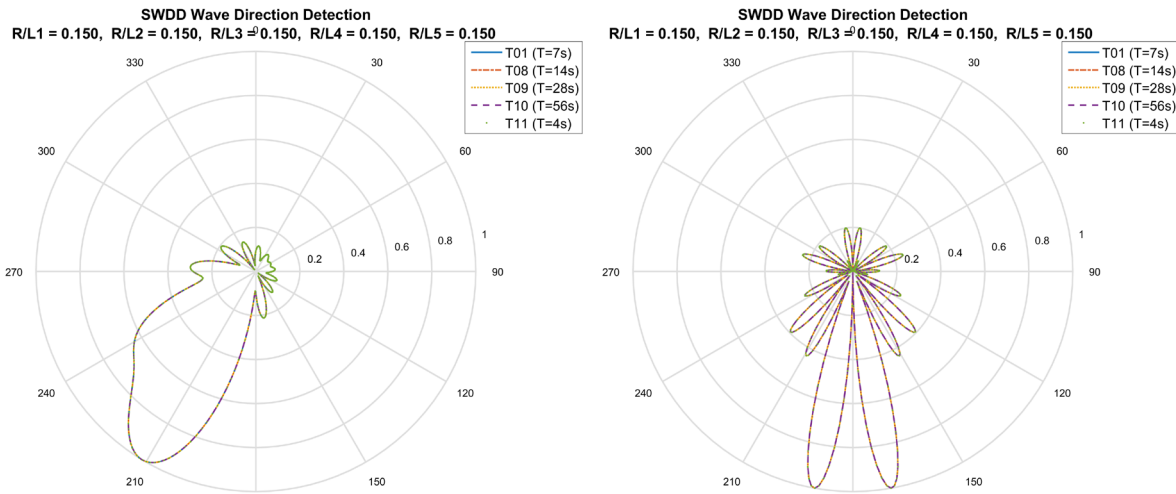


Figure 73: Wave dipole for respectively testcase F1 2 wavelengths (a) and testcase F2 80 wavelengths away (b).

**T104**
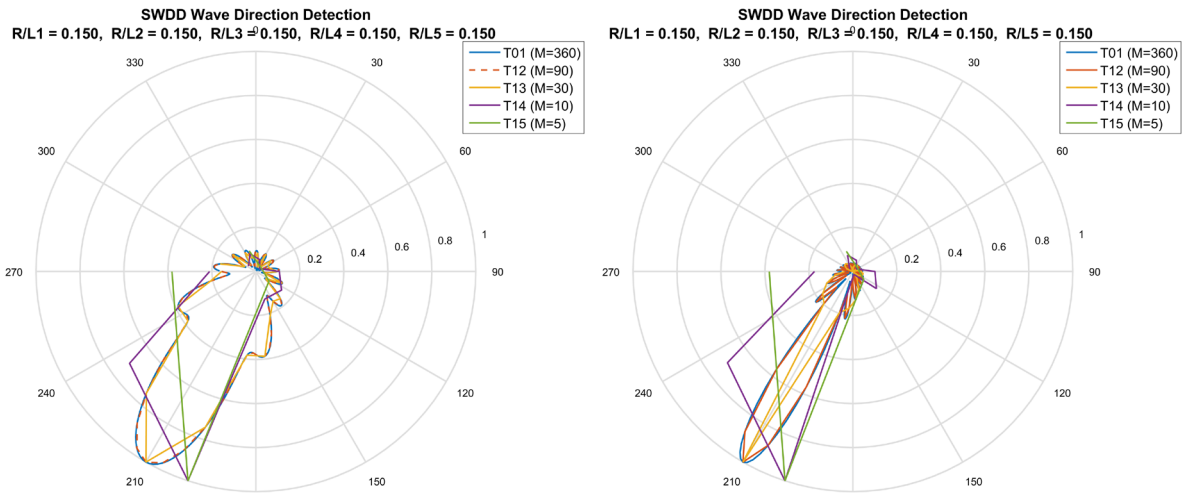


Figure 74: Wave source for respectively testcase E1 2 wavelengths (a) and testcase E2 80 wavelengths away (b).
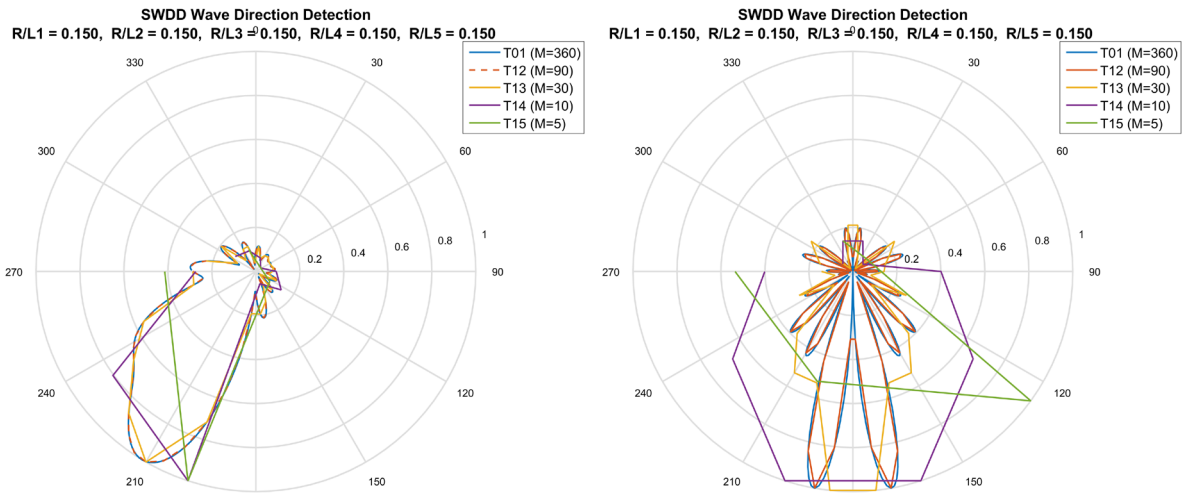


Figure 75: Wave dipole for respectively testcase F1 2 wavelengths (a) and testcase F2 80 wavelengths away (b).

**T105**
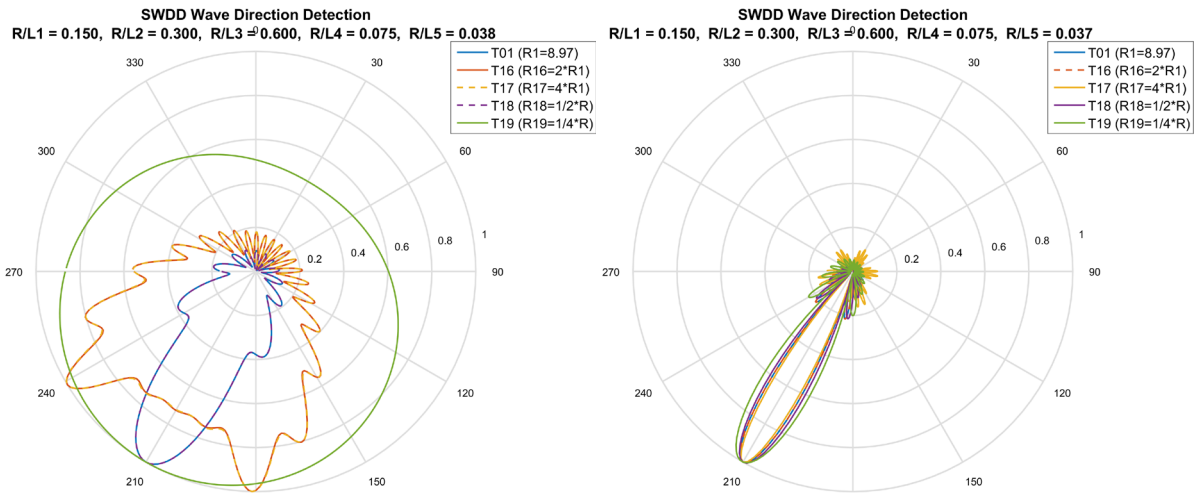


Figure 76: Wave source for respectively testcase E1 2 wavelengths (a) and testcase E2 80 wavelengths away (b).
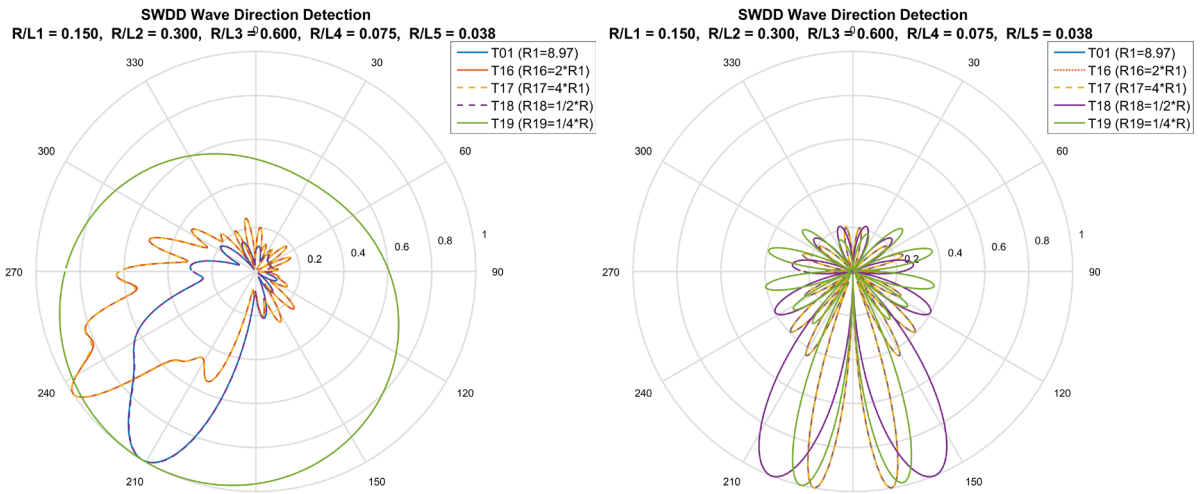


Figure 77: Wave dipole for respectively testcase F1 2 wavelengths (a) and testcase F2 80 wavelengths away (b).

**T106**
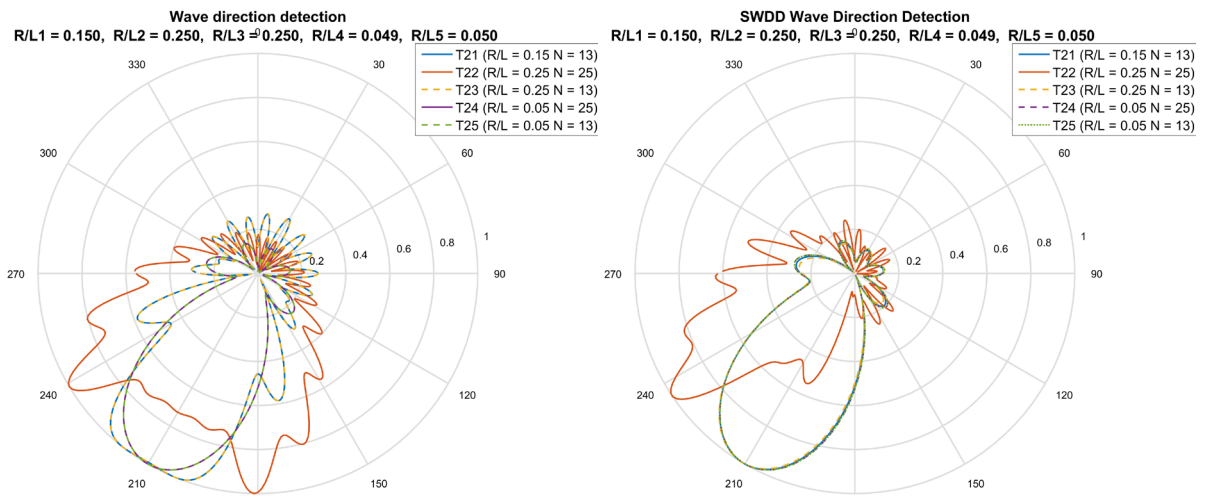


Figure 78: Wave source for respectively testcase E1 2 wavelengths (a) and testcase E2 80 wavelengths away (b).

# I  Reconstruction plot SWDD sensitivity analyses using a wave source and dipole

**Case E1: T101**
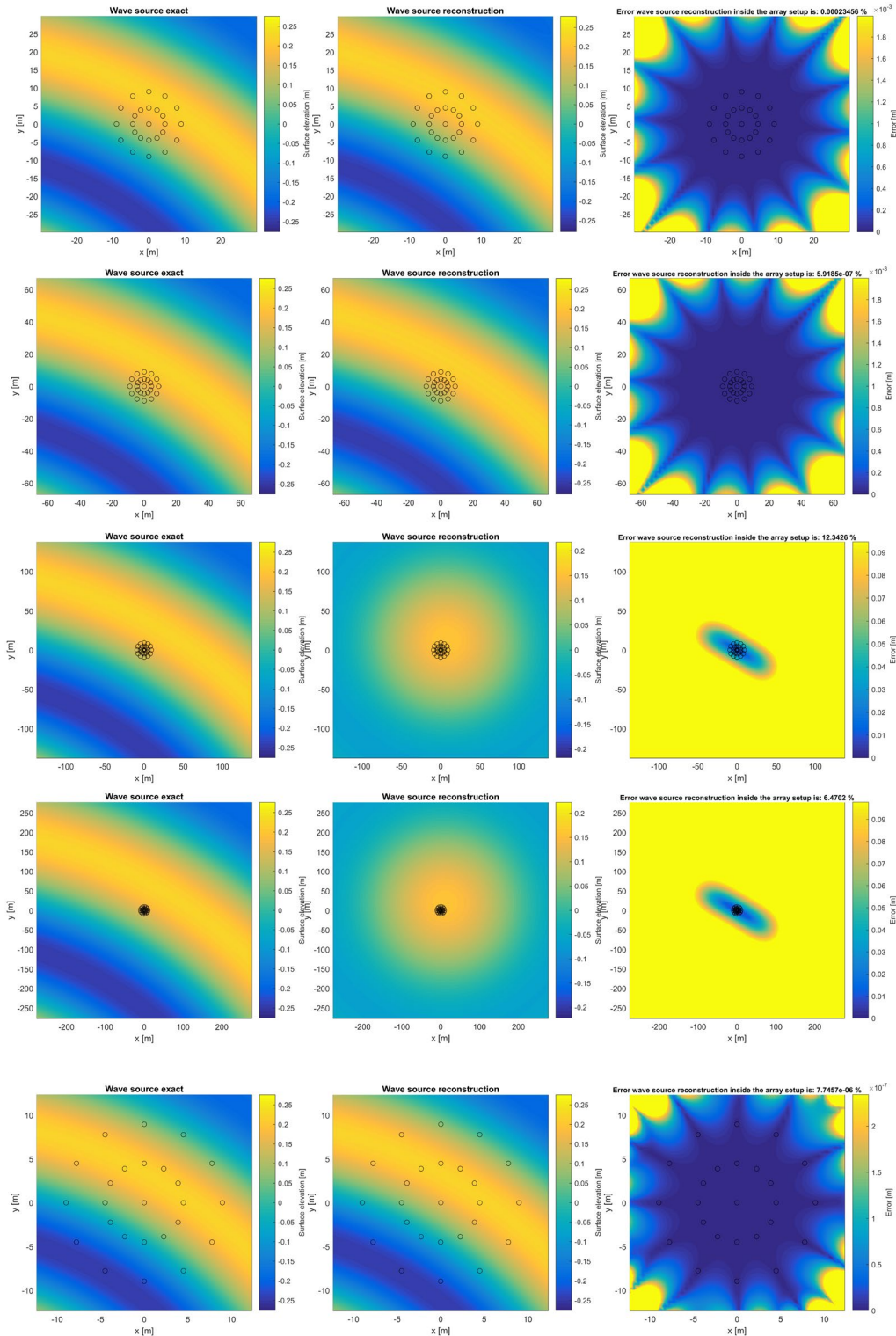


Figure 79: Respectively R01 - R05 for the wave source 2 wavelengths away under an angle of 30° for  caseE1: T101.

**Case E1: T102**
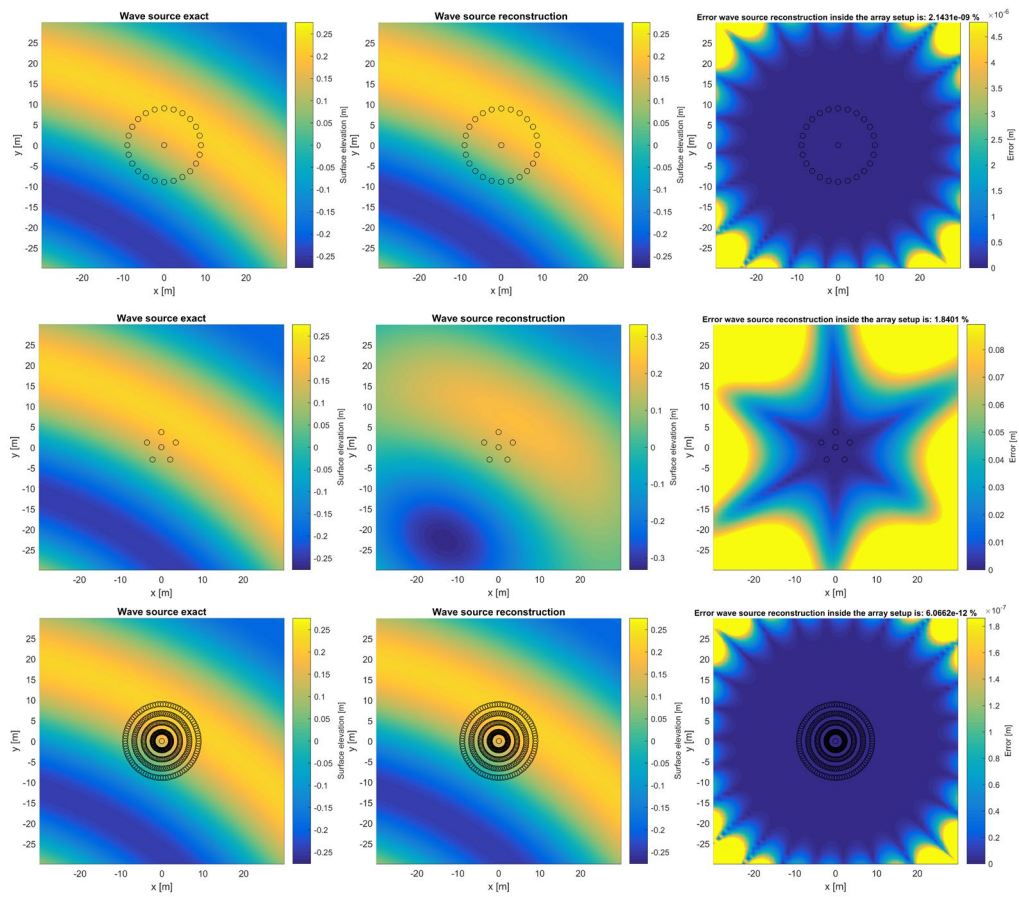


Figure 80: Respectively R06, R07, R20 for the wave source 2 wavelengths away under an angle of 30° for case E1: T102.

**Case E1: T103**
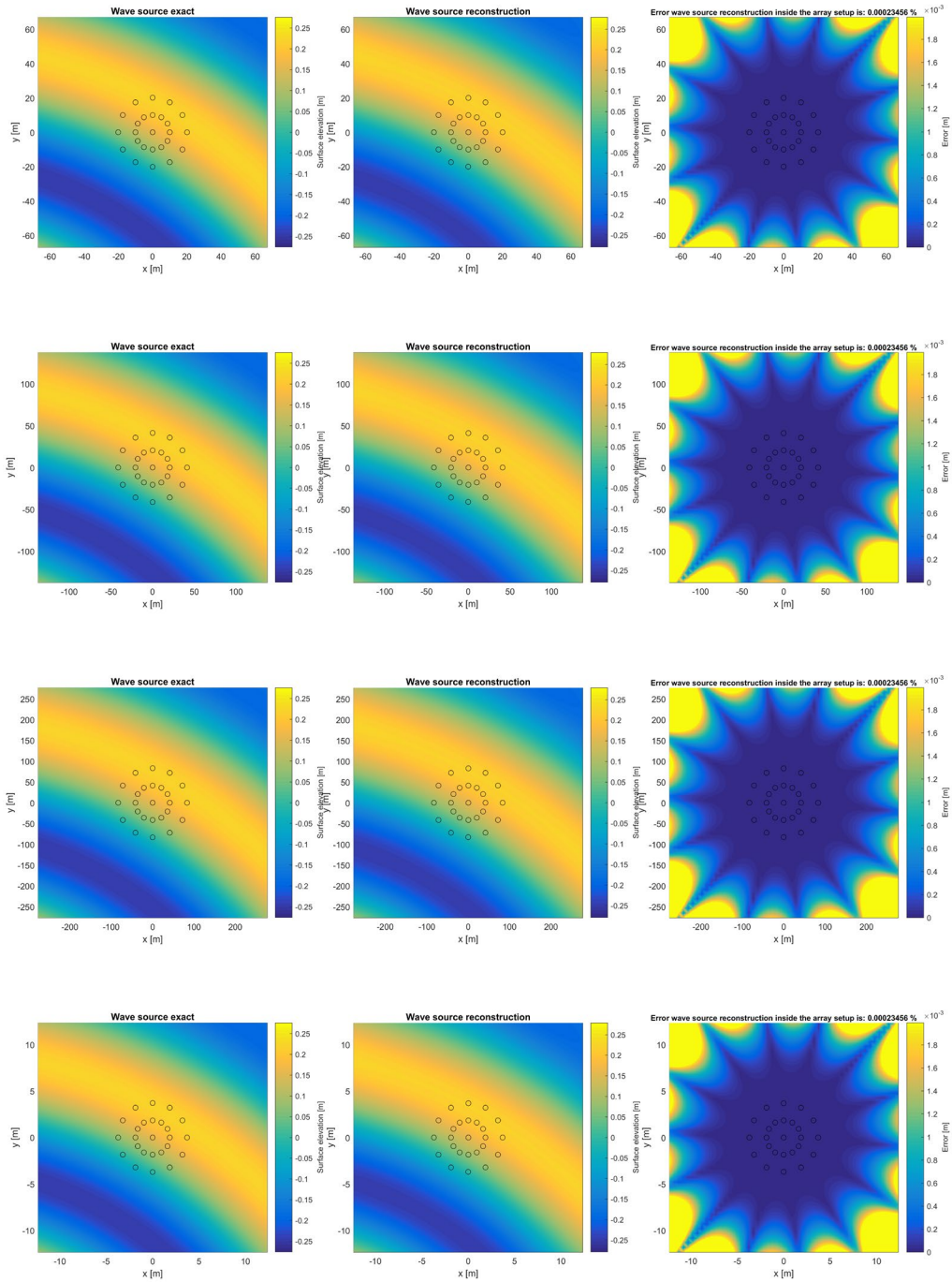


Figure 81: Respectively R08 - R11 for the wave source 2 wavelengths away under an angle of 30° for case E1: T103.

**Case E1: T105**
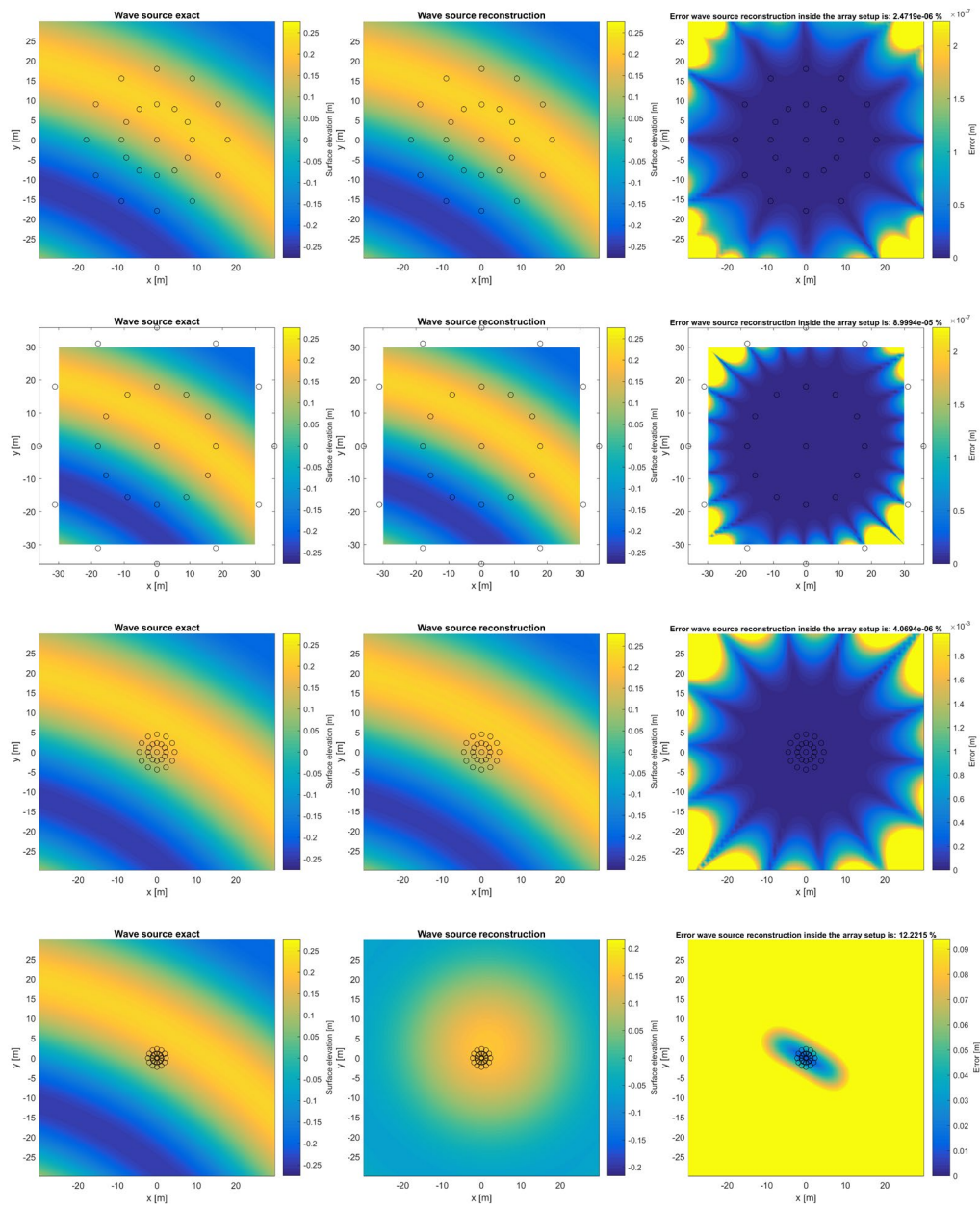


Figure 82: Respectively R16 - R19 for the wave source 2 wavelengths away under an angle of 30° for case E1: T105.

**Case E1: T106**
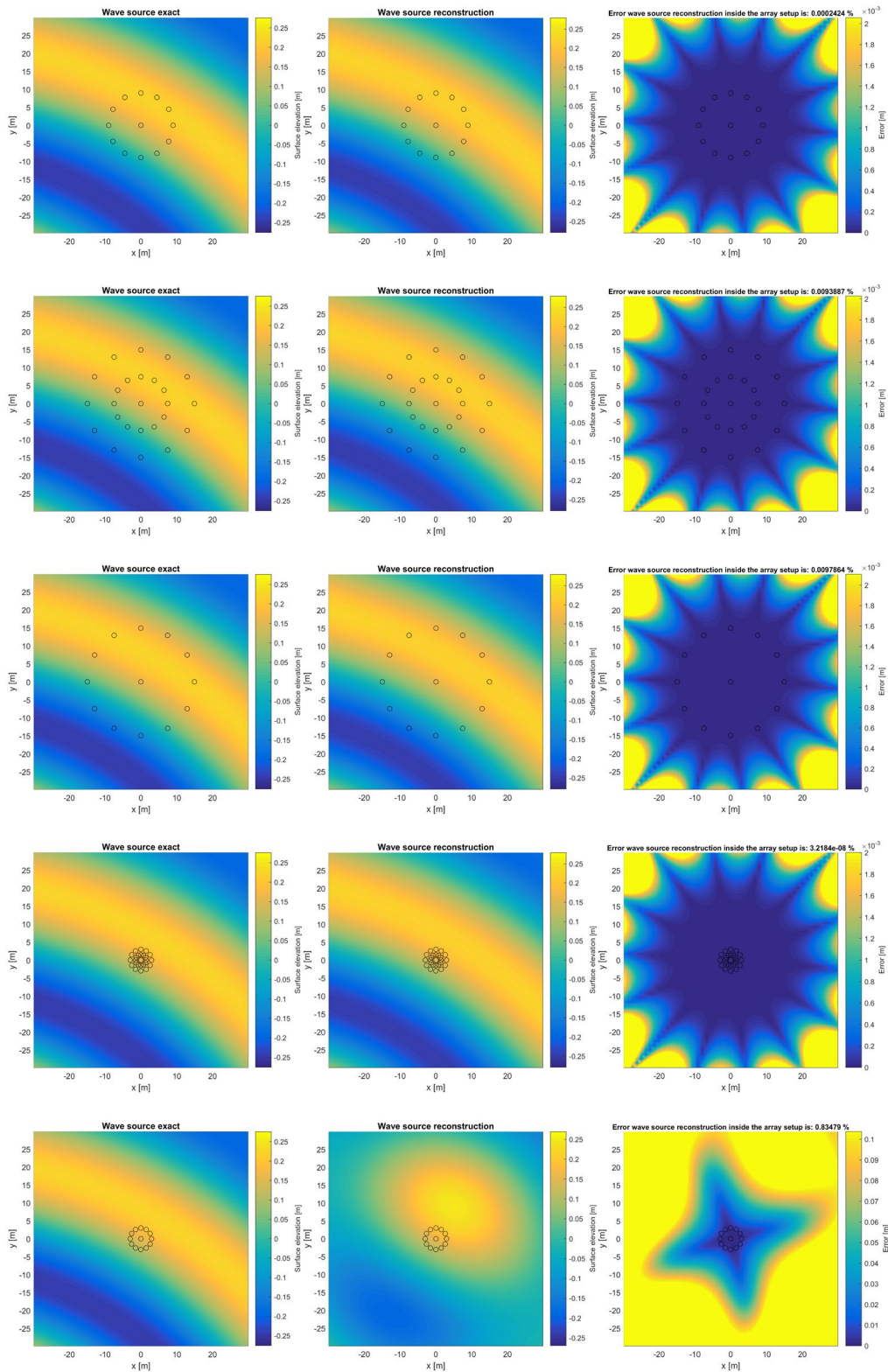


Figure 83: Respectively R21 - R25 for the wave source 2 wavelengths away under an angle of 30° for case E1: T106.

**Case F2: T101, T102, T103 and T105**

For the wave dipole 80 wavelengths away without an angle the obtained reconstructed errors are presented in a small size. The array setup is the same as for the wave source 2 wavelengths away under an angle of 30° from Figure 79 to Figure 82. Figure 84 displays the resulted wave field for T101, T102, T103 and T105 for testcase F3.
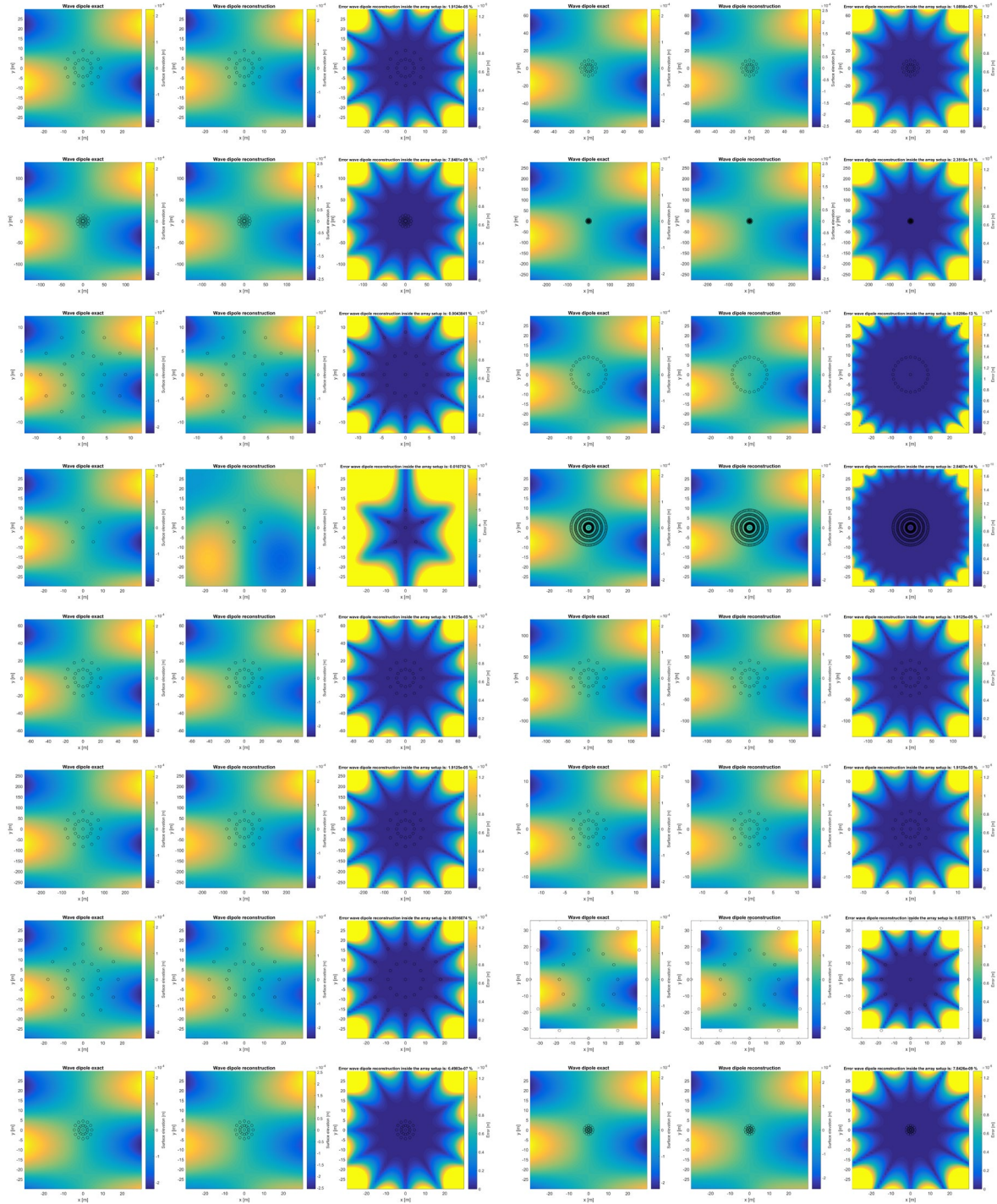


Figure 84: Respectively R01 - R11 and R16 - R19 for the wave dipole 80 wavelengths away
under an angle of 0° for case F2: T101, T102, T103 and T105.

# J  Correlations characteristics

The main lobe width is correlated to the number of lobes and the ratio between the main lobe divided by the total area by respectively -0.77 and 0.85.

### Hankel cases
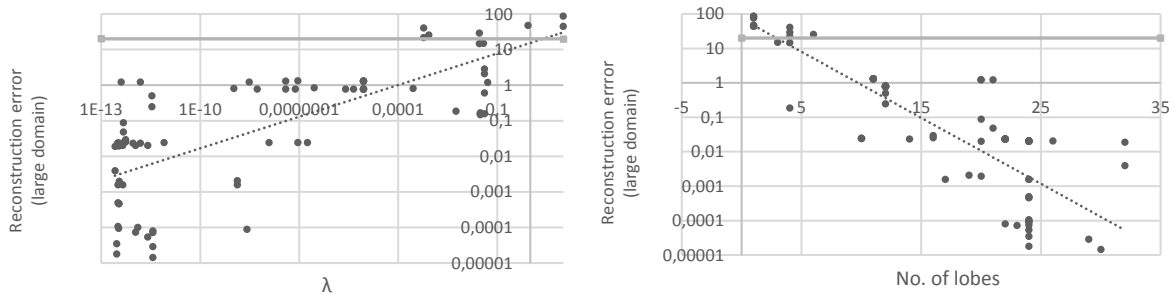


Figure 85: Shows the (correlation) plots between the reconstruction error on the large domain and respectively the lambda parameter of 0.82 (a) and the no. of lobes of -0.64 (b) considering the complete dataset from all cases performed using the Hankel function.
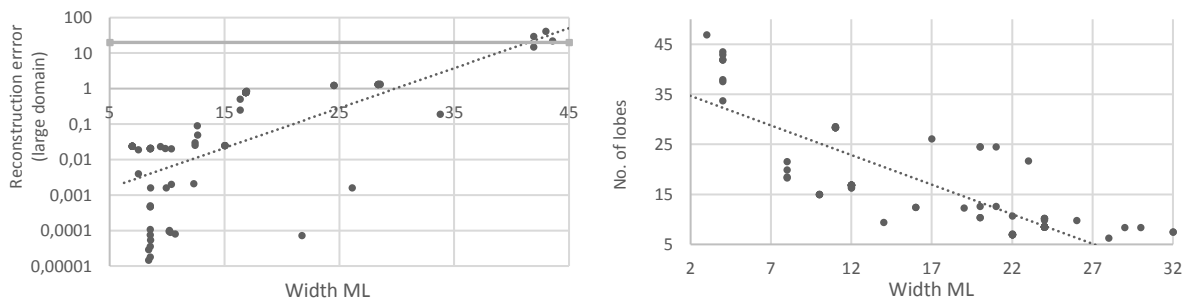


Figure 86: Shows the (correlation) plot between the reconstruction error on the large domain and main lobe width of 0.74 (a) and shows the (correlation) plot between the no. of lobes and the main lobe width of -0.77 (b) both considering the complete dataset from all cases performed using the Hankel function.

### WIHA cases
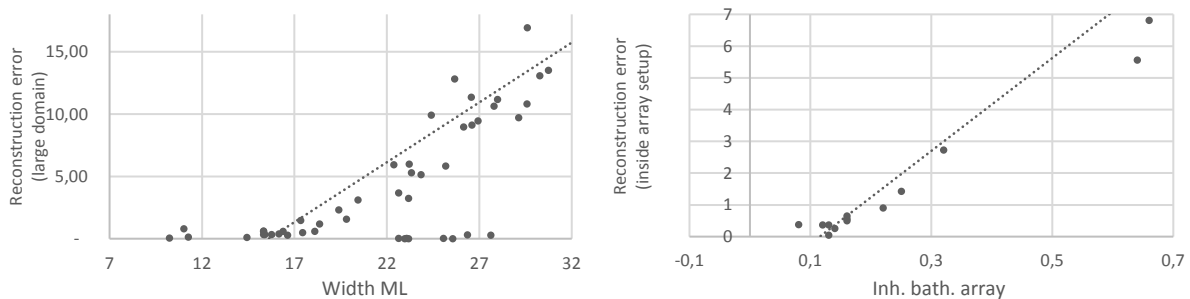


Figure 87: Shows the (correlation) plot between the reconstruction error on the large domain and the main lobe width considering the complete dataset from all cases performed using WIHA output of 0.84 (a) and the (correlation) plot between the reconstruction error inside the array setup and the inhomogeneity value for the bathymetry considering the complete dataset from all cases performed using WIHA output of 0.95.

# K  Wave dipole

Table 27 below presents the most important characteristics of the obtained polar plots from the SWDD analysis for case F1 where the Hankel *dipole* function is used with the output location located $2L$ away.

Table 27: The SWDD results for the different tests of case F1 where the most important characteristics of the presented polar plots are summarized with given values for the Hankel dipole nearby ($2L$) with a wave direction of 210° and a wave curvature of 0.50 (wavelength divided by the distance to the source). The 'standard' array exists of 25 gauges in 2-rings.

| Test | Run | Description | $\frac{R}{L}$ | $\lambda$ | N | No. of lobes | Width ML [°] | $\rho_{lobe}$ $\left(\frac{a_{maxSL}}{a_{ML}}\right)$ | Inh. curv. ang. $R/R_C$ | Error $\varepsilon_{recon,inside}$ [%] | Error $\varepsilon_{recon,large}$ [%] |
|---|---|---|---|---|---|---|---|---|---|---|---|
| **T101.F1** *varied T* | R01.3 | T = 7 s | 0.15 (8.97/60) | 8.67e-6 | 25 | 11 | 28.35 | 0.32 | 0.075 | 1.00e-3 | 1.33 |
| | R02.3 | T = 14 s | 0.067 (8.97/134) | 3.87e-8 | 25 | 11 | 28.52 | 0.32 | 0.034 | 5.68e-6 | 1.33 |
| | R03.3 | T = 28 s | 0.033 (8.97/272) | 16.98 | 25 | 1 | n.a. | 1.00 | 0.017 | 6.22 | 45.00 |
| | R04.3 | T = 56 s | 0.016 (8.97/561) | 9.84 | 25 | 1 | n.a. | 1.00 | 0.008 | 3.26 | 45.46 |
| | R05.3 | T = 4 s | 0.364 (8.97/25) | 1.52e-12 | 25 | 20 | 24.51 | n.a. | 0.182 | 2.28e-1 | 1.24 |
| **T102.F1** *Diff. array setup* | R06.3 | 1-ring | 0.15 (8.97/60) | 1.33e-9 | 25 | 17 | 26.11 | 0.35 | 0.075 | 1.70e-9 | 1.60e-3 |
| | R07.3 | CERC-6 | 0.15 (8.97/60) | 5.80e-4 | 6 | 4 | 43.54 | 0.26 | 0.075 | 0.97 | 22.18 |
| | R20.3 | dense 4-rings | 0.15 (8.97/60) | 3.63e-12 | 361 | 23 | 31.71 | n.a. | 0.075 | 5.47e-12 | 7.28e-5 |
| **T103.F1** *varied T, but* R/L *constant* | R08.3 | T = 14 s | 0.15 (20.09/134) | 8.67e-6 | 25 | 11 | 28.35 | 0.32 | 0.075 | 1.00e-3 | 1.33 |
| | R09.3 | T = 28 s | 0.15 (41.24/275) | 8.67e-6 | 25 | 11 | 28.35 | 0.32 | 0.075 | 1.00e-3 | 1.33 |
| | R10.3 | T = 56 s | 0.15 (83.02/553) | 8.67e-6 | 25 | 11 | 28.35 | 0.32 | 0.075 | 1.00e-3 | 1.33 |
| | R11.3 | T = 4 s | 0.15 (3.70/25) | 8.67e-6 | 25 | 11 | 28.35 | 0.32 | 0.075 | 1.00e-3 | 1.33 |
| **T105.F1** *varied R* | R16.3 | R = 2·R1 | 0.30 (17.95/60) | 3.95e-13 | 25 | 21 | 24.51 | n.a. | 0.15 | 8.37e-2 | 1.24 |
| | R17.3 | R = 4·R1 | 0.60 (35.89/60) | 3.01e-9 | 25 | 20 | 24.51 | n.a. | 0.30 | 1.24 | 1.24 |
| | R18.3 | R = ½ R1 | 0.075 (4.49/60) | 8.87e-8 | 25 | 11 | 28.52 | 0.32 | 0.038 | 3.39e-5 | 1.34 |
| | R19.3 | R = ¼ R1 | 0.038 (2.24/60) | 18.91 | 25 | 1 | n.a. | 1.00 | 0.019 | 6.16 | 44.85 |

Table 28 below presents the most important characteristics of the obtained polar plots from the SWDD analysis for case F2 where the Hankel *dipole* function is used with the output location located 80 wavelengths away (*y*-axis) without an angle.

Table 28: The SWDD results of case F2 where the most important characteristics of the presented polar plots are summarized with given values for a wave direction of 180°, $80L$ away. The 'standard' array exists of 25 gauges in 2-rings.

| Test | Run | Description | $\frac{R}{L}$ | $\lambda$ | N | No. of lobes | Width ML [°] | $\rho_{lobe}$ $\left(\frac{a_{maxSL}}{a_{ML}}\right)$ | $\rho_{ML}$ $\left(\frac{A_{ML}}{A_{total}}\right)$ | Error $\varepsilon_{recon,inside}$ [%] | Error $\varepsilon_{recon,large}$ [%] |
|---|---|---|---|---|---|---|---|---|---|---|---|
| **T101.F2** *varied T* | R01.4 | T = 7 s | 0.15 (8.97/60) | 3.16e-13 | 25 | 22 | 6.95 | 0.44 | 0.41 | 1.91e-5 | 2.37e-2 |
| | R02.4 | T = 14 s | 0.067 (8.97/134) | 8.93e-8 | 25 | 10 | 15.00 | 0.40 | 0.55 | 1.09e-7 | 2.47e-2 |
| | R03.4 | T = 28 s | 0.033 (8.97/272) | 1.21e-8 | 25 | 10 | 15.01 | 0.40 | 0.55 | 7.85e-9 | 2.47e-2 |
| | R04.4 | T = 56 s | 0.016 (8.97/561) | 7.86e-12 | 25 | 10 | 15.02 | 0.40 | 0.55 | 2.35e-11 | 2.47e-2 |
| | R05.4 | T = 4 s | 0.364 (8.97/25) | 1.52e-12 | 25 | 22 | 6.95 | 0.44 | 0.42 | 4.40e-3 | 2.37e-2 |
| **T102.F2** *Diff. array setup* | R06.4 | 1-ring | 0.15 (8.97/60) | 2.88e-13 | 25 | 22 | 7.12 | 0.39 | 0.46 | 9.03e-13 | 3.93e-6 |
| | R07.4 | CERC-6 | 0.15 (8.97/60) | 5.50e-3 | 6 | 4 | 33.75 | 0.52 | 0.72 | 1.08e-2 | 0.19 |
| | R20.4 | dense 4-rings | 0.15 (8.97/60) | 3.24e-12 | 361 | 28 | 6.25 | 0.38 | 0.51 | 2.85e-14 | 3.83e-7 |
| **T103.F2** *varied T, but* R/L *constant* | R08.4 | T = 14 s | 0.15 (20.09/134) | 3.16e-13 | 25 | 22 | 6.95 | 0.44 | 0.42 | 1.91e-5 | 2.37e-2 |
| | R09.4 | T = 28 s | 0.15 (41.24/275) | 3.16e-13 | 25 | 22 | 6.95 | 0.44 | 0.42 | 1.91e-5 | 2.37e-2 |
| | R10.4 | T = 56 s | 0.15 (83.02/553) | 3.16e-13 | 25 | 22 | 6.95 | 0.44 | 0.42 | 1.91e-5 | 2.37e-2 |
| | R11.4 | T = 4 s | 0.15 (3.70/25) | 3.16e-13 | 25 | 22 | 6.95 | 0.44 | 0.42 | 1.91e-5 | 2.37e-2 |
| **T105.F2** *varied R* | R16.4 | R = 2·R1 | 0.30 (17.95/60) | 9.12e-13 | 25 | 22 | 6.95 | 0.44 | 0.42 | 1.60e-3 | 2.37e-2 |
| | R17.4 | R = 4·R1 | 0.60 (35.89/60) | 4.27e-13 | 25 | 22 | 6.93 | 0.44 | 0.42 | 2.37e-2 | 2.37e-2 |
| | R18.4 | R = ½ R1 | 0.075 (4.49/60) | 1.73e-7 | 25 | 10 | 15.00 | 0.40 | 0.55 | 6.50e-7 | 2.47e-2 |
| | R19.4 | R = ¼ R1 | 0.038 (2.24/60) | 3.58e-13 | 25 | 14 | 9.39 | 0.40 | 0.39 | 7.84e-9 | 2.36e-2 |

### Intermediate findings wave dipole

The intermediate findings are based on the results from cases F1 ($2L$ away containing high wave-crest curvature and wave amplitude variation) and F2 ($80L$ away containing wave amplitude variation) summarized in Table 27 and Table 28 and the polar plots presented in appendix H. The findings from tests T101 - T103 and T105 are consecutively treated for both cases with emphasis on the differences between specific cases to be able to explain the effect of wave-crest curvature and wave amplitude variation.

A first indication for the accuracy limit of the reconstruction error inside the array and the reconstruction error on a large domain are respectively 2.0% and 20.0% (error in wave direction is unknown).

*First observations testcase F*

Considering both reconstruction errors and the proposed accuracy limits in case F2 (minimal wave-crest curvature) all runs – R01 up R19 – are analysed accurately by the SWDD method. Wave amplitude variations has no effects on the accuracy of the results of the SWDD method. When wave-crest curvature effects are present (in case F1), it becomes clear that especially the low $R/L$ values are negatively influenced, because for these runs not enough difference in the phase is present due to the small array setup. The reconstruction error on the large domain for the CERC-6 array setup is relatively high, due to the low number of gauges used.

It also strikes out that for T101 - T105 in case F1, when the angular inhomogeneity value ($R/R_c$) of wave-crest curvature in the array setup gets higher, the errors get lower (due to increasing radius of the array setup for a constant distance from the wave source to the array centre of $L/R_c = 0.50$). Where it can be concluded that according to this trend, the SWDD method has no problems with analysing wave-crest curvature effects, especially for larger radius values when more wave information is present for an array setup where the distance from the wave source to the array centre of $L/R_c = 0.50$. Like in case E1, it seems this inhomogeneity value ($R/R_c$) does not represent the error well.

*Testcase F test T101*

In test T101 in both cases F1 and F2, where the wavelength is varied – and thus the parameter $R/L$ is varied: 0.016 - 0.364 – it becomes clear that for higher values of $R/L$ the results get more accurate on a regular bathymetry, considering both reconstruction errors. In case F1, where wave-crest curvature and wave amplitude variation are present, the following range of applicability is found: $R/L > 0.033$.

The difference between the results of case F1 and F2 can be explained due to the presence of wave-crest curvature, the reconstruction errors becomes larger when wave-crest curvature is present, especially considering lower $R/L$ values ( < 0.033).

*Testcase F test T102*

Test T102.F1 and T102.F2 show that the CERC-6 array setup results are less accurate compared to the results of the other considered array setups, containing a reconstruction error of respectively 0.97% and 0.02% inside the array setup and a reconstruction error on the large domain *(L* by *L)* of 22.18% and 0.19%. Considering the proposed accuracy limitations, it becomes clear that the reconstruction error inside the array setup and the found direction are both accurate. However, the error in the reconstruction on the large domain becomes inaccurate, which can be explained due to the low number of gauges present. If only interested in the main direction for monochromatic waves the CERC-6 is considered suitable. However, high directional resolutions are not possible. The errors found for the circular arrays and the dense array are all negligible.

*Testcase F test T103*

In test T103, for both cases F1 and F2, it becomes clear that the wavelength has no influence on the accuracy of the results of the SWDD method when the $R/L$ value of the array setup is kept constant at 0.15 for a constant bathymetry and number of gauges.

*Testcase F test T105*

In test T105.F1, where wave-crest curvature is present and the radius of the array setup has been varied up to *2.40L*, the following range of applicability is found: *0.075 ≤ R/L ≤ 1.50*. The lower limit is present due to the fact that not enough variation in the phase is present for the SWDD method to analyse. And the higher limit is present due to the relatively low number of wave gauges for such large radius-values. When a dense array setup is considered this upper limitation is expected to extend to a higher value.

# L Polar plots WIHA cases

## T101
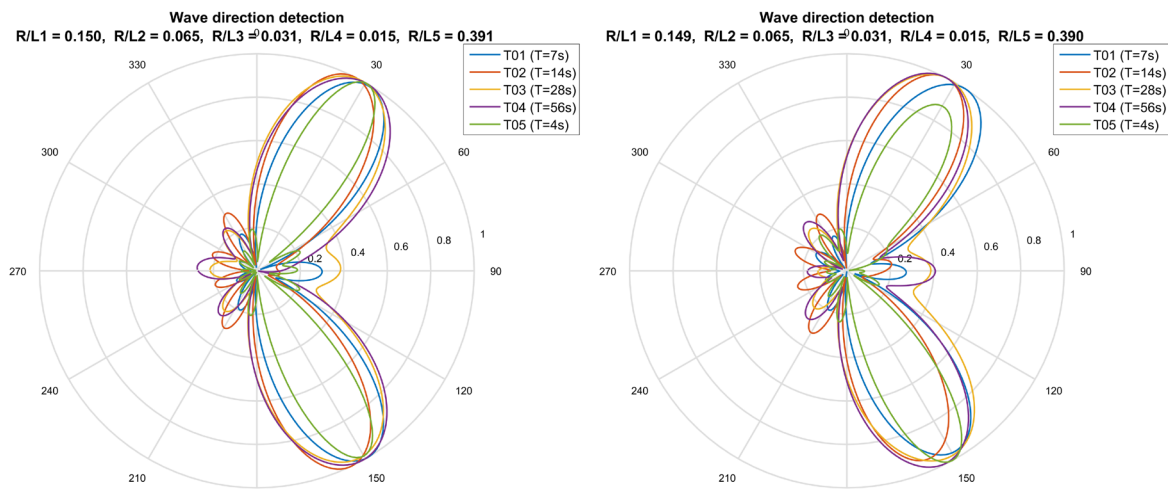


Figure 88: Respectively the obtained polar plot for test T101 testcase G1 and G2.
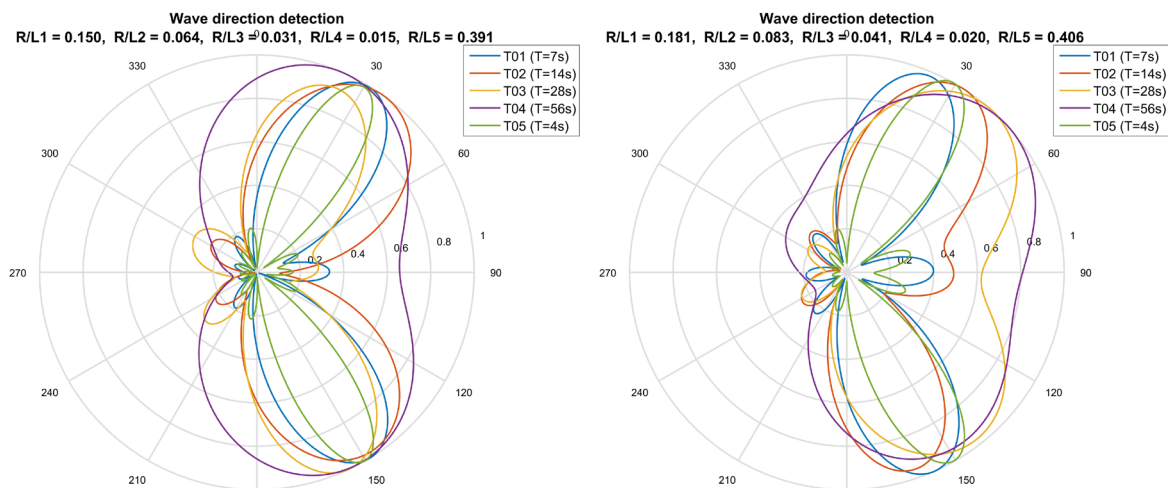


Figure 89: Respectively the obtained polar plot for test T101 testcase G3 and G4.

**T102**
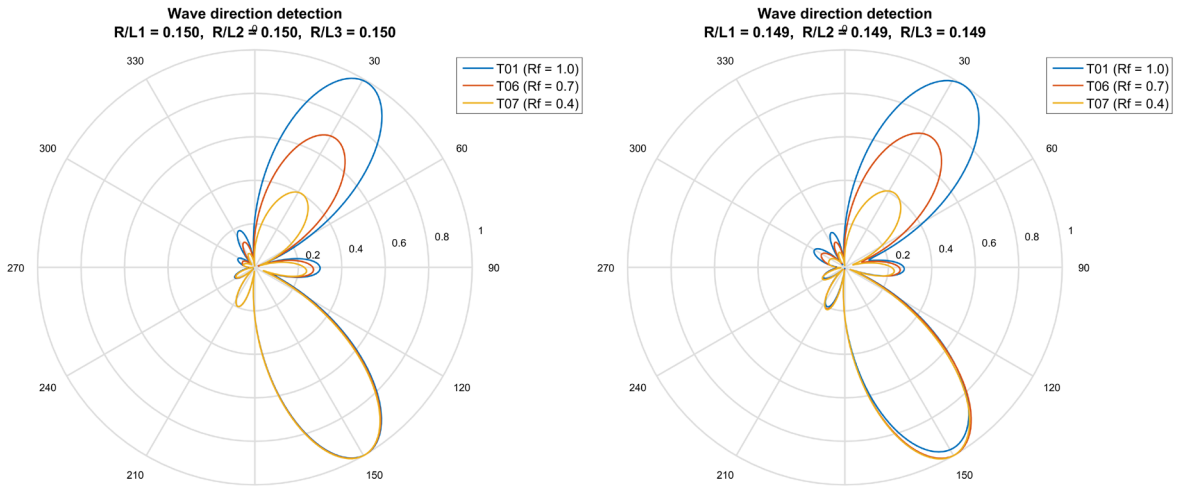


Figure 90: Respectively the obtained polar plot for test T102 testcase G1 and G2.
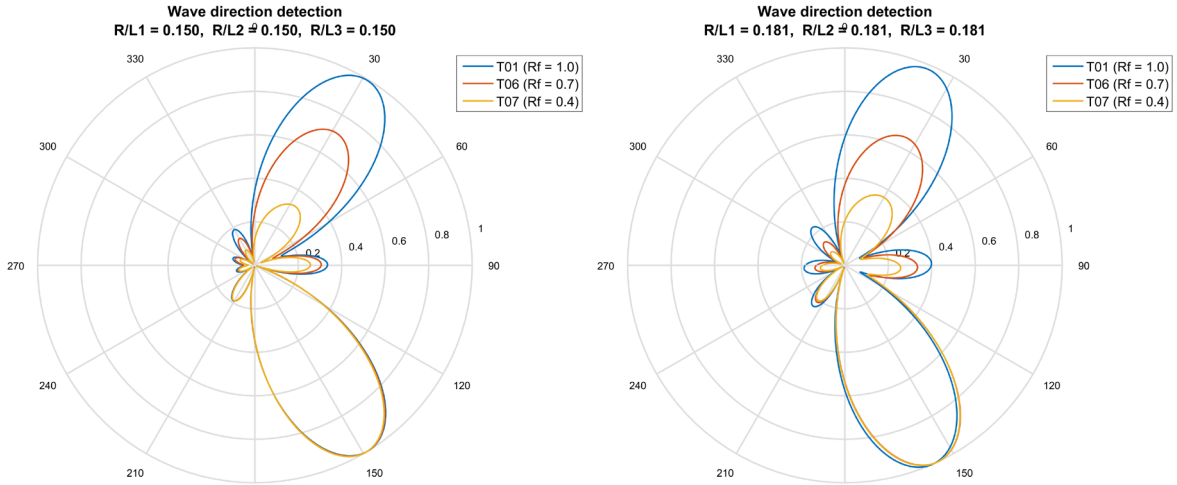


Figure 91: Respectively the obtained polar plot for test T102 testcase G3 and G4.

# T103
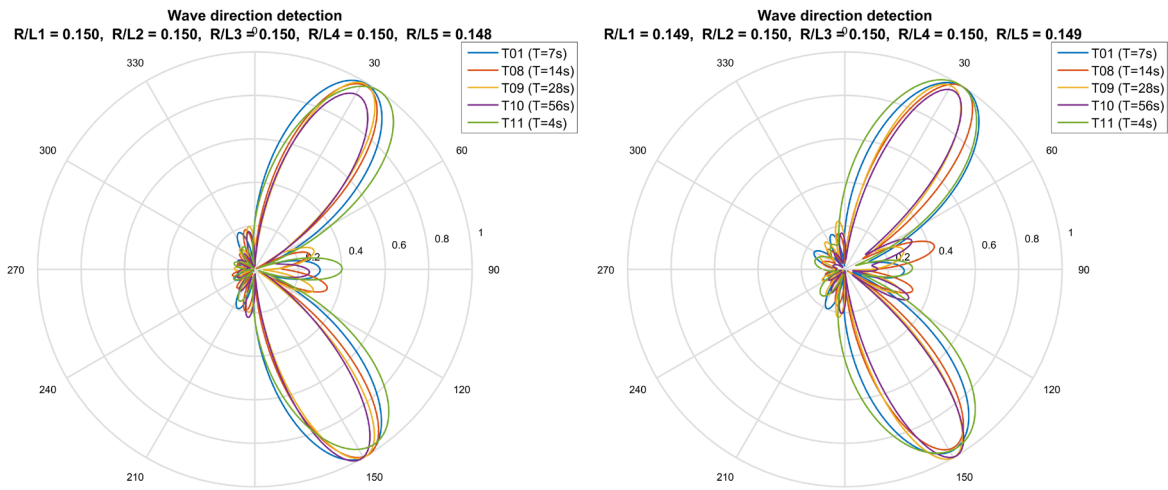


Figure 92: Respectively the obtained polar plot for test T103 testcase G1 and G2.
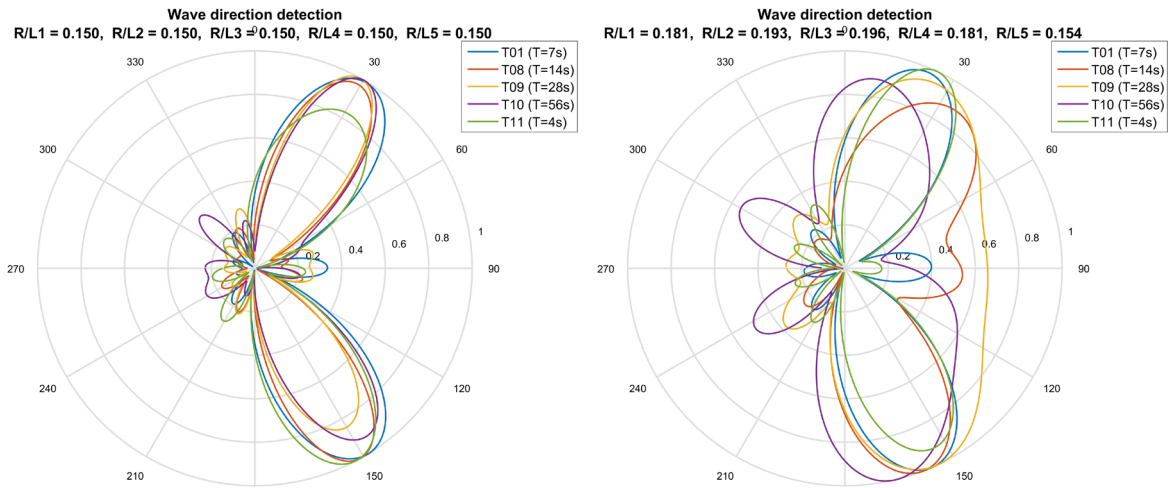


Figure 93: Respectively the obtained polar plot for test T103 testcase G3 and G4.

**T104**
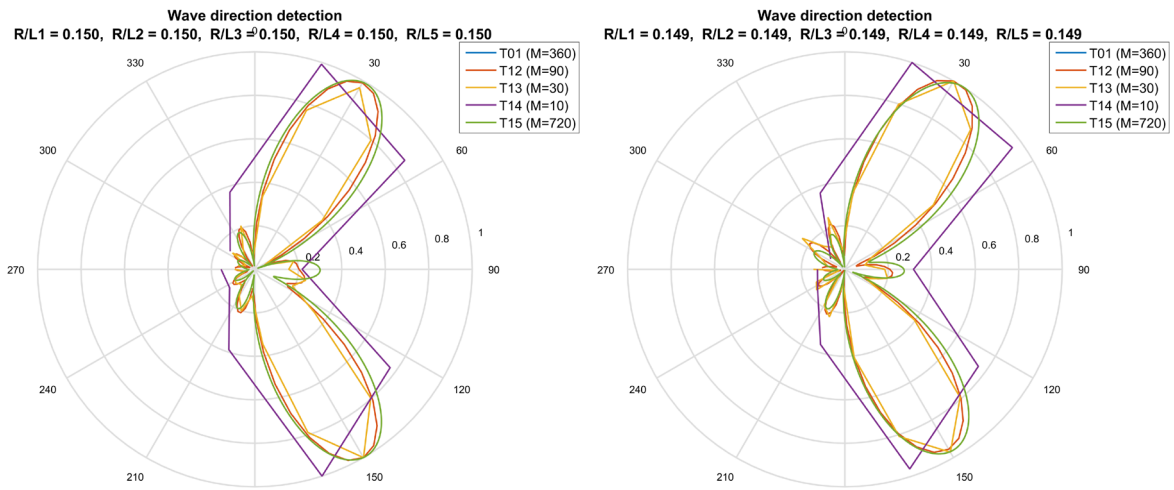


Figure 94: Respectively the obtained polar plot for test T104 testcase G1 and G2.
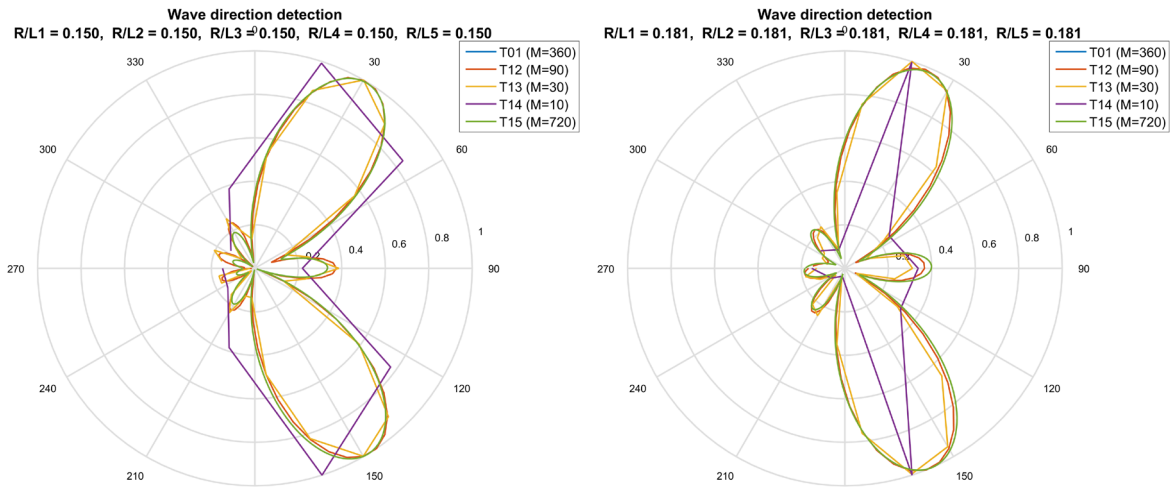


Figure 95: Respectively the obtained polar plot for test T104 testcase G3 and G4.

**T105**
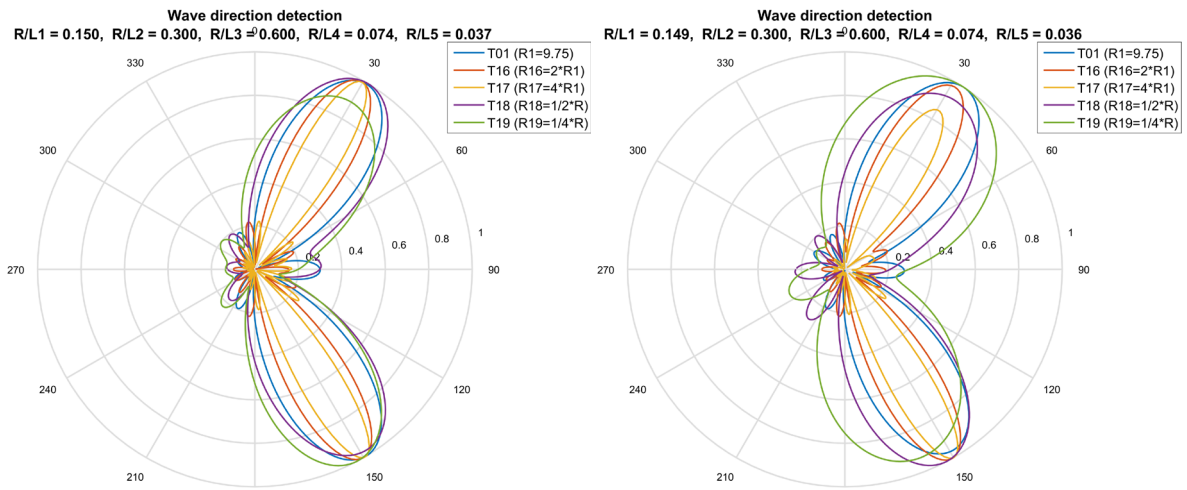


Figure 96: Respectively the obtained polar plot for test T105 testcase G1 and G2.
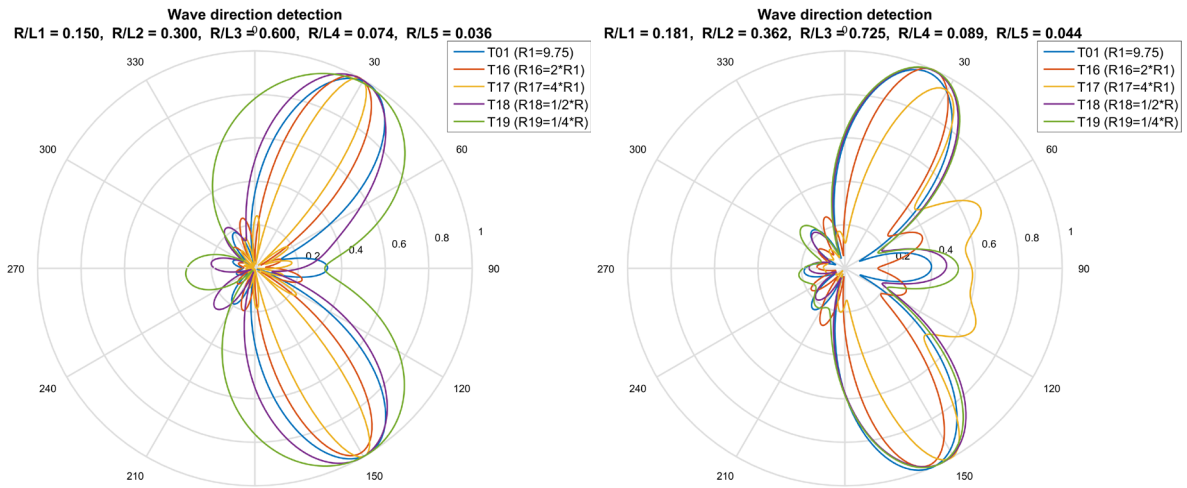


Figure 97: Respectively the obtained polar plot for test T105 testcase G3 and G4.

# M  Reconstruction plots SWDD sensitivity analysis using WIHA output

**Testcase G1: T101**
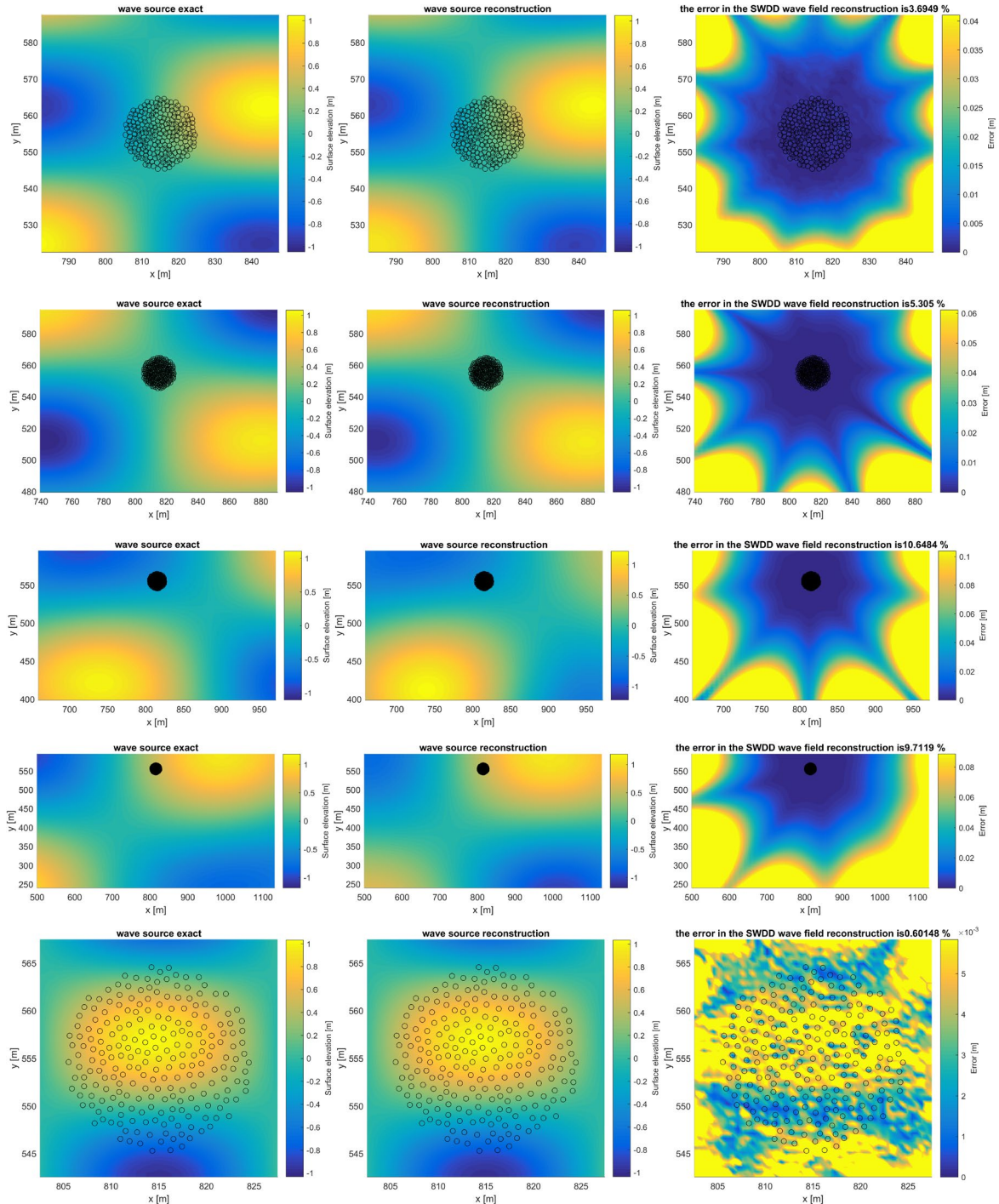


Figure 98: reconstructed wave fields for the sensitivity analyses of the SWDD method using WIHA output for testcase G1 test 101.

**Testcase G1: T103**
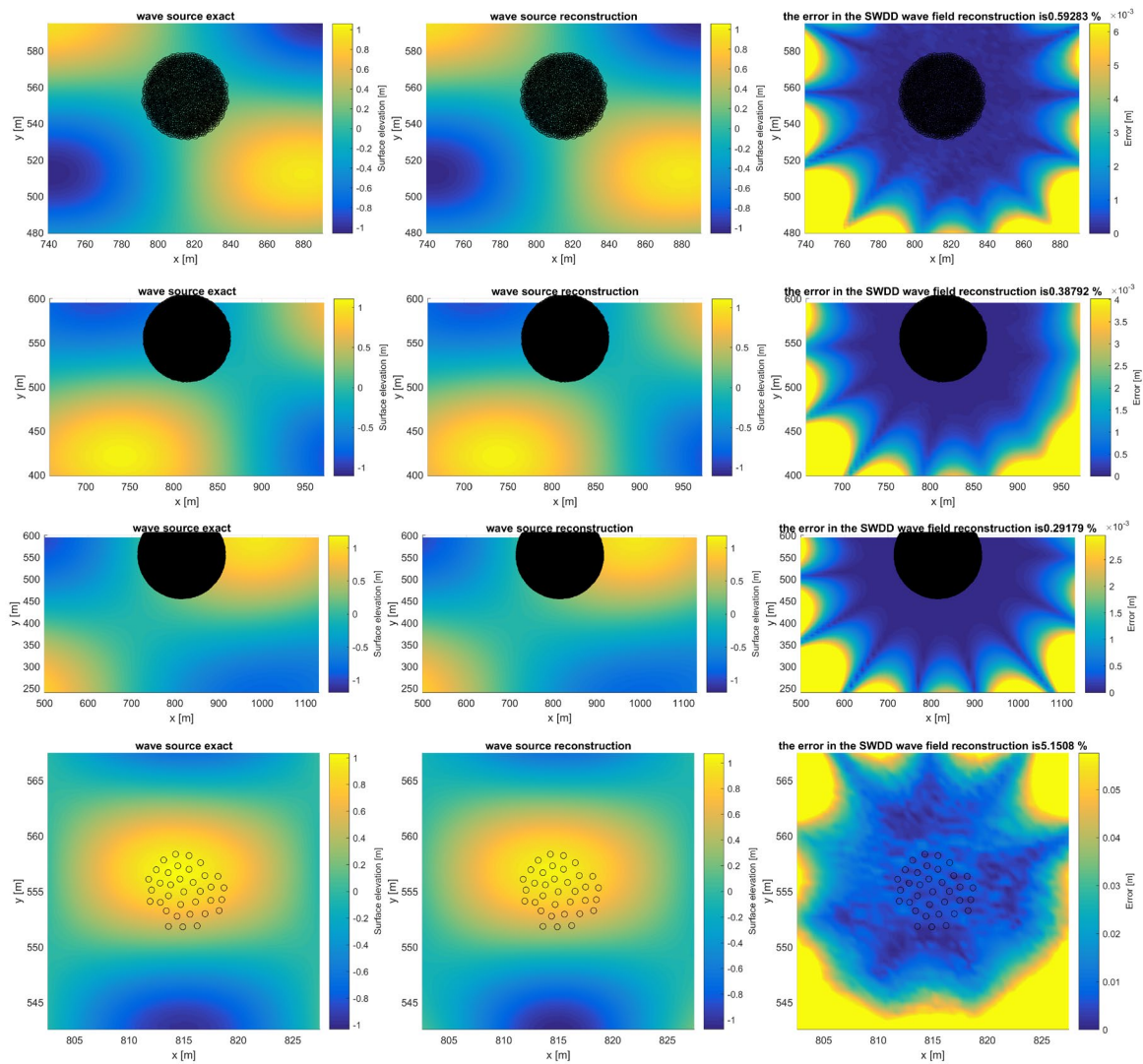


Figure 99: reconstructed wave fields for the sensitivity analyses of the SWDD method
using WIHA output for testcase G1 test 103.

**Testcase G1: T105**
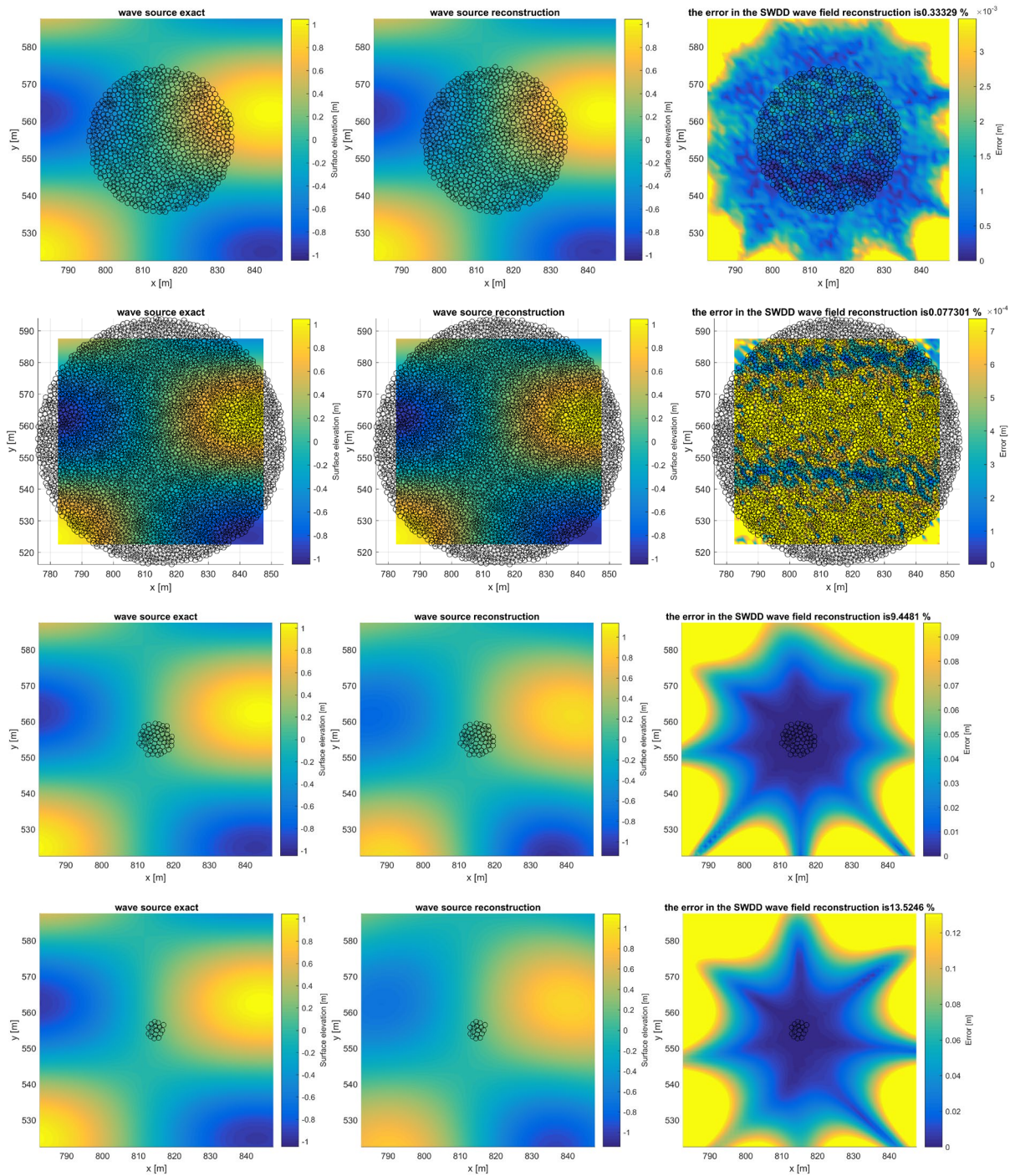


Figure 100: reconstructed wave fields for the sensitivity analyses of the SWDD method using WIHA output for testcase G1 test 105.

# N  Comparison with BDM / MLM / MEM

## SWDD spectrum
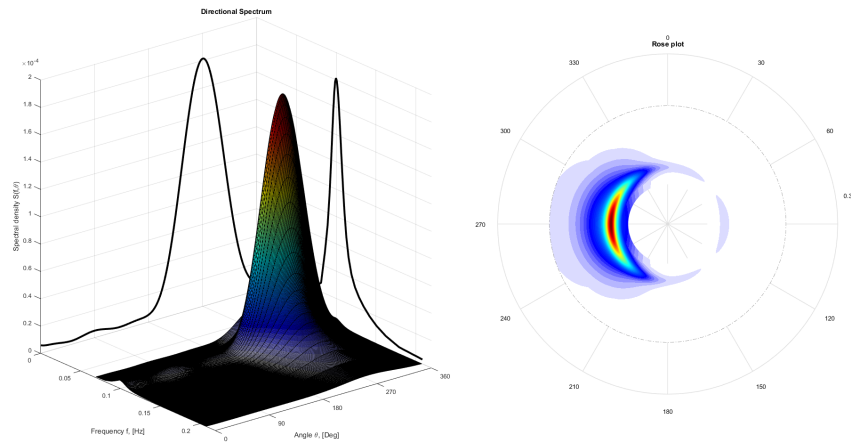


Figure 101: The obtained 2D wave spectrum (a) and polar rose plot (b) by the SWDD method using a CERC-6 array setup with $R = 0.50L_p$.

## Comparison with BDM and MLM

### BDM spectral results
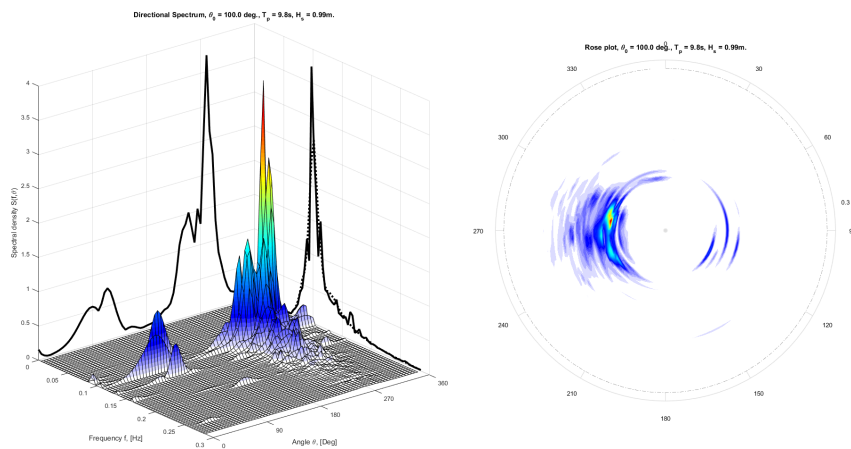


Figure 102: The obtained 2D wave spectrum (a) and polar rose plot (b) by the BDM method using a dense array setup containing 25 gauges with $R = 0.15L_p$.
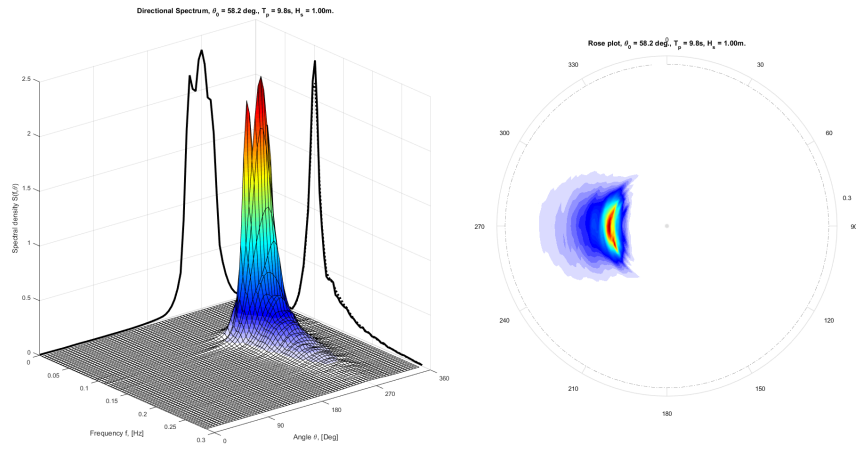
Figure 103: The obtained unimodal 2D wave spectrum (a) and polar rose plot (b) by the BDM method using a CERC-6 array setup with $R = 0.15L_p$.
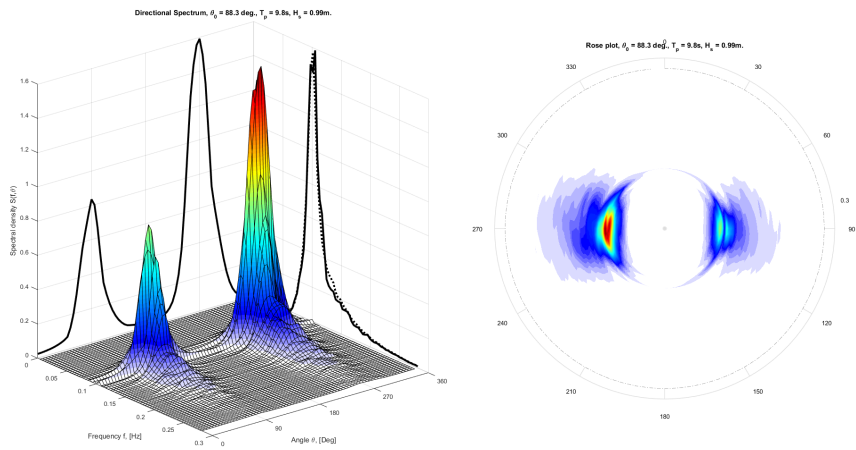


Figure 104: The obtained bimodal 2D wave spectrum (a) and polar rose plot (b) by the BDM method using a CERC-6 array setup with $R = 0.15L_p$.

## MLM spectral results
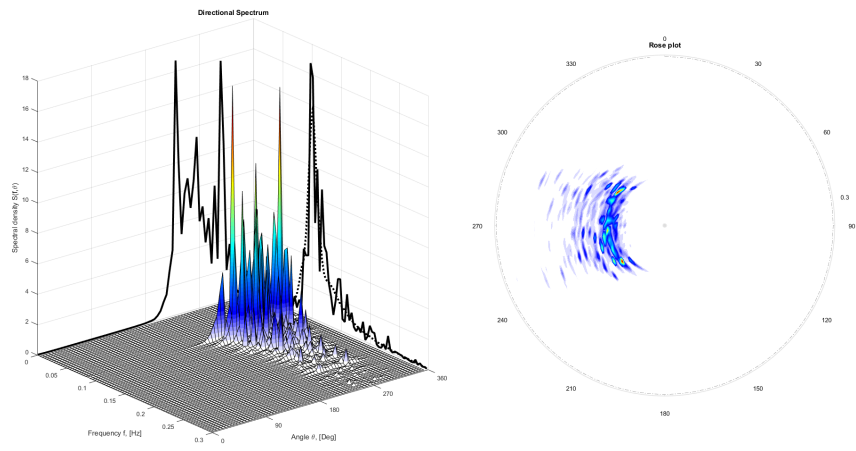


Figure 105: The obtained 2D wave spectrum (a) and polar rose plot (b) by the MLM method using a dense array setup containing 25 gauges with $R = 0.15L_p$.
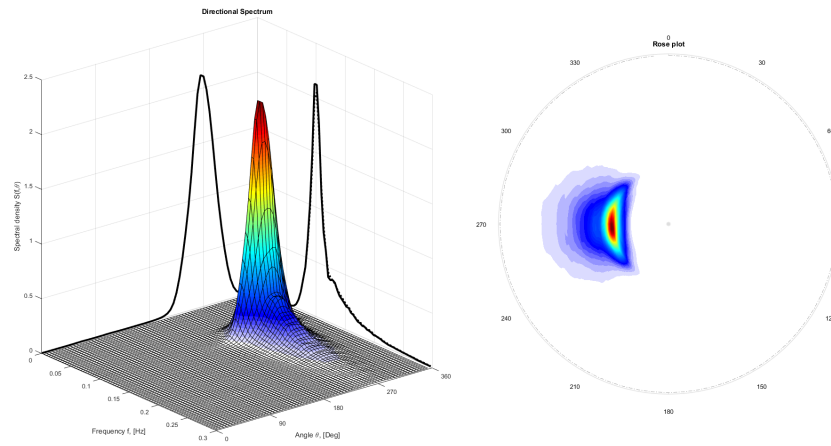
Figure 106: The obtained 2D wave spectrum (a) and polar rose plot (b)
by the MLM method using a CERC-6 array setup containing 25 gauges with $R = 0.15L_p$.
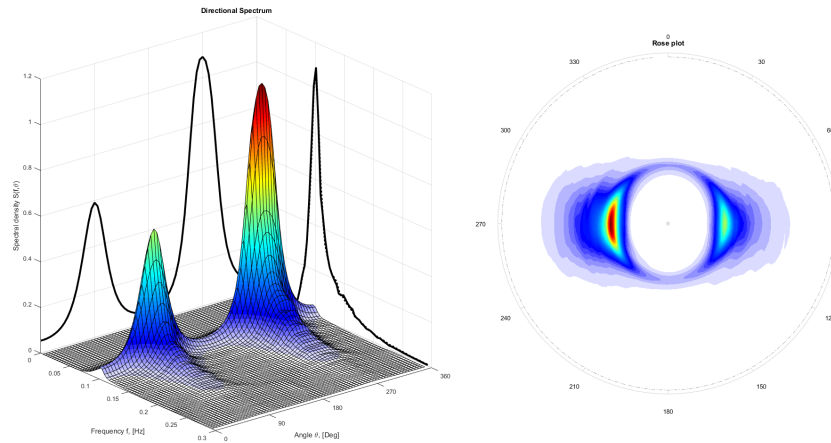


Figure 107: The obtained 2D wave spectrum (a) and polar rose plot (b)
by the MLM method using a CERC-6 array setup containing 25 gauges with $R = 0.15L_p$.

## Comparison with MEM

The SWDD method is also used to analyse the wave spectra on several output locations (GRSM 1 - 4) in the by WIHA computed navigation channel case. Where at the four output locations, GRSM 1 - 4, wave directions computed using the MEM method are known, obtained from Dusseljee et al., (2014). For the MEM method and the laboratorial results the directional spreading is unknown. The targeted directional spreading at GRSM 1 was 23.5°. The found directional spreading for the GRSM 1 gauge by SWDD is 23°.

Table 29: Main wave directions found in the navigation channel case C1 for the GRSM gauges
by the directional wave-analysis MEM method and SWDD method.

| Gauge No. | MEM dir. [°] | SWDD dir. [°] |
|-----------|-------------|---------------|
| GRSM 1 | 176 | 177 |
| GRSM 2 | 166 | 160 |
| GRSM 3 | 172 | 176 |
| GRSM 4 | 178 | 183 |
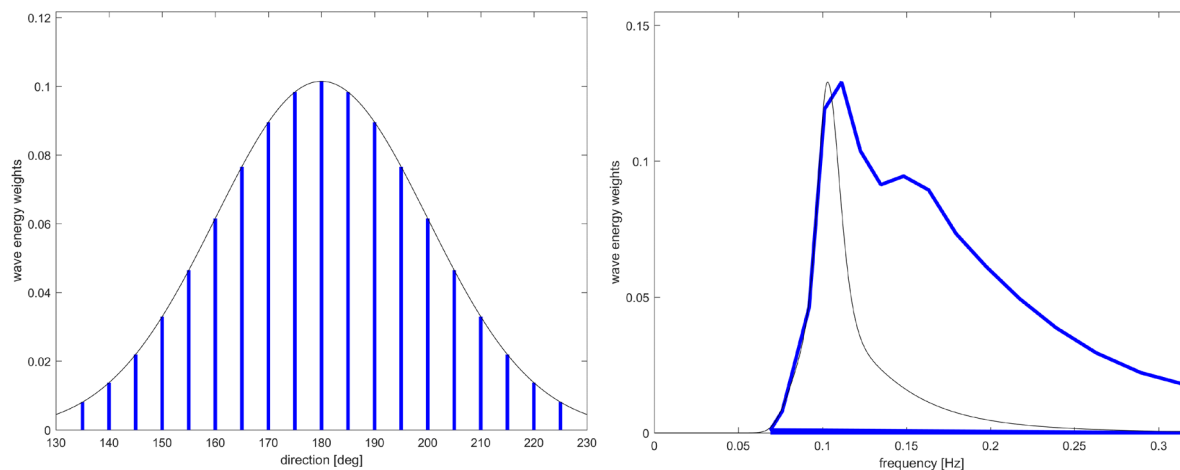
Figure 108: The input spectra for respectively the direction and frequency for the Navigation channel case C1.
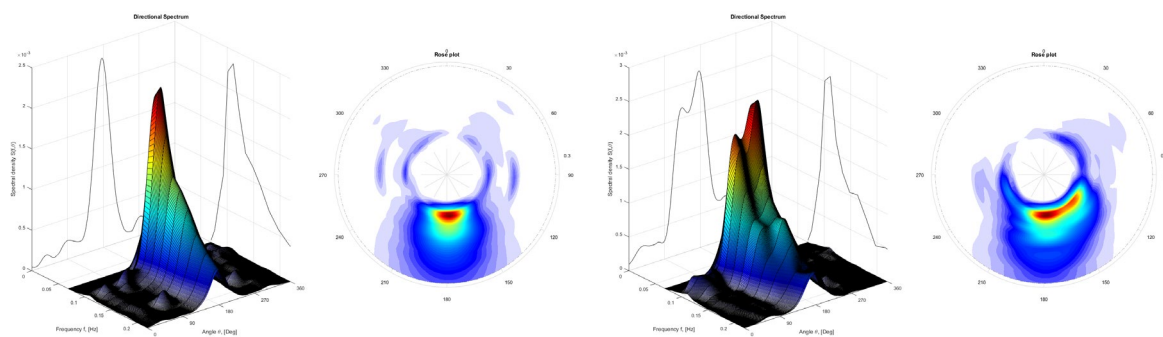


Figure 109: The obtained wave spectra by SWDD for respectively
the output locations GRSM1 and GRSM 2 in the navigation channel case.
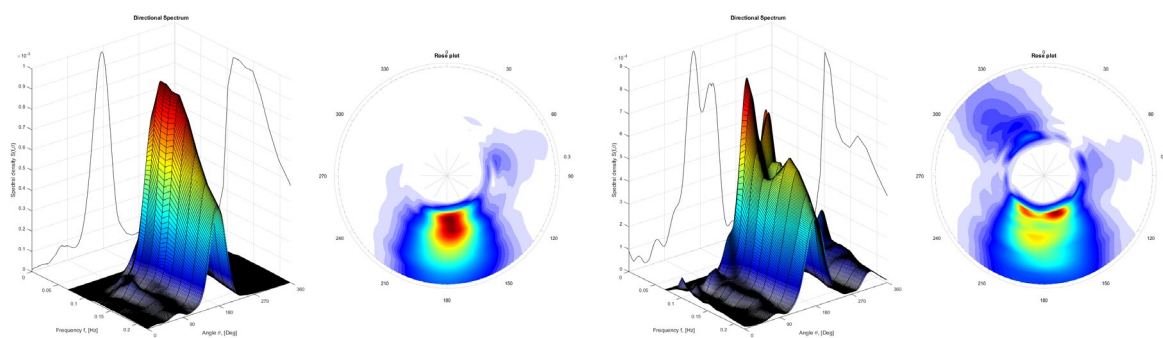


Figure 110: The obtained wave spectra by SWDD for respectively
the output locations GRSM3 and GRSM 4 in the navigation channel case.

# O  Additional SWDD analyses using WIHA model results
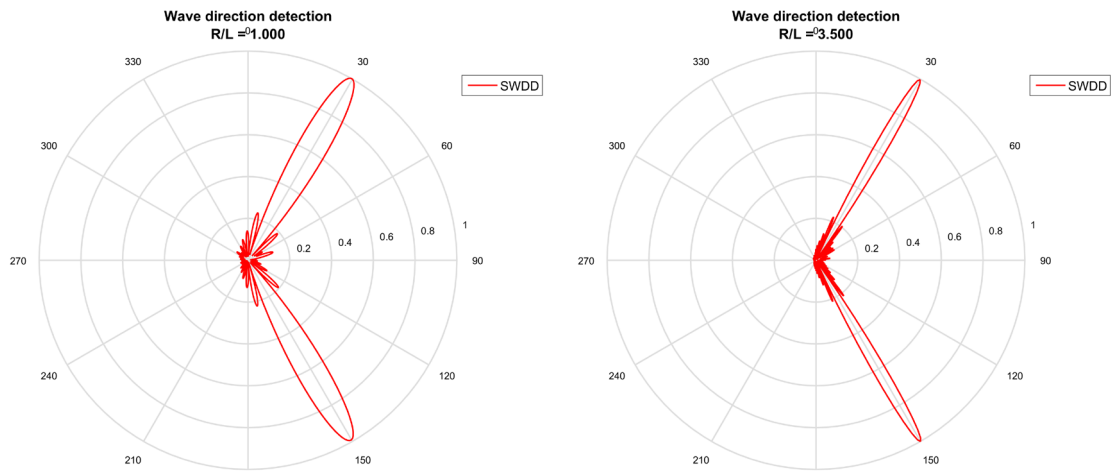


Figure 111: Obtained polar plots by the SWDD analysis using WIHA model results. For a radius of $1L$ the obtained directional resolution becomes $7.50°$ and for $3.50L$ the obtained directional resolution becomes $3.50°$.
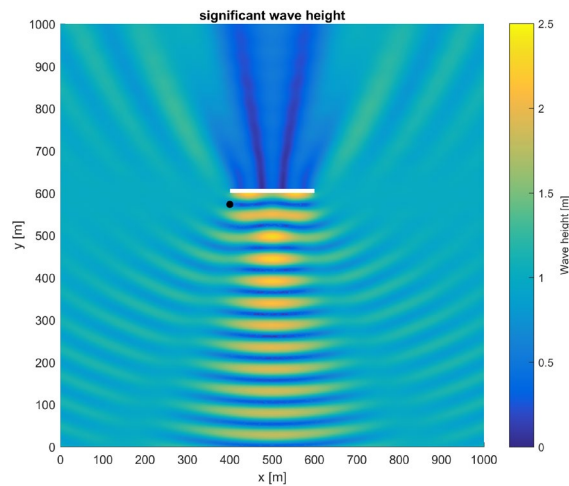


Figure 112: The used domain to analyse the influence of the distance of the array centre (black dot) to the diffraction source, varying from $0.15L$ - $2L$.
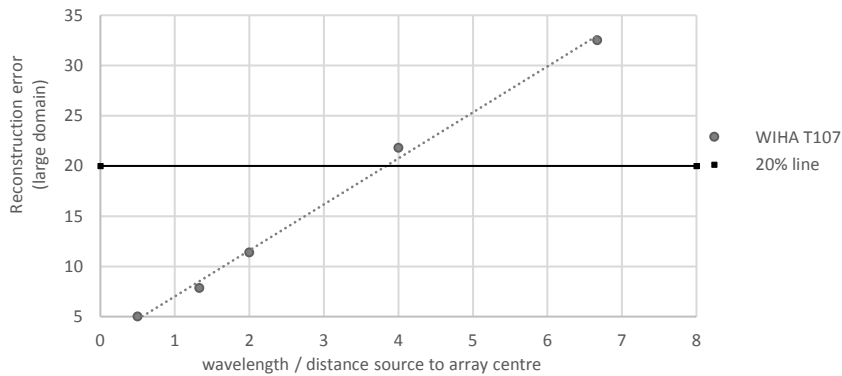


Figure 113: The results for varying the distance of the array centre to the diffraction source.

# Bibliography

Abramowitz, M., Stegun, I.A., Miller, D., 1965. Handbook of mathematical functions with formulas, graphs and mathematical tables (national bureau of standards applied mathematics series no. 55). J. Appl. Mech. https://doi.org/10.1115/1.3625776

Airy, G.B., 1845. Tides and waves. Encycl. Metrop. London, Sci. Dep.

Baldock, T.E., Simmonds, D.J., 1999. Separation of incident and reflected waves over sloping bathymetry. Coast. Eng. 38, 167–176.

Battjes, J.A., 1974. Surf similarity, in: Proc. 14h Int. Conf. Coastal Eng. pp. 466–480.

Battjes, J.A., Janssen, J.P.F.M., 1978. Energy loss and set-up due to breaking of random waves, in: Proc. 16th Int. Conf. Coastal Eng. pp. 569–587.

Benoit, M., 1993. Extensive comparison of directional wave analysis methods from gauge array data, in: Proc. 2nd Symp. Ocean Wave Measurement and Analysis. New Orleans, pp. 740–754.

Benoit, M., Frigaard, P., Schäffer, H.A., 1997. Analyzing multidirectional wave spectra: a tentative classification of available methods. Proc. 1997 IAHR Conf. 131–158.

Berkhoff, J.C.W., 1972. Computation of combined refraction - diffraction, in: Proc. 13th Int. Conf. Coastal Eng. Vancouver, pp. 471–490.

Booij, N., Holthuijsen, L.H., Ris, R.C., 1996. The "SWAN" wave model for shallow water. Coast. Eng. 668–676. https://doi.org/10.1109/MEI.2007.288479

Capon, J., 1969. High-resolution frequency-wavenumber spectrum analysis. Proc. IEEE 57, 1408–1418.

Capon, J., Greenfield, R.J., Kolker, R.J., 1967. Multidimensional maximum-likelihood processing of a large aperture seismic array. Proc. IEEE 55, 192–211.

Casulli, V., Stelling, S.G., 1998. Numerical simulation of 3D quasi-hydrostatic, free-surface flows. J. Hydraul. eng. 124, 678–686.

Chamberlain, P.G., Porter, D., 1995. The modified mild-slope equation. J. Fluid Mech. 291, 393–407.

Davis, R.E., Regier, L.A., 1977. Methods for estimating directional wave spectra from multi-element arrays. J. Mar. Res. 453–477.

de Jong, M.P.C. De, Borsboom, M.J.A., 2012. A practical post-processing method to obtain wave parameters from phase-resolving wave model results. Int. J. Ocean Clim. Syst. 3, 203–216. https://doi.org/10.1260/1759-3131.3.4.203

de Jong, M.P.C. De, Borsboom, M.J.A., 2009. Calculation of low-frequency waves in shallow water and comparison with common practice in diffraction methods. proc. Int. Conf. Ocean. offshore Arct. eng. 1–11.

de Jong, M.P.C. De, Borsboom, M.J.A., 2007. Shallow water initiative (HAWAI), WP1 : Nearshore wave modelling.

Demirbilek, Z., Panchang, V., 1998. GCWAVE: a coastal surface water wave model of the mild-slope equation. Washinton.

Donelan, M., Babanin, A., Sanina, E., Chalikov, D., 2015. A comparison ofmethods for estimating directional spectra of surface waves. J. Geophys. Res. 5040–5053. https://doi.org/10.1002/2015JC010808

Dusseljee, D., Klopman, G., Van Vledder, G., Riezebos, H.J., 2014. Impact of harbor navigation channels on waves: a numerical modelling guideline. Coast. Eng. Proc. 1, 1–12.

Eckart, C., 1952. The propagation of gravity waves from deep to shallow water, in: Gravity Waves. National Bureau of Standards, Washington, pp. 156–173.

Eikema, B.J.O., Attema, Y., Talstra, H., Bliek, A.J., Wit, L. De, Dusseljee, D.W., 2018. Spectral modeling of wave propagation in coastal areas with a harbor navigation channel. PIANC world Congr. Panama 2018 1–16.

Frigaard, P., Andersen, T.L., 2010. Technical Background Material for the Wave Generation Software AwaSys 5, DCE Technical reports, No. 64. Aalborg.

Frigaard, P., Brorsen, M., 1995. A time-domain method for separating incident and reflected irregular waves. Coast. Eng. 24, 205–215.

Goda, Y., Suzuki, Y., 1976. Estimation of incident and reflected waves in random wave experiments, in: Proc. 15th Int. Conf. Coastal Eng., ASCE, Hawaii. pp. 828–845.

Hansen, P.C., 2000. The L-curve and its use in the numerical treatment of inverse problems 2, 1–24.

Hansen, P.C., 1992. Analysis of discrete ill-posed problems by means of the L-curve. SIAM Rev. 34, 561–580. https://doi.org/10.1137/1034115

Hashimoto, N., Kobune, K., Kameyama, Y., 1987. Directional spectrum estimation from a bayesian approach. Rep. port Harb. Res. inst. 26, 62–76.

Hasselmann, K., Barnett, T.P., Bouws, E., Carlson, H., Cartwright, D.E., Enke, K., Ewing, J., Gienapp, H., Hasselmann, D., Kruseman, P., Meerburg, A., Muller, P., Olbers, D.J., Richter, K., Sell, W., Walden, H., 1973. Measurements of wind-wave growth and sweel decay during the JONSWAP 46.

Hawkes, P.J., Ewing, J.A., Harford, C.M., Klopman, G., Standsberg, C.T., Benoit, M., Schäffer, H.A., 1997. Comparative Analyses of Multidirectional Wave Basin Data, in: Proc. 27th IAHR Congress. San Fransisco, p. 45.

Hewitt, E., Hewitt, R.E., 1979. The Gibbs-Wilbraham phenomenon: An episode in fourier analysis. Arch. Hist. Exact Sci. 21, 129–160. https://doi.org/10.1007/BF00330404

Holthuijsen, L.H., 2007. Waves in oceanic and coastal waters. Cambridge University Press, New York.

Homma, S., 1950. On the behavior of seismic sea waves around circular island. Geophys. Mag. 199–208.

Horn, R.A., Johnson, C.R., 2013. Matrix analysis, 2nd ed. Cambridge University Press, New York.

Isobe, M., Kondo, K., 1984. Method for estimating directional wave spectrum in incident and reflected wave field. Proc. 19th Conf. Coast. Eng. 467–483.

Jakobsen, M.M., 2015. Manual for wave generation and analysis: software in Matlab. Aalborg. https://doi.org/DCE Technical reports, No. 191

Janssen, T.T., Van Dongeren, A.R., Kuiper, C., 2001. Phase resolving analysis of multidirection wave trains, in: Ocean Wave Measurement and Analysis, Proc., 4th Int. Symp. Waves. pp. 377–386. https://doi.org/10.1017/CBO9781107415324.004

Klopman, G., 2018b. Deterministic multi-directional wave analysis (working paper).

Klopman, G., 2018a. Mild-slope model WIHA (working paper).

Kostense, J.K., Meijer, K.L., Dingemans, M.W., Mynett, A.E., van den Bosch, P., 1986. Wave energy dissipation in arbitrarily shaped harbours of variable depth. Coast. Eng. Proc. 1, 2002–2016. https://doi.org/http://dx.doi.org/10.9753/icce.v20.%p

Krogstad, H.E., 1988. Maximum likelihood estimation of ocean wave spectra from general arrays of wave gauges. Model. Identif. Control. https://doi.org/10.4173/mic.1988.2.3

Lacoss, R., 1971. Data adaptive spectral analysis methods. Geophys. Mag. 36, 661–675. https://doi.org/10.1190/1.1440203

Legendre, A., 2015. Chapter 2: Linear least squares problems (numerical methods in matrix computations). Springer International Publishing Switzerland. https://doi.org/10.1007/978-3-319-05089-8

Longuet-Higgins, M.S., Stewart, R.W., 1962. Radiation stresses and mass transport in surface gravity waves with application to `surf beats'. J. Fluid Mech. 13, 481–504.

Lygre, A., Krogstad, H.E., 1986. Maximum entropy estimation of the directional distribution in ocean wave spectra.pdf. J. Phys. Oceanogr. 16, 2052–2060.

Mansard, E.P.D., Funke, E.R., 1980. The measurement of incident and reflected spectra using a least squares method, in: Proc. 17th Int. Conf. Coastal Eng., ASCE, New York. pp. 154–172.

Mei, C.C., 1989. The applied dynamics of ocean surface waves, 2nd ed, Adv. Ser. on Ocean Eng. World Scientific, Singapore.

Miles, J.W., 1957. On the generation of surface waves by shear flows. J. Fluid Mech. 185–204.

Monteban, D., 2016. MSc Thesis: Numerical modelling of wave agitation in ports and access channels.

Panicker, N.N., Borgman, L.E., 1970. Directional spectra from wave-gage arrays. Coast. Eng. 12, 117–136.

Phillips, O.M., 1957. On the generation of waves by turbulent wind. J. Fluid Mech. 417–445.

Pierson, W.J., Moskowitz, L.A., 1964. Proposed Spectral Form for Fully Developed Wind Seas Based on the

Similarity Theory of S. A. Kitaigorodskii. J. Geophys. Res. 69, 5181–5190.

Porter, D., 2003. The mild-slope equations. J. Fluid Mech. 494, 51–63. https://doi.org/10.1017/S0022112003005846

Rusu, E., Soares, C.G., 2013. Modeling waves in open coastal areas and harbors with phase-resolving and phase-averaged models. J. Coast. Res. 29, 1309–1325. https://doi.org/10.2112/JCOASTRES-D-11-00209.1

Seelig, W.N., Ahrens, J.P., 1981. Estimation of wave reflection and energy dissipation coefficients for beaches, revetments and breakwaters. Springfield.

Sommerfeld, A., 1896. Mathematische theorie der diffraction. Math. Ann. 47, 317–374. https://doi.org/10.1007/BF01447273

Thompson, L.L., 2006. A review of finite-element methods for time-harmonic acoustics. J. Acoust. Soc. Am. 119, 1315–1330. https://doi.org/10.1121/1.2164987

Tikhonov, A.N., Arsenin, V.Y., 1977. Solutions of ill-posed problems. John Wiley & Sons, New York.

van der Ven, P.P.D., Deltares, 2016. Benchmark tests of wave penetration in harbours.

Wang, S., Hsu, T., Weng, W., Ou, S., 2008. A three-point method for estimating wave reflection of obliquely incident waves over a sloping bottom. Coast. Eng. 55, 125–138. https://doi.org/10.1016/j.coastaleng.2007.09.002

Zanuttigh, B., van der Meer, J.W., 2006. Wave reflection from coastal structures, in: Proc. 30th Int. Conf. Coastal Eng. pp. 4337–4349.

Zelt, J.A., Skjelbreia, J.E., 1992. Estimating incident and reflected wave fields using an arbitrary number of wave gauges, in: Proc. 23rd Int. Conf. Coastal Eng., ASCE, Venice. pp. 777–789.